

# Thermochemical storage materials

***Citation for published version (APA):***

Heijmans, K. (2021). *Thermochemical storage materials: advances in molecular modeling and applications*. [Phd Thesis 1 (Research TU/e / Graduation TU/e), Mechanical Engineering]. Eindhoven University of Technology.

***Document status and date:***

Published: 17/12/2021

***Document Version:***

Publisher's PDF, also known as Version of Record (includes final page, issue and volume numbers)

***Please check the document version of this publication:***

- A submitted manuscript is the version of the article upon submission and before peer-review. There can be important differences between the submitted version and the official published version of record. People interested in the research are advised to contact the author for the final version of the publication, or visit the DOI to the publisher's website.
- The final author version and the galley proof are versions of the publication after peer review.
- The final published version features the final layout of the paper including the volume, issue and page numbers.

[Link to publication](#)

***General rights***

Copyright and moral rights for the publications made accessible in the public portal are retained by the authors and/or other copyright owners and it is a condition of accessing publications that users recognise and abide by the legal requirements associated with these rights.

- Users may download and print one copy of any publication from the public portal for the purpose of private study or research.
- You may not further distribute the material or use it for any profit-making activity or commercial gain
- You may freely distribute the URL identifying the publication in the public portal.

If the publication is distributed under the terms of Article 25fa of the Dutch Copyright Act, indicated by the "Taverne" license above, please follow below link for the End User Agreement:

[www.tue.nl/taverne](http://www.tue.nl/taverne)

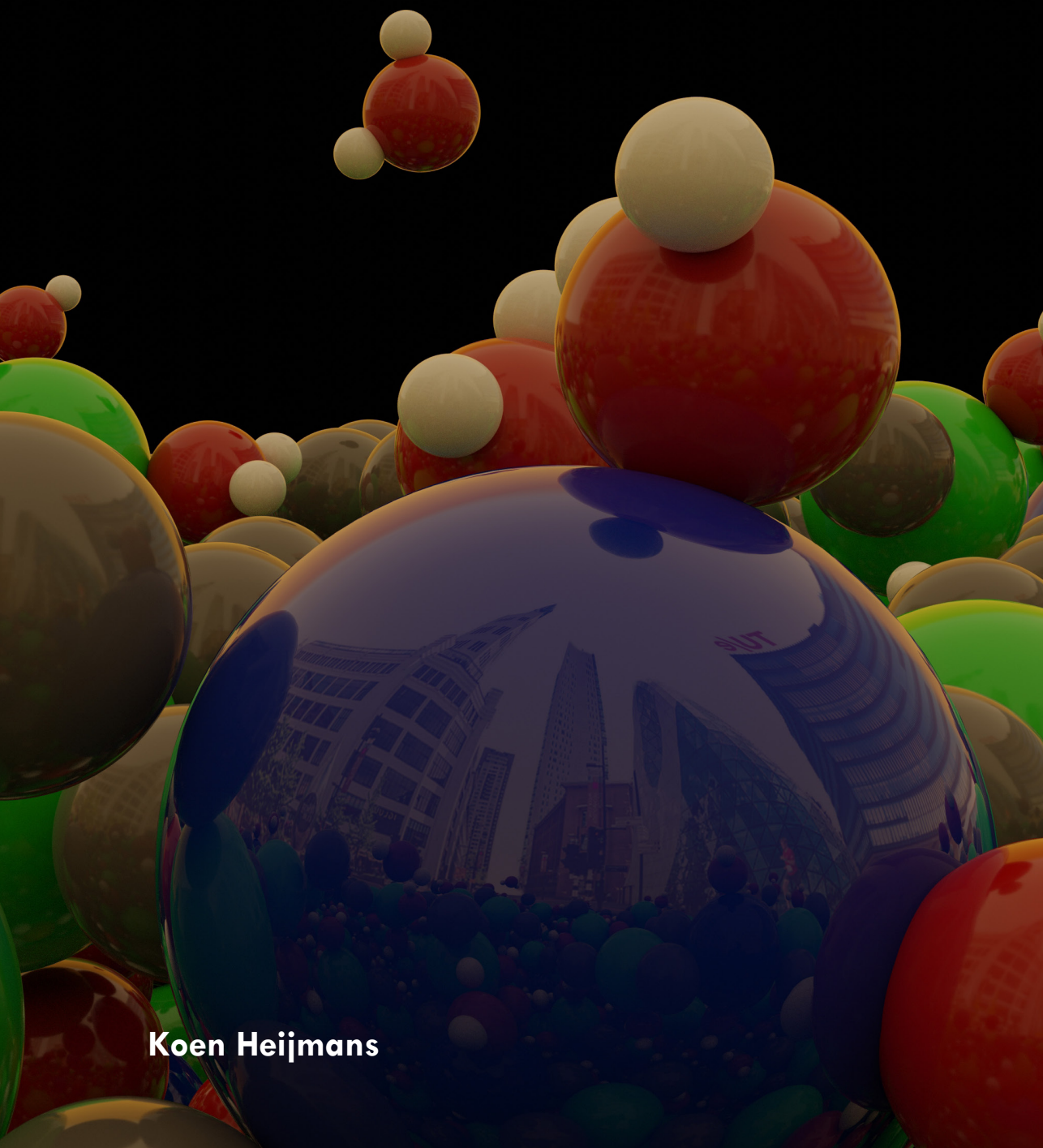
***Take down policy***

If you believe that this document breaches copyright please contact us at:

[openaccess@tue.nl](mailto:openaccess@tue.nl)

providing details and we will investigate your claim.

# Thermochemical energy storage: advances in molecular modeling



**Koen Heijmans**

# **THERMOCHEMICAL STORAGE MATERIALS: ADVANCES IN MOLECULAR MODELING AND APPLICATIONS.**

PROEFSCHRIFT

ter verkrijging van de graad van doctor aan de  
Technische Universiteit Eindhoven, op gezag van de  
rector magnificus prof.dr.ir. F.P.T. Baaijens, voor een  
commissie aangewezen door het College voor  
Promoties, in het openbaar te verdedigen  
op 17 december 2021 om 13:30 uur

door

Koen Heijmans

geboren te Eindhoven

Dit proefschrift is goedgekeurd door de promotoren en de samenstelling van de promotiecommissie is als volgt:

voorzitter:	Prof. dr.	L.P.H. de Goey
1 <sup>e</sup> promotor:	Prof. dr. ir.	D.M.J. Smeulders
copromotor:	dr.	S.V. Gaastra–Nedea
leden:	Prof. dr. ir.	J.M.V.A. Koelman
	Prof. dr.	S. Calero
	Prof. dr. ir.	T.J.H. Vlugt (Technische Universiteit Delft)
	Prof. dr.	L.F. Cabeza (University of Lleida)
	Prof. dr.	E.J. Meijer (Universiteit van Amsterdam)
	Prof. dr.	J.D.R. Harting (Helmholtz Institute Erlangen-Nürnberg)

*Het onderzoek of onderwerp dat in dit proefschrift wordt beschreven is uitgevoerd in overeenstemming met de TU/e Gedragscode Wetenschapsbeoefening*





*Printed by:* Ipskamp Printing B.V.

Copyright © 2021 K. Heijmans

Copyright of the individual chapters containing published articles belongs to the publisher of the journal listed at the beginning of the respective chapters. All rights reserved. No part of this publication may be reproduced, distributed, or transmitted in any form or by any means, including photocopying, recording, or other electronic or mechanical methods, without the prior permission of the copyright owner.

A catalogue record is available from the Eindhoven University of Technology Library  
ISBN: 978-90-386-5415-7



# CONTENTS

<b>Summary</b>	<b>vii</b>
<b>1 Introduction</b>	<b>1</b>
1.1 Thermal Energy Storage. . . . .	2
1.1.1 Thermochemical Materials . . . . .	4
1.2 Introduction to Computational Modeling. . . . .	7
1.2.1 Density Functional Theory. . . . .	8
1.2.2 Molecular Models . . . . .	12
1.3 Thesis Outline . . . . .	19
<b>2 Chemical Analysis of Doped Salts Hydrates</b>	<b>23</b>
2.1 Methods . . . . .	26
2.1.1 Exploration of New Doped Structures . . . . .	26
2.1.2 Chemical Bonding Analysis . . . . .	28
2.2 Results & Discussion . . . . .	29
2.2.1 Convex Hull – Stability of the Explored Structures . . . . .	29
2.2.2 Storage Density . . . . .	32
2.2.3 Chemical Bonding Analysis . . . . .	34
2.2.4 Atomic Charges . . . . .	35
2.2.5 H–Cl Interactions . . . . .	35
2.3 Conclusions. . . . .	39
<b>3 ReaxFF Development and Application for Calcium Chloride Hydrates</b>	<b>41</b>
3.1 Introduction . . . . .	42
3.2 Computational Methods . . . . .	43
3.2.1 Quantum Mechanical (QM) Computations . . . . .	44
3.2.2 Reactive Force Field (ReaxFF) . . . . .	44
3.2.3 Metropolis Monte Carlo (MMC) Parameterization . . . . .	45
3.2.4 Material Properties Calculation . . . . .	47
3.3 Results and Discussion . . . . .	49
3.3.1 ReaxFF Re-parameterization Results. . . . .	49
3.3.2 Material Characterization . . . . .	51
3.3.3 Expansion and Crack Formation . . . . .	59
3.4 Conclusions. . . . .	60
<b>4 Advanced Diffusion Methods for H<sub>2</sub>O in Salt Hydrates</b>	<b>63</b>
4.1 Introduction . . . . .	64
4.2 Methodology . . . . .	66
4.2.1 Parallel to the Bin . . . . .	67
4.2.2 Perpendicular to the Bin for Homogeneous Regions . . . . .	68

4.2.3	Perpendicular to the Bin for Inhomogeneous Regions . . . . .	69
4.2.4	ReaxFF. . . . .	69
4.3	Validation . . . . .	70
4.3.1	Validation Homogeneous System: Liquid Water . . . . .	70
4.3.2	Validation Inhomogeneous System: Water Vapor–Liquid Interface. . . . .	71
4.4	Results & Discussion – Salt Hydrates . . . . .	72
4.4.1	Dehydration of $\text{CaCl}_2 \cdot 2\text{H}_2\text{O}$ . . . . .	72
4.4.2	Diffusion in $\text{CaCl}_2 \cdot 2\text{H}_2\text{O}$ . . . . .	74
4.5	Conclusions. . . . .	77
<b>5</b>	<b>ReaxFF for Vapor–Liquid Equilibrium</b>	<b>79</b>
5.1	Introduction . . . . .	80
5.2	Methodology . . . . .	81
5.2.1	ReaxFF. . . . .	81
5.2.2	Gibbs Ensemble Monte Carlo . . . . .	84
5.3	Results . . . . .	85
5.3.1	ReaxFF- $\text{lg}_{\text{CO}_2}$ & ReaxFF- $\text{lg}_{\text{H}_2\text{O}}$ Validation. . . . .	85
5.3.2	GEMC–ReaxFF Validation . . . . .	88
5.3.3	VLE with GEMC–ReaxFF. . . . .	88
5.4	Conclusions. . . . .	90
<b>6</b>	<b>ReaxFF for Hydration Characteristics of Salts</b>	<b>93</b>
6.1	Introduction . . . . .	94
6.2	Methodology . . . . .	96
6.2.1	GCMC . . . . .	96
6.2.2	Biased ReaxFF–GCMC . . . . .	98
6.2.3	Force Fields . . . . .	101
6.3	Results & Discussion . . . . .	102
6.3.1	WCA–GCMC Validation . . . . .	102
6.3.2	Gaussian Preference Validation . . . . .	104
6.3.3	Hydration of Magnesium Chloride Hexahydrate Clusters . . . . .	104
6.3.4	Hydration of Magnesium Chloride Clusters . . . . .	106
6.4	Conclusions. . . . .	108
<b>7</b>	<b>ReaxFF Development and Application for Combined Salt Hydrates</b>	<b>111</b>
7.1	Introduction . . . . .	112
7.2	ReaxFF Development . . . . .	112
7.2.1	MMC ReaxFF Parameterization . . . . .	113
7.3	Characterization of Doped Salt Hydrates . . . . .	116
7.3.1	Stability Doped Structures . . . . .	116
7.3.2	Dehydration . . . . .	117
7.3.3	Hydrolysis Resistance . . . . .	121
7.4	Discussion . . . . .	121
<b>8</b>	<b>Conclusion &amp; Outlook</b>	<b>125</b>
8.1	Conclusion . . . . .	126
8.2	Outlook . . . . .	129

<b>A Appendix – Developed Reactive Force Fields</b>	<b>131</b>
<b>B Appendix – Chemical Analysis of Doped Salts Hydrates</b>	<b>143</b>
B.1 Crystal structure change . . . . .	143
<b>C Appendix – ReaxFF Calcium Chloride Hydrates</b>	<b>145</b>
C.1 Dehydration . . . . .	145
C.2 Structures for surface energy calculation . . . . .	146
<b>D Appendix – Derivation Smoluchowski Survival Probability</b>	<b>149</b>
D.1 Homogeneous survival probability . . . . .	149
D.2 Inhomogeneous survival probability . . . . .	151
<b>E Appendix – H<sub>2</sub>O &amp; CO<sub>2</sub> ReaxFF Optimization</b>	<b>153</b>
E.1 CO <sub>2</sub> – ReaxFF MMC optimization . . . . .	154
E.1.1 Geometry optimization of single molecule. . . . .	154
E.2 H <sub>2</sub> O . . . . .	157
<b>F Appendix – GCMC</b>	<b>161</b>
F1 Acceptance rules for GCMC . . . . .	161
F2 WCA parameters . . . . .	163
F3 Gaussian preference . . . . .	164
F4 GCMC hydration results . . . . .	165
<b>G Appendix – MMC Results Calcium–Magnesium Hydrates Combined Force Field</b>	<b>167</b>
<b>References</b>	<b>171</b>
<b>Acknowledgements</b>	<b>195</b>
<b>Curriculum Vitae</b>	<b>197</b>
<b>List of Publications</b>	<b>199</b>



# SUMMARY

In the transition towards a future sustainable energy society, a reliable energy storage system is key to fully utilizing renewable energy sources like solar energy. A storage is required to bridge the mismatch between the intermittent renewable energy supply and the societies' fluctuating energy demand. Thermochemical energy storage is a highly appealing solution for storing energy. The active materials for such a storage are known as thermochemical materials (TCMs). Salt hydrates are among the most studied TCMs for domestic applications due to their availability, costs, operating temperature, and achievable energy density. Thermochemical energy storage, based on salt hydrates, relies on a reversible chemical reaction and works according to three basic steps. Step (1), in times of an energy surplus, the storage is charged by using the surplus energy to dehydrate the salt, via an endothermic reaction, into a lower hydrated salt and water vapor. Step (2), in times of balanced energy supply and demand, the water and salt are kept separately, and no energy is lost. Step (3), in times of a lack of energy supply, the system is discharged, with a heat-releasing exothermic reaction, by recombining the dried salt hydrate with the water vapor into a higher salt hydrate. This storage concept allows one to store heat with low losses over extended periods in a relatively compact volume.

The two salt hydrates,  $\text{MgCl}_2 \cdot n\text{H}_2\text{O}$ , and  $\text{CaCl}_2 \cdot n\text{H}_2\text{O}$  ( $n=0,1,2,4,6$ ) are promising TCMs to be used in the domestic environment because they have relatively high hydration energies; they are widely available; and their reaction equilibrium temperatures are in range with domestic heating applications. However, challenges related to the material's stabilities, kinetics, melting temperatures, deliquescence, and undesired side reactions withhold them from practical applications. In this sense, we used multiple molecular level simulation methods to study their key characteristics related to these challenges. The molecular modeling methods helped to gain more insights into characteristics like water and heat transport through the salts. Furthermore, these methods help predicting the effect of molecular-sized modifications which might aid the thermochemical heat storage performance.

We used Density Functional Theory (DFT) and Molecular Dynamics (MD) algorithms to investigate these two salts separately, as well as a promising combination of them ( $\text{Mg}_{(1-x)}\text{Ca}_x\text{Cl}_2 \cdot n\text{H}_2\text{O}$ ). DFT, in combination with the genetic algorithm USPEX, was used to study the stability and crystal formation of  $\text{Mg}_{(1-x)}\text{Ca}_x\text{Cl}_2 \cdot n\text{H}_2\text{O}$ . It revealed that the combined structures are less stable than the pure structures with marginal differences. Furthermore, DFT-based chemical bonding analyses showed a promising decrease in the undesired H-Cl interaction in a Ca-rich environment compared to pure  $\text{MgCl}_2$ . This is caused by the stronger Ca-Cl interaction and a less polar  $\text{H}_2\text{O}$  molecule in such environment.

In combination with reactive force fields (ReaxFF), MD simulations are used to analyze the salts' heat and mass transfer properties. The used ReaxFFs are developed with a Metropolis Monte Carlo force field optimizer in combination with accurate DFT refer-

ence data. The MD studies predict a low thermal conductivity of the salts, comparable to experimentally observed values. A low thermal conductivity reduces the applicability of the salts as TCM in terms of power output and the occurrence of local hotspots. Furthermore, a Smoluchowski-diffusion-equation-based method showed an extremely low water diffusion for bulk crystalline salt structures. Low water mobility results in local overhydrated spots and low power outputs. However, this method also revealed that local imperfections in the salt crystal, like cracks, pores, and doping, significantly improve water diffusion and dehydration. This increased water mobility aids the salt hydrates as TCM application.

Next to the heat and mass transfer phenomena, it is essential to gain insight into the salts' phase equilibria, at which temperatures and vapor pressures the (de)hydration reaction occurs. For this reason, a ReaxFF Grand Canonical Monte Carlo (ReaxFF-GCMC) algorithm was developed. The ReaxFF-GCMC algorithm was complemented with the relative computationally cheap Weeks-Chandler-Andersen (WCA) potential to improve this algorithm's efficiency. The alternation between WCA and ReaxFF potential makes it possible to scan many interactions with the WCA potential and accordingly recompute the most probable situations with the more expensive but accurate reactive force field. The WCA-ReaxFF-GCMC algorithm captured the deliquescence behavior of  $\text{MgCl}_2 \cdot n\text{H}_2\text{O}$ , in agreement with experiments, and showed the multiple-step hydration process of the salt. A prerequisite for accurately describing the salt-vapor interaction is the accurate description of water vapor. In this respect, the ReaxFF required extra improvement in terms of long-range dispersion interactions of  $\text{H}_2\text{O}$ . This added dispersion interaction to the ReaxFF for  $\text{H}_2\text{O}$  was validated by computing the Vapor-Liquid Equilibrium (VLE) curve with a Gibbs ensemble Monte Carlo (GEMC) algorithm. This validation required the developed ReaxFF-GEMC combination.

The newly developed ReaxFF for combined  $\text{Mg}_{(1-x)}\text{Ca}_x\text{Cl}_2 \cdot n\text{H}_2\text{O}$  salt, based on the combination of the separate  $\text{MgCl}_2 \cdot n\text{H}_2\text{O}$ ,  $\text{CaCl}_2 \cdot n\text{H}_2\text{O}$ , and  $\text{H}_2\text{O}$  ReaxFFs, was used to explore and analyze doped salts and compare their performance with respect to their pure counterparts. Comparable to the crystal imperfections, the combined salt results in improved water mobility. The ReaxFF also confirmed the DFT results of decreased crystal stability by combining the salts. As a result of the decreased stability, no reduction of the undesired hydrolysis side reaction ( $\text{H-Cl}$  formation) was observed despite the decreased  $\text{H-Cl}$  interaction for Ca-doped  $\text{MgCl}_2 \cdot n\text{H}_2\text{O}$  structures.



# 1

## INTRODUCTION

*Every end has a beginning.*

*The main application and used methodologies of this dissertation are introduced in this first chapter. Section 1.1 introduces the thermochemical energy storage concept, section 1.2 introduces the used methodologies, and section 1.3 defines the research outline and including chapters.*

## 1.1. THERMAL ENERGY STORAGE

Climate change and environmental degradation, caused by anthropogenic pollution and greenhouse gas emissions, are one of the major challenges for humanity. With the European Green Deal, the EU committed to a plan where it aims for a climate-neutral society by 2050 [1]. In other words, an economy with net-zero greenhouse gas emissions. The vision of this Green Deal follows the Paris Agreement, which is subjected to keep the global temperature increase to  $1.5^{\circ}\text{C}$ , or at least well below  $2^{\circ}\text{C}$  [2]. In the transition towards a climate-neutral society, a significant cut in greenhouse gas emissions can be made for the domestic heat demand, since hot tap water and space heating combined account for 79% of the final energy use of EU households [3]. To reduce this domestic heat demand, besides conventional measures like upgrading conventional boilers, using high-performance insulation, and solar collectors, one could aim for a net-zero energy demand by storing excess heat in times of high supply - e.g., in summer - and use it in times of high demand - e.g., in winter [4]. Figure 1.1 shows an example of the yearly mismatch between solar heat supply and domestic heat demand. The annual natural gas use for a  $70\text{ m}^2$  apartment in Eindhoven is given by the red line, which includes both space heating and hot tap water heating. The estimated heat supply that is yielded by  $14\text{ m}^2$  solar collectors in Eindhoven, is given by the blue line. For the computation of the energy yield by the solar collectors, an efficiency of 50% is assumed and climate data is taken from the Koninklijk Nederlands Meteorologisch Instituut (KNMI). For the given year, the total annual energy demand is roughly 88% of the total annual energy yield of the solar collectors\*. The figure clearly shows the mismatch between annual heat demand and solar heat supply. The use of a seasonal heat storage system could bridge the mismatch between summer and winter, thereby reducing the natural gas demand of the given apartment. One must note that for the given example, no specific assumption is made regarding the heat loss that occurs during storage. Furthermore, the given apartment is poorly insulated, in the transition towards a sustainable design this would be the first step according to the Trias Energetica concept [5]. Upgrading the insulation would significantly decrease the yearly heat demand.

There are multiple concepts to store excess heat for a later usage. Heat can be stored in sensible heat storage, latent heat storage, sorption heat storage, or as a combination of these. In Table 1.1 some examples of these storage concepts are provided, including some often considered materials. In a sensible heat storage system, energy is stored by raising a medium's temperature and thermally insulating it from the environment. Conventional domestic hot water boilers are based on this principle [6]. The advantage is its simplicity, availability of the medium (most often water), and the maturity of the concept [4]. However, the volumetric energy capacity for a sensible heat storage system is relatively low compared to the other methods [7, 8], thus one would require large amounts of it. For example, water with a temperature lift of  $70^{\circ}\text{C}$  stores  $0.29\text{ GJ/m}^3$ . In this case, the illustrated example of Figure 1.1 would require approximately  $90\text{ m}^3$  of water. The estimated volume only regards the required space for the water itself and excludes the required space for the system (e.g., insulation, heat exchangers, etc.). Additionally, even a very well insulated water tank loses heat over time, which makes it less suitable for

\*For the missing data for the natural gas use from the 1st till the 18th of November 2017, a similar energy demand is assumed as the first available week - 18–25th of November.

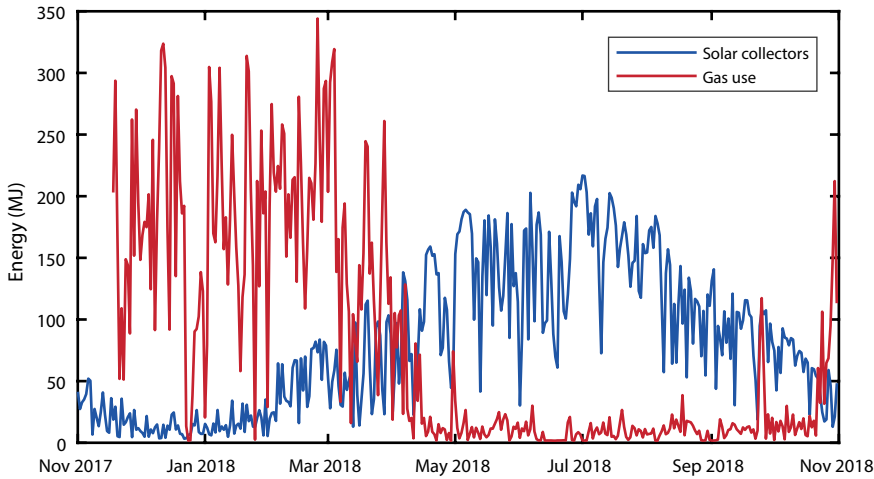


Figure 1.1: Example of yearly natural gas use for a small apartment located in Eindhoven (including domestic heating and hot tap water) given in red, versus the energy yield of  $14 \text{ m}^2$  solar collector with an assumed 50% efficiency, given in blue.

long-term storage.

In a latent heat storage system, energy is stored in the latent heat for fusion and freezing (respectively, melting and solidification) of a phase-changing material [13, 14]. Materials used for such a system are known as Phase Changing Materials (PCMs). Due to the relatively large enthalpy change related to the phase change of the material, it can in general achieve a 3–4 times higher storage density compared to sensible storage systems with a temperature lift of  $20^\circ\text{C}$  [9], similar to the previously given example of the hot water sensible storage system with a temperature lift of  $70^\circ\text{C}$ . The operational thermal window is limited around the melting / solidification point of the material. This narrow temperature window resulted in a wide range of PCMs, for different temperatures ranges [12]. Next to the limited temperature range, PCMs face difficulties regarding (long-term) chemical stability and dilution effects [15, 16].

The third alternative is sorption heat storage, which is defined as the phenomenon of fixating a gas or vapor (sorbate) by a condensed liquid or solid (sorbent) [7]. There are two basic types, physical sorption (physisorption), and chemical sorption (chemisorption). By physisorption, most often vapor adsorption on a solid surface is considered. In this case, the main attraction between sorbate and sorbent is based on van der Waals forces. Whereas by chemisorption, the sorbate is absorbed in the medium, and the attraction is dominated by strong ionic and/or covalent interactions. Based on its interactions, chemisorption systems are often referred to as *thermochemical energy storage* [7], which will be the used terminology in this thesis. Due to the stronger bonds involved, the latter typically has a larger sorption energy, and thereby it can achieve a higher storage density [7], up to  $1\text{--}3 \text{ GJ/m}^3$ . This is however a theoretical value based on the reaction enthalpy of the thermochemical material (TCM). In practice, the volu-

Table 1.1: Examples of volumetric storage densities for different types of storage with some selected materials. With  $T_{\text{lift}}$  as temperature lift for sensible storage,  $T_{\text{melt}}$  as melting temperature for the latent heat storage, and  $T_{\text{sorp.}}$  as desorption temperature for the sorption storage.

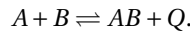
System	Storage density (GJ/m <sup>3</sup> )	Comment
<b>Sensible</b>		
concrete	0.04	$\Delta T_{\text{lift}} = 20\text{ }^{\circ}\text{C}$
granite	0.05	$\Delta T_{\text{lift}} = 20\text{ }^{\circ}\text{C}$
water	0.08	$\Delta T_{\text{lift}} = 20\text{ }^{\circ}\text{C}$
water	0.3	$\Delta T_{\text{lift}} = 70\text{ }^{\circ}\text{C}$
<b>Latent</b>		
water	0.3	$T_{\text{melt}} = 0\text{ }^{\circ}\text{C}$
paraffins	0.2	$T_{\text{melt}} \approx 5\text{--}130\text{ }^{\circ}\text{C}$ [9]
salt hydrates	0.3	$T_{\text{melt}} \approx 5\text{--}130\text{ }^{\circ}\text{C}$ [9]
salts	0.6–1.5	$T_{\text{melt}} \approx 300\text{--}800\text{ }^{\circ}\text{C}$ [9]
<b>Sorption</b>		
zeolites	0.4–0.6	physisorption $T_{\text{sorp.}} \approx 150\text{--}200\text{ }^{\circ}\text{C}$ [10]
salt hydrates	1–3	chemisorption $T_{\text{sorp.}} \lesssim 250\text{ }^{\circ}\text{C}$ [11]
hydrides / oxides / carbonates	1–3	chemisorption $T_{\text{sorp.}} \gtrsim 250\text{ }^{\circ}\text{C}$ [12]

metric storage density relies on operating conditions and includes system components like the heat exchanger, condenser, and material pores [17], which significantly reduces the overall system density. Nonetheless, it is important to aim for TCMs with a high reaction enthalpy. In the IEA–SHC Task 42/24 meeting, it was agreed that in order to have a compatible thermochemical heat storage system it must achieve a 4 to 8 times higher volumetric storage density than the conventional hot water storage [17]. Next to the potentially higher storage density, another advantage is that it hardly loses energy over time because the energy is stored in the bond breaking and formation between sorbate and sorbent and not as sensible heat. On the other side, with each separate discharging moment, the TCM itself is heated, resulting in an energy loss related to the thermal capacity of the material. In general, thermochemical energy storage technology is way less mature than other storage technologies [4] and still faces many challenges. However, due to its promising advantages of high storage capacity and no heat losses over time, it recently attracts much attention [7, 8, 18–22] to overcome these challenges.

This thesis focuses on advanced numerical molecular modeling of potential thermochemical storage materials (TCMs), namely  $\text{MgCl}_2 \cdot n\text{H}_2\text{O}$  and  $\text{CaCl}_2 \cdot n\text{H}_2\text{O}$  ( $n = 0, 1, 2, 4, 6$ ), to study their characteristics and improve their applicability.

### 1.1.1. THERMOCHEMICAL MATERIALS

As described before, thermochemical energy storage is based on a reversible reaction between two components, as visualized in Figure 1.2 and according to the reaction:



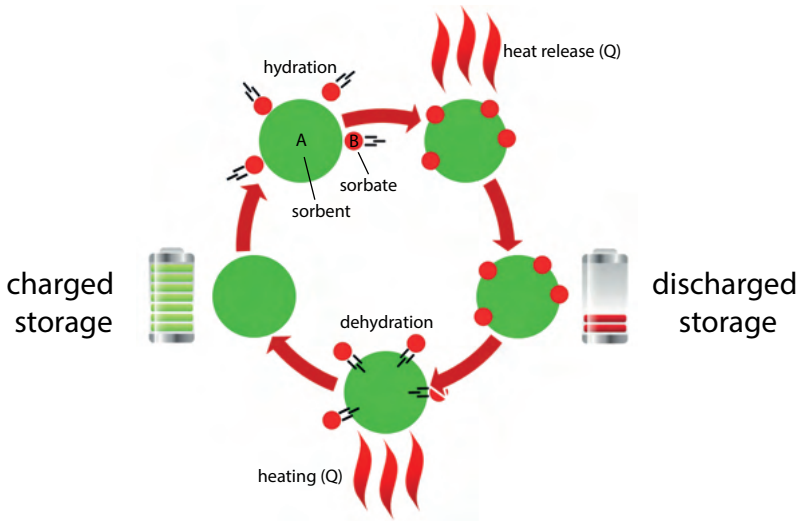
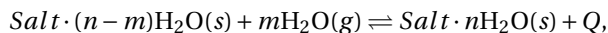


Figure 1.2: Visual representation of the thermochemical heat storage concept.

When there is a surplus of heat (e.g., May to October in the example Figure 1.1), the excess heat ( $Q$ ) is used to split material  $AB$ , via an endothermic reaction, into sorbent  $A$  and sorbate  $B$ . When there is a lack of heat (e.g., November to April in the example Figure 1.1), the sorbent  $A$  and sorbate  $B$  are combined via an exothermic reaction to material  $AB$ , and heat  $Q$  is released. Especially, thermochemical heat storage systems based on gas–solid sorption mechanisms have theoretical high energy storage densities. Where the amount of heat that is stored, is the condensation energy of the sorbate plus the reaction enthalpy of the materials. Since heat is stored in the binding – or to better say, dissociation – energy between  $A$  and  $B$ , no sensible heat is lost during (long) inactive storage periods.

The gas–solid sorption systems can be roughly divided into two groups based on the bond strength between the sorbent and sorbate, (1) strong chemisorption, and (2) weak chemisorption [18]. (1) Strong chemisorption systems (e.g., metallic hydrides, hydroxides, carbonates) have a strong bond and thus a high storage capacity. Therefore, they also require medium to high thermochemical storage operating temperatures, which are dictated by the reaction equilibrium. Hydrogen systems like metal hydrides and hydroxide systems typically operate at medium temperature ( $250 < T < 450$  °C), carbonates typically operate at high temperature ( $T > 450$  °C) [23]. Because of the high operating conditions, these are usually large-scale systems applied in industrial processes. (2) Weak chemisorption systems (e.g., salt in combination with water, ammonia, ethanol, or methanol) have a weaker bond strength and thereby lead to lower operating temperatures ( $T < 250$  °C). The lower operating temperatures makes them ideal for domestic heating since these temperatures can be reached by solar collectors for the built environment. Most often, weak chemisorption systems make use of salt hydrates in combination with water vapor because of practical reasons like the presence of water vapor in

the air. These systems make use of the hydration energy of the salt, following:



When heated, the salt hydrate dissociates into water and a lower hydrated or anhydrous salt. Vica versa, if water vapor is added, it hydrates into a higher hydrated salt. Some salts have multiple hydration levels ( $n$ ), which allows multiple thermodynamic equilibria. An ideal thermochemical material (TCM) has a high energy storage density, is affordable, has high cycle stability with fast kinetics, and should be non-toxic. In this view, large amounts of different salts have been reviewed [8, 11, 24].

However, these salts in their pure form come with different challenges, like the undesired melting for the higher hydrates of  $\text{CaCl}_2 \cdot n\text{H}_2\text{O}$  [25, 26]; deliquescence of  $\text{CaCl}_2 \cdot n\text{H}_2\text{O}$  [24, 27]; the metastable zone around the equilibrium for  $\text{K}_2\text{CO}_3 \cdot 1.5\text{H}_2\text{O}$  [28, 29], a low cyclability [30–32]; high toxicity ( $\text{GdCl}_3$ ,  $\text{NiCl}_2$ ,  $\text{Na}_2\text{S}$ ,  $\text{MnI}_2$ ,  $\text{VOSO}_4$ , and  $\text{CuCl}_2$ ) or involve toxic side products ( $\text{HCl}$  and  $\text{H}_2\text{S}$  gas) [11, 33–35]; are highly corrosive [36–38]; include slow kinetics [24]; have a low thermal conductivity [39], or come at a high price and low availability [11]. Therefore, selecting a precious TCM is a trade-off between the potentially achievable energy storage density and the challenges inherently related to the characteristics of the material.

Two promising TCM salt hydrates, with a relative high sorption energy ( $2 - 3 \text{ GJ}/\text{m}^3$ ) are  $\text{MgCl}_2 \cdot n\text{H}_2\text{O}$  and  $\text{CaCl}_2 \cdot n\text{H}_2\text{O}$  ( $n = 0, 1, 2, 4, 6$ ). They are widely available, limiting their costs [33, 40], and the hydration reactions of these salts occur at temperatures corresponding to domestic heating applications [33, 34]. However, in practice, not all hydration levels can be reached. Both salts suffer from deliquescence [19] at room conditions,  $25^\circ\text{C}$  and a water vapor pressure of 12 mbar [24, 27]. Additionally,  $\text{CaCl}_2 \cdot 4\text{H}_2\text{O}$  and  $\text{CaCl}_2 \cdot 6\text{H}_2\text{O}$  have low melting temperatures in the range of the storage operation window [25, 26]. Both deliquescence and melting lead to agglomerates and clogging of the storage system. A major disadvantage of  $\text{MgCl}_2$  hydrates is irreversible hydrolysis side reaction when dehydrating the salt at  $135^\circ\text{C}$  [33, 34].  $\text{HCl}$  is not only a highly toxic and corrosive gas, such an irreversible side reaction degrades the storage energy capacity slowly over time. These shortcomings cap the practical use to a smaller selection of hydration levels ( $\text{MgCl}_2 \cdot 2\text{H}_2\text{O} \leftrightarrow \text{MgCl}_2 \cdot 6\text{H}_2\text{O}$ , and  $\text{CaCl}_2 \cdot 0\text{H}_2\text{O} \leftrightarrow \text{CaCl}_2 \cdot 2\text{H}_2\text{O}$ ) for the pristine salts and thereby limit the storage energy density.

Recently, much attention for TCM research is focused on enhancing pure salts to overcome their drawbacks. Enhancements are investigated regarding combining salts [31, 41, 42]. Another often studied approach is the addition of carrier materials to increase the stability, cyclability, and/or thermal conductivity. This can be done by encapsulation of the salt with shells [43], adding compounds like vermiculite or binders [44–46], or impregnation of salts in porous materials [47–52]. Unfortunately, addition of non/low reacting matter leads to a reduction of the energy storage density. Most recently, promising studies are done by doping of pure salts [53–57] with other salts, or by the synthesis of (new) double salts [48, 58–60]. These studies on enhanced/new salts show varying results on important TCM characteristics. Notwithstanding, still many enhancements or combinations are open to explore and more fundamental research is needed to get a better understanding of the improvement. This thesis covers the use of advanced atomic and molecular modeling methods to study the promising combination [59, 60]

of  $\text{MgCl}_2 \cdot n\text{H}_2\text{O}$  and  $\text{CaCl}_2 \cdot n\text{H}_2\text{O}$  as TCM.

## 1.2. INTRODUCTION TO COMPUTATIONAL MODELING

The history of computational methods started in the period during and after the second world war. The first electronic computer, the ENIAC (Electronic Numerical Integrator And Computer), was built and used by a team of engineers and scientists (including John von Neumann and Nicholas Metropolis) to perform simulations for the study and development of nuclear weapons. The first algorithm ran on this machine was a computational statistical model that described a thermonuclear reaction written by Metropolis and co-workers. This model relies heavily on random numbers and is therefore named *Monte Carlo*, based on the story of an uncle of one of the co-workers Stanislaw Ulam, who occasionally borrowed money for gambling in the Monte Carlo casino [61–63]. In 1946, the ENIAC, weighing more than 30 tons and containing more than 17,000 vacuum tubes, could execute up to 5,000 additions per second [64]<sup>†</sup>. Currently, modern supercomputers can perform in the order of  $10^{15}$  (peta) Floating-Point Operations per second (FLOPS) [65]. Thus, allowing computer simulations that involve a much higher number of operations to solve and/or predict physical systems' behavior in all kinds of research topics – physics, chemistry, biology, astrophysics, climatology, economics, engineering, and many more.

In material science, computer simulations can be used to understand and predict the behavior and properties of materials. Of course, one can argue that many of these properties can also be obtained from experiments – e.g., it is much easier to measure the freezing point of water than to extract it from a computer simulation [63]. However, this argument does only hold for experimental conditions near atmospheric conditions for known materials. In contrast, the strength of computer simulations is that they can be applied with the same ease at extreme conditions – e.g., at rarefied gas conditions [66], extreme heat loads [67], or at extreme pressures in geological studies [68]. Next to the simulation of extreme conditions, computational models can provide valuable insight at scales which are hard to observe [69, 70], or models can be used as an exploratory tool for new/undiscovered materials [71–74].

In this work, multiple computational models are used – Density Functional Theory (DFT), Molecular Dynamics (MD), and Monte Carlo (MC) methods – from the electronic level up to the atomic and molecular level. For the DFT section, we mainly follow the original papers of Hohenberg, Kohn, and Sham [75, 76], as well as the reviews by Martin [77], Fiolhais et al. [78], and Tranca [79]. For the molecular sections, we mainly follow the book by Frenkel & Smit [63], and the review paper by Goga et al. [80]. For the reactive force field sections, we mainly follow the original papers by van Duin et al. [81, 82], and for the force field optimizer the paper by Iype et al. [83]. In this introductory chapter they will be briefly introduced, and relevant parts are discussed in further detail in the concerning chapters. The models were computed on an in-house high-performance computer or the Dutch national high-performance computing facility Cartesius.

---

<sup>†</sup>approximately 500 FLOPS.

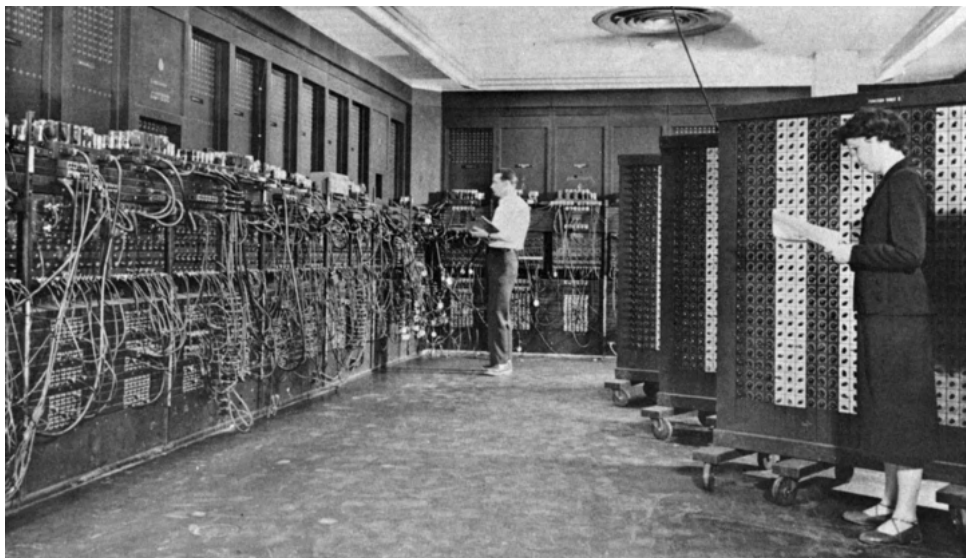


Figure 1.3: ENIAC, first large-scale electronic computer (U.S. Army photo, ca. 1947-1955)

### 1.2.1. DENSITY FUNCTIONAL THEORY

In order to study chemical interactions between electrons, atoms, and molecules, Density Functional Theory (DFT) is used in this work. The basics are explained in this section. However, to fully understand the basics, first the many-body Schrödinger relation is introduced. The well-known Schrödinger equation is a linear partial differential equation which includes the wave function of a quantum-mechanical system. For a non-relativistic<sup>‡</sup> time-independent<sup>§</sup> system, it is given by:

$$H|\Psi\rangle = E|\Psi\rangle \quad (1.1)$$

or, more specific for a non-magnetic system with  $M$  atoms and  $N$  electrons:

$$H \cdot \Psi(r_1, r_1, \dots, r_N, R_1, R_1, \dots, R_M) = E \cdot \Psi(r_1, r_1, \dots, r_N, R_1, R_1, \dots, R_M), \quad (1.2)$$

with  $H$  as the Hamiltonian,  $\Psi$  the many-body wave function, and  $E$  the energy of the system. In the further reading, all capital indexes refer to the nuclei and lower case indexes refer to electronic properties.  $r$  are the electronic positions, and  $R$  are the nuclear position. For the given system, the wave function has a  $3(N + M)$  dimensional space. In essence, this equation can be used to theoretically describe and/or predict structures and properties of atoms, molecules, solids, and eventually new materials. It is however still far from a straightforward implementation and except for some very simple systems – like the particle in a box or the hydrogen atom – it is impossible to solve analytically. To solve many-body systems, some approximations and theorems are needed.

<sup>‡</sup>Assumption that all of the elements move a speed much lower than the speed of light.

<sup>§</sup>The solution of the time-independent Schrödinger equation results in stationary states, and the probability density is independent of time.



The Hamiltonian of equation 1.2 is a summation of the kinetic energies ( $T$ ) and inter-particle potentials ( $V$ ), it can be written as:

$$H = H_{\text{nucl}} + T_{\text{el}} + V_{\text{nucl-nucl}} + V_{\text{nucl-el}} + V_{\text{el-el}}, \quad (1.3)$$

with the index  $\text{nucl}$  for the nuclei, and  $\text{el}$  for the electrons. The first simplification step is led by the adiabatic, or so called *Born–Oppenheimer*, approximation [84]. It assumes that the wave function for nuclei and electron can be treated separately, based on the fact that electrons are much lighter than atoms. As a result, the electrons will instantaneously adapt to the heavier nuclei position, and from an electronic point of view, the atoms can be seen as fixed points in space. This approximation decouples the motion of electron from the motion of nuclei. As a results, equation 1.3 can be written in an electronic part:

$$H_{\text{el}}(\{r_i\}; \{\mathbf{R}_{\text{fix}}\}) = T_{\text{el}}(\{r_i\}) + V_{\text{nucl-el}}(\{r_i\}; \{\mathbf{R}_{\text{fix}}\}) + V_{\text{el-el}}(\{r_i\}), \quad (1.4)$$

and a nuclear part:

$$H_{\text{nucl}}(\mathbf{R}) = T_{\text{nucl}}(\mathbf{R}) + V_{\text{nucl-nucl}}(\mathbf{R}) + E_{\text{el}}(\mathbf{R}). \quad (1.5)$$

In which  $V_{\text{nucl-nucl}}(\mathbf{R})$  is the repulsive Coulomb interactions between nuclei, and  $E_{\text{el}}(\mathbf{R})$  is the energy of the electronic system with nuclei at positions  $\mathbf{R}$ . For conciseness, in the remaining explanation, we will focus on the electronic interactions. Using Rydberg atomic units and setting the constants to  $\hbar = 1$ ,  $m_e = \frac{1}{2}$ ,  $e^2 = 2$ ,  $c = \frac{2}{\alpha} = 274.074^{\text{¶}}$ , the kinetic and potential Hamiltonian contributions can be written as [79]:

$$T_{\text{el}} = - \sum_{i=1}^N \nabla_{r_i}^2, \quad (1.6)$$

$$V_{\text{el-el}} = - \sum_{i,j=1; i \neq j}^N \frac{1}{|\mathbf{r}_i - \mathbf{r}_j|}, \quad (1.7)$$

$$V_{\text{nucl-el}} = - \sum_{i=1}^N \sum_{I=1}^M \frac{Z_I}{|\mathbf{R}_I - \mathbf{r}_i|}. \quad (1.8)$$

The Born–Oppenheimer approximation, reduces the complexity by a lot, without losing much accuracy. However, it would still be an enormous task to solve the Schrödinger equation based on equations 1.4 and 1.5. Only the electronic part of the Schrödinger equation already operates in a  $3N$  dimensional space, and it would require an enormous amount of computational power to solve for a system including more than just a few electrons. At this point, DFT and its approximations come to the scene.

**The Hohenberg–Kohn theorems** Instead of solving the demanding wavefunctions, DFT uses the charge density to solve the electronic system. This treatment reduces the  $3N$ -dimensional space to a 3-dimensional one. To achieve this reducement, DFT is based on two theorems by Hohenberg and Kohn [75]. The first theorem states that: *the external*

<sup>¶</sup>Energy: 1 Ry  $\simeq$  13.6058 eV, and length scale is the Bohr radius  $\alpha_B = 0.529177 \text{ \AA}$

potential  $V_{\text{ext}}(\mathbf{r})$  acting on a system of electrons is a unique functional of the electronic density  $\rho(\mathbf{r})$ . Given that the interaction between the nuclei and electrons is known via:

$$E_{\text{nuc-el}}[\rho] = \int \rho(\mathbf{r}) V_{\text{nuc-el}}(\mathbf{r}) d\mathbf{r}, \quad (1.9)$$

and the assumption that  $\rho(\mathbf{r})$  is correct, this provides that the ground state electronic energy  $E$  equals [75]:

$$E[\rho(\mathbf{r})] \equiv \int \rho(\mathbf{r}) V_{\text{nuc-el}}(\mathbf{r}) d\mathbf{r} + (T_{\text{el}} + V_{\text{el-el}})[\rho(\mathbf{r})] = \int \rho(\mathbf{r}) V_{\text{ext}}(\mathbf{r}) d\mathbf{r} + F[\rho(\mathbf{r})]. \quad (1.10)$$

where  $F[\rho(\mathbf{r})]$  is an unknown but universal functional, valid for all electronic systems and any external potential. The second theorem is related to the variation principle and states that: *E is at its minimum for the correct  $\rho(\mathbf{r})$* <sup>||</sup>. Thus, the energy of an approximated solution  $E[\rho']$  is always higher than the true ground state of the system  $E_0[\rho_0]$ .

$$E[\rho'] > E_0[\rho_0]. \quad (1.11)$$

With these two theorems, and if  $F[\rho(\mathbf{r})]$  is known and sufficiently simple, the solution of equation 1.10 would merely be an minimization problem of the electronic density function in a 3-dimensional space. Unfortunately, the unknown universal function  $F[\rho(\mathbf{r})]$  has to be solved.

**The Kohn–Sham equations** Where the Hohenberg–Kohn theorems provides us with the statement that the ground state of an electronic system can be reached by a minimization of  $E$  with respect to  $\rho(\mathbf{r})$ . The Kohn–Sham equations [76] construct a method to approximate  $E[\rho]$ , which is needed to compute  $E$ . First, it is convenient to separate the long range Coulomb interactions – which we will name  $E_{\text{H}}$  because its analogy to the classical treatment of Hartree – from  $F[\rho(\mathbf{r})]$  and describe it in the classical way:

$$F[\rho(\mathbf{r})] = E_{\text{H}} + G[\rho(\mathbf{r})] = \int \int \frac{\rho(\mathbf{r}) - \rho(\mathbf{r}')}{|\mathbf{r} - \mathbf{r}'|} d\mathbf{r} d\mathbf{r}' + G[\rho(\mathbf{r})], \quad (1.12)$$

and the ground state total electronic energy (equation 1.10) becomes:

$$E_{\text{ext}}[\rho(\mathbf{r})] = \int \rho(\mathbf{r}) V_{\text{ext}}(\mathbf{r}) d\mathbf{r} + \int \int \frac{\rho(\mathbf{r}) - \rho(\mathbf{r}')}{|\mathbf{r} - \mathbf{r}'|} d\mathbf{r} d\mathbf{r}' + G[\rho(\mathbf{r})]. \quad (1.13)$$

In which  $G[\rho(\mathbf{r})]$  is a universal function like  $F[\rho(\mathbf{r})]$ . Kohn–Sham proposed a method to approximate  $G[\rho(\mathbf{r})]$  by separation in single non-interacting electrons ( $T_{\text{s}}[\rho(\mathbf{r})]$ ) contributions and an *exchange correlation* energy  $E_{\text{xc}}[\rho(\mathbf{r})]$ , whose ground state density equals the ground state density of the interacting system  $\rho_{\text{s}}(\mathbf{r}) = \rho(\mathbf{r})$ .

$$G[\rho(\mathbf{r})] \equiv T_{\text{s}}[\rho(\mathbf{r})] + E_{\text{xc}}[\rho(\mathbf{r})]. \quad (1.14)$$

With the non-interacting one-particle kinetic energy  $T_{\text{s},i}$  and the one-particle potential  $v_{\text{s},i}$ , the one-particle Schrödinger equation can be exactly solved to obtain the single

---

<sup>||</sup>Under the condition  $N = \int \rho(\mathbf{r}) d\mathbf{r}$ .

particle orbital  $\phi_{s,i}$ . The total  $T_s$  is obtained via simple summation of all non-interacting single particles:

$$T_s[\rho] = \sum_{i=1}^N \langle \phi_{s,i}([\rho], \mathbf{r}) | -\nabla_i^2 | \phi_{s,i}([\rho], \mathbf{r}) \rangle. \quad (1.15)$$

The exchange and correlation energy describes the difference between the true electronic Hamiltonian  $H_{\text{el}}$  and the approximated system:

$$E_{\text{xc}}[\rho] = (T_{\text{el}}[\rho] - T_s[\rho]) + (V_{\text{el-el}}[\rho] - E_{\text{H}}[\rho]). \quad (1.16)$$

With the single-particle contribution,  $E_{\text{el}}$  is given by rewriting equation 1.13:

$$E_{\text{el}} = \int \rho(\mathbf{r}) V_{\text{ext}}(\mathbf{r}) d\mathbf{r} + \iint \frac{\rho(\mathbf{r}) - \rho(\mathbf{r}')}{|\mathbf{r} - \mathbf{r}'|} d\mathbf{r} d\mathbf{r}' + T_s[\rho] + E_{\text{xc}}[\rho]. \quad (1.17)$$

Via a variation principle and regrouping of the Kohn–Sham equation one obtains:

$$\nu_s([\rho], \mathbf{r}) = V_{\text{ext}}(\mathbf{r}) + \int \frac{\rho(\mathbf{r}')}{|\mathbf{r} - \mathbf{r}'|} d\mathbf{r}' + V_{\text{xc}}[\rho], \quad (1.18)$$

with

$$V_{\text{xc}}[\rho] = \frac{\delta E_{\text{xc}}[\rho]}{\delta \rho(\mathbf{r})}. \quad (1.19)$$

Accordingly, the density can be found by solving for all given electrons ( $N$ ) the one-electron Schrödinger equation:

$$\{-\nabla^2 + \nu_s([\rho], \mathbf{r})\} \phi_{s,i} = \epsilon_{s,i} \cdot \phi_{s,i}, \quad (1.20)$$

and,

$$\rho(\mathbf{r}) = \sum_{i=1}^N |\phi_{s,i}(\mathbf{r})|^2. \quad (1.21)$$

By iterating  $\rho(\mathbf{r})$  over the Kohn–Sham equations 1.18–1.21, until self-consistency, one can start with an estimated  $\rho_{\text{initial}}(\mathbf{r})$  and end with a good approximation of the true  $\rho(\mathbf{r})$ .

In the end, the only unknown is the energy and correlation function  $E_{\text{xc}}[\rho(\mathbf{r})]$ . However, there are good approximations for this term, for example, a well-known basic approximation, under slow varying  $\rho(\mathbf{r})$ , gives  $E_{\text{xc}}[\rho(\mathbf{r})]$  equal to [76]:

$$E_{\text{xc}}[\rho(\mathbf{r})] = \int \rho(\mathbf{r}) \epsilon_{\text{xc}}(\rho(\mathbf{r})) d\mathbf{r}. \quad (1.22)$$

$\epsilon_{\text{xc}}$  in the equation above, is the exchange correlation function of a single electron in a uniform electron gas, which can be exactly analytically computed. This approximation for  $E_{\text{xc}}$ , is called the *local density approximation* (LDA) [76], which is the oldest\*\* and probably most simple one. However, since then, much more advanced exchange and correlation functions are successfully introduced, like the Generalized Gradient Approximation (GGA).

\*\*Already introduced in the original paper that introduced the Kohn–Sham equations

The groundbreaking work of DFT – more precisely, the ability to solve the Schrödinger equation for larger systems – has brought the field of computational chemistry much further [85], and provided the science community with key insights. However, despite the simplifications and recent improvements, it is still a computationally demanding task to solve. Thereby, plane-wave DFT is limited to systems up to  $\lesssim 1000$  atoms, when ran on a supercomputer facility. For larger systems, more approximations are needed, and one can use molecular methods as explained in the following sections.

### 1.2.2. MOLECULAR MODELS

DFT solves atomic interactions on an electronic level with high accuracy. However, due to the high computational cost, it can only be applied to a limited set of atoms. Molecular Dynamics (MD) and Monte Carlo (MC) molecular methods do not explicitly include electronic interactions but treat atomic interaction via empirical potentials. This simplified approach is in favor of the computational cost, where the number of bodies is reduced to the atoms<sup>††</sup> and allows much larger numbers of atoms to be simulation over a longer time period. In MD and MC simulations, instantaneous information is measured, like the atomic positions, velocities, and their interacting forces. However, in experiments, this information is not measured, but rather macroscopic properties like the temperature and pressure averaged over the time and volume of the experiment [63]. The relation between these different computational "experiment" measurements and the real-world experiment is described by statistical mechanics. Therefore, before the MD and MC methodologies are introduced, one must first understand their fundamentals in statistical mechanics.

### STATISTICAL MECHANICS

Statistical mechanics arose from classical thermodynamics and acts on the interface between classical mechanics and quantum mechanics (QM). Classical mechanics is used to model the exchange of energy by the description of *macroscopic* (measurable) system parameters like the temperature and pressure near equilibrium. It is considered macroscopic because of the use of the large scale measurable and empirical description of a system, without the *microscopic* description of individual particles like molecules, atoms, electrons, and quantum-mechanical states. The microscopic interpretation of this concept was later provided with the development of statistical mechanics, mainly attributed to Ludwig Boltzmann, James Clerck Maxwell, and Josiah Willard Gibbs. A mathematical framework is offered with statistical mechanics, which relates the classical thermodynamic description of matter to their constituent particles and their interactions. This relation is made with statistical methods and probability theories on large collections of microscopic states called ensembles. All possible states that can be found of a system are called the state space, and the microscopic states in the ensemble (probability distribution over states) are virtual, independent copies of the system's various states in the state space. Different equilibrium ensembles can be considered [86, 87], from which the three most commonly discussed and used ensembles in MD and MC are discussed below. In the limit of many particles, these systems describe an identical

---

<sup>††</sup>or clusters of atoms for example in coarse-grained models

macroscopic behavior, and it is a matter of convenience which ensemble is used for the problem to be studied [88].

**Micro-canonical (NVE) ensemble** An ensemble in which the number of particles  $N$ , the volume  $V$ , and the total energy  $E$  is specified, is considered to be the micro-canonical ensemble. The other properties, for instance, the temperature  $T$  or pressure  $p$ , are allowed to fluctuate. Based on the postulate of equal a priori probabilities: "A system has an equal probability of being in any microstate that is consistent with its current macrostate", the micro-canonical ensemble contains, with equal probability, states that are consistent with the given specifications. This gives a probability  $P = 1/W$  of finding a state equals, in which  $W$  are the number of microstates within the range around  $E$ . The macroscopic function related to this ensemble is the Boltzmann entropy, given by  $S = k_B \log W$ , where  $k_B$  is the Boltzmann constant.

**Canonical (NVT) ensemble** An ensemble in which the number of particles  $N$ , the volume  $V$ , and the temperature  $T$  is specified, is considered to be the canonical ensemble. The other properties of the system are allowed to fluctuate. The temperature is specified by equilibrating the system with a heat bath that has given a precise temperature. The states in the ensemble are found with the probability depending energy  $E(N, V)$  of the state, which gives the canonical partition function of the ensemble:  $Z(N, V, T) = \sum_j e^{-E_j(N, V)/k_B T}$ . The macroscopic relation to this ensemble is the Helmholtz free energy:  $F = -k_B T \log Z$ . The characteristics and practice of fixing  $N$ ,  $V$ , and  $T$ , makes it a convenient and often used ensemble in Molecular Dynamics.

**Grand-canonical ( $\mu VT$ ) ensemble** An ensemble in which the chemical potential  $\mu$ , the volume  $V$ , and the temperature  $T$  is specified, is considered to be the grand-canonical ensemble. The other properties of the system are allowed to fluctuate. This means that the number of particles  $N$  is allowed to fluctuate, and it is a useful ensemble to study the loading of molecules ( $N$ ) at a given chemical potential, depending on the temperature and pressure. The Grand-canonical partition function is given by:  $\mathcal{Z}(\mu, V, T) = \sum_j e^{-(E_j - \mu N_j)/k_B T}$ .

## MOLECULAR DYNAMICS

Molecular Dynamics (MD) is a computational algorithm that models a system from a molecular approach by basically sampling a statistical ensemble ( $NVT, NpT, NVE$ ) over time. The first MD simulation [63], performed by Alder and Wainwright in 1956, was a model of sphere particles [89]. To avoid criticism, they modeled hard spheres because the dynamics are exactly known and the results were not an effect of computer arithmetic [90]. Not much later, in 1959, the first "real" materials were modeled in the investigation of radiation damage in copper [91].

MD is based on treating atoms as classical objects via point masses; these atoms are given an initial velocity  $\mathbf{v}$  and position  $\mathbf{r}$ , and interact with each other via an interatomic potential  $E$ :

$$-\nabla E(\mathbf{r}) = \mathbf{F}(\mathbf{r}) = m \frac{d^2 \mathbf{r}}{dt^2}, \quad (1.23)$$

with  $\mathbf{F}$  as the interacting force. The interatomic potential is described in a force field that captures relevant physical forces like van der Waals and Coulomb forces. In the next section, this will be discussed in more detail. With many-body systems ( $N > 2$ ) we have a system that can not be solved analytically, and integration of Newton's laws of motion is used to solve the dynamics of the system. There are multiple integration methods, from which the stable velocity Verlet [92] is an often used one. It gives position of the consecutive time step via:

$$\mathbf{r}_i(t + \Delta t) = \mathbf{r}_i(t) + \mathbf{v}_i(t)\Delta t + \frac{1}{2} \frac{d^2 \mathbf{r}_i(t)}{dt^2} \Delta t^2, \quad (1.24)$$

and the velocity of the consecutive time step via:

$$\mathbf{v}_i(t + \Delta t) = \mathbf{v}_i(t) + \frac{1}{2} \left( \frac{d^2 \mathbf{r}_i(t)}{dt^2} + \frac{d^2 \mathbf{r}_i(t + \Delta t)}{dt^2} \right) \Delta t. \quad (1.25)$$

$\Delta t$  is the time step, which is desired to be large to increase the simulated time but must be small enough to avoid large computational errors. When reactive force fields are used,  $\Delta t$  is most often 0.25 fs ( $0.25 \times 10^{-15}$  s) to include vibrational frequencies of molecular bonds which are in the order of  $10^{13} - 10^{14}$  Hz.

In practice, MD is used to study many-body systems from which the average behavior can be taken by solving the system over a natural time evolution. It is thereby considered to be ergodic<sup>‡‡</sup>, and microstates of the entire state space are sampled. It is a powerful method from which many systems and properties can be studied. However, the ergodic hypothesis requires that the measured time is greater than the longest relaxation time in the system, making the study of "slow" events (e.g., rare events, slow diffusion processes, nucleation) cumbersome or even impossible by simple MD.

**Reactive and non-reactive force fields** The interactions between the atoms in an MD simulation are described with a force field. There are many different force fields available, which are not necessarily good or bad. They rather describe different interactions and are developed for different applications, phenomena and/or materials. For example, Siepmann and Martin developed numerous transferable force fields regarding phase equilibria (TraPPE) [93, 94]; Calero and coworkers [95–99] developed force fields for porous media; in the group of van Duin, many reactive force fields (ReaxFF) are developed to study reactive systems [81, 82]. In our group, and in this work, multiple reactive force fields to model TCMs are developed regarding  $\text{CaCl}_2 \cdot n\text{H}_2\text{O}$  (chapter 3),  $\text{MgCl}_2 \cdot n\text{H}_2\text{O}$  [100],  $\text{H}_2\text{O}$  and  $\text{CO}_2$  (chapter 5), and  $\text{Ca}_x\text{Mg}_{1-x}\text{Cl}_2 \cdot n\text{H}_2\text{O}$  (chapter 7).

Most force fields are a summation of the intermolecular and intramolecular forces, as given in Figure 1.4. The intramolecular forces, are associated with chemically bonded ( $E_{\text{bonded}}$  atoms within the same molecule, like chemical bonds, bond angles, and bond dihedrals. The intermolecular forces are associated with nonbonded ( $E_{\text{non-bonded}}$ ) atomic interactions, like dispersion and electrostatic forces.

$$\begin{aligned} E &= E_{\text{bonded}} + E_{\text{non-bonded}} \\ &= E_{\text{bond stretch}} + E_{\text{bond angles}} + E_{\text{torsion}} + \dots + E_{\text{dispersion}} + E_{\text{electrostatic}} + \dots \end{aligned} \quad (1.26)$$

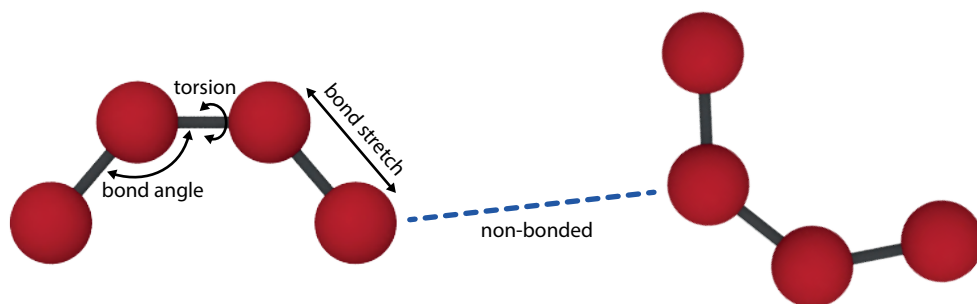


Figure 1.4: Example of intra- and intermolecular bonds.

In many non-reactive force fields, the bonded interaction like bond stretch and bond angles are described with a harmonic potential [97, 98]  $E_{\text{bond angle}} = k(\theta - \theta_0)^2$ ,  $E_{\text{bond stretch}} = k_b(r - r_0)^2$ . With  $k_b$  and  $k_\theta$  as elastic constants.  $r$ ,  $r_0$ ,  $\theta$  and  $\theta_0$  are the bond distance, equilibrium bond distance, angle, and equilibrium angle, respectively. For some applications, it turns out that rigid molecules with fixed bonds and angles are sufficient to reach a high enough accuracy [99]. In non-reactive force fields, the nonbonded van der Waals term is often described with the well-known Lennard–Jones (LJ) potential, and the electrostatic term is often computed with the Coulomb equation [63, 93–99] in combination with the Ewald summation [101].

$$E_{\text{non-bonded}} = E_{\text{LJ}} + E_{\text{Coulomb}} = 4\epsilon \left[ \left( \frac{\sigma}{r} \right)^{12} - \left( \frac{\sigma}{r} \right)^6 \right] + \frac{q_i q_j}{4\pi\epsilon_0 r} \quad (1.27)$$

with  $r$  as the interatomic distance,  $\epsilon_0$  as the electric constant, and  $\epsilon$ ,  $\sigma$ ,  $q_i$ , and  $q_j$  are parametrized values of the Lennard–Jones energy parameter, atomic diameter, and partial charges for atoms  $i$  and  $j$ , respectively. The first term of the LJ potential represents the short-range repulsive term between atoms; the second term of the LJ potential represents the long-range attractive dispersion term ( $1/r^6$ ); the third term represents the Coulomb interaction. The given LJ potential is an example of a 2-body interaction. Many-body interaction potentials are also available at the cost of a higher computational power but result in a higher accuracy for polarization or dispersion effects. Furthermore, bond stretching, angle bending, and torsion forces correspond to 2-body, 3-body, and 4-body interactions terms, respectively. Non-reactive force field have been successful in the modeling numerous atoms and molecules. However, these potentials are in general only applicable near equilibrium with a fixed charge and reactivity and are therefore, not applicable to study reactive systems with including transition states or undergo chemical changes [102]. In this sense, multiple alternative reactive force fields have been developed.

The Embedded-Atom Method (EAM) [103, 104] introduced the concept of a local electronic density function, in which the atom is embedded, that allows the bond strength between atoms to change. The EAM method is considered to be a good descriptor to

††A system for which time averages and ensemble averages are equal is said to be ergodic.

metals and alloys. However, the lack of angular terms makes it less convenient to use for systems with strong covalent bonds. Similar or related methods are known, like the Finnis-Sinclair potentials [105], the modified embedded-atom method (MEAM) [106], and the Stillinger-Weber potentials [107]. These methods consist of distinguishable energy terms to model the reaction and are therefore considered as separated format bond-order concepts. Alternatively, integrated formats are developed to model reactive systems, this second format integrates the bond-order in the potential energy term [102]. The first integrated method was introduced by the Abell model [108] in which the included bond-order term depends on the local environment of the bonded atoms. Tersoff [109, 110] improved this method by adding effects of the angles and symmetry to the bond-order term<sup>§§</sup>, and Brenner extended it by adding a coordination term which enables modeling of radicals [111], and later on, with angular and coordination terms to improve the method for carbon-based materials [112]<sup>¶¶</sup>. The Tersoff potentials are considered to be good descriptors of semi-conducting materials. The limitation of these traditional reactive force field, is the lack of dynamical (variable) atomic charges which are allowed to change during the simulation. This is solved by two more recent developed methods, namely the charge-optimized many-body (COMB) method [113–118], and the reactive force field (ReaxFF) method [81, 82]. Both methods allow variable-charged atoms that can change during the simulation. The COMB method bases the bond-order directly on the coupled dynamical computed charges, as function of the environment. It determines the charge state of an atom or ion and the type and strength of the bond follows automatically. ReaxFF determines the bond-order directly on the interatomic distance. ReaxFF is originally developed for hydrocarbon systems [81], which has led the focus on reproducing energy barriers, while the EAM and COMB methods are developed from a material science point of view and focus rather on elastic properties [119]. Next to classical treatments of atoms in molecular modeling, there are also some semi-empirical QM based methods like the Density Functional Tight Binding (DFTB) [120] approach, that allow the treatment of large systems. DFTB is an approximate method for DFT, thereby, a step closer to ab-initio modeling. It uses pseudopotentials as interatomic energy descriptors. It is approximately one order of magnitude slower than reactive force fields, and depending on the system or property investigated it can offer a better or worse description when compared with ReaxFF [121–123].

In this work, mainly the ReaxFF formalism<sup>\*\*\*</sup> is used, based on the general description of reactive systems by which TCMs can be studied [40, 125, 126]. Modeling of bond breaking and formation is at the expense of a higher computational cost. However, it is still many orders of magnitude faster than QM methods like DFT. ReaxFF was initially developed by the van Duin group [81, 82] and aimed to bridge the gap between QM calculations and non-reactive MD. Next to the ability of modeling chemical reactions, it also leads to the fact that an atom in a different configuration (e.g., oxygen in MgO, H<sub>2</sub>O, or O<sub>2</sub>) is described by the same parameters. The potential in ReaxFF is a summation of different energy terms:

$$E_{\text{RxFF}} = E_{\text{bond}} + E_{\text{vdW}} + E_{\text{Coul}} + E_{\text{val}} + E_{\text{pen}} + E_{\text{under}} + E_{\text{over}} + E_{\text{tors}} + E_{\text{conj}} + E_{\text{others}}. \quad (1.28)$$

<sup>§§</sup>Known as the Abell-Tersoff or Tersoff potential.

<sup>¶¶</sup>Known as the Abell-Tersoff-Brenner, Brenner, or REBO potential.

<sup>\*\*\*</sup>Implemented in the Software for Chemistry & Materials (SCM) [124] modeling package.



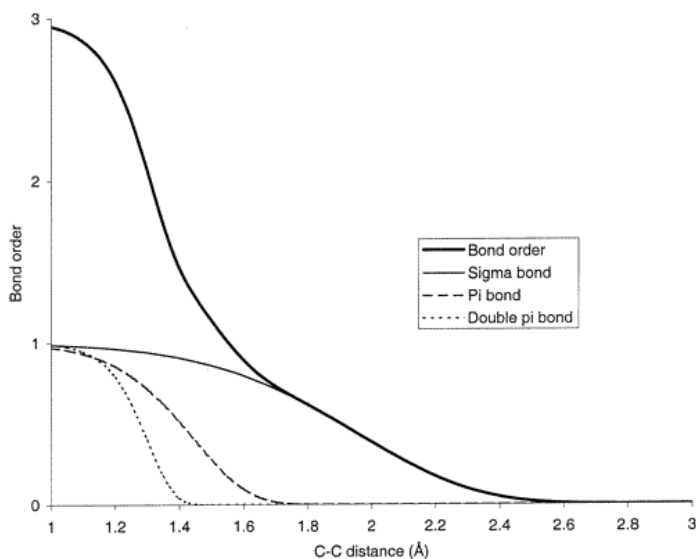


Figure 1.5: Interatomic distance dependency of the carbon-carbon bond order, given by equation 1.29. Reprinted with permission from A. C. T. van Duin, S. Dasgupta, F. Lorant, and W. A. Goddard, *The Journal of Physical Chemistry A* 2001 105 (41), Copyright 2021 American Chemical Society.

In this summation, the non-covalent bonded interactions are described with the terms  $E_{\text{vdW}}$  and  $E_{\text{Coul}}$ , which account for the van der Waals and Coulomb interactions, respectively. The  $E_{\text{bond}}$  term accounts for the covalently bonded atoms. The terms  $E_{\text{val}}$ ,  $E_{\text{tors}}$ ,  $E_{\text{pen}}$ ,  $E_{\text{under}}$ ,  $E_{\text{over}}$ , and  $E_{\text{conj}}$  describe the valence and torsion contributions, 'penalty' energies, under- and over-coordination, and conjugated systems, respectively.  $E_{\text{others}}$  can include other terms for specific systems, like H-bonds or extra dispersion interactions (see Chapter 5). The bond order (BO) between atoms is described by a summation of empirical relations for the  $\sigma$ -bond ( $BO_{ij}^{\sigma}$ ), the  $\pi$ -bond ( $BO_{ij}^{\pi}$ ), and the  $\pi\pi$ -bond ( $BO_{ij}^{\pi\pi}$ ). These terms depend on the distance  $r_{ij}$  between the atoms  $i$  and  $j$  [81].

$$\begin{aligned}
 BO_{ij} &= BO_{ij}^{\sigma} + BO_{ij}^{\pi} + BO_{ij}^{\pi\pi} \\
 &= \exp \left[ p_{\text{bo}1} \left( \frac{r_{ij}}{r_0^{\sigma}} \right)^{p_{\text{bo}2}} \right] + \exp \left[ p_{\text{bo}3} \left( \frac{r_{ij}}{r_0^{\pi}} \right)^{p_{\text{bo}4}} \right] \\
 &\quad + \exp \left[ p_{\text{bo}5} \left( \frac{r_{ij}}{r_0^{\pi\pi}} \right)^{p_{\text{bo}6}} \right],
 \end{aligned} \tag{1.29}$$

in which  $r_0^{\sigma}$ ,  $r_0^{\pi}$ , and  $r_0^{\pi\pi}$  are the bond radii for the  $\sigma$ ,  $\pi$ , and  $\pi\pi$  bond, respectively. The  $p_{\text{bo}}$  values are fitted parameters to experimental or first-principle results. Each  $BO_{ij}$  term has a maximum value of 1, and when all bond-orders contribute BO could add up to 3. An example of this bond-order relation is given in Figure 1.5. As mentioned before, the ability of dynamical charges is an important feature of ReaxFF, which enables accurate modeling of reactive systems. In ReaxFF the Electronegativity Equalization Method [127]

(EEM) is used to compute atomic charge distributions.

Independent on the type of force field, their parameters need to be obtained. This can be done by parameterization using reference data. For example, to optimize the nonbonded interactions, reference data from experiments can be used. For the bonded parameters, QM reference data (like DFT) can be used, which will be discussed within the next subsection.

### (METROPOLIS) MONTE CARLO

Monte Carlo (MC) methods are a group of computational algorithms that use repeated random sampling to obtain numerical results. As mentioned before, the first algorithm to run on an electronic computer was an MC algorithm. In 1953, Metropolis, Rosenbluth, Rosenbluth, Teller, and Teller improved the efficiency and developed the Metropolis Monte Carlo method [128], which ran on the MANIAC computer in Los Alamos [61]. Compared to standard MC, "Instead of choosing configurations randomly, then weighting them with  $\exp(-E/kT)$ , we choose configurations with a probability  $\exp(-E/kT)$  and weight them evenly." [128] In this way, statistical ensembles can be sampled more efficiently, and similar to MD, macroscopic properties can be obtained from these ensembles. In contrast to MD, it does not use time integration to sample the state space but a stochastic approach. The study of dynamical properties are thereby not directly possible. However, the non-dynamical behavior is also its strength, where high energy barriers, rare events, and slow diffusion – too computational time consuming for MD – can be circumvented by smart MC algorithms. For practical efficiency, new states in the MC ensemble are generated by performing trial moves (modifications) from the old state. In this way, only minor modifications near the realistic previous state are explored, thereby, improving the acceptance probability of the new state. It thereby performs a random walk over the Markov Chain, and the moves are accepted or rejected based on the probability of finding the system in a certain state and the probability of attempting the trial move [63]. Different trial moves can be performed, e.g., translation, rotation, (re)insertion, or deletion of a molecule or atom [129]. Each move has its own acceptance rule. The acceptance rule for basic translation is given as an example below [63].

$$\text{acc}(o \rightarrow n) = \min[1, \exp(-\beta[E_n - E_o])], \quad (1.30)$$

with  $\text{acc}(o \rightarrow n)$  as the acceptance probability of going from the old (previous) state to a new state,  $\beta$  is the reciprocal of the thermodynamic temperature  $\beta = 1/k_B T$ ,  $T$  as absolute temperature,  $E_n$  the energy of the new state, and  $E_o$  as the energy of the old state. The outcome of each move contributes as a new state to the ensemble of all states.

**Metropolis Monte Carlo force field optimization** Force fields empirically describe the interaction potentials between atoms in a molecular model. Parameters of these empirical potentials can be obtained from fitting them to a reference data set with a known result. A ReaxFF force field contains many correlated parameters ( $\gg 100$ ). This gives an enormous state space of combinations of parameters. To efficiently scan this large state space, one could also use the Metropolis Monte Carlo (MMC) algorithm [83], analogous to the Metropolis Monte Carlo to sample the large state space of a molecular system efficiently. The MMC force field optimizer aims to minimize the cumulative squared error

(Error) of the energy difference between the force field and the corresponding reference data:

$$\text{Error} = \sum_{i=1}^n \left[ \frac{X_{i,\text{ref}} - X_{i,\text{ff}}}{\sigma_i} \right]^2. \quad (1.31)$$

With  $X_{i,\text{ref}}$  as reference data – for example from accurate QM DFT data – and  $X_{i,\text{ff}}$  as corresponding values computed with the force field. Each data point  $i$  in the reference set can be weighted with  $\sigma_i$ , to emphasize specific interactions during the optimization. The MMC algorithm searches for the global minimum of the cumulative error by randomly modifying a set of selected force field parameters every MC cycle. After the modification, the new error (Error<sub>new</sub>) is calculated with the new force field. Accordingly, the new set of force field parameters are accepted according to:

$$P = \min \left[ 1, \exp \left( - \frac{(\text{Error}_{\text{new}} - \text{Error}_{\text{old}})}{k_B T} \right) \right] \quad (1.32)$$

With Error<sub>old</sub> as the previous cumulative error of the old force field, and  $T$  is an artificial absolute temperature. In this way, if the error is lower, the force field modifications are accepted; if the error is higher, the modifications are accepted with a probability related to the Boltzmann distribution. By simulated annealing,  $T$  decreases slowly over the cycles, initially larger error are accepted (high  $T$ ) than towards the end of the optimization (low  $T$ ). This allows escaping local minima of the state space in the beginning of the optimization, and eventually explores the area close to the lowest found error. Reference data ( $X_{i,\text{ref}}$ ) can include all kinds of information, for example, information on charges, heat of formation, bond stretching, bond bending of gas molecules, equation of state, reaction enthalpies, proton shifts. It is vital that the reference data set contains relevant data regarding the problem to be studied.

## 1.3. THESIS OUTLINE

This thesis uses multiple molecular level methods to study the potential use of combined salt hydrates, based on MgCl<sub>2</sub> and CaCl<sub>2</sub>, for thermochemical heat storage. These methods include the very fundamental ab-initio level computations via Density Functional Theory (DFT), up to the all-atomic models covering reactive (ReaxFF) Molecular Dynamics (MD) and Monte Carlo (MC) algorithms. The thesis is constructed in a way where it starts from the smallest scale (DFT), and goes up to the large modeling scales (MD and MC). Most chapters are published in a peer reviewed journal, in this case, the only minor changes to the original published work regard referencing to work also presented in this thesis.

### Chapter 2: Chemical Analysis of Doped Salts Hydrates

This chapter contains the research regarding the most fundamental modeling level of this thesis. Using DFT in combination with advanced chemical bonding analysis, the potential thermochemical heat storage material of combined MgCl<sub>2</sub> and CaCl<sub>2</sub> are studied and characterized in terms of crystal stability, volumetric energy density, and hydrolysis resistance. *This chapter is published as peer reviewed paper and is entitled: Exploring the*

*Electronic Structure of New Doped Salt Hydrates,  $Mg_{1-x}Ca_xCl_2 \cdot nH_2O$ , for Thermochemical Energy Storage [130].*

### **Chapter 3: ReaxFF Development and Application for Calcium Chloride Hydrates**

After the previous chapter provided insight into the chemical bonding and reactivity of Mg/Ca salt hydrates, this chapter focuses on the development and validation of a reactive force field (ReaxFF) for MD and MC. In this sense, the development of the ReaxFF for pristine  $CaCl_2 \cdot nH_2O$  hydrates is discussed. Next to  $CaCl_2$ , there is a ReaxFF developed and validated for  $MgCl_2 \cdot nH_2O$  collaboration with A. D. Pathak [100]. However, this will not be discussed in this chapter. *This chapter is published as peer reviewed paper and is entitled: Development of a Reactive Force Field for  $CaCl_2 \cdot nH_2O$ , and the Application to Thermochemical Energy Storage [131].*

### **Chapter 4: Advanced Diffusion Methods for $H_2O$ in Salt Hydrates**

In order to gain insight into water mobility in and around TCMs, the diffusion of water is studied in this chapter. This mobility is an important design parameter for thermochemical heat storage applications, since it affects storage properties like the power output, and could prevent agglomerations. To obtain diffusion coefficients from MD, most often the well-known Einstein's method or Green–Kubo method is used. However, these are not valid in and around inhomogeneous system, where a partly hydrated salt that is surrounded with vapor is a inhomogeneous systems. Additionally, local diffusion information is needed to study the effects of pores, cracks, and voids. In this chapter, a diffusion tool based on the survival probability of particles in a small bin near the region of interest is explained and applied on  $CaCl_2 \cdot 2H_2O$ . *This chapter is submitted to a peer reviewed journal and is entitled: Advanced diffusion methods for  $H_2O$  in salt hydrates.*

### **Chapter 5: ReaxFF for Vapor–Liquid Equilibrium**

To accurately study (de)hydrated salts utilizing MD and MC models it is crucial to have a reliable force field that can describe  $H_2O$  in vapor as well as liquid phase. Therefore, in this chapter, the development of a  $H_2O$  ReaxFF force field is discussed. Furthermore, this new ReaxFF is tested and validated with a newly developed Gibbs Ensemble (GE) ReaxFF model. This model is able to obtain vapor-liquid equilibriums of fluids at saturation conditions. Next to the development of the new force fields, the development of this new GE-ReaxFF is extensively discussed. *This chapter is published as peer reviewed paper and is entitled: Gibbs Ensemble Monte Carlo for Reactive Force Fields to Determine the Vapor–Liquid Equilibrium of  $CO_2$  and  $H_2O$  [132].*

### **Chapter 6: ReaxFF for Hydration Characteristics of Salts**

In the previous chapter, the development of the GE–ReaxFF model is discussed. This model forms the foundation of the newly developed Grand–canonical Monte Carlo (GCMC) ReaxFF model. This chapter describes the development of the GCMC–ReaxFF model. Furthermore, the newly developed algorithm is applied to pure  $MgCl_2 \cdot nH_2O$  to study its hydration characteristics. *This chapter is published as peer reviewed paper and is entitled: Reactive Grand–Canonical Monte Carlo Simulations for Modeling Hydration of  $MgCl_2$ .*

**Chapter 7: ReaxFF Development and Application for Combined Salt Hydrates**

Building on the previous chapters, this chapter discusses the development of a new reactive force field for the combined salt of  $\text{Mg}_{1-x}\text{Ca}_x\text{Cl}_2 \cdot n\text{H}_2\text{O}$ . By means of this force field, the potential for this combined salt as thermochemical heat storage material is studied, and import storage properties have been characterized for the new salt.

**Chapter 8: Conclusion & Outlook**

A conclusive chapter that summarizes and discusses the findings of this thesis. Additionally, we hypothesis on possible future directions of this research field.



# 2

## CHEMICAL ANALYSIS OF DOPED SALTS HYDRATES

*Cutting the uncuttable.*

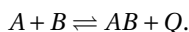
*The word atom is derived from the Greek word atomos, which means "uncuttable".*

**ABSTRACT:** Both  $\text{MgCl}_2 \cdot n\text{H}_2\text{O}$  and  $\text{CaCl}_2 \cdot n\text{H}_2\text{O}$  have their own shortcoming characteristics within the operational temperature of the thermochemical heat storage applications. While the higher hydrates of  $\text{CaCl}_2 \cdot n\text{H}_2\text{O}$  ( $n=4,6$ ) have a low melting point, the lower hydrates of  $\text{MgCl}_2 \cdot n\text{H}_2\text{O}$  ( $n=0,1,2$ ) can form the highly toxic and corrosive HCl gas. Both shortcomings cap the individual use of these salts to a restricted range of the available hydrates. A combination of these two salts showed to have the potential to overcome these shortcomings. This chapter focuses on finding stable configurations of potential superior salt hydrate combinations by using the evolutionary algorithm USPEX as well as manual mutations of known pristine structures. The new found structures are less stable than the pure salts, but stable enough to be combined. Extensive electronic density derived tools, like the DDEC6 bond orders and net atomic charges, as well as Bader topological analysis, are used to predict the HCl gas formation based on the chemical environment in the new metastable structures. We find that doping  $\text{MgCl}_2 \cdot n\text{H}_2\text{O}$  with calcium is considerably reducing HCl formation compared to its pure form. Caused by a combination of the stronger Ca–Cl interaction than Mg–Cl, and a less polar  $\text{H}_2\text{O}$  molecule in a calcium environment than in a magnesium environment. This provides the possibility to shift the  $p,T$ -equilibrium curve of HCl outside the thermal storage operational window.

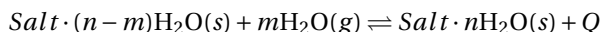
---

This chapter is published as peer reviewed article: Heijmans, K., Tranca, I.C., Gaastra-Nedea, S.V. and Smeulders, D.M.J., Exploring the Electronic Structure of New Doped Salt Hydrates,  $\text{Mg}_{1-x}\text{Ca}_x\text{Cl}_2 \cdot n\text{H}_2\text{O}$ , for Thermochemical Energy Storage. *The Journal of Physical Chemistry C*, 124(45), pp.24580-24591 (2020).

In the transition towards a new energy society, based on renewable sources, a long term energy storage is key to bridge the mismatch between solar irradiation and heat demand of different users. Such a system can make a major contribution, since hot tap water and space heating combined account for 79% of the final energy use of EU households [3]. Therefore, there is a growing interest in a storage system which stores large amounts of heat, with negligible heat losses over long time periods, in a compact design. Thermochemical heat storage has the means to achieve this goal. It stores heat in a reversible reaction between a sorbate and a sorbent [7, 21, 22] according to the reaction:



When there is an excess of heat, the sorbate ( $A$ ) and the sorbent ( $B$ ) are combined via an endothermic reaction to material  $AB$ , while heat ( $Q$ ) is released. In times of abundant heat, heat is used to split the material  $AB$ , via an endothermic reaction, back to the original sorbate ( $A$ ) and sorbent ( $B$ ). Especially, thermochemical heat storage systems based on gas-solid sorption mechanisms have theoretical high energy storage capacities, compared to other heat storage system. These solid sorption systems can roughly be divided in two groups, weak chemisorption of vapors in salts (e.g salt in combination with water, ammonia, ethanol, or methanol), and strong chemisorption (e.g. metallic hydrides, hydroxides, carbonates) [18]. Strong chemisorption reactions form a strong bond between the sorbent and sorbate, which results in medium to high thermochemical storage operating temperatures. For example, hydrogen systems like metal hydrides, and hydroxide systems typically operate at medium temperature ( $523 < T < 723$  K), and carbonates at high temperature ( $T > 723$  K) [23]. Accordingly, these systems are usually applied in industry. Weak chemisorption interactions lead to low operating temperatures ( $T < 523$  K), which makes them ideal for domestic heating. Weak chemisorption systems make use of salt hydrates mostly in combination with water vapor, because of practical reasons like the abundance of water vapor in air. The reversible (de)hydration reaction of the salts can occur in multiple hydration steps, following:



When salt hydrates are heated, they dissociate in water vapor and a lower hydrate or anhydrous salt. When water is added to an anhydrous or lower hydrate salt, they combine to a higher hydrate, and heat is released. Ideal thermochemical materials (TCM) for such storage should have a high energy densities, be affordable, have a high cycle stability, fast kinetics, and should be non-toxic. In this sense, large amounts of different salts have been studied and reviewed [7, 11, 18, 19, 21, 22, 133]. A promising group of these TCM salt hydrates are the chloride-based  $MgCl_2 \cdot nH_2O$  and  $CaCl_2 \cdot nH_2O$  ( $n = 0, 1, 2, 4, 6$ ). The main reasons are the relatively high sorption energy ( $2 - 3$  GJ/ $m^3$ ), their costs, and their availability [40]. Furthermore, the reactions of these salts occur at temperatures corresponding to domestic heating applications [33]. Dehydration temperatures range from 36–214 °C, depending on the current hydration level. Thus  $MgCl_2 \cdot nH_2O$  dehydrates at temperatures of 214, 125–127, 101–104, 68–72 °C, for  $n = 1, 2, 4, 6$  respectively, and  $CaCl_2 \cdot nH_2O$  dehydrates at 36–41, 49–54, 71, 112 °C, for  $n = 1, 2, 4, 6$  respectively [11]. In practice, mainly the hydration levels  $n = 2 - 6$  for pristine  $MgCl_2 \cdot nH_2O$ , and  $n = 0 - 2$  for pristine  $CaCl_2 \cdot nH_2O$  are considered as TCM, due to different concerns when



these pure salts are used. A point of concern is the deliquesce [19], which occurs for both salts already at low temperatures ( $25^{\circ}\text{C}$ ) if the water vapor pressure is sufficiently high enough (12 mbar) [11, 24, 27]. Besides, in the case of calcium chloride, higher hydrates like  $\text{CaCl}_2 \cdot 4\text{H}_2\text{O}$  and  $\text{CaCl}_2 \cdot 6\text{H}_2\text{O}$  have low melting temperatures, which are in the range of the storage operation window [25, 26]. Both phenomena, deliquesce and melting, can lead to agglomerates and clog the storage system. A major disadvantage of  $\text{MgCl}_2$  hydrates is hydrolysis (formation of  $\text{HCl}$ ) above  $135^{\circ}\text{C}$  [33, 34] ( $\text{MgCl}_2 \cdot \text{H}_2\text{O}(\text{s}) \rightarrow \text{MgOHCl}(\text{s}) + \text{HCl}(\text{g})$ ).

This is an undesired irreversible reaction, which degrades the storage materials, and most importantly,  $\text{HCl}$  is a highly toxic and corrosive gas. These shortcomings of  $\text{MgCl}_2$  and  $\text{CaCl}_2$  salts cap the use of the entire range of the hydrates, and make them less convenient to be used as TCM.

$\text{CaCl}_2 \cdot n\text{H}_2\text{O}$  is more resistant against hydrolysis than  $\text{MgCl}_2 \cdot n\text{H}_2\text{O}$  [59]. On the other hand,  $\text{MgCl}_2 \cdot 6\text{H}_2\text{O}$  has a higher melting point than  $\text{CaCl}_2 \cdot 6\text{H}_2\text{O}$  and remains solid within the storage operation window. This implies that a potential combination of  $\text{MgCl}_2 \cdot n\text{H}_2\text{O}$  and  $\text{CaCl}_2 \cdot n\text{H}_2\text{O}$  could have superior characteristics compared to their isolated pure components, regarding increased stability and reduced hydrolysis. This assumption is supported by multiple studies [31, 41, 55, 60, 134]. Rammelberg et al [31, 41] experimentally showed an improved cyclability for a mixture of  $\text{MgCl}_2/\text{CaCl}_2$ . Pathak et al. [60] found, using Density Functional Theory (DFT), that a double salt of  $\text{CaCl}_2$  and  $\text{MgCl}_2$  is more resistant to hydrolysis than the individual pure compounds. Furthermore, diffusion of water through the salt crystals is typically very slow [40, 53], limiting the applicability of these salts as TCM. Imperfections in the crystal, e.g. stresses created by defects, boundaries, impurities, and interfaces could promote the diffusion of water [53, 100, 135]. Müller et al. [55] experimentally observed for a similar system of magnesium oxides, doped with 0–40% calcium, a significant increased water dissociation rate. This doping enhances the hydration rate as well as the cycle stability, with the optimum value being found for 10% doping. They supported their experimental findings with DFT calculations, which indicated that the calcium dopant expanded the surface lattice of  $\text{MgO}$  towards the  $\text{CaO}$  surface and it increased water dissociation.

Huinink et al. [53] showed that for bulk  $\text{MgCl}_2 \cdot 4\text{H}_2\text{O}$  and  $\text{MgCl}_2 \cdot 6\text{H}_2\text{O}$  an interstitial water molecule diffuses faster than the water molecules fixed in the coordination shells of the magnesium ion. Additionally, they concluded that a substituted calcium atom into a bulk magnesium crystal can absorb and pin the interstitial water molecule, limiting its mobility. However, Huinink et al. focused on bulk material, where the diffusion can be orders of magnitude lower than in regions close to the surface [100, 135], which is the region Müller et al. did their findings. The surface characteristics play an important role for many salt-like structures, as low reactivity and cycle stability are correlated to the critical inhibition of water near the surface [55, 136], and an increased lattice at the surface promotes the water dissociation. This increased water dissociation could improve water dehydration and transport, which are important design parameters for heat storage systems [19, 137]. As listed before, the different dehydration temperatures do not exactly match between the pure salts. In this sense, new/intermediate dehydration temperatures could be expected when the salts are combined. Alternatively, different dehydration onset temperatures could act as nucleation sites in the combination of the

salts.

Based on these previous studies,  $\text{MgCl}_2$  doped with calcium could improve key material properties for thermochemical storage. The AFLOW-CHULL platform [138] computed the convex hull for ternary combinations of Ca, Mg, and Cl. They found as the only stable structures: pure Ca, pure Mg, pure Cl,  $\text{CaCl}_2$ ,  $\text{MgCl}_2$ , and  $\text{CaCl}_2$ . In the present work, we extended the search, and focused on the combinations of  $\text{MgCl}_2 \cdot n\text{H}_2\text{O}$  and  $\text{CaCl}_2 \cdot n\text{H}_2\text{O}$ , because of the heat storage application. In this sense, we used the evolutionary algorithm USPEX [71–73], as well as manually doped crystals, in order to predict new structures of  $\text{Mg}_{(1-x)}\text{Ca}_x\text{Cl}_2 \cdot n\text{H}_2\text{O}$  ( $n = 0, 2, 4, 6$ ;  $x = [0, 1]$ ). Afterwards, using first principle analysis tools, the chemical effect of doping on the stability of the crystals, hydrolysis, and the volumetric energy density of the storage material were investigated.

## 2.1. METHODS

### 2.1.1. EXPLORATION OF NEW DOPED STRUCTURES

Two methods were used to explore new possible combinations of  $\text{MgCl}_2 \cdot n\text{H}_2\text{O}$  and  $\text{CaCl}_2 \cdot n\text{H}_2\text{O}$ , manually doping the structures and automatic structure generation using the evolutionary algorithm USPEX. The stability of these new combinations was analyzed using the convex hull method.

#### MANUALLY DOPED STRUCTURES

Manually doped structures were created for all the hydrates. We started from the experimentally known salt hydrates structures,  $\text{MgCl}_2$  [139],  $\text{CaCl}_2$  [139],  $\text{MgCl}_2 \cdot 2\text{H}_2\text{O}$  [140],  $\text{CaCl}_2 \cdot 2\text{H}_2\text{O}$  [141],  $\text{MgCl}_2 \cdot 4\text{H}_2\text{O}$  [142],  $\text{CaCl}_2 \cdot 4\text{H}_2\text{O}$  [143],  $\text{MgCl}_2 \cdot 6\text{H}_2\text{O}$  [144], and  $\text{CaCl}_2 \cdot 6\text{H}_2\text{O}$  [145]. In these known structures Mg atoms were gradually substituted by Ca atoms and vice versa ( $\text{Mg} \leftrightarrow \text{Ca}$ ), as shown in Figure 2.1. This resulted in numerous  $\text{Mg}_{(1-x)}\text{Ca}_x\text{Cl}_2 \cdot n\text{H}_2\text{O}$  crystals, with  $x = [0, 1]$  and  $n = 0, 2, 4, 6$ . The generated structures were relaxed using the DFT Vienna Ab-initio Simulation Package (VASP) [146]. The PBE [147] exchange correlation functions, with the PAW [148, 149] scheme were used to describe the ion-electron interactions. The DFT-D3 [150], including the Becke–Johnson damping [151], was used to describe the dispersion interactions. Each generated structure was relaxed until all forces on the atoms were lower than  $0.026 \text{ eV}/\text{\AA}$ . Accordingly, the structures stabilities were analyzed by computing the convex hull.

#### USPEX

In the search for new crystal structures, it is practically impossible to sample all the possible different configurations in which the atoms and the unit cell of a crystal can arrange, due to the large number of the degrees of freedom present. Fortunately, not the entire space has to be sampled, but only some small regions around a known minimum. In order to achieve this, efficient methods are needed to explore these small regions [71]. In the search for new stable combinations of anhydrous  $\text{MgCl}_2$  and  $\text{CaCl}_2$ , next to the manually doped structures, the evolutionary algorithm USPEX [71, 73, 152, 153] was used in combination with its variable composition tool [72, 154]. This is an efficient and proved evolutionary algorithm for crystal structures prediction, e.g. various ionic, covalent, metallic, and molecular structures.

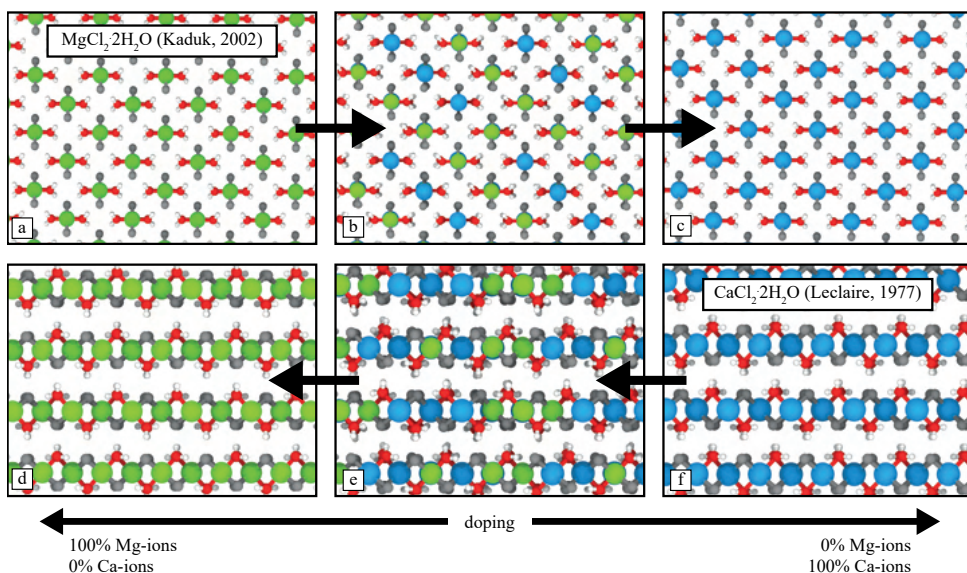


Figure 2.1: Schematic representation of the approach for manually creating the doped salt hydrates [134]. The example of the dihydrate salts,  $\text{MgCl}_2 \cdot 2\text{H}_2\text{O}$  and  $\text{CaCl}_2 \cdot 2\text{H}_2\text{O}$ , is presented, with these two salts constituting both the starting/ending point [140, 141]. Green spheres represents magnesium atoms, blue the calcium, grey the chlorides, red the oxygens, and light grey the hydrogens.

USPEX uses random structures as well as combinations and perturbations of the most promising structures of previous generations to create a new generation of structures. From the new generation the most promising structures will be selected, next to a set of random generated structures. The selection of most stable structures, in combination with good variation operators, allows one to zoom in on the most promising configurations, with the lowest amount of free energy, and converge to the most stable state. The random generated structures prevents one to be stuck around a single local minimum, and explore other completely different solutions. The generated USPEX structures were relaxed using VASP with the same accuracy as the manually doped structures.

## CONVEX HULL

To study the thermodynamical stability of the different combined salt hydrates the convex hull was used. This provides insights into the stability of the individual doped structures, relative to the pure structures. The convex hull is the surface of the formation energy as function of the chemical composition, which passes through all thermodynamically stable structures that are the lowest in energy. All structures which are higher in energy, will be above this surface and can be considered as metastable structures. These metastable structures will possibly decompose, over (infinite) time, into a linear combinations of the more stable structures located on the convex hull. The energy distance between the convex hull and any structure ( $E_{\text{CH}}$ ) gives us a measure for the (meta)stability of the structure.

To create the convex hull for each doped hydrate, we considered the original pristine

Table 2.1: Example calculation for the convex hull, where the energy difference from the convex hull ( $E_{CH}$ ) can be computed by subtracting the reference energy ( $E_{ref}$ ) of the pristine systems from the energy of the compound systems ( $E_{mix}$ ).

Mixture		Energy difference with convex hull ( $E_{CH}$ )
Salt A	Salt B	
100%	0%	$E_{CH} = E_{mix} - 1 \times E_{ref,A} - 0 \times E_{ref,B} = 0$
95%	5%	$E_{CH} = E_{mix} - 0.95 \times E_{ref,A} - 0.05 \times E_{ref,B}$
90%	10%	$E_{CH} = E_{mix} - 0.9 \times E_{ref,A} - 0.1 \times E_{ref,B}$
...	...	
$n$	$m$	$E_{CH} = E_{mix} - n \times E_{ref,A} - m \times E_{ref,B}$
...	...	
0%	100%	$E_{CH} = E_{mix} - 0 \times E_{ref,A} - 1 \times E_{ref,B} = 0$

Table 2.2: Type of interactions [165] based on Bader Topological analysis. With  $\rho$  as the electronic density,  $V$  the potential energy density, and  $G$  as the kinetic energy density.

Interaction	$\nabla^2 \rho(r)$	$ V /G$
Covalent	$< 0$	$> 2$
Transition	$> 0$	$1 < \dots < 2$
Ionic, vdW	$> 0$	$< 1$

crystals of  $MgCl_2$  [139],  $CaCl_2$  [139],  $MgCl_2 \cdot 2H_2O$  [140],  $CaCl_2 \cdot 2H_2O$  [141],  $MgCl_2 \cdot 4H_2O$  [142],  $CaCl_2 \cdot 4H_2O$  [143],  $MgCl_2 \cdot 6H_2O$  [144], and  $CaCl_2 \cdot 6H_2O$  [145] as reference. The doped structures were compared to these reference structures by subtracting the reference energy multiplied by the fraction of the reference. An example of this calculation is given in Table 2.1. Furthermore, a ternary convex hull was created, combining the hydrates, using  $MgCl_2$ ,  $CaCl_2$ , and the  $H_2O$  gas molecule as reference structures.

### 2.1.2. CHEMICAL BONDING ANALYSIS

The inter-atomic bonds of the most stable structures were qualified and quantified using the electron density based methods, the Bader Topological Analysis, and the Density Derived Electronic and Chemical (DDEC6) approach.

For the characterization of the bond strength we used the Density Derived Electronic and Chemical (DDEC6) method [155–157]. This method, which can provide reliable bond orders (BO) and net atomic charges (NAC), has been previously used to investigate the interactions and reactivity of various systems, e.g. molecular systems [158, 159], 2D materials [160], porous media [161].

To characterize the type of interactions (ionic, vdW, covalent, or a combination) between the atoms, the Quantum Theory of Atoms in Molecules (QTAIM) was used [162–164]. Within this framework we investigated the topological analysis of the electron density, whereby the electron density characteristics at the bond critical points, as well as the values of the Laplacian, kinetic and potential energy densities, can offer insight into both the strength and the type of the interactions present. [162–165], see Table 2.2.

## 2.2. RESULTS & DISCUSSION

Using evolutionary algorithms and electronic density derived tools, the effect of doping magnesium chloride hydrates with calcium and vice versa, is studied. The crystals stability (convex hull), the potential volumetric energy density (storage density), and the atomic interactions are quantified and qualified. Furthermore, trends in the effect of doping on the HCl interactions are explored

### 2.2.1. CONVEX HULL – STABILITY OF THE EXPLORED STRUCTURES

New combinations of  $\text{MgCl}_2 \cdot n\text{H}_2\text{O}$  and  $\text{CaCl}_2 \cdot n\text{H}_2\text{O}$  ( $n = 0, 2, 4, 6$ ) were explored using manually built configurations. Additionally, the set of configurations for the anhydrous salt ( $\text{MgCl}_2$ ,  $\text{CaCl}_2$ ) was expanded by using the evolutionary algorithm USPEX, in order to gain more knowledge on the possible combinations and structures. The use of USPEX for the di- and tetrahydrated salts was not feasible, because of the high amount in degrees of freedom when 4 or more variable atoms/molecules are included.

The evolutionary algorithm USPEX search resulted in more than 3400 generated anhydrous structures, containing 18–36 atoms, over 25 generations. The known experimental structures of pure salts were used as seeds in the search, to enable a good start for a subset of the first generation. The convex hull of the most stable generated USPEX structures is shown in Figure 2.2a, with pure  $\text{MgCl}_2$  on the left, and pure  $\text{CaCl}_2$  on the right side of the x-axis. The energy is given per block of  $\text{MgCl}_2/\text{CaCl}_2$ . As shown in Figure 2.2a, all the new found structures with USPEX are above the dashed line. This line represents the convex hull and joins the most stable structures, in our case the pure  $\text{MgCl}_2$  and pure  $\text{CaCl}_2$ . This indicates that all found doped structures are metastable compared to the pure structures. This outcome agrees with the Aflow [138] database, which only contained the metastable combined structure  $\text{MgCaCl}_4$  (represented with a red circle in Figure 2.2a), and does not report on any stable combination besides the pristine structures.

The results of the manually doped anhydrous and hydrated structures are given in Figure 2.2b, which also includes the most stable structures from USPEX. Similar structures were found, however, for the higher amount of doping ( $\gtrsim 20\%$ ) USPEX found more stable structures than we found by manually doping the anhydrous structures. One can immediately see that all the energies of the manual doped structures are also above the convex hull. Therefore, the convex hull turns out to be a straight surface between the pure salts. This indicates that all the generated combined structures are thermodynamically less stable than their pure compounds, and over (infinite) time the metastable doped structures could decompose into the pure forms of  $\text{MgCl}_2 \cdot n\text{H}_2\text{O}$  and  $\text{CaCl}_2 \cdot n\text{H}_2\text{O}$ . The metastable compounds could cause undesired reduced melting temperatures for the compound structures, which was already a problematic issue for the higher hydrates of  $\text{CaCl}_2 \cdot n\text{H}_2\text{O}$ . However, the energy difference of the most stable doped structures for  $n = 0, 2, 4$  (found along the dashed line in Figure 2.2b) with the convex hull is small ( $E_{\text{CH}} < 0.05$  eV per block of  $\text{MgCl}_2/\text{CaCl}_2/\text{H}_2\text{O}$ ), especially for low amounts of doping ( $< 20\%$ ), when compared with the inherent energy fluctuation in the order of 0.025 eV at room temperature. Therefore, we could assume that these generated doped structures are stable enough, and the energy difference is not large enough to let the doped structures decompose into grains of pure salts. For the hexahydrate ( $n = 6$ ), one could

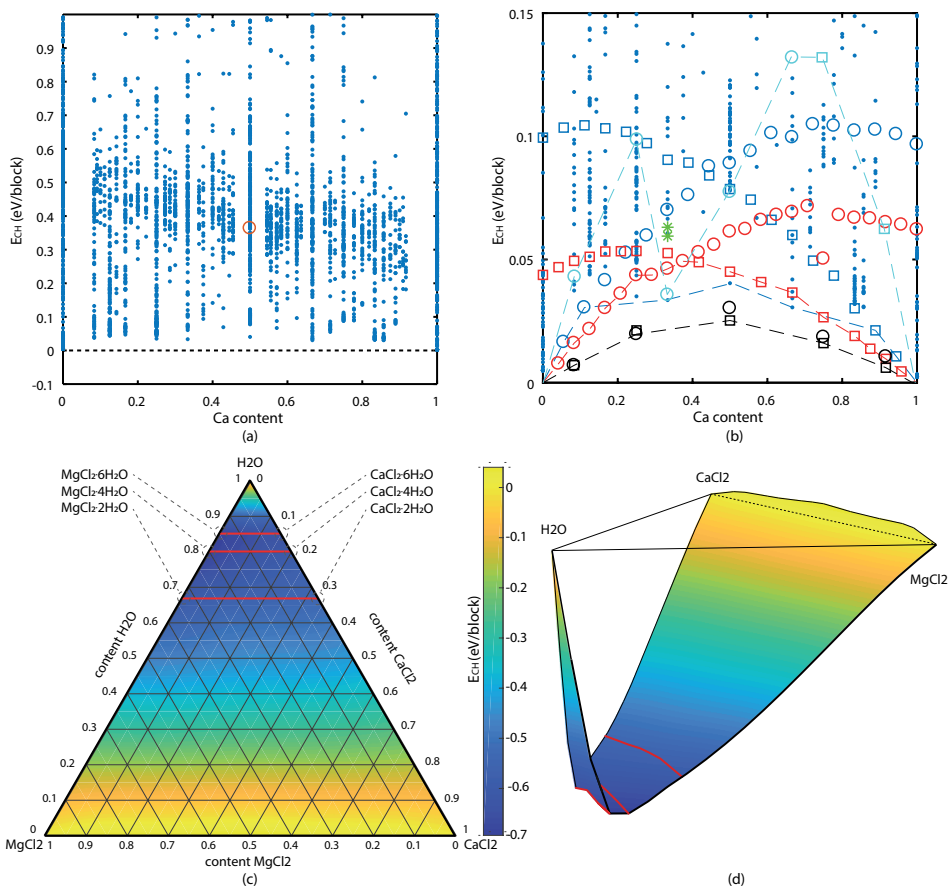


Figure 2.2: (a) USPEX convex hull for non-hydrated combinations of  $MgCl_2$  and  $CaCl_2$  ( $E < 1$  eV/block). The energy is given per interchangeable block of  $MgCl_2/CaCl_2$ , thus per block of 3 atoms. The black dashed line represents the convex hull. The red circle indicates the metastable  $MgCaCl_4$  structure given in the Aflow [138] database. (b) Convex hull of doped salt anhydrous and hydrated salts. The blue dots represent the most stable ( $E_{CH} < 0.15$  eV/block) USPEX structures, the blue symbols represents the manually doped anhydrous structures (circle = doped  $CaCl_2$ ; square = doped  $MgCl_2$ ), red symbols the dihydrate structures (circle = doped  $CaCl_2 \cdot 4H_2O$ ; square = doped  $CaCl_2 \cdot 2H_2O$ ), black symbols the tetrahydrate structures (circle = doped  $MgCl_2 \cdot 4H_2O$ ; square = doped  $CaCl_2 \cdot 4H_2O$ ), and cyan symbols the hexahydrate structures (circle = doped  $MgCl_2 \cdot 6H_2O$ ; square = doped  $CaCl_2 \cdot 6H_2O$ ). The convex hull energy is given in eV per block  $MgCl_2$  or  $CaCl_2$ . The two green asterisks  $^{**}$  are two experimentally found [141, 166] and relaxed tachyhydrite structures ( $CaMg_2Cl_6 \cdot 12H_2O$ ). The dashed lines connect the structures which are further considered in this study. (c) Ternary Figure of doped  $MgCl_2 \cdot nH_2O$  and  $CaCl_2 \cdot nH_2O$ , with  $MgCl_2(s)$ ,  $CaCl_2(s)$ , and  $H_2O(g)$  as reference structures. The energy is given in eV per block of ( $MgCl_2/CaCl_2/H_2O$ ). The red lines highlight the di-, tetra-, and hexahydrate structures. (d) 3D visualization of the ternary convex hull.



conclude that in general doping increases instability more, compared to the lower hydrates, except for the case around 33% calcium content. In practice this is also the case for pristine  $\text{CaCl}_2 \cdot 6\text{H}_2\text{O}$ , which is hardly studied as TCM material because it melts at room temperature [11, 24, 27]. The decreased stability implies that doping  $\text{CaCl}_2 \cdot 6\text{H}_2\text{O}$  with magnesium does not prevent the undesired melting. The drop in  $E_{\text{CH}}$  for the hexahydrate structures with 33 – 66% calcium are caused by a distortion in the interaction plane parallel to the lattice  $c$ -direction, as shown in Appendix B. This leads to a stabilization of the crystal compared to the structures with lower amount of calcium ( $\leq 25\%$ ). The higher amount of calcium ( $\geq 75\%$ ) structures are structures corresponding the  $\text{CaCl}_2 \cdot 6\text{H}_2\text{O}$  topology.

Furthermore, we notice that for higher amount of doping, the anhydrous and dihydrate original structures of the undoped materials are no longer the preferred structures. But rather that of the dopant. Thus, for anhydrous structures the combination of  $\text{Mg}_{(1-x)}\text{Ca}_x\text{Cl}_2$  ( $x > 44\%$ ) in  $\text{MgCl}_2$  structure is less stable than the same combination but in the  $\text{CaCl}_2$  structure, and vice versa  $\text{Mg}_{(1-x)}\text{Ca}_x\text{Cl}_2$  ( $x < 44\%$ ) in  $\text{CaCl}_2$  structure is less stable than the same combination in  $\text{MgCl}_2$  structure. For the dihydrate structures this effect is also present, with the switch around 40%, however with a lower energy difference between the different structures. For the tetrahydrates this effect is not observed. Thus the preference of the crystal structure of the dopant becomes lower with an increasing amount of water in the crystal. Besides the hydration level, this effect could be also due to the fact that anhydrous  $\text{MgCl}_2$  adopts a different crystal structure than  $\text{CaCl}_2$  (rhombohedral vs orthorhombic crystal system). On the other hand, their corresponding hydrates crystallize in the orthorhombic and monoclinic crystal systems. The orthorhombic–monoclinic phase transition (in this case occurring for the hydrate variant) is more often reported in literature than the orthorhombic–rhombohedral phase transition (in this case occurring for the anhydrous variant).

Interestingly, the experimental structures of tachyhydrite [166, 167] ( $\text{CaMg}_2\text{Cl}_6 \cdot 12\text{H}_2\text{O}$ ), are higher in energy than the generated doped structures. This could indicate that this is a metastable structure, or it is stabilized by entropy. The dashed lines (blue for anhydrous, red for dihydrates, black for tetrahydrates, and cyan for hexahydrates) in Figure 2.2b connect the most stable doped structures. These structures were used for further analysis in this study. Including the obtained ternary convex hull, which is given in Figure 2.2c, and in a 3D in Figure 2.2d. The 3D Figure shows the relative low energy difference with the convex hull of the doped structures within each hydrate, compared to the convex hull energy difference between doped structures of the different hydrates ( $\sim 0.6$ – $0.7$  eV). Close observation of Figures 2.2c and 2.2d shows a heat of formation of 0.60 eV, 0.69 eV, 0.68 eV, 0.54 eV, 0.61 eV, and 0.64 eV for  $\text{MgCl}_2 \cdot 2\text{H}_2\text{O}$ ,  $\text{MgCl}_2 \cdot 4\text{H}_2\text{O}$ ,  $\text{MgCl}_2 \cdot 6\text{H}_2\text{O}$ ,  $\text{CaCl}_2 \cdot 2\text{H}_2\text{O}$ ,  $\text{CaCl}_2 \cdot 4\text{H}_2\text{O}$ , and  $\text{CaCl}_2 \cdot 6\text{H}_2\text{O}$  respectively. Thus, slightly higher values for the  $\text{MgCl}_2$  hydrate reactions. The values are given per mol of  $\text{MgCl}_2/\text{CaCl}_2/\text{H}_2\text{O}$  block, which equals a heat of formation of 0.91 eV, 0.87 eV, 0.80 eV, 0.81 eV, 0.76 eV, and 0.75 eV per mol of  $\text{H}_2\text{O}$  respectively. The heat of formation per mol  $\text{H}_2\text{O}$  is in agreement with reference values of the NBS tables [168], which are derived from measured reaction enthalpies and corrected to standard conditions. The comparison is given in Table 2.3.

Table 2.3: Heat of formation for the considered reactions compared with calculated values from NBS tables [168]. <sup>§</sup> energy given per mol of  $\text{MgCl}_2/\text{CaCl}_2/\text{H}_2\text{O}$ , as given in Figure 2.2c; <sup>†</sup> energy given per mol  $\text{H}_2\text{O}$ ; <sup>‡</sup> energy given per mol  $\text{H}_2\text{O}$  calculated from NBS tables [168] at standard conditions ( $T = 298 \text{ K}$ ,  $p = 1 \text{ bar}$ ).

phase transition $\text{MgCl}_2 \cdot n\text{H}_2\text{O}$	Heat of formation		NBS tables [168] ( $\text{eV}/n_{\text{H}_2\text{O}})$ <sup>‡</sup>
	this work ( $\text{eV}/(n_{\text{MgCl}_2} + n_{\text{H}_2\text{O}}))$ <sup>§</sup>	( $\text{eV}/n_{\text{H}_2\text{O}})$ <sup>†</sup>	
0 - 2	0.60	0.91	0.80
0 - 4	0.69	0.87	0.75
0 - 6	0.68	0.80	0.70
2 - 4	–	0.83	0.70
4 - 6	–	0.66	0.60
$\text{CaCl}_2 \cdot n\text{H}_2\text{O}$	( $\text{eV}/(n_{\text{CaCl}_2} + n_{\text{H}_2\text{O}}))$ <sup>§</sup>		
0 - 2	0.54	0.81	0.65
0 - 4	0.61	0.76	0.64
0 - 6	0.64	0.75	0.65
2 - 4	–	0.71	0.63
4 - 6	–	0.73	0.69

### 2.2.2. STORAGE DENSITY

The volumetric energy density of a thermal energy storage is an important design parameter, and it is a unique selling point of TCMs towards conventional thermal energy storage systems. In this sense, we computed the sorption energy of the different doped salts, to gain insight into the theoretical achievable energy density of the TCM storage. The sorption energy was computed using the most stable structures (connected by the dashed lines in Figure 2.2b) via:

$$E_{\text{sorp},x,m \rightarrow n} = E_{\text{Mg}_{(1-x)}\text{Ca}_x\text{Cl}_2 \cdot n\text{H}_2\text{O}} - E_{\text{Mg}_{(1-x)}\text{Ca}_x\text{Cl}_2 \cdot m\text{H}_2\text{O}} - (n - m) \times E_{\text{H}_2\text{O}}, \quad (2.1)$$

where  $E_{\text{sorp},x,m \rightarrow n}$  is the sorption energy between hydrates  $m$  and  $n$  at a given doping content  $x$  of calcium.  $E_{\text{Mg}_{(1-x)}\text{Ca}_x\text{Cl}_2 \cdot n\text{H}_2\text{O}}$  is the crystal energy of the higher hydrate,  $E_{\text{Mg}_{(1-x)}\text{Ca}_x\text{Cl}_2 \cdot m\text{H}_2\text{O}}$  the crystal energy of the lower hydrate, and  $E_{\text{H}_2\text{O}}$  the energy of water vapor. Accordingly, the volumetric energy density ( $E_{\text{vol}}$ ) was computed using the volume ( $V_n$ ) of the higher hydrated structure:

$$E_{\text{vol},x} = \frac{|E_{\text{sorp},x,m \rightarrow n}|}{V_{n,x}}. \quad (2.2)$$

As different amounts of doping ( $x$ ) are present for the variable hydration numbers, an interpolation was used in order to generate the  $x$ -dependent variables from eq. 2.1, 2.2. In Figure 2.3a, the results are given for the volumetric energy density. The asterisks (\*) indicate calculated storage densities, using the formation energies of the NBS tables [168] divided by the volume of the experimental structures. The small discrepancy between these computed volumetric energy density is mostly caused by the difference in formation energy.

The material densities of the different doped salt hydrates are given in Figure 2.3b. When considering the pristine structures (pure  $\text{MgCl}_2 \cdot n\text{H}_2\text{O}$ , and pure  $\text{CaCl}_2 \cdot n\text{H}_2\text{O}$ )



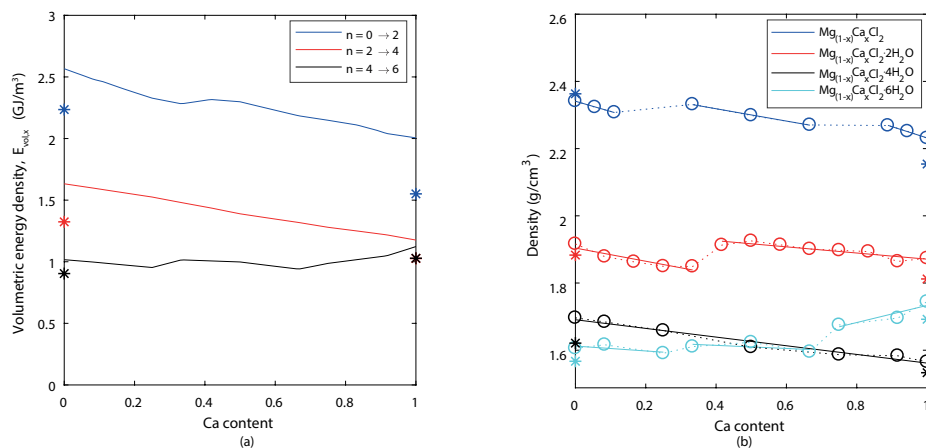


Figure 2.3: (a) Volumetric energy density of doped crystal structures. The red line represents the anhydrous to dihydrate ( $n = 0 \rightarrow n = 2$ ) reaction. The blue line represents the dihydrate to tetrahydrate ( $n = 2 \rightarrow n = 4$ ) reaction. The black line represents the tetrahydrate to hexahydrate ( $n = 4 \rightarrow n = 6$ ) reaction. The asterisks represent the calculated values using the NBS tables data [168]. (b) Density of doped salt hydrate crystals. Blue represents the anhydrous structures  $\text{Mg}_{(1-x)}\text{Ca}_x\text{Cl}_2$ , red the dihydrate structures  $\text{Mg}_{(1-x)}\text{Ca}_x\text{Cl}_2 \cdot 2\text{H}_2\text{O}$ , black the tetrahydrate structures  $\text{Mg}_{(1-x)}\text{Ca}_x\text{Cl}_2 \cdot 4\text{H}_2\text{O}$ , and cyan represents the hexahydrate structures  $\text{Mg}_{(1-x)}\text{Ca}_x\text{Cl}_2 \cdot 6\text{H}_2\text{O}$  with  $x$  as the amount of Ca content. The dotted lines follow the most stable structures of the hydrates connected by the dashed lines in Figure 2.2b.

the density difference between magnesium chloride and calcium chloride salts is -5, -2, -8, and 9% for anhydrous, dihydrate, tetrahydrate, and hexahydrate respectively. However, when considering the trends of smaller separate sections of the anhydrous, dihydrate, and hexahydrate doped structures, the density decrease is relatively larger than the overall trend. These smaller sections are indicated by the solid lines in Figure 2.3b (the sections of 0–11%, 33–66%, and 89–100% calcium content for anhydrous structures; 0–33%, and 42–100% calcium content for dihydrate structures; 0–25%, 33–66%, and 75–100% calcium content for hexahydrate structures). This effect is caused by a change in crystal structure and leads to extra voids, particularly for smaller amounts of doping. E.g. anhydrous  $\text{MgCl}_2$  already increases with 1.3% in volume when only 10% of calcium is added. Similar,  $\text{MgCl}_2 \cdot 2\text{H}_2\text{O}$  already increases with 1.0% in volume, and  $\text{MgCl}_2 \cdot 6\text{H}_2\text{O}$  increases with 0.4% in volume when 10% of calcium is added. This is much larger than what the overall trends of the volume increase suggests, from which one would expect a volume increase of 0.5, 0.2, 0.8, and -9% when 10% of calcium is added to the magnesium structures. Thus, when small amounts of calcium are added to  $\text{MgCl}_2 \cdot n\text{H}_2\text{O}$ , as long as it will remain its original pristine crystal structure, the steric effect of the larger calcium atom will cause an even larger volume increase. Accordingly, near the crystal surface these steric effects may promote valuable water dissociation and kinetics, as shown before in similar systems [55, 135]. This effect of a relative large volume increase is not present for the tetrahydrate structures, which can be linked to the fact that we did not observe a clear preferred crystal structure for this hydration level at different amounts of doping, but only small energy differences in the convex hull, as shown in Figure 2.2b.

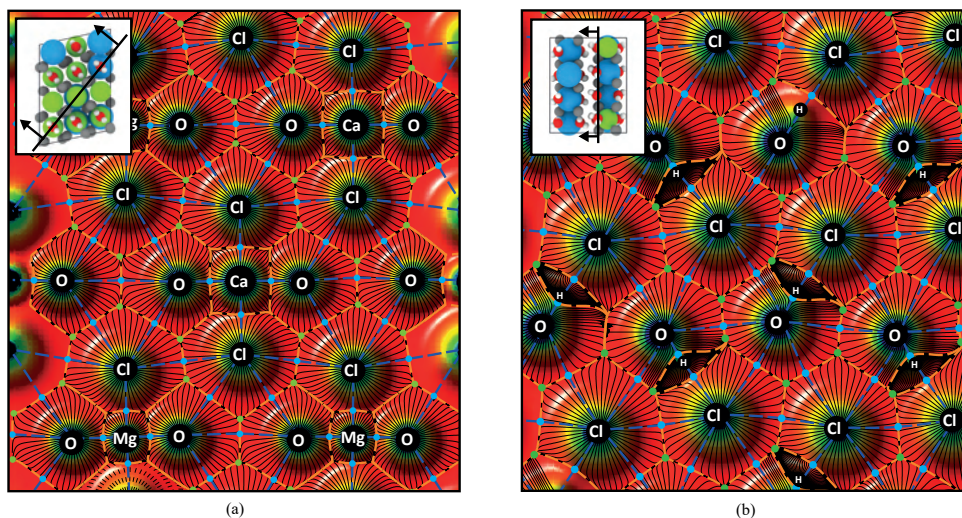


Figure 2.4: Topological analysis, with relevant section planes for (a)  $\text{Mg}_{0.75}\text{Ca}_{0.25}\text{Cl}_2 \cdot 2\text{H}_2\text{O}$  and (b)  $\text{Ca}_{0.75}\text{Mg}_{0.25}\text{Cl}_2 \cdot 2\text{H}_2\text{O}$  [134]. The inset Figures indicate the locations of the sections. The graphical colored background represents the electronic density in the plane. The superimposed lines allow for the topological analysis. The dashed blue lines designate bond paths, while the orange ones enclose the atomic basins. The blue dots designate the bond critical points (BCP), and the green dots the ring critical points. The black lines are the gradient field lines.

### 2.2.3. CHEMICAL BONDING ANALYSIS

To study the interaction between atoms in doped crystals, the Bader Topological analysis, as well as DDEC6 methodology were used. Both methods are electronic density based tools to qualify and quantify interactions between atoms. For this study, all the doped crystals of the dihydrate form were used ( $\text{Ca}_x\text{Mg}_{(1-x)}\text{Cl}_2 \cdot 2\text{H}_2\text{O}$ , with  $x = [0, 1]$ ). The dihydrate was chosen because HCl formation mainly happens when heating the lower ( $n = 1, 2$ ) hydrates [33, 34]; and there are known experimental structures for both pure magnesium and calcium chloride dihydrate structures.

The Bader Topological analysis builds upon the electronic density, and its Laplacian, at critical points within the crystal. An example of this analysis is given in Figure 2.4, where two relevant section planes are presented for  $\text{Mg}_{0.75}\text{Ca}_{0.25}\text{Cl}_2 \cdot 2\text{H}_2\text{O}$  and  $\text{Ca}_{0.75}\text{Mg}_{0.25}\text{Cl}_2 \cdot 2\text{H}_2\text{O}$ . These section planes were chosen because they show the Ca/Mg–O, Ca/Mg–Cl, O–H, and H–Cl interactions. From these section planes one can also see, e.g. the larger electronic radius of calcium compared to magnesium; the fact that hydrogen, although is closely – and thus strongly – bonded with oxygen, also shares a bond critical point (BCP) with chlorine.

At the BCP the kinetic and potential energy densities were computed, From their combination (see Table 2.2), information on the type of the interactions can be obtained (reported in Table 2.4). Additionally, in Table 2.4 we also report the DDEC6 bond orders (BO), which provides information on the amount of bonding electron pairs between atoms. From Table 2.4, one can see that O–H bonds are strongly covalent, while the H–Cl bonds are also covalent, albeit with a more significant polar character. The magnesium

and calcium bonds are around the transition point, but slightly more ionic than covalent. When adding calcium to the structure, the bond order between O–H increases, making this bond stronger, and the water molecule more stable. Simultaneously, this bond becomes slightly less covalent. From Table 2.4 we also notice that the Ca–Cl bonds have 17% stronger bonds (bond orders) than the Mg–Cl bonds. This further suggest that the presence of calcium in a structure will decrease its likelihood for HCl formation, compared with the presence of magnesium. The sum of bond order (SBO) is the summation of all BO per atom, and provides information on how much the electrons shells of the atoms are filled, and points to the reactivity of the atoms. The values of the SBOs from Table 2.5, indicates that the Ca atoms – following the formation of stronger bonds with Cl – have a higher SBO than Mg, and will be less reactive, accommodating less water molecules. This can be correlated to the experimental results where magnesium chloride can easier go up to a higher level of hydrates, the higher hydrates melt at a higher temperatures than hydrated calcium chloride crystals [25], and the observed less stable  $\text{CaCl}_2 \cdot 6\text{H}_2\text{O}$  related structures in the convex hull of Figure 2.2b.

#### 2.2.4. ATOMIC CHARGES

DDEC6 net atomic charges for the dihydrate doped systems are given in Table 2.6. From this table, one can see that the average NAC remains similar for Mg, Ca, and Cl across different amount of Mg and Ca. However, both the positive charge of H and the negative charge of O (both from  $\text{H}_2\text{O}$ ) decrease gradually with the increase of Ca presence. A less polar water molecule will be less reactive, and thus hinder the formation of the undesired HCl.

#### 2.2.5. H–CL INTERACTIONS

The Bader topological analysis, as well as the DDEC6 method, were performed on all the generated dihydrate structures. This made possible to investigate the H–Cl interaction within the structures, and analyze possible trends. Accordingly, these trends could explain why  $\text{CaCl}_2 \cdot n\text{H}_2\text{O}$  is more resistant to hydrolysis than  $\text{MgCl}_2 \cdot n\text{H}_2\text{O}$ . Furthermore, it could be used to study if doping could help  $\text{Mg}_{(1-x)}\text{Ca}_x\text{Cl}_2 \cdot n\text{H}_2\text{O}$  to become more resistant to hydrolysis. In this section we take a look at the trends in the H–Cl bond based on the chemical environment. In the previous paragraphs, it was already shown that chloride is stronger bonded to calcium than magnesium, and the polarity of the water molecule decreases with higher amounts of calcium. In this section we consider the H–Cl interaction within the different dihydrate crystals. To study this interaction, the local environment of the water molecule and chlorine atom which are involved in the selected H–Cl interaction was analyzed. More precisely, for a selected H–Cl bond, we investigated for the chlorine atom if it is (a) bonded to two Mg atoms, (b) bonded to one Mg and one Ca, (c) bonded to two Ca atoms. Simultaneously, for the corresponding water molecule we investigated if the oxygen atom was bonded to a magnesium or to calcium atom. This approach graphically depicted in Figure 2.5, and it provides insights on the effect of doping on the H–Cl interaction.

The difference in charge ( $\Delta q_{\text{H-Cl}}$ ) between the hydrogen and chlorine atoms (from the respective  $\text{H}_2\text{O}$  and  $\text{Ca/MgCl}_2$  molecules), versus their bond order is plotted in Figure 2.6a for all the different kind of environments an H–Cl bond can have. Relative to the

Table 2.4: Chemical bonding analysis [134].  $\text{Mg}_{(1-x)}\text{Ca}_x\text{Cl}_2 \cdot 2\text{H}_2\text{O}$  starting from  $\text{MgCl}_2 \cdot 2\text{H}_2\text{O}$ , and  $\text{Ca}_x\text{Mg}_{(1-x)}\text{Cl}_2 \cdot 2\text{H}_2\text{O}$  starting from  $\text{CaCl}_2 \cdot 2\text{H}_2\text{O}$ , with  $x$  as the percentage of Ca. The bond order (BO) is computed within the DDEC6 approach. The potential energy density ( $E_{\text{pot}}$ ), and the kinetic energy density ( $E_{\text{kin}}$ ), are calculated within the QTAIM method at the bond critical points between the atoms, and the ratio is indicative for the type of the bond (see Table 2.2).

bond	$x$ % Ca	$\text{MgCl}_2 \cdot 2\text{H}_2\text{O}$ crystal structure		$\text{CaCl}_2 \cdot 2\text{H}_2\text{O}$ crystal structure	
		BO	$\frac{ E_{\text{pot}} }{E_{\text{kin}}}$	BO	$\frac{ E_{\text{pot}} }{E_{\text{kin}}}$
Mg–Cl	0%	$0.20 \pm 0.019$	0.86	$0.18 \pm 0.005$	0.86
	25%	$0.19 \pm 0.016$	0.86	$0.18 \pm 0.010$	0.86
	50%	$0.20 \pm 0.014$	0.86	$0.18 \pm 0.012$	0.86
	75%	$0.20 \pm 0.009$	0.86	$0.18 \pm 0.011$	0.85
	100%	–	–	–	–
Ca–Cl	0%	–	–	–	–
	25%	$0.24 \pm 0.017$	0.97	$0.22 \pm 0.011$	0.96
	50%	$0.24 \pm 0.018$	0.97	$0.21 \pm 0.014$	0.95
	75%	$0.24 \pm 0.012$	0.96	$0.22 \pm 0.012$	0.95
	100%	$0.24 \pm 0.011$	0.96	$0.22 \pm 0.009$	0.95
Mg–O	0%	$0.29 \pm 0.000$	0.88	$0.28 \pm 0.000$	0.89
	25%	$0.28 \pm 0.003$	0.88	$0.28 \pm 0.003$	0.89
	50%	$0.28 \pm 0.005$	0.88	$0.28 \pm 0.004$	0.89
	75%	$0.27 \pm 0.004$	0.87	$0.28 \pm 0.003$	0.89
	100%	–	–	–	–
Ca–O	0%	–	–	–	–
	25%	$0.29 \pm 0.004$	0.99	$0.28 \pm 0.004$	0.98
	50%	$0.29 \pm 0.006$	0.99	$0.28 \pm 0.006$	0.99
	75%	$0.28 \pm 0.004$	0.98	$0.28 \pm 0.004$	0.98
	100%	$0.28 \pm 0.000$	0.97	$0.28 \pm 0.000$	0.98
O–H	0%	$0.74 \pm 0.000$	7.12	$0.74 \pm 0.002$	6.99
	25%	$0.75 \pm 0.005$	7.06	$0.75 \pm 0.005$	6.86
	50%	$0.75 \pm 0.006$	6.96	$0.75 \pm 0.006$	6.80
	75%	$0.76 \pm 0.005$	6.66	$0.76 \pm 0.006$	6.73
	100%	$0.76 \pm 0.001$	6.84	$0.76 \pm 0.002$	6.68
H–Cl	0%	$0.12 \pm 0.000$	1.15	$0.12 \pm 0.008$	1.14
	25%	$0.12 \pm 0.005$	1.13	$0.12 \pm 0.023$	1.15
	50%	$0.13 \pm 0.006$	1.14	$0.12 \pm 0.014$	1.14
	75%	$0.13 \pm 0.005$	1.12	$0.13 \pm 0.011$	1.14
	100%	$0.13 \pm 0.001$	1.12	$0.13 \pm 0.008$	1.14

Table 2.5: Average Sum of Bond Orders (SBO) for the doped structures

system	%Mg	%Ca	Mg	Ca	Cl	O	H
MgCl <sub>2</sub> ·2H <sub>2</sub> O + 0% Ca	100%	0%	1.39	–	1.15	2.13	0.92
MgCl <sub>2</sub> ·2H <sub>2</sub> O + 25% Ca	75%	25%	1.37	1.62	1.11	2.10	0.93
MgCl <sub>2</sub> ·2H <sub>2</sub> O + 50% Ca	50%	50%	1.39	1.61	1.12	2.08	0.93
MgCl <sub>2</sub> ·2H <sub>2</sub> O + 75% Ca	25%	75%	1.37	1.57	1.09	2.07	0.94
MgCl <sub>2</sub> ·2H <sub>2</sub> O + 100% Ca	0%	100%	–	1.59	1.06	2.04	0.94
CaCl <sub>2</sub> ·2H <sub>2</sub> O + 100% Mg	100%	0%	1.33	–	1.16	2.15	0.93
CaCl <sub>2</sub> ·2H <sub>2</sub> O + 75% Mg	75%	25%	1.33	1.51	1.15	2.13	0.94
CaCl <sub>2</sub> ·2H <sub>2</sub> O + 50% Mg	50%	50%	1.32	1.48	1.12	2.11	0.94
CaCl <sub>2</sub> ·2H <sub>2</sub> O + 25% Mg	25%	75%	1.32	1.50	1.10	2.09	0.95
CaCl <sub>2</sub> ·2H <sub>2</sub> O + 0% Mg	0%	100%	–	1.50	1.08	2.07	0.95

Table 2.6: Average Net Atomic Charges for atoms in the doped crystal structures [134]

system	% Mg	%Ca	Mg	Ca	Cl	O	H
MgCl <sub>2</sub> ·2H <sub>2</sub> O + 0% Ca	100%	0%	1.340	-	-0.604	-0.870	0.402
MgCl <sub>2</sub> ·2H <sub>2</sub> O + 25% Ca	75%	25%	1.343	1.295	-0.608	-0.857	0.400
MgCl <sub>2</sub> ·2H <sub>2</sub> O + 50% Ca	50%	50%	1.337	1.301	-0.602	-0.849	0.395
MgCl <sub>2</sub> ·2H <sub>2</sub> O + 75% Ca	25%	75%	1.342	1.314	-0.604	-0.839	0.391
MgCl <sub>2</sub> ·2H <sub>2</sub> O + 100% Ca	0%	100%	-	1.305	-0.603	-0.827	0.389
CaCl <sub>2</sub> ·2H <sub>2</sub> O + 100% Mg	100%	0%	1.361	-	-0.608	-0.868	0.394
CaCl <sub>2</sub> ·2H <sub>2</sub> O + 75% Mg	75%	25%	1.362	1.339	-0.605	-0.860	0.394
CaCl <sub>2</sub> ·2H <sub>2</sub> O + 50% Mg	50%	50%	1.362	1.347	-0.608	-0.850	0.391
CaCl <sub>2</sub> ·2H <sub>2</sub> O + 25% Mg	25%	75%	1.365	1.343	-0.605	-0.843	0.387
CaCl <sub>2</sub> ·2H <sub>2</sub> O + 0% Mg	0%	100%	-	1.344	-0.605	-0.836	0.385

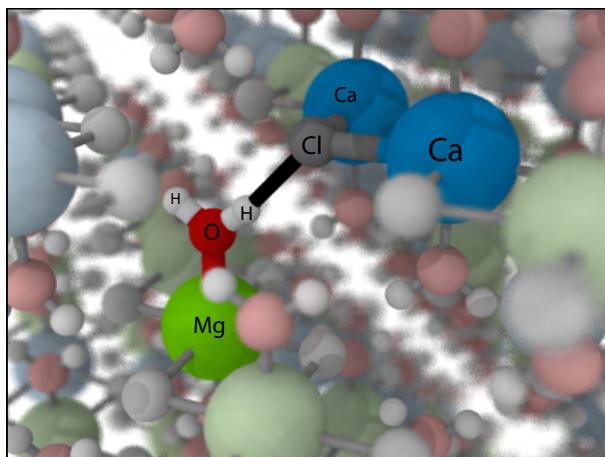


Figure 2.5: Visual representation of H–Cl interaction in Ca/Mg environment. The interaction is visualized as a black line [134]

highest charge difference in pristine  $\text{MgCl}_2 \cdot 2\text{H}_2\text{O}$ , the charge difference decreases on average with 0.7% when chlorine binds with one calcium atom, and with 1.6% if chlorine is bonded to two calcium atoms. Furthermore, the charge difference for these atoms will decrease further with an average of 0.7% if the oxygen atom bonds with calcium instead of magnesium. This results in a total drop 2.3% when moving from pristine  $\text{MgCl}_2 \cdot 2\text{H}_2\text{O}$  to pristine  $\text{CaCl}_2 \cdot 2\text{H}_2\text{O}$ .

Simultaneously, relative to the pristine  $\text{MgCl}_2 \cdot 2\text{H}_2\text{O}$  structure, the H–Cl bond order increases 2.8% if chlorine is bonded to two calcium atoms. Additionally, the H–Cl bond order will on average increase further with approximately 10% if the associated oxygen atom is bonded to calcium instead of magnesium. In the end, this results in a higher H–Cl bond order by 11.3% for pristine  $\text{CaCl}_2 \cdot 2\text{H}_2\text{O}$  compared to pristine  $\text{MgCl}_2 \cdot 2\text{H}_2\text{O}$ . We observed before that chlorine has also a higher bond order with calcium than magnesium, thus there is a positive correlation between the H–Cl bond order and the Cl–Mg/Ca bond order. Therefore, the chlorine atom will be harder to dissociate from a calcium atom than a magnesium atom, and the H–Cl bond is less likely to be formed in a calcium rich environment despite its higher bond order. In this sense we plotted in Figure 2.6b the H–Cl bond order divided by the Cl–Mg/Ca bond order. If we consider this ‘relative’ bond order  $\left( \text{BO}_{\text{rel}} = \frac{\text{BO}_{\text{H-Cl}}}{\text{BO}_{\text{Ca/Mg-Cl}}} \right)$ , we see that, because both the H–Cl and Ca/Mg–Cl bond order increase when going from a magnesium to calcium rich environment, the relative H–Cl bond order ( $\text{BO}_{\text{rel}}$ ) does not increase. It actually even decreases slightly from an average relative bond order of  $\text{BO}_{\text{rel,H-Cl-MgMg}} = 0.32$  to  $\text{BO}_{\text{rel,H-Cl-CaCa}} = 0.28$  when comparing a chlorine atom that is two times bonded to a magnesium atom with a chlorine atom that is two times bonded to a calcium atom. Additionally, the H–Cl charge difference decreases with a few percentages. The change is only a few percentages, however, we know from experiments that pure magnesium chloride salt hydrates suffer from HCl formation, while this does not happen for calcium chloride salt hydrates within the



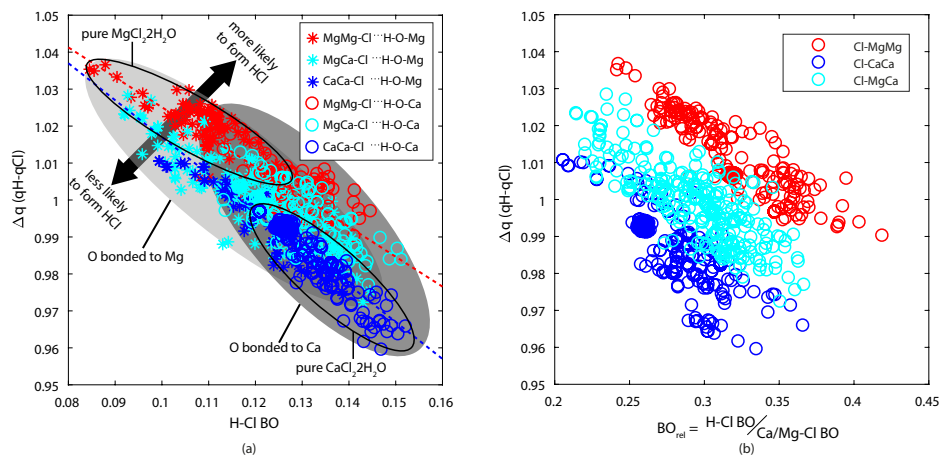


Figure 2.6: (a) Effect of calcium and magnesium environment on the interaction between the H and Cl atoms. The H-Cl bond order is given on the x-axis, and the charge difference between the H and Cl atom ( $\Delta q_{H-Cl}$ ) is given on the y-axis. The asterisks (\*) and circles (o) represent the different interactions of the oxygen atom with magnesium and calcium respectively. The gray shaded areas represent the differently bonded oxygen atoms. The different colors represent the different interactions of chlorine atom. The red dashed line is a fit through the data where chlorine is bonded to two magnesium atoms, while the blue dashed line is a fit through the data where chlorine is bonded to two calcium atoms. The black circles represent the pure structures. (b) Effect of calcium and magnesium environment on the interaction between the H and Cl atoms. The H-Cl relative bond order ( $BO_{rel}$ ) is given on the x-axis, and the charge difference between the H and Cl atom ( $\Delta q_{H-Cl}$ ) is given on the y-axis.

application temperature window. Thereby, a small decrease in charge difference could be enough for excluding the H-Cl formation in thermal storage applications.

## 2.3. CONCLUSIONS

In order to improve low-temperature TCMS, extensive ab-initio analysis was performed in order to investigate the impact of calcium doping on  $MgCl_2 \cdot nH_2O$  and that of magnesium doping on  $CaCl_2 \cdot nH_2O$ . Manual doped anhydrous and hydrated  $Mg_{(1-x)}Ca_xCl_2 \cdot nH_2O$  structures were created by interchanging Mg and Ca atoms in known  $MgCl_2 \cdot nH_2O$  and  $CaCl_2 \cdot nH_2O$  structures. Additionally, the evolutionary algorithm USPEX was used to explore new stable, anhydrous, combinations of  $MgCl_2$  and  $CaCl_2$ . The generated structures pointed out that the doped systems will be less stable than the pure salts. However, the energy difference between the metastable doped structures and the pure salts is small, thereby, decompositions of the doped crystals into the more stable pure crystals will likely not occur. The hexahydrate structures, were more affected by the doping than the lower hydrates. Nonetheless a distortion in the  $MgCl_2 \cdot 6H_2O$  crystals with calcium content above 25% resulted in a positive crystal stabilization.

The density was found to decrease, and volume to increase, with increasing the calcium content in the salts due to the larger calcium atom. Especially for low amounts of doping, when the crystal topology will not change, a significant volume increase occurs. Both the lower density and lower water sorption energy for calcium chloride sys-

tems lowers the practical achievable energy storage density of the material. On the other hand, previous studies [55, 135] showed that voids and defects, created by doping, could have an enhanced effect on the water dissociation, especially near the surface of the salt.

Chemical bonding analysis showed that a weaker interaction is present between Mg–Cl, compared to Ca–Cl. The combination of the weaker Mg–Cl interaction and the more polar H<sub>2</sub>O molecule in magnesium chloride salt hydrates, compared to calcium chloride hydrates, give rise to HCl formation. This is a highly undesired side reaction in magnesium chloride based salts for heat storage [33, 34]. Further analysis of the chemical environment of the H–Cl interaction showed that the presence of the calcium atoms has a reducing effect on the H–Cl formation. This provided the possibility to shift the HCl formation outside the operational window of the thermochemical energy storage by doping magnesium chloride systems with calcium.



# 3

## REAXFF DEVELOPMENT AND APPLICATION FOR CALCIUM CHLORIDE HYDRATES

**ABSTRACT:** *Inherent bulk crystal defects like cracks, pores, and grain boundaries promoted during the (de)hydration cycle of the TCM, affect its material properties. ReaxFF is used to investigate  $\text{CaCl}_2 \cdot n\text{H}_2\text{O}$  properties, as well as the effect of crystal defects on them. In this sense, a new ReaxFF force field is developed, which can describe stable  $\text{CaCl}_2 \cdot n\text{H}_2\text{O}$  structures, accurate descriptions of crystal surface energies, and multiple material indicators like charges, reaction enthalpies, and radial distribution functions. The new force field is further used to investigate the thermal conductivity, dehydration mechanisms/kinetics, and crack formation upon heating of the crystal. The thermal conductivity is found to be 1.1 and 0.5 W/mK for respectively  $\text{CaCl}_2$  and  $\text{CaCl}_2 \cdot 2\text{H}_2\text{O}$ , which is in good agreement with experimental results. Additionally, we investigated the influence of grain boundaries and the salts' anisotropic crystal morphology and found that both grain boundaries and the typical layered structure in z-direction lower the thermal conductivity. By investigating dehydration mechanisms, it is shown that initial dehydration is 1.9–2.5 times lower in the z-direction, also due to the typical layered morphology. For all directions, superficial dehydrated  $\text{CaCl}_2$  layers impede dehydration of core layers, but cracks and pores significantly promote it. These molecular-scale findings reveal nanoscale opportunities that could benefit the TCM.*

---

This chapter is published as peer reviewed article: Heijmans, K., Klein Holkenberg, B., Nab, S., Pathak, A.D., Gastra-Nedeia, S.V. and Smeulders, D.M.J., Development of a Reactive Force Field for  $\text{CaCl}_2 \cdot n\text{H}_2\text{O}$ , and the Application to Thermochemical Energy Storage. *Computational Material Science*, 197, 110595 (2021).

### 3.1. INTRODUCTION

In the transition from fossil to renewable energy sources, solar energy is an essential resource. Unfortunately, this source introduces problems related to the mismatch between its intermittent supply – due to seasonal, daily, and geographical variations – and the energy demand. Therefore, energy storages are needed to bridge this mismatch between supply and demand. Thermochemical storage materials (TCM) are currently investigated as an alternative to the already domestically and industrially used sensible (e.g., hot water) and latent (e.g., phase changing) heat storage systems [18, 169, 170]. TCM's main advantages of over sensible and latent heat storage are the high storage density and low heat loss. The  $\text{CaCl}_2 \cdot n\text{H}_2\text{O}$  salt hydrate ( $n = 0, 2, 4, 6$ ), is an often mentioned and tested TCM candidate [30, 47, 52, 59, 171, 172]. The main reason for these hydrates as seasonal heat storage materials is the theoretical energy density 1-3 GJ/m<sup>3</sup> (a conventional hot water tank with a temperature lift of 80 K has a theoretical energy density of 0.3 GJ/m<sup>3</sup>), price, widespread availability, and operating temperatures [11, 22, 169].

Unfortunately,  $\text{CaCl}_2 \cdot n\text{H}_2\text{O}$  also has its shortcomings as TCM. A point of concern is the higher hydrates' tendency to become liquid (deliquescence) if the vapor pressure is high enough [27, 173, 174]. Furthermore, for fast and complete dehydration, high temperatures are required. However, if one exceeds the salt hydrates' melting temperature, agglomerates are formed, leading to the clogging of the storage system. This is also mainly a concern to the higher hydrates of  $\text{CaCl}_2 \cdot n\text{H}_2\text{O}$  ( $n=4,6$ ), which have melting temperatures [20, 175, 176] in the range of domestic heat storage operational temperatures. This undesired deliquescence and melting problems, cap the material use, make it harder to operate, and limit TCM cyclability. Additionally, upon hydration and dehydration cycles of the TCM, significant stresses are introduced and form crystal imperfections like cracks [177], pores, and grain boundaries. These imperfections may both have positive and negative effects on some material properties. Not only the before mentioned problematic properties of  $\text{CaCl}_2 \cdot n\text{H}_2\text{O}$  are affected by them, but also TCM properties like thermal conductivity and  $\text{H}_2\text{O}$  diffusion; and indirectly on the functioning of key storage properties like (de)hydration rates [177], TCM cyclability, and power output. However, the exact individual effect of different crystal imperfection is hard to measure by experiments.

Numerous proposals were made and studied to overcome the shortcomings of salt hydrates. For example, promising proposals are made that focus on combinations of salt hydrates to avoid certain pure salts' shortcomings and simultaneously benefit from the advantages of other salts [31, 178]. These combinations can be made in the form of mixtures [31, 178] or doped and compound salts [60] (see chapter 2) in which the dopant introduces steric and electronic imperfections [55] that benefit specific TCM properties. Furthermore, proposals in terms of encapsulation [47, 179] and impregnation [10, 52, 180–183] of the salts into host materials are studied to improve the storage systems' cyclability and stability.

These concepts aim to improve the TCM based on advanced material combinations and provide possible solutions to make salt hydrates more viable for thermochemical energy storage. However, to further exploit these concepts, more fundamental knowledge is needed to better understand why and how these combinations can be superior. Molecular Dynamics (MD) is a useful tool to study dynamics and kinetics of materials at

a molecular level and thereby increase knowledge on heat and mass flows in materials [184]. In this sense, ReaxFF [81, 82] is used before to investigate material properties of  $\text{MgCl}_2 \cdot n\text{H}_2\text{O}$  as TCM [40, 100, 135]. Next to material properties calculation of perfect crystals, molecular dynamics is especially a useful tool to investigate the effect of material imperfections, such as the before mentioned cracks, pores, and grain boundaries [69, 135].

Therefore, we parameterized a ReaxFF force field for  $\text{CaCl}_2 \cdot n\text{H}_2\text{O}$  in order to perform an extensive exploratory study to characterize its TCM's properties, including crystal imperfections. As fundament, we used the  $\text{CaCl}_2 \cdot n\text{H}_2\text{O}$  reactive force field developed by Pathak et al. [185], which accurately replicates kinetics. However, this original force field showed unphysical disintegration of the higher hydrated crystals, and re-parametrization was needed. To encounter this disintegration problem, we present a ReaxFF training protocol that resulted in the new transferable and stable  $\text{CaCl}_2 \cdot n\text{H}_2\text{O}$  ( $n=0,2$ ) reactive force field. This protocol is based on an iterative use of predicted MD trajectories by intermediate force fields in the reference training set. The final newly developed force field is applied to study the dehydration, thermal conductivity, and heating effect on the crack formation. Since these salts are typically anisotropic structures, the thermal conductivity and dehydration are studied in x-, y-, and z-direction. Additionally, the effect of crystal grain boundaries on the thermal conductivity is calculated.

### 3.2. COMPUTATIONAL METHODS

The present study aims to investigate the dehydration dynamics of salt hydrates for TCM heat storage application. These dynamics include chemical reactions between the different elements in the salt hydrates. Quantum Mechanical (QM) computations can capture these chemical reactions with a high accuracy. Unfortunately, QM is computationally very expensive making it hard to obtain transport properties such as  $\text{H}_2\text{O}$  diffusion and (de)hydration. Molecular Dynamics (MD) based on a reactive force field (ReaxFF) [81, 82] can capture the chemical reactions as well and is less computationally expensive than QM. These ReaxFFs are typically developed with QM calculations, as explained in the next sections. Therefore, we used ReaxFF, which bridges the atomic length scale to molecular level and brings the computation of important TCM characteristics within the computationally accessible scope.

Initially, we started with a  $\text{CaCl}_2$  ReaxFF [185], which accurately predicted reaction enthalpies of different  $\text{CaCl}_2$  hydration reactions, shown in Figure 3.1. Unfortunately, this initial ReaxFF showed undesired disintegration of  $\text{CaCl}_2 \cdot n\text{H}_2\text{O}$  bulk systems, as shown in Figure 3.6. To overcome this disintegration, we improved the initial ReaxFF to a new ReaxFF that can correctly describe  $\text{CaCl}_2 \cdot n\text{H}_2\text{O}$  bulk systems, using a Metropolis Monte Carlo (MMC) optimization algorithm [83]. The MMC method uses accurate QM data to parameterize ReaxFF. Among the QM data, MD-frames were used, which improved the parametrization significantly. The optimization protocol used to obtain the improved ReaxFF for  $\text{CaCl}_2 \cdot n\text{H}_2\text{O}$  ( $n=0,2$ ) is visually shown in Figure 3.2. As the Figure shows, QM calculations are used as input for the Metropolis Monte Carlo optimizer, which trains the force field. Accordingly, the new force field is used in MD simulations to obtain atom trajectories of crystals. If the crystal disintegrates, the force field is retrained by the MMC, and snapshot of the wrong MD trajectories accurately recomputed on QM

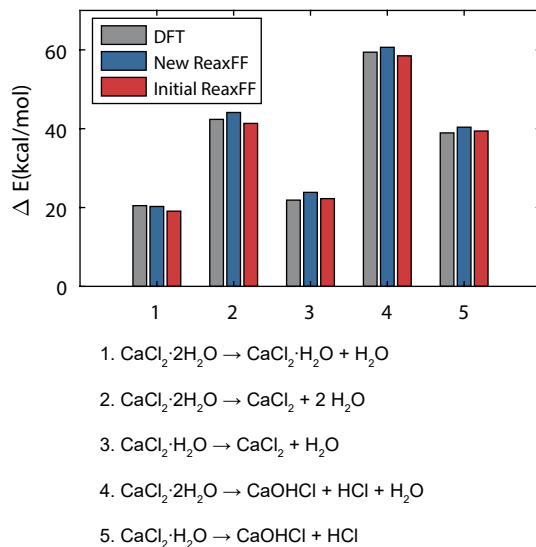


Figure 3.1: Comparison of the reaction enthalpies of several reactions of  $\text{CaCl}_2$  hydrates, predicted by DFT, the initial ReaxFF, and the new ReaxFF.

level and added as new data point to the training set. When the new force field is stable, it is further used to compute material properties. These different steps in developing the new force field are extensively explained in the corresponding sections.

### 3.2.1. QUANTUM MECHANICAL (QM) COMPUTATIONS

Density Functional Theory (DFT) is used as the QM method to compute  $\text{CaCl}_2 \cdot n\text{H}_2\text{O}$  periodic and non-periodic structures accurately. Non-periodic structures (gas systems) containing data for varying bonds and angles within different molecules are computed with Perdew-Wang (GGA-PW92) exchange-correlation function [186]. This is implemented in the ADF software [187, 188] and has been successfully used before to model  $\text{CaCl}_2$  hydrates [59, 189]. The periodic crystal structures for the training set are computed with the Vienna Ab initio Simulation Package (VASP) [146], using the PBE [147] exchange-correlation functions together with the PAW [148, 149] scheme. DFT-D3 [150], including Becke-Johnson [151] damping, was used to describe long-range dispersion interactions. The structures were considered as converged if all forces on the atoms are smaller than  $0.026 \text{ eV}/\text{\AA}$ .

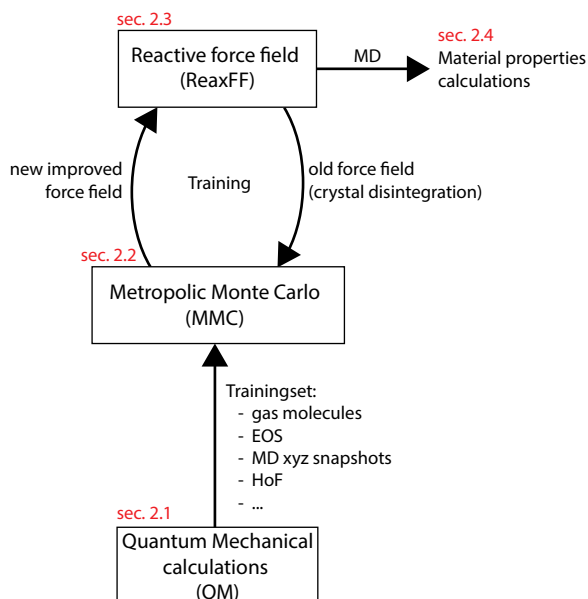


Figure 3.2: Visual representation of the used methodologies to come up with a reliable and transferable ReaxFF.

### 3.2.2. REACTIVE FORCE FIELD (REAXFF)

A reactive force field [81, 82] (ReaxFF) uses the following empirical potential, which summarizes different energy terms

$$E_{\text{system}} = E_{\text{bond}} + E_{\text{angle}} + E_{\text{torsion}} + E_{\text{H-bond}} + E_{\text{lp}} + E_{\text{over}} + E_{\text{under}} + E_{\text{conj}} + E_{\text{vdW}} + E_{\text{Coul}} + E_{\text{others}}. \quad (3.1)$$

Together these energy terms describe the total energy of a system.  $E_{\text{bond}}$  is the energy term that includes the energy related to the bond order ( $\sigma$ ,  $\pi$ , and  $\pi\pi$ ) given by a continuous function that depends on the distance between the atoms. This term enables ReaxFF to capture chemical reactions in MD simulations.  $E_{\text{angle}}$  and  $E_{\text{torsion}}$  are, respectively, the three-body valence angle term and the four-body torsion term.  $E_{\text{H-bond}}$  includes the H-bond term.  $E_{\text{lp}}$  entails energy contributions from the lone pairs.  $E_{\text{over}}$  and  $E_{\text{under}}$  are two energy penalties coming from over- and under coordination.  $E_{\text{vdW}}$  and  $E_{\text{Coul}}$  are, respectively, the non-bonded van der Waals and Coulomb interactions between the atoms, and  $E_{\text{others}}$  can be any extra terms assigned for some specific systems.

### 3.2.3. METROPOLIS MONTE CARLO (MMC) PARAMETERIZATION

The functions of the energy terms in ReaxFF (explained in section 3.2.2) include parameters that define the potential energy surface. These parameters can be obtained from fitting to the QM data set. This fitting could ultimately result in a ReaxFF, which replicates the potential energy surface of the same system described by the computationally

more expensive QM method. A ReaxFF force field contains many correlated parameters, which makes the fitting difficult. Thereby, the fitting is done by a Metropolis Monte Carlo (MMC) optimizer[83], which tries to minimize the cumulative squared error (Error) of the energy difference between ReaxFF and QM:

$$\text{Error} = \sum_{i=1}^n \left[ \frac{X_{i,\text{QM}} - X_{i,\text{ReaxFF}}}{\sigma_i} \right]^2. \quad (3.2)$$

With  $X_{i,\text{QM}}$  as quantum mechanical reference data from DFT and  $X_{i,\text{ReaxFF}}$  as corresponding values computed with ReaxFF. Each data point  $i$  is weighted with  $\sigma_i$ . The MMC algorithm aims to obtain the cumulative error's global minimum by modifying every iteration multiple selected parameters of the ReaxFF force field in a random direction. After a modification, the new error (Error<sub>new</sub>) is calculated with the new modified ReaxFF parameters, and the random changes are accepted according to simulated annealing with the following probability:

$$P = \min \left[ 1, \exp \left( - \left( \frac{\text{Error}_{\text{new}} - \text{Error}_{\text{old}}}{k_B T} \right) \right) \right] \quad (3.3)$$

With Error<sub>old</sub> as the previous cumulative error,  $k_B$  as the Boltzmann constant, and  $T$  is an artificial temperature that slowly decreases over the number of cycles.

The QM data ( $X_{i,\text{QM}}$ ) training set includes information on charges, heat of formation, bond stretching and bond bending of gas molecules, bond bending in bulk structures, equation of state, reaction enthalpies of (de)hydration and hydrolysis, proton shifts, and MD frames from intermediate "less accurate" ReaxFF force fields. In the latter case, adding the MD frames to the data set required the extra iterative loop over the training. Because it significantly increased the results, we explain it extensively below.

### MD FRAMES AS QM DATA FOR REAXFF PARAMETRIZATION

To improve the ReaxFF for accurate bulk systems description, we extended the training set with MD frames. Furthermore, an extra iterative loop was introduced, in which these MD frames were compared with DFT. This extra iterative loop in the parameterization process is schematically given in Figure 3.3 and includes the steps below.

1. With a currently trained force field, a ReaxFF MD simulation is performed on the unit cell.
2. During this simulation, several uncorrelated MD frames are extracted.
3. Single point energy DFT calculations are performed on these MD frames.
4. The single point energy DFT calculations are added to the training set as a reference structure.
5. Metropolis Monte Carlo (MMC) force field parameterization is continued with the extended training set.

6. A new (intermediate) ReaxFF is created.
7. The (intermediate) ReaxFF is tested; if it is able to describe the bulk structures and keeps them stable, the training is stopped. Otherwise, the ReaxFF test is used to get new MD frames, which will be included in the next training set for the parameterization.

This loop was repeated until a ReaxFF force field was obtained which proved to be sufficiently stable and accurate. Accordingly, the final parameterized ReaxFF was used to compute  $\text{CaCl}_2 \cdot n\text{H}_2\text{O}$  ( $n=0,2$ ) material properties.

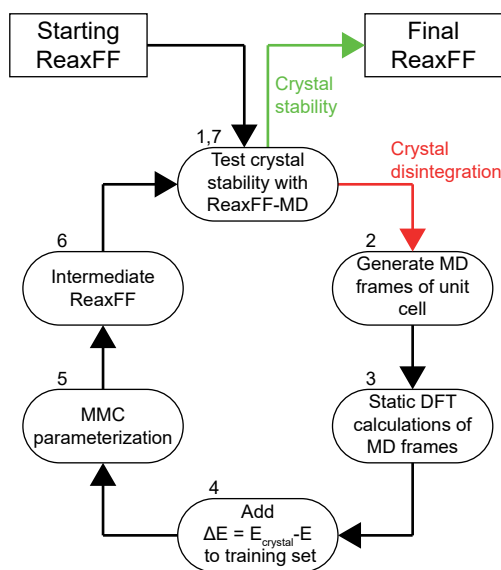


Figure 3.3: A representation of adding MD frames (extended detail of sec. 2.2 and sec. 2.3 in figure 3.2) to the training set, in order to improve the crystal stability.

### 3.2.4. MATERIAL PROPERTIES CALCULATION

The flow of heat and mass (dehydration product) through the reactive salt hydrate is critical for the design of gas-solid based thermochemical storage systems [137]. Salt hydrate TCMs typically come with low thermal conductivity, and low kinetics, which impose severe constraints on the storage systems. In this sense, we used the newly developed ReaxFF force field to study the dehydration mechanism of  $\text{CaCl}_2 \cdot 2\text{H}_2\text{O}$ , and compute its thermal conductivity. In general, salt hydrate crystals have a strong anisotropic morphology, as shown in Figure 3.4. Thus the thermal conductivity and the dehydration mechanism are studied for x-, y-, and z-direction. Next to anisotropy, bulk TCMs include cracks and grain boundaries, which change bulk material characteristics [177, 190] compared to single crystalline 'ideal' bulk material. Therefore, we also studied imper-

fect crystals regarding thermal conductivity and crystal deformation upon heating of  $\text{CaCl}_2 \cdot 2\text{H}_2\text{O}$ .

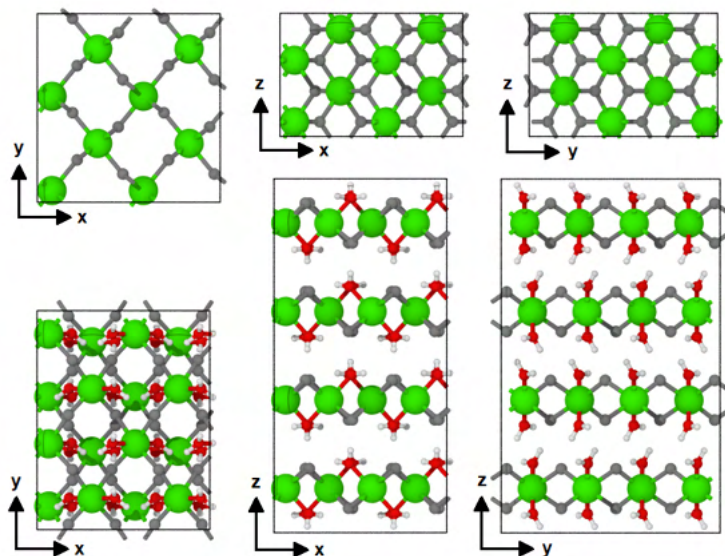


Figure 3.4: Crystal structures of  $\text{CaCl}_2$  [191] and  $\text{CaCl}_2 \cdot 2\text{H}_2\text{O}$  [141].

### DEHYDRATION

(De)hydration mechanisms are an important characteristic of salt hydrates that are used as TCM and influence the power output, local over-hydrated spots, and storage charging times. Fundamental insight of the dehydration process could be useful to optimize the TCM based energy storage at system level. In this sense, we studied the dehydration mechanisms and rates for  $\text{CaCl}_2 \cdot 2\text{H}_2\text{O}$ . We have created multiple  $\text{CaCl}_2 \cdot 2\text{H}_2\text{O}$  slabs with vacuums in x-, y-, or z-direction. These vacuums allowed  $\text{H}_2\text{O}$  molecules produced from dehydration to diffuse to the surface and evaporate from slab. This was done at temperatures ranging from 300 to 500 K. The first step to create the slabs was the construction and equilibration of a supercell. Equilibration was done for  $3 \times 10^5$  iterations, with a timestep of 0.25 fs, in an NPT simulation at 1 bar. After equilibration, the periodic crystals we placed in a box with a 1000 Å length in one direction to create the vacuum dehydration driving force in that direction. The periodic structures were placed in the vacuum in such a way that no covalent Ca–Cl and H–O bonds were cut, and dangling atoms are shifted by one box length to satisfy the under-coordinated atoms. This resulted in slabs with a  $6 \times 6$  lattice size parallel to the vacuum, and a  $3 \times$  lattice in the direction of the vacuum. Accordingly, the slab was simulated at the given temperature. Every water molecule that dehydrates into the vacuum increases the vapor pressure with roughly 45 mbar at ideal gas assumption. A practical thermochemical heat storage system operates with vapor pressures of 2–20 mbar [190]. To conserve the vacuum's dehydration driving



force and align with experimental dynamics, all evaporated  $\text{H}_2\text{O}$  molecules (at a distance larger than 30 Å from the slab surface) were removed every 0.125 ps.

### THERMAL CONDUCTIVITY

It is useful to get insight into salt hydrates' thermal conductivity when used as TCM. These materials have, in general, low thermal conductivity. The thermal conductivity determines heat fluxes through the system, and dissipation of heat fluxes could prevent local hot-spots, where undesired melting of the crystal or crystal deformation can happen. Furthermore, low thermal conductivity requires a fine grid of the heat exchanger in fixed-bed systems [19, 137, 183].

The thermal conductivity of different systems was computed using the steady-state Non-Equilibrium MD (NEMD) method. This method has proved its applicability before in similar systems [69, 100]. Different regions within a crystal slab are coupled to different temperatures through a Berendsen thermostat. Two regions are strongly coupled (damping constant  $\tau = 100$  fs) to a temperature of 330 K and 300 K, respectively, acting as a heat source and sink. In between these two strongly coupled regions, the crystal is weakly coupled to a thermostat (damping constant  $\tau = 100$  ps), which results in negligible heat in/outflows. When using the NEMD method to compute the thermal conductivity of a material, finite size effects could occur because the heat source and sink impede the mean free path of the energy carrier [69, 192, 193]. To exclude this effect, we computed the thermal conductivity for one systems at different sizes. Furthermore, the distance between heat source and sink was kept at similar distance for a systematic comparison between the different directions. As a result, a heat flux is generated from the heat source at 330 K towards the heat sink at 300 K, through the weakly-coupled region, and a temperature gradient appears over the crystal. By linear fitting to the heat fluxes and the temperature gradient, the thermal conductivity can be computed using Fick's law for heat energy fluxes,

$$Q = -k \frac{dT}{dx}, \quad (3.4)$$

With  $Q$  as the heat flux obtained from the heat source and sink,  $\frac{dT}{dx}$  from the fit over the temperature gradient, and  $k$  as the unknown thermal conductivity. Since the salt crystals are anisotropic, and to get a complete view of the thermal properties, the thermal conductivity is computed for different directions with periodic and non-periodic systems. In Figure 3.5 the two different typical systems are visualized. In practice, salt hydrate bulk material is never a completely perfect crystal. Therefore, the effect off an grain boundary on the thermal conductivity is included in the thermal conductivity calculations.

### EXPANSION AND CRACK FORMATION

Upon heating hydrated salt crystals, to regenerate the thermochemical storage system, local dissociated  $\text{H}_2\text{O}$  molecules and thermal expansion induce large stresses and pressures within the crystal, and induce large forces on mechanical appliances within the storage systems. Furthermore, after evaporation, cracks are introduced in the anhydrous crystal [190], these cause cracks and deformations could enhance future (de)hydration [177]. Therefore, we studied a heating  $\text{CaCl}_2 \cdot 2\text{H}_2\text{O}$  crystal at a rate of 2 mK per iteration starting from 300 K and using a Berendsen thermostat.

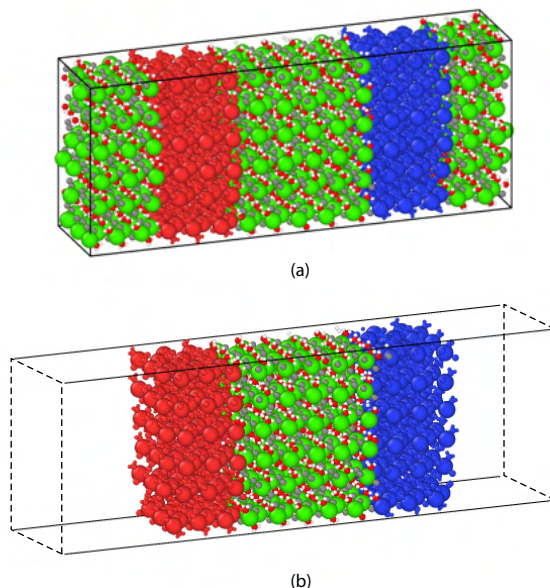


Figure 3.5: (a) Simulation cell of  $\text{CaCl}_2 \cdot 2\text{H}_2\text{O}$  crystal using periodic boundaries. (b) Simulation cell of  $\text{CaCl}_2 \cdot 2\text{H}_2\text{O}$  crystal using free boundaries. Heat source and sink are respectively indicated with red and blue.

### 3.3. RESULTS AND DISCUSSION

#### 3.3.1. REAXFF RE-PARAMETERIZATION RESULTS

Re-parameterization of the initial old ReaxFF was needed to avoid undesired disintegration of bulk systems. This undesired disintegration of  $\text{CaCl}_2 \cdot 2\text{H}_2\text{O}$  systems described by the initial ReaxFF can be observed from Figure 3.7, 3.6 and 3.8. Figure 3.6 shows the structures after a short (0.25 ns) MD-NPT simulation at 300 K and 1 bar. At these conditions the system should remain crystalline, which is clearly the case for the new force field but not for the initial one. As reference the experimentally found structure of  $\text{CaCl}_2 \cdot 2\text{H}_2\text{O}$  [141] is also given. Figure 3.7 shows the Radial Distribution Function (RDF) between Ca-Ca, Ca-Cl, and Ca-O of the initial ReaxFF (red), and the newly developed ReaxFF (blue) both at 300 K, compared with the experimental "ideal" crystals' RDF (gray). The first peak for the Ca-Cl and Ca-O of the original ReaxFF matches well with the experimental structure. However, the tail also shows evident disintegration. When comparing the Ca-Ca RDF it is clear that the initial ReaxFF force field does not describe a crystalline  $\text{CaCl}_2 \cdot 2\text{H}_2\text{O}$  structure, which should be the case since it does not dehydrate at 300 K. The newly developed ReaxFF does describes a crystalline structures and matches well with the experimental RDF. Re-parameterization of the initial ReaxFF was done, using MD-frames as input data. The energy difference between static calculated MD frames, and the geometry optimized crystal, are shown in Figure 3.8. Since the reference is the geometry optimized DFT structure, all MD trajectory frames should have an energy difference above zero. nonetheless, most of the anhydrous and all the di-

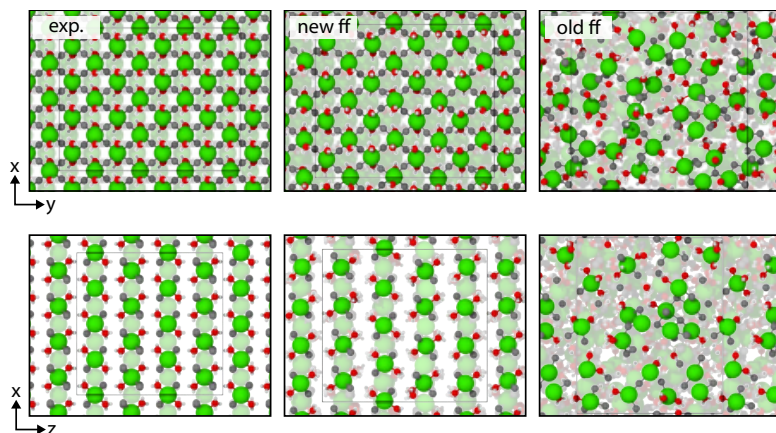


Figure 3.6: Comparison of the experimental  $\text{CaCl}_2 \cdot n\text{H}_2\text{O}$  structure with the new and initial ReaxFF MD structure after 0.25 ns at 300 K and 1 bar. For clarity only the front atoms are shown in full color.

hydrate MD trajectory frames computed with the initial ReaxFF force field show energy differences below zero. These frames are thus incorrectly seen as more stable where they should be less stable, as shown by the DFT calculation. In the anhydrous case, the initial force field's energy difference is approximately around zero, where the energy difference for the dihydrate is even below zero. This confirms the observed behavior of disintegration of the  $\text{CaCl}_2 \cdot 2\text{H}_2\text{O}$  system but not for the  $\text{CaCl}_2$  system when the initial force field is used; in the latter case, the energy differences are apparently not sufficient to disintegrate the crystal. The newly parameterized force field does show a good match with the DFT reference, and one can conclude that adding the MD frames to the training set considerably improved the force field.

Next to the MD frames, multiple other reference data points are included to the training set, namely, charges, reaction enthalpies (figure 3.1), dissociation curves, angle in gas molecules, angles in bulk structures, equation of state, and surfaces. A small selection of this data set, including the result of the newly developed force field, is shown in Figure 3.9. For the complete data set we refer you to the Supplementary Material of the original published paper [131]. From the training results, a small crystal expansion is expected for periodic systems from the newly developed force field. An MD-NPT simulations confirms this expansion for both the original and new force field. The density decreases with 17% and 16% in the case of  $\text{CaCl}_2$ , and 12% and 3% in the case of  $\text{CaCl}_2 \cdot 2\text{H}_2\text{O}$ , for respectively the original and new ReaxFF force field. Furthermore, the surface energies are calculated with the new ReaxFF in [100], [010], and [001] direction for both  $\text{CaCl}_2$  and  $\text{CaCl}_2 \cdot 2\text{H}_2\text{O}$ , via:

$$E_{\text{surface}} = \frac{E_{\text{system}} - nE_{\text{bulk}}}{2A} \quad (3.5)$$

With  $E_{\text{surface}}$  as the surface energy,  $E_{\text{system}}$  as the energy of a relaxed slab with a surface in a given direction,  $E_{\text{bulk}}$  as the energy of a relaxed periodic unit cell,  $n$  as the number of unit cells in the slab, and  $A$  as the surface area of the slab. The resulting values are

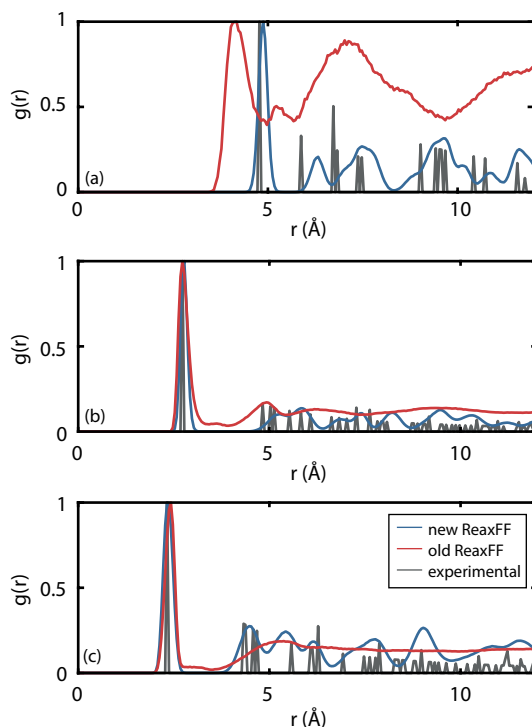


Figure 3.7: Comparison of RDFs for  $\text{CaCl}_2 \cdot 2\text{H}_2\text{O}$  for the experimental structure and after MD at atmospheric pressure and 300 K. (a) is Ca-Ca, (b) is Ca-Cl, and (c) is Ca-O. All first peaks, are normalized to one for a clear comparison.

given in Table 3.1, and compared with DFT. In Appendix C, the resulting relaxed surface slabs are shown, and Tables C.1 and C.2 confirm minimal changes regarding the Ca–Ca distance between surface atoms and bulk atoms. As shown in Figure 3.9, the surface energies of anhydrous  $\text{CaCl}_2$ , were included in the MMC training data, as a result, the new ReaxFF values match closely with DFT. Additionally, we computed the surface energies of  $\text{CaCl}_2 \cdot 2\text{H}_2\text{O}$ , these were not included in the MMC training data. However, these dihydrate surfaces also closely match with the DFT reference, which confirms the transferability and robustness of the new ReaxFF.

### 3.3.2. MATERIAL CHARACTERIZATION

After the ReaxFF force field was successfully trained to describe  $\text{CaCl}_2 \cdot n\text{H}_2\text{O}$  systems, it was used to study important TCM characteristics, such as dehydration mechanisms, thermal conductivity, and crack formation upon heating. Similar to other salt hydrate crystal morphologies,  $\text{CaCl}_2 \cdot n\text{H}_2\text{O}$  has a strongly anisotropic structure. In the case of  $\text{CaCl}_2 \cdot 2\text{H}_2\text{O}$ , the crystal has an orthorhombic structure, typically  $\text{CaCl}_2$  layered in the  $z$ -direction with the Ca atoms ordered in a checkerboard pattern in the  $xy$ -plane, as shown in Figure 3.4. The O–Ca–O connection is orthogonal to the  $y$ -direction, and makes a  $47^\circ$

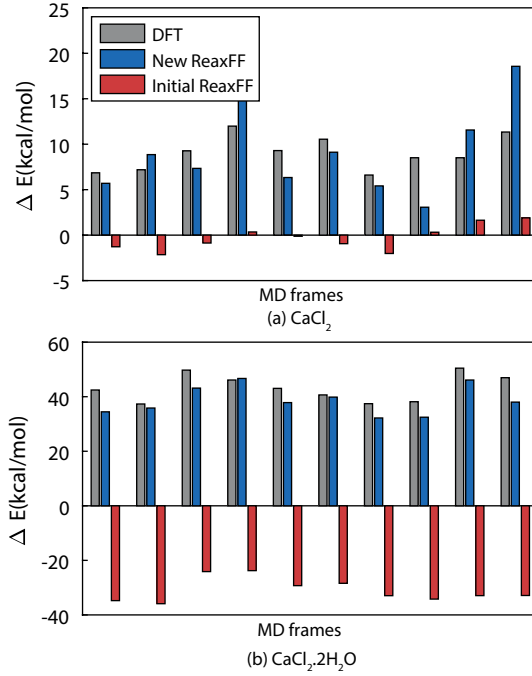


Figure 3.8: Energy differences between MD frames and the experimental unit cell, calculated with DFT (blue), static initial ReaxFF (gray), and static new ReaxFF (red). For bulk systems of (a)  $\text{CaCl}_2$ , and (b)  $\text{CaCl}_2 \cdot 2\text{H}_2\text{O}$ . The MD frames were generated with the initial  $\text{CaCl}_2 \cdot n\text{H}_2\text{O}$  ReaxFF.

angle with the x-direction. Because of the anisotropic character, we considered the material property computations in all three different directions.

### DEHYDRATION

Dehydration rates and mechanisms are important characteristic for TCMs. In this sense, we studied dehydration mechanisms of  $\text{CaCl}_2 \cdot 2\text{H}_2\text{O}$ . This was done separately for x-, y-, and z-direction, at temperatures ranging from 300 K to 500 K. Results of this simulations are shown in Figure C.1 of Appendix C. At 300 K no dehydration is observed, at 400 K some dehydration is observed which increases even more at 500 K. This can be confirmed with experimental results where dehydration of  $\text{CaCl}_2 \cdot 2\text{H}_2\text{O}$  starts at 344 K and

Table 3.1: Surface energy ( $\text{J}/\text{m}^2$ ) by DFT and the new ReaxFF

Surface	$\text{CaCl}_2$		$\text{CaCl}_2 \cdot 2\text{H}_2\text{O}$	
	DFT	ReaxFF	DFT	ReaxFF
001	0.52	0.58	0.19	0.08
010	0.39	0.38	0.38	0.33
100	0.41	0.40	0.38	0.23

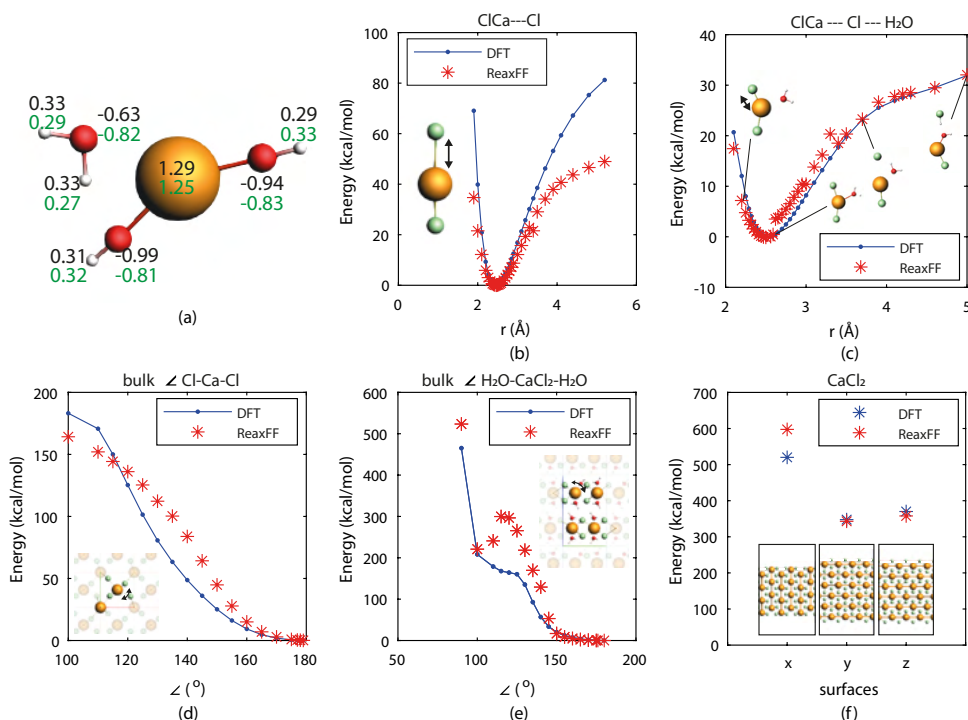


Figure 3.9: Subset of Metropolis Monte Carlo training data set. With (a) charges, black is DFT and green is ReaxFF; (b) dissociation energy of  $\text{ClCa-Cl}$ , (c) dissociation energy of  $\text{ClCa-Cl}$  with water molecule around it, (d)  $\text{Cl-Ca-Cl}$  angle distortion in  $\text{CaCl}_2$  crystal, (e)  $\text{H}_2\text{O-CaCl}_2\text{-H}_2\text{O}$  angle distortion in  $\text{CaCl}_2 \cdot 2\text{H}_2\text{O}$  crystal, (f) [100], [010], and [001] surfaces of  $\text{CaCl}_2$  crystal.

higher [11, 190]. These simulations were done with crystal slabs in a 1000 Å vacuum. However, every evaporated water molecule significantly increases the vapor pressure in the vacuum. Therefore, for each direction at 500 K, longer simulations were applied in which evaporated water molecules were removed. A comparison between these two methods, with and without removal, is shown in Figure C.1 of Appendix C. When water molecules are not removed, an equilibrium will be reached before the crystal is completely dehydrates, when water molecules are removed the vacuum driving force for the dehydration is maintained.

Figure 3.10, gives the dehydration for different orientations at 500 K with removal of evaporated water molecules. For the x-, and y-direction a similar behavior is observed, yet with initially a slightly different rate. At the start, fast dehydration is observed, which can be mainly attributed to the surface water molecules that are hardly impeded by other atoms ( $R_{x,1}$  in Figure 3.10). After some time, the outer layers are dehydrated temporarily slowing down dehydration ( $R_{x,2}$  in Figure 3.10). When the outer layers lose their crystallinity and some pores are formed, an increase of dehydration is observed again ( $R_{x,3}$  in Figure 3.10). Yet after approximately 5 ns, when more water molecules are dehydrated, a thicker amorphous and largely anhydrous  $\text{CaCl}_2$  layer is formed at the outer

layers of the slabs. This thicker layers blocks further fast dehydration, and a slow and constant rate behavior is observed for the remainder of water molecules. To indicate the linear behavior after 7.5 ns, a linear fit is shown from 7.5–15 ns ( $R_{x,4}$  in Figure 3.10). For the z-direction, the behavior is slightly different, till 3 ns a non-linear dehydration is observed, in this regime the water molecules in the outer layer are dehydrated, either direct or indirect via some pores. However, after this point the layered characteristics of the crystal in z-direction blocks further rapid dehydration, and a very slow linear rate is observed, which is impeded by the  $\text{CaCl}_2$  layered structure. After 12 ns, in the amount of dehydrated water molecules in z-direction is 1.9 and 2.5 times lower than x- and y-direction respectively. To characterize the dehydration mechanisms further, structures

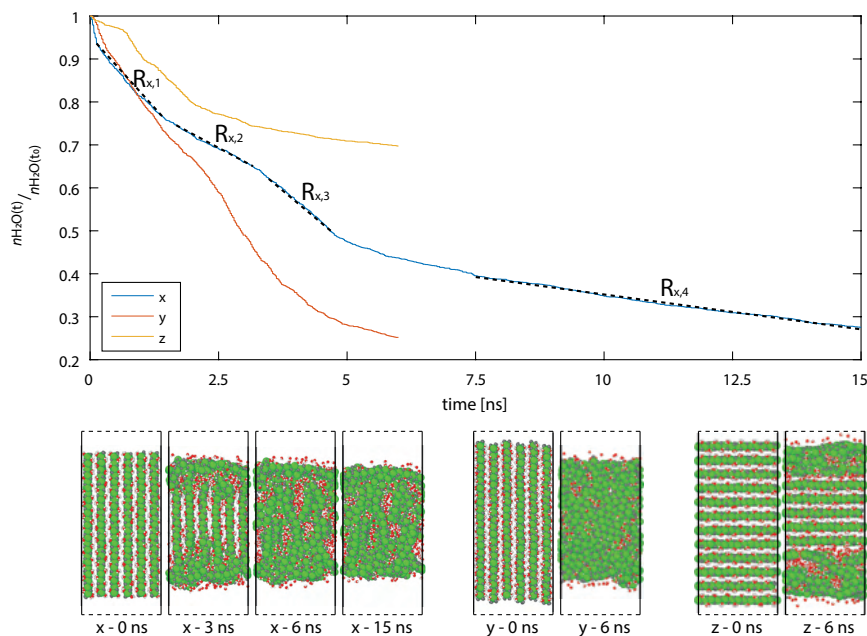
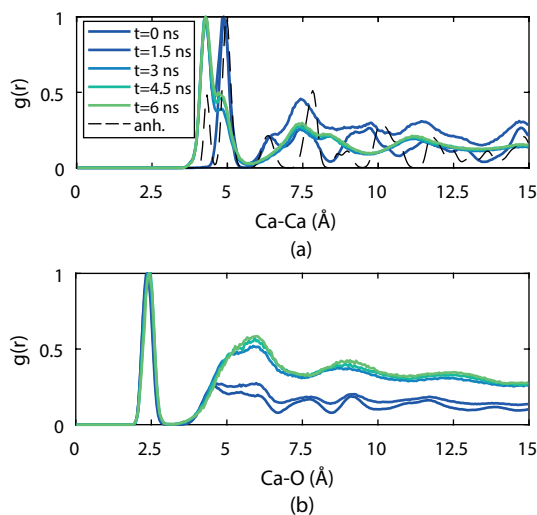


Figure 3.10: Dehydration of  $\text{CaCl}_2 \cdot 2\text{H}_2\text{O}$  at 500 K for x, y, and z orientation of the slab. In x-direction the simulation is extended to reach steady state, and to compute the dehydration rate at steady state.

were taken from the dehydration simulations at different times ( $t = 0, 1.5, 3$ , and  $6$  ns). These structures were put in a vapor saturated environment, in order to stop further dehydration, and characterize the systems at a steady state equilibrium. These restarted simulations were performed over 250 ps, after which RDFs and the spatial density distribution of atoms were computed. Due to the dehydration, anhydrous  $\text{CaCl}_2$  is formed at the outer layers impeding further dehydration. This is confirmed by the RDFs at different timesteps given in Figure 3.11 for the system with vacuum in y-direction. In Figure 3.12a-f, the spatial density distribution is given for oxygen and calcium atoms for all three directions. For both x-, and y-direction a clear decrease of oxygen atoms, thus water, over time is present in Figure 3.12a-b. Furthermore, at the surfaces in the final con-



Figure 3.11: RDF of  $\text{CaCl}_2 \cdot 2\text{H}_2\text{O}$  structures at different times of dehydration.Table 3.2: Computed thermal conductivity ( $\text{Wm}^{-1}\text{K}^{-1}$ ) of perfect  $\text{CaCl}_2$  and  $\text{CaCl}_2 \cdot 2\text{H}_2\text{O}$  crystals.

Direction	$\text{CaCl}_2$		$\text{CaCl}_2 \cdot 2\text{H}_2\text{O}$	
	Periodic	Free	Periodic	Free
x	$1.14 \pm 0.09$	$1.24 \pm 0.22$	$0.47 \pm 0.03$	$0.49 \pm 0.12$
y	$1.11 \pm 0.17$	$1.36 \pm 0.19$	$0.75 \pm 0.03$	$0.85 \pm 0.17$
z	$0.89 \pm 0.02$	$1.09 \pm 0.09$	$0.10 \pm 0.02$	$0.36 \pm 0.04$

figuration a dip is present, with a lower number of water molecules than in bulk. This dip is present due to the presence of the anhydrous  $\text{CaCl}_2$  layer, which is simultaneously presented in Figure 3.12d-e. For the dehydrated system with vacuum in z-direction, the behavior is slightly different. The number of oxygen atoms does hardly decline over time in bulk because of the layered structure in z-direction. Therefore, also a slow but sharp dehydration front can be observed, where layer by layer water is evaporated.

### THERMAL CONDUCTIVITY

For both hydrates ( $n = 0, 2$ ) the thermal conductivity is computed in all directions, with both periodic and free boundaries, as shown in Figure 3.5. A typical result for a periodic system is given in Figure 3.13, in which the in- and outgoing heat flux and the temperature profile are given. The free boundaries were included to make it possible to study grain boundary effects on the thermal conductivity. Each system was simulated 3 times over 0.4 ns, to obtain standard deviations, and results are given in Table 3.2.

To exclude finite size effects [69, 192, 193] the thermal conductivity for was recomputed for a larger distance between the heat source and sink ( $\sim 33 \text{ \AA} \rightarrow 92 \text{ \AA}$ ) for the periodic  $\text{CaCl}_2 \cdot 2\text{H}_2\text{O}$  crystal in y-direction. The computed thermal conductivity for



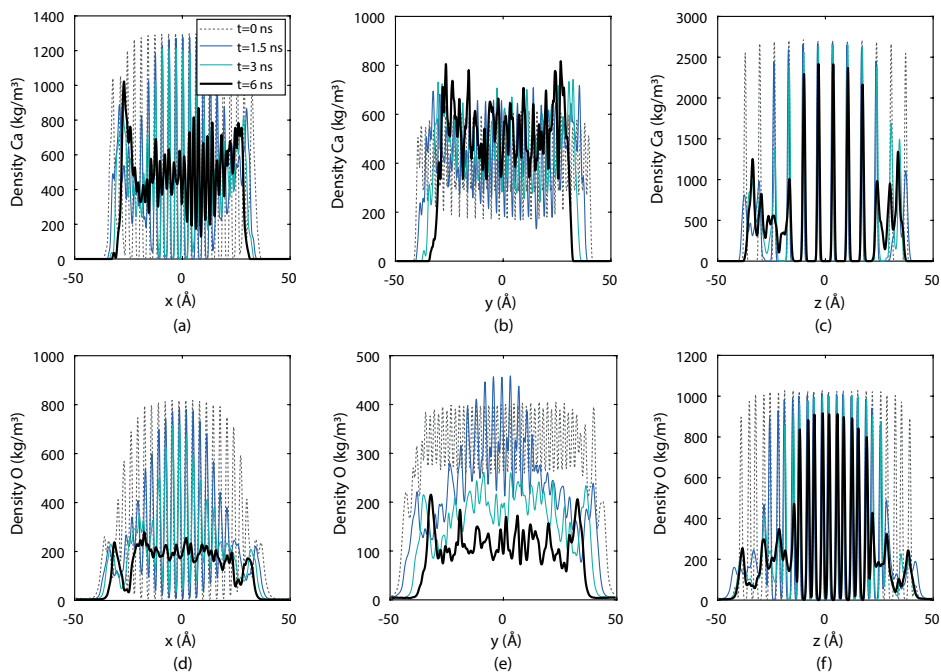


Figure 3.12: Density profiles of dehydrated slabs at different timesteps. (a) Density of Ca atoms with a vacuum in x-direction, (b) Density of Ca atoms with a vacuum in y-direction, (c) Density of Ca atoms with a vacuum in z-direction, (d) Density of O atoms with a vacuum in x-direction, (e) Density of O atoms with a vacuum in y-direction, (f) Density of O atoms with a vacuum in z-direction.

the larger system was found to be  $0.69 \text{ W m}^{-1} \text{ K}^{-1}$ , which similar to the shorter system, thus finite size effects can be neglected. This was also found by a similar calculation for  $\text{MgCl}_2 \cdot n\text{H}_2\text{O}$  crystals [100] at these NEMD crystal sizes. Furthermore, to obtain a consistent comparison between all different structures in different directions, we kept the distance between heat source and sink similar. For all systems, the computed thermal conductivity is higher when free boundaries are used compared to periodic boundaries. In similar NEMD calculations [194], comparable results were found, where the slightly lower thermal conductivity for periodic systems can be attributed to the higher scattering effect of the heat source and sink in periodic systems compared to systems with free boundaries. The average thermal conductivity for the anhydrous crystal is approximately  $1.1 \text{ W/mK}$ , with a slightly higher value for x-, and y-direction than the z-direction. The average computed thermal conductivity for the dihydrate  $\text{CaCl}_2 \cdot 2\text{H}_2\text{O}$  crystal is on average approximately  $0.6 \text{ W/mK}$ , the highest in y-direction ( $\approx 0.8 \text{ W m}^{-1} \text{ K}^{-1}$ ), slightly lower in x-direction ( $\approx 0.5 \text{ W m}^{-1} \text{ K}^{-1}$ ), and considerably lower in z-direction ( $\approx 0.1 \text{ W m}^{-1} \text{ K}^{-1}$ ). These different thermal conductivities can be explained by geometrical features within crystal structures, which influence the phononic dispersion and ballistic thermal conductance [195–197]. These results are in the same order as experimentally found thermal conductivities which obtained 0.31-0.39

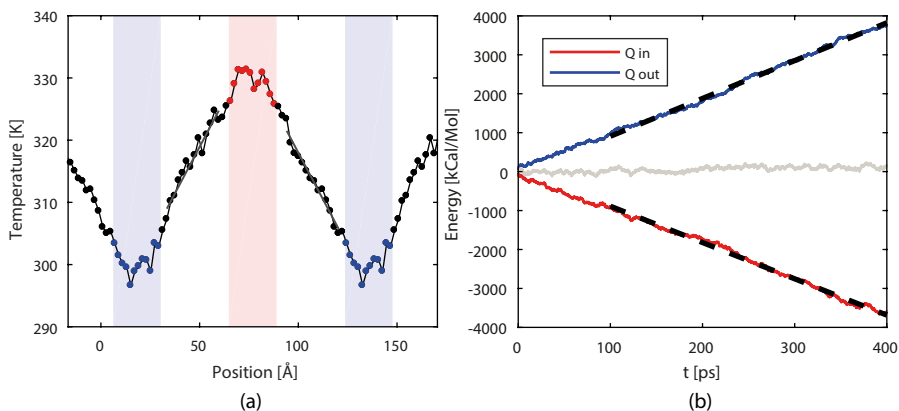


Figure 3.13: (a) Typical temperature profile for  $\text{CaCl}_2 \cdot 2\text{H}_2\text{O}$  in y-direction in a periodic domain, with heat source (red) and sink (blue). The dashed curve is a linear fit to the weakly coupled region. (b) Typical heat flux in and out of respectively the heat source and sink.

W/mK [198] for  $\text{CaCl}_2$  powders and 1.09 W/mK [199] for  $\text{CaCl}_2 \cdot 6\text{H}_2\text{O}$ . The experimental found thermal conductivity of dry  $\text{CaCl}_2$  is a bit lower than our value. However, we assumed a perfect crystal where the experiment used powder, which influences the thermal conductivity as proven in the next section on grain boundaries. Furthermore, the thermal conductivity are in the same order as previous MD studies, in which a thermal conductivity of 0.3 W/mK [100] was found for  $\text{CaCl}_2 \cdot 2\text{H}_2\text{O}$ .

Bulk TCMs are not single crystal structures, but composed of many grains. In this sense, next to perfect crystals, we studied the thermal behavior at grain boundaries, since these interfaces influence heat fluxes [69, 200, 201]. A grain boundary was build in x-direction by small rotations of two separated grains around the z-axis in opposite direction, with an angle such that periodicity in y-, and z-direction was still applicable. An angle of  $5.9^\circ$  and  $7.2^\circ$  provided this requirement, for  $\text{CaCl}_2$  and  $\text{CaCl}_2 \cdot 2\text{H}_2\text{O}$  respectively. Because both crystals were rotated in opposite direction, this gives an angle of  $11.8^\circ$  and  $14.4^\circ$ , respectively. A schematic representation for the  $\text{CaCl}_2$  system is given in Figure 3.14. Accordingly, a simulation was run over 50 ps from 0 K to 300 K, which resulted in a merged system, and another 50 ps was simulated to confirm an equilibrated system. After equilibration, the NEMD simulation was performed with similar settings as the perfect crystals, and a typical resulting temperature profile can be found in Figure 3.14. In Table 3.3 the resulting computed thermal conductivity analysis is given for the systems with grain boundaries. The angle between the perfect crystals was  $11.8^\circ$  and  $14.4^\circ$  for respectively the anhydrous and dihydrate systems, which we both computed three times. The computed thermal conductivities over the perfect parts of the systems show a good match with the perfect systems. The decrease of thermal conductivity can be attributed to the extra introduced scattering events by the grain boundary. The computed Thermal Boundary Resistance (TBR) is in the order  $1 - 5 \times 10^{-9} \text{ W m}^2 / \text{K}$ , which is comparable to other (reactive) grain boundaries [69]. The third simulated grain boundary for  $\text{CaCl}_2 \cdot 2\text{H}_2\text{O}$  shows a relative low resistance ( $0.62 \times 10^{-9} \text{ W m}^2 \text{ K}^{-1}$ ), caused by a

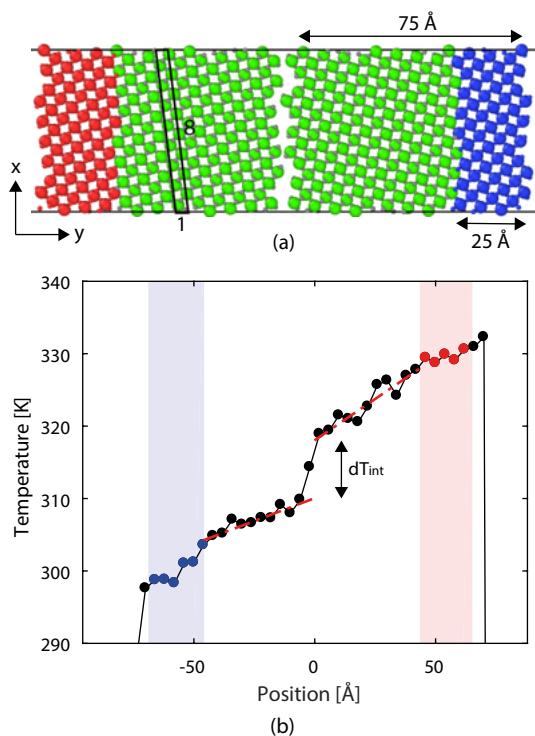


Figure 3.14: Temperature gradient over  $\text{CaCl}_2$  system with a grain boundary.

reacted and merged interface [201] that increases the opportunity of inelastic scattering. The computed thermal conductivities over the perfect parts are comparable to the computed thermal conductivity of the perfect crystals.

### 3.3.3. EXPANSION AND CRACK FORMATION

To regenerate the storage system, and dehydrate the salt, the material is heated. Therefore, we studied what happens with the hydrated  $\text{CaCl}_2 \cdot 2\text{H}_2\text{O}$  when it is heated. This result is given in Figure 3.15, and shows that  $\text{CaCl}_2 \cdot 2\text{H}_2\text{O}$  dehydrates before it melts. Upon heating, first only a small thermal expansion in x-direction is observed, this is also the direction in which the particles make a  $47^\circ$  angle with the x-direction and the xy-planar  $\text{CaCl}_2$  layers. This angle causes the crystal to expand in this direction. The water molecules are perpendicular aligned with the y-direction and the xy-planar, thereby, the crystal hardly expands in this direction. At higher temperatures, far above the dehydration temperature, the water molecules gain enough energy to push the xy-planed  $\text{CaCl}_2$  layers apart, forming cracks between the  $\text{CaCl}_2$  layers, and the system quickly expands in this direction. This effect creates room for all the water molecules to immediately dissociate shortly after the rapid expansion in z-direction since we are already far above the dehydration temperature. Due to the dissociating water molecules, room is made for

Table 3.3: Thermal boundary resistance of grain-boundary.  $k_{\text{perfect}}$  is the computed thermal conductivity ( $\text{Wm}^{-1}\text{K}^{-1}$ ) over the perfect parts of the system,  $TBR$  is the computed thermal boundary resistance ( $\text{Wm}^{-2}\text{K}^{-1}$ ).

	$\text{CaCl}_2$				$\text{CaCl}_2 \cdot 2\text{H}_2\text{O}$			
	1	2	3	avg. $\pm$ sd.	1	2	3	avg. $\pm$ sd.
$k_{\text{perfect}}$	0.60	0.78	0.62	$0.66 \pm 0.08$	0.85	0.78	0.62	$0.75 \pm 0.1$
$TBR \times 10^{-9}$	1.39	1.38	2.63	$1.8 \pm 0.58$	2.82	5.33	0.62	$2.92 \pm 1.92$

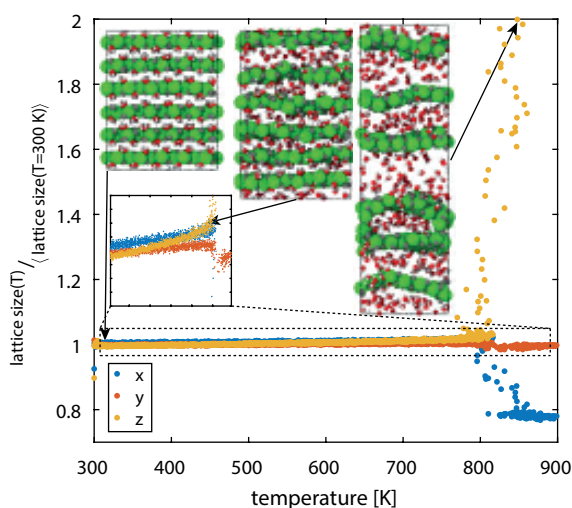


Figure 3.15: Effect of lattice expansion on heating the periodic  $\text{CaCl}_2 \cdot 2\text{H}_2\text{O}$  system in the range from 300-900 K.

the xy-planed  $\text{CaCl}_2$  layers in x-direction. Before the dissociation, the water molecules occupied some space due to the  $47^\circ$  angle, empty  $\text{H}_2\text{O}$  voids causes the crystal to shrink in x-direction. Again, the y-direction is hardly effected because the water molecules did not influence the  $\text{CaCl}_2$  packing from the start.

This heating study shows that  $\text{CaCl}_2 \cdot 2\text{H}_2\text{O}$  will crack in the xy-plane, in between the  $\text{CaCl}_2$  layers, which can be expected when considering the typical topology of the crystal. In practice, this will happen at a lower temperature where dehydrating water make room for the system to expand.

### 3.4. CONCLUSIONS

A new ReaxFF for  $\text{CaCl}_2 \cdot n\text{H}_2\text{O}$  is developed in order to get more fundamental insight into key TCM properties such as dehydration mechanisms, thermal conductivity, and crack formation upon heating. These properties are key as they could cause or prevent local hot-spots, agglomerations, or overhydration. The newly generated ReaxFF is based on an existing  $\text{CaCl}_2 \cdot n\text{H}_2\text{O}$  ReaxFF [185], which was intentionally limited to predicting kinetics. A new optimization protocol was established to preserve the crystal geometry

of salt hydrates. New data was added to the training set, including MD-trajectories predicted by intermediate force fields. The corresponding energies of these MD-trajectories in the training set were computed by DFT. This protocol significantly increased the performance of the ReaxFF regarding the stability of  $\text{CaCl}_2 \cdot n\text{H}_2\text{O}$  bulk structures. Next to the desired increased stability of crystal structure, the new force field proved to accurately predict the surface energies in multiple directions and capture correctly the RDFs for both  $\text{CaCl}_2$  and  $\text{CaCl}_2 \cdot 2\text{H}_2\text{O}$ .

Salt hydrate structures have a strong anisotropic morphology, therefore the dehydration characteristics and the thermal conductivity is computed in x-, y-, and z-direction. The orientation of the crystal hydrate has a strong influence on the dehydration rate, where the dehydration rate in z-direction is much slower than x-, and y-direction due to the typical layered character of the  $\text{CaCl}_2 \cdot 2\text{H}_2\text{O}$  structure. After the initial 12 ns, already 1.9 and 2.5 times more water molecules are dehydrated in these direction respectively. In all directions, dehydrated superficial  $\text{CaCl}_2$  layers impede evaporating  $\text{H}_2\text{O}$  molecules and slow the dehydration down. Cracks and pores are needed to create pathways through these outer layers for the evaporation of inner  $\text{H}_2\text{O}$  molecules. In case of the thermal conductivity, the layered characteristic in z-direction also causes a lower thermal conductivity compared to other directions. The thermal conductivity is computed to be approximately  $1.1 \text{ W/mK}$  and  $0.5 \text{ W/mK}$  for anhydrous  $\text{CaCl}_2$  and hydrated  $\text{CaCl}_2 \cdot 2\text{H}_2\text{O}$ , respectively. This is in the same order as experimental values of  $\text{CaCl}_2 \cdot n\text{H}_2\text{O}$  [198, 199]. Thus, nano scale modifications that interfere with the strong layered morphology in z-direction, could benefit the overall dehydration and thermal conductivity.

Bulk TCM salt hydrates are never a complete perfect crystal, but contain many grains. In this sense, the influence of a grain boundary is studied for  $\text{CaCl}_2$  and a Thermal Boundary resistance (TBR) of  $2.92e-9 \text{ Wm}^2/\text{K}$  is computed. This is comparable for other (reactive) grain boundaries [69]. The effect of heating the  $\text{CaCl}_2 \cdot 2\text{H}_2\text{O}$  is studied to gain insight in possible crack formation upon drying the salt. Due to the typical  $\text{CaCl}_2$  layers in the xy-plane, with intermediate water, cracks are also formed this plane in between these  $\text{CaCl}_2$  layers. The successful newly developed transferable  $\text{CaCl}_2 \cdot n\text{H}_2\text{O}$  force field allowed detailed characterization of the salt as TCM. In future studies, this ReaxFF force field can be used to study effects of modification of the salt to promote its use for heat storage applications. An example of such a possible study is the combination of the pure salt with another salt (see chapter 2), and the effect of this mixture on the dehydration mechanism and rate. Furthermore, it creates the opportunity for detailed research on the effect of crack, pores, and grain boundaries on thermal and mass fluxes through the salt.



# 4

## ADVANCED DIFFUSION METHODS FOR H<sub>2</sub>O IN SALT HYDRATES

**ABSTRACT:** *Slow diffusion of water through salt hydrates limit the power output of a thermochemical energy storage. Simultaneously, slow water diffusion gives rise to local over-hydrated spots. Recent studies show that cracks and pores in the salt crystal increase the (de)hydration rate. In this sense, we analyzed the diffusion behavior of water in crystalline  $\text{CaCl}_2 \cdot 2\text{H}_2\text{O}$  and around crystal imperfections, like cracks and pores, through reactive force fields molecular dynamics. A Smoluchowski diffusion equation-based method was used to perform this diffusion study. This method enabled the possibility to study a local diffusion behavior instead of the often used global diffusion methods. We found that the diffusion of  $\text{H}_2\text{O}$  is extremely low in the crystalline regions of the  $\text{CaCl}_2 \cdot 2\text{H}_2\text{O}$  ( $< 10^{-10} \text{ m}^2/\text{s}$ ), which corresponds with literature for similar salts. However, in cracks, pores, and amorphous regions of the salt, the diffusion is significantly higher ( $\geq 10^{-9} \text{ m}^2/\text{s}$ ). Thereby, this enhanced local diffusivity explains why imperfections of the crystalline salt hydrate can improve its characteristics for thermochemical heat storage applications.*

---

This chapter is in preparation to be submitted for to a peer reviewed journal.

## 4.1. INTRODUCTION

In the search towards a viable energy storage system, that is able to efficiently store energy to bridge the mismatch between renewable energy supply and energy demand, thermochemical heat storage has gained much attention and has been intensively studied [18, 19, 22]. With the thermochemical energy storage concept, energy is stored in a reversible exo-/endothermic reaction between different elements. Numerous salts are studied as potential thermochemical material (TCM) [11, 169]. With salt hydrates, energy can be stored in times of a surplus of heat by using the heat in endothermic dehydration of the salt. In times of a lack of heat, the dehydrated salt is hydrated again via an exothermic reaction, and heat is released. Among others,  $\text{CaCl}_2 \cdot n\text{H}_2\text{O}$  ( $n = 0, 2, 4, 6$ ) is a potential TCM candidate due to its price [11], and relatively high absorption energy around the operating temperature of domestic energy storage systems [202]. However, like many salt hydrates, it suffers from slow kinetics. This not only reduces the possible power output but can also cause agglomerates and clogging of the system. On the other side, upon hydration and dehydration cycles, cracks and pores are formed, which improve water transport through the cracked crystal and, consequently, increase the kinetics and the power output of the system [177]. However, detailed information on the water mobility in and around these cracks is needed to further exploit this phenomenon. Furthermore, accurate diffusion coefficients are crucial in the selection of a potential TCM candidate and for the design of a valuable thermochemical storage application.

Molecular Dynamics (MD) is a powerful tool to study key dynamical characteristics of heat storage materials [53, 100, 131, 184]. Next to that, MD can be used to study the diffusion of water in porous media [203, 204] or confined regions [205]. In Chapter 3, we used MD to study the dehydration of  $\text{CaCl}_2 \cdot 2\text{H}_2\text{O}$  and found that the dehydration is strongly dependent on the crystal orientation and morphology. Furthermore, we found that some dehydrated  $\text{CaCl}_2$  layers impede further dehydration but cracks and pores significantly increase it. In this work, we study the diffusion of  $\text{H}_2\text{O}$  through salt hydrates, specifically in and around crystal imperfections like cracks, pores, and grain boundaries of the salt hydrates. There is a complex inhomogeneous interplay between liquid water, water vapor, and (crystalline) salt in this region. Hence, it requires a local and detailed method to study the water diffusion in this region.

The diffusion of fluid is macroscopically described by Fick's law  $\mathbf{J} = -D\nabla c$ , which relates the flux  $\mathbf{J}$  of a species to the concentration gradient  $\nabla c$  by the diffusion constant  $D$ . When we consider the simple case of a labeled molecule that we follow when it diffuses in a fluid consisting of the same molecules, we have the so-called self-diffusion. With the assumptions that the labeled species was initially concentrated at the origin, and the conservation of mass, we could rewrite Fick's law to Fick's second law of diffusion, which connects the concentration profile to the diffusion [63]:

$$\frac{c(\mathbf{r}, t)}{\partial t} = D\nabla^2 c(\mathbf{r}, t) \quad (4.1)$$

where  $c(\mathbf{r}, t)$  is the concentration profile depending on its position  $\mathbf{r}$  and time  $t$ . Einstein was the first who derived equation (4.1), which resulted in the well known Einstein method to compute the self diffusion:

$$D = \lim_{t \rightarrow \infty} \frac{1}{2dt} \langle |\mathbf{r}(t) - \mathbf{r}(0)|^2 \rangle, \quad (4.2)$$



with  $d$  as the dimensionality of the system. This Einstein method relates the macroscopic property self-diffusion  $D$  to the Mean Squared Displacement (MSD) of particles  $\langle |\mathbf{r}(t) - \mathbf{r}(0)|^2 \rangle$ . Practically, the slope of the MSD over long time periods can be used to the self-diffusion. Alternatively, one could rearrange equation (4.2) in terms of velocities of the particles, and obtain the Green-Kubo relation:

$$D = \frac{1}{d} \int_0^\infty dt \langle \mathbf{v}(t) \cdot \mathbf{v}(0) \rangle, \quad (4.3)$$

in this equation  $\langle \mathbf{v}(t) \cdot \mathbf{v}(0) \rangle$  is the so-called velocity autocorrelation function (VACF). Both the MSD and VACF can be directly obtained via MD-generated particle trajectories. Therefore, both methods are an often used way to compute the diffusion of a species by means of MD. However, as both methods are derived on the assumption of Fick's law and free boundary conditions, they are not valid for confined fluids or inhomogeneous systems [206]. In the latter case, the methods are only valid if one simulates long enough that the followed particles sample all regions, and as a consequence, the result describes the overall diffusion coefficient of the entire system. Where, especially for inhomogeneous or confined fluids, one is interested in a more local diffusion coefficient.

In case of inhomogeneous systems, the diffusion of fluids should be computed by the Smoluchowski diffusion equation [207], which describes the evolution of the probability density  $p(\mathbf{r}, t)$  depending on its location  $\mathbf{r}$  and time  $t$  [208]:

$$\frac{\partial p(\mathbf{r}, t)}{\partial t} = \nabla \cdot \mathbf{D} \left( e^{-\beta F(\mathbf{r})} \right) \cdot \nabla \left[ e^{\beta F(\mathbf{r})} p(\mathbf{r}, t) \right], \quad (4.4)$$

with  $\beta$  as the reciprocal of the thermodynamic temperature  $\beta = 1/(k_B T)$ ,  $k_B$  is the Boltzmann constant, and  $T$  is the temperature.  $F(\mathbf{r})$  is the free energy surface, or potential mean force (PMF) [209]. This given PDE Smoluchowski diffusion equation is hard to solve analytically for a small region around inhomogeneity. Liu et al. [206] proposed a method in which the domain is divided into small layers or bins. In each bin, the parallel and perpendicular components of the diffusion are computed separately. It is shown that the parallel component can be computed by relating the MSD to the survival probability of the particles in the considered bin. The diffusion perpendicular to the bin can be obtained by fitting the survival probability of particles from a Langevin Dynamics simulation to the survival probability of an MD simulation. In the continuation, Franco et al. [209] used the same method for the parallel contribution but derived a new analytical solution for the perpendicular contribution based on the assumption of a linear PMF in the bin. The benefit of this method is that all diffusion contributions can be obtained from particle trajectories generated by a single MD simulation.

To study the water diffusion in and around inhomogeneous salt hydrates structures, we developed a method to locally solve the Smoluchowski diffusion equation, analogous to the method of Franco et al. [209]. Accordingly, the resulting analytical solution for the survival probability is fitted to the MD obtained survival probability of particles in a small layer of the entire simulation box. This approach provides fundamental insight into water diffusion in and around cycled salt hydrates and allows quantification of the effects of crystal imperfections on the diffusion of water in  $\text{CaCl}_2 \cdot 2\text{H}_2\text{O}$ . Accordingly, these numbers provide helpful information regarding water mobility in TCMs for the macroscopic design of storage applications.

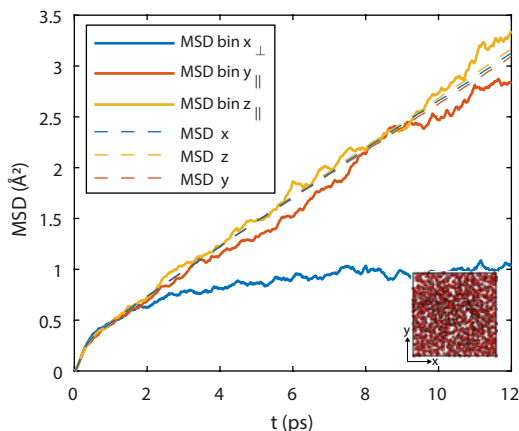


Figure 4.1: MSD in different direction of liquid water (homogeneous) as given in the inset, solid lines are MSD with bins in the  $yz$ -plane, dashed lines are MSD without bins. The inset represents the MD simulated liquid water box.

In the Methodology section, the Smoluchowski diffusion equation based method is explained. The direction parallel to the bin is explained first, then the direction perpendicular to the bin. In the Validation section, the method is validated on water systems. Firstly, for a periodic homogeneous liquid water system, by which it can be compared with the Einstein's and Green–Kubo's method. Secondly, for a water vapor–liquid interface, by which it can be compared with Franco's method [209]. After validation, in the Results & Discussion section, the method is used to study the water diffusion in and around inhomogeneous regions of  $\text{CaCl}_2 \cdot 2\text{H}_2\text{O}$ . These findings provide valuable information for designing thermochemical heat storage applications based on salt hydrates as active material.

## 4.2. METHODOLOGY

In molecular dynamics simulations, most often, either Einstein's method or the Green–Kubo autocorrelation method is used to determine the self-diffusion coefficient of a fluid. However, these do not hold when applied to small sub-layers (bins) of the entire domain. In Figure 4.1, a typical example is given when the basic Einstein's method is used for a periodic homogeneous liquid water simulation and illustrates that it cannot be used for diffusion calculations in small bins. In this figure, the MSDs of particle trajectories are compared for a system with and without bins. In a bin, fast particles will leave earlier than slower particles, and particles that have left the bin do not contribute to the MSD calculation anymore. Thereby, the perpendicular diffusion calculation is affected by the maximum length of the trajectory and capped by the size of the bin. This effect is also present for the parallel contributions, be it less visible.

Additionally, the well-known Einstein and Green–Kubo methods are not applicable near inhomogeneities [206, 209]. In Figure 4.2, an inhomogeneous example system is

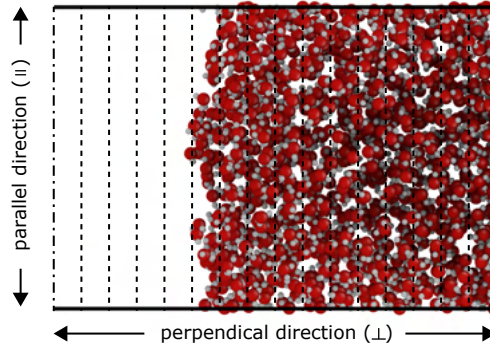


Figure 4.2: Example of water vapor–liquid interface, with bins to compute local diffusion.

given in terms of a water vapor–liquid interface. For such systems, especially near the inhomogeneity, the diffusion characteristics can be important. The given system is divided into small bins, for which in each bin the diffusion coefficients are desired to be known.

In the case of a small sub-layer and/or inhomogeneous region, a more advanced method is needed. Such a method is discussed in the following sections. First, the solution for direction parallel to the bin  $D_{\parallel}$  will be shown. Secondly, the solution for the perpendicular direction  $D_{\perp}$  in a homogeneous region will be shown, and thereafter, for the perpendicular direction in an inhomogeneous region.

#### 4.2.1. PARALLEL TO THE BIN

For the diffusion in a small bin, one could assume a constant diffusion  $D$  within the entire bin. With this assumption, the Smoluchowski diffusion equation (4.4) can be rewritten in 1D as [209]:

$$\frac{\partial p(r, t)}{\partial t} = \frac{\partial}{\partial r} \left[ D_{\parallel} e^{-\beta F(r)} \frac{\partial}{\partial r} \left[ e^{\beta F(r)} p(r, t) \right] \right]. \quad (4.5)$$

for position  $r$ ,  $F(r)$  is the PMF, that is related to ratio of the local density  $\rho(r)$  and the average density  $\rho_{avg}$  via:

$$\frac{\rho(r)}{\rho_{avg}} = e^{-\beta F(r)}. \quad (4.6)$$

For both the homogeneous as the inhomogeneous systems, one could assume homogeneity for the parallel direction if in the latter case the bins are oriented perpendicular to the inhomogeneity. This gives  $\rho(r) = \rho_{avg}$ , and the gradient of  $F(r)$  that equal to zero. As a consequence, the 1D Smoluchowski equation (4.5) becomes Fick's second law. Were it not for the small bins, one could simply use Einstein's or Green-Kubo's method. However, in the case of bins, Liu et al. [206] showed that the diffusion in parallel direction of the bin equals:

$$D_{\parallel, r} = \lim_{t \rightarrow \infty} \frac{1}{2dtP(t)} \langle |r(t) - r(0)|^2 \rangle, \quad (4.7)$$

in which  $r$  is the parallel direction, and  $P(t)$  is the survival probability of the particles in the bin. This survival probability can be directly obtained from MD:

$$P(t) = \frac{1}{\tau} \sum_{t_0}^{\tau} \frac{N(t_0, t_0 + t)}{N(t_0)}, \quad (4.8)$$

where  $N(t_0)$  are the initial number of particles in the bin at time  $t_0$ , and  $N(t_0, t_0 + t)$  are the number of particles not have left the bin after time  $t_0 + t$ . This number is averaged over  $\tau$  starting times.

#### 4.2.2. PERPENDICULAR TO THE BIN FOR HOMOGENEOUS REGIONS

Similar to the parallel direction of the bins, for homogeneous regions in perpendicular direction to the bin  $\rho(r) = \rho_{\text{avg}}$ . Thus the gradient of  $F(r)$  equals zero. In this case, equation (4.5) simplifies to:

$$\frac{\partial p(r, t)}{\partial t} = D_{\perp} \left[ \frac{\partial^2 p(r, t)}{\partial r^2} \right]. \quad (4.9)$$

With the Dirichlet boundary condition, which implicates that once the particles have left the bin, at position 0 or  $L$ , and re-enter they are not reconsidered,

$$p(0, t) = p(L, t) = 0, \quad (4.10)$$

and the Dirac delta initial condition [206],

$$p(r, 0) = \delta(r - \frac{1}{2}L) \quad (4.11)$$

equation 4.9 can be written as:

$$p(r, t) = \frac{2}{L} \sum_{n=1}^{\infty} \sin \left[ \frac{n\pi}{2} \right] \sin \left[ \frac{n\pi}{L} r \right] \exp \left[ - \left( \frac{n\pi}{L} \right)^2 D_{\perp} t \right]. \quad (4.12)$$

In practice, the Dirichlet boundary condition is not used in the MD simulation but only for the analysis [206]. Furthermore, in the analysis, the starting point of particle trajectories is when a H<sub>2</sub>O molecule passes the center of the bin, according to the Dirac delta initial start condition. Instead of the Dirac delta initial condition, Franco et al. used a locally dependent initial density. In Appendix D.1 the full derivation of this equation is given. Integration of this probability density function from 0 to  $L$  leads to the survival probability:

$$P_{\text{homo}}(t) = \int_0^L p(r, t) dr = \sum_{n=1}^{\infty} \frac{2}{n\pi} \sin \left[ \frac{n\pi}{2} \right] (1 - \cos[n\pi]) \exp \left[ - \left( \frac{n\pi}{L} \right)^2 D_{\perp} t \right], \quad (4.13)$$

which describes the survival probability of particles in a specific bin between 0 and  $L$  in a homogeneous region. Due to the different initial condition, Franco et al. analytically derive the time integrated probability function. However, as a consequence of our initial condition, we fit the survival probability of equation 4.13 to the MD survival probability equation (4.8) to obtain  $D_{\perp}$ .

### 4.2.3. PERPENDICULAR TO THE BIN FOR INHOMOGENEOUS REGIONS

In the perpendicular direction to the bin, near density inhomogeneities  $\rho(r) \neq \rho_{avg}$ , and the gradient of the PMF is not zero. For this case, Franco et al. [209] showed that for small bins, one could approximate the PMF with a linear relation:

$$-\beta F(r) = \omega r + C, \quad (4.14)$$

with  $\omega$  as gradient. Accordingly, the natural logarithm is also linear:

$$\ln \left[ \frac{\rho(r)}{\rho_{avg}} \right] = \omega r + C. \quad (4.15)$$

As a result, the 1D Smoluchowski diffusion equation (4.5) can be rewritten for the perpendicular diffusion near inhomogeneities as:

$$\frac{\partial p(r, t)}{\partial t} = D_{\perp} \left[ \frac{\partial^2 p(r, t)}{\partial r^2} - \omega \frac{\partial p(r, t)}{\partial r} \right]. \quad (4.16)$$

Using the Dirichlet boundary conditions and the initial Dirac delta condition, the probability density distribution equation 4.16 can be written as:

$$p(r, t) = \frac{2}{L} \exp \left[ \frac{\omega}{2} r - \frac{\omega L}{4} \right] \sum_{n=1}^{\infty} \sin \left[ \frac{n\pi}{2} \right] \sin \left[ \frac{n\pi}{L} r \right] \exp \left[ - \left( \left( \frac{n\pi}{L} \right)^2 + \frac{\omega^2}{4} \right) D_{\perp} t \right]. \quad (4.17)$$

In Appendix D.2, the full derivation of this equation is given. Accordingly, via integration by parts of probability density function (4.17) from 0 to L we get the survival probability:

$$\begin{aligned} P_{inhomo}(t) &= \int_0^L p(r, t) dr = \\ &\exp \left[ -\frac{\omega L}{4} \right] \sum_{n=1}^{\infty} \sin \left[ \frac{n\pi}{2} \right] \frac{2n\pi}{(n\pi)^2 + \left( \frac{L\omega^2}{2} \right)} \\ &\left( 1 - \exp \left[ \frac{\omega L}{2} \right] \cos[n\pi] \right) \exp \left[ -D_{\perp} t \left( \left( \frac{n\pi}{L} \right)^2 + \frac{\omega^2}{4} \right) \right], \end{aligned} \quad (4.18)$$

which describes the survival probability of particles in a specific bin between 0 and L near an inhomogeneous region. To obtain the diffusion in the given bin, this survival probability can be fitted to the MD survival probability (equation 4.8) to obtain  $D_{\perp}$ . Note that when this equation is used for a homogeneous region, the density profile is constant and  $\omega = 0$ , this equation reduces to equation 4.13 for homogeneous systems.

### 4.2.4. REAXFF

In order to model the water mobility in and around  $\text{CaCl}_2 \cdot 2\text{H}_2\text{O}$  crystal cracks, pores, and grain boundaries, we used the reactive force field (ReaxFF) formalism [81, 82, 124]. This MD method is developed to bridge the gap between expensive quantum mechanical (QM) calculation and conventional non-reactive MD. QM includes bond breaking and formation but at a high computational cost such that only small systems can be considered. On the other side, with conventional non-reactive MD, large systems can be

considered but not bond breaking or formation. ReaxFF bridges this gap by using empirical relations, which are parameterized on accurate QM or experimental data [83], to describe bond orders. The ReaxFF force field used in this chapter was developed in Chapter 3 for the dehydration description of the CaCl<sub>2</sub>·*n*H<sub>2</sub>O (*n* = 0, 2) salt hydrates. Each simulation was performed in an NVT ensemble. However, for the salt dehydration simulation, the evaporated H<sub>2</sub>O molecules were removed every 0.25 ps. The ReaxFF module of the SCM software package [124] was used. The Velocity Verlet time integration method [210] with a timestep of 0.25 or 0.5 fs was used, depending on the system's characteristics. The Berendsen thermostat [211] was used to control the temperature of the simulation. For the diffusion calculation, every 125 fs of the MD simulation coordinates were stored for the pure water systems and every 25 fs for the salt systems.

## 4

### 4.3. VALIDATION

The method was validated for a homogeneous liquid water system and compared to the conventional MSD and Green–Kubo methods. The inhomogeneous solution was validated with a water vapor–liquid interface and compared with previous results of Liu et al. [206] and Franco et al. [209].

#### 4.3.1. VALIDATION HOMOGENEOUS SYSTEM: LIQUID WATER

To validate the diffusion calculation based on the Smoluchowski diffusion equation for a small subregion (bin), it was compared with the standard Einstein's method and the Green–Kubo autocorrelation method. For this test case, a  $31.08 \times 31.08 \times 31.08$  Å periodic homogeneous box was simulated at 300 K with 1000 H<sub>2</sub>O molecules water, as given in the inset of Figure 4.1. For the Einstein's and Green–Kubo's methods, the entire simulation box was used to compute the diffusion. For the diffusion calculation with the survival probability, bins with a width of 5 Å were used. A bin width of 5 Å was chosen after careful optimization in the compromise between accessing local information on the (by definition non-local) diffusion characteristics and the need to obtain sufficient data for its computation. In Figure 4.1, the resulting MSDs for the different directions are shown with the dashed lines, it clearly shows a linear MSD, and the diffusion can be calculated by fitting Einstein's equation 4.2. The solid lines in Figure 4.1 represent the MSD for the case when bins are used. It clearly shows that the diffusion can not be obtained with the conventional Einstein's method for the normal direction to the bin. In this direction, the MSD quickly goes to a minimum correlated to the width of the bin, because particles that have left the bin do not contribute anymore to the MSD.

In Table 4.1, the resulting diffusion coefficients are given for the homogeneous water simulation. The diffusivity is computed in x-, y-, and z-direction with the Einstein method; with the Green-Kubo method, only the overall diffusivity can be computed; with the survival probability fit, the diffusivity is computed in all three directions with bins of 5 Å in the yz-plane. From these results, it is shown that the diffusion coefficient can be well estimated with fitting equation (4.13) to the, by MD generated, results of equation (4.8). For all diffusion calculations, the results are slightly lower than expected for water at room conditions  $\sim 2 \times 10^{-9}$  m<sup>2</sup>/s [212], which can be attributed to the force field, that is optimized for CaCl<sub>2</sub>·*n*H<sub>2</sub>O (*n* = 0, 2) salt hydrates rather than water diffusion

Table 4.1: Diffusivity ( $10^{-9}$  m<sup>2</sup>/s) homogeneous water. The direction to perpendicular to the bin is not applicable for the Green-Kubo methodology, where only the overall diffusion is obtained.

Method	Direction to bin	
	parallel (y, z)	perpendicular (x)
Einstein	$1.22 \pm 0.1$	$1.3 \pm 0.1$
Green-Kubo	1.37	—
Smoluchowski (eqs. 4.7, 4.13)	1.22	1.54

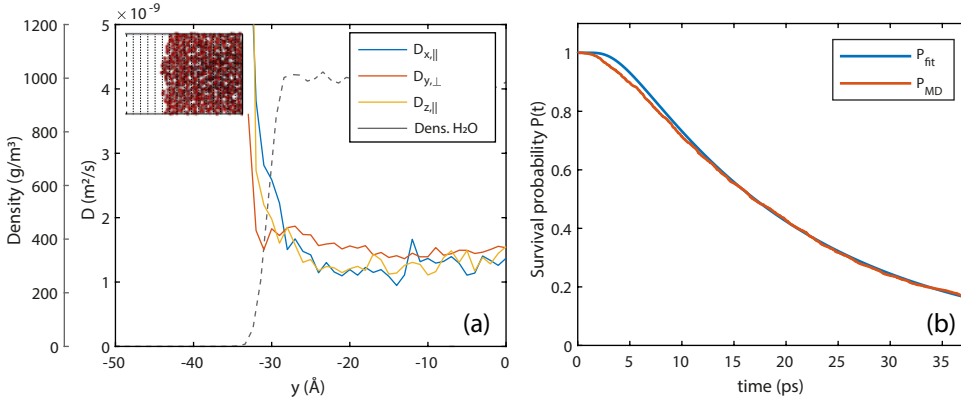


Figure 4.3: (a) Computed diffusion coefficients over the vapor-liquid interface (as shown in the inset) for x-, y-, and z-direction. The dashed line represents the H<sub>2</sub>O density. (b) Survival probability of a given bin in the liquid region at  $x = -10$  Å of the vapor-liquid simulation. The red line represents the survival probability obtained from MD (eq. 4.8). The Blue line represent a fit of the analytical solution of the Smoluchowski diffusion equation (eq 4.18) to obtain the diffusion coefficient.)

coefficients.

#### 4.3.2. VALIDATION INHOMOGENEOUS SYSTEM: WATER VAPOR-LIQUID INTERFACE

To validate the inhomogeneous solution of the Smoluchowski diffusion equation, a water vapor-liquid interface was simulated at 300 K, in a  $32.00 \times 1000 \times 30.75$  Å simulation box with 2000 H<sub>2</sub>O molecules. In Figure 4.3a, diffusion profiles over the vapor-liquid interface is shown for x-, y-, and z-direction, with the interface in x-direction. In Figure 4.3b, the survival probability of H<sub>2</sub>O molecules in a given bin is plotted along with a fitted survival probability of the Smoluchowski diffusion equation (4.18).

The results of Figure 4.3a show a similar trend as found by Liu et al. [206]. In bulk, far from the interface, the diffusion is equal in all directions. Closer to the vapor-liquid interface, the diffusion coefficient increases due to the lower number of H-bonds [213, 214] and thereby a lower friction. Furthermore, the diffusion parallel to the interface (parallel to the bin) is higher than the diffusion perpendicular to the bin. This is related to the higher diffusion barrier perpendicular to the interface compared to the parallel direction, but lower for bulk region [206].

## 4.4. RESULTS & DISCUSSION – SALT HYDRATES

This work was motivated to gain insights into the mobility of H<sub>2</sub>O in and around salt hydrates as TCMs, both for perfect crystalline structures as well as for imperfect structures. After the validation, the proposed diffusion calculation method was used to compute diffusion coefficients in and around CaCl<sub>2</sub>·2H<sub>2</sub>O slabs. In Chapter 3, we already studied the dehydration of perfect CaCl<sub>2</sub>·2H<sub>2</sub>O crystal slabs in different directions. We found that the anisotropic morphology of the salt crystal has a major effect on the dehydration. Furthermore, a partly dehydrated layer impedes further dehydration of underlying hydrated material. However, pores created by dehydration assist further dehydration. Here, we quantify this behavior by means of diffusion studies and create additional CaCl<sub>2</sub>·2H<sub>2</sub>O slabs with artificial cracks and voids. These structures are compared regarding the dehydration rate compared to the perfect slabs in Section 4.4.1. In Section 4.4.2 the influence of crystal defects on the diffusion are investigated.

4

### 4.4.1. DEHYDRATION OF CaCl<sub>2</sub>·2H<sub>2</sub>O

Different CaCl<sub>2</sub>·2H<sub>2</sub>O crystal slabs were created and heated to 500 K to simulate and study their dehydration characteristics. These slabs were placed in a vacuum, and every 0.25 ps, the evaporated H<sub>2</sub>O molecules (located at a distance larger than 30 Å from the slab) were removed to preserve the dehydration force. Perfect slabs, starting from the experimental structure [141], are simulated with a vacuum in x-, y-, or z-direction as shown in Figure 4.4 b–d. In Chapter 3, we extensively discuss the dehydration results, and we found that dense dried (dehydrated) CaCl<sub>2</sub> layers/regions form a barrier for dehydration of underlying H<sub>2</sub>O molecules. In contrast, emerged pores allow faster dehydration. The dense dried CaCl<sub>2</sub> regions and emerged pores are clearly visible in the images, created with iRASPA [215], of Figure 4.4 b–d.

To get more insight into these effects and quantify their impacts, we used the structures of the perfect slabs at 3 and 6 ns for the diffusivity calculation. Therefore, we restarted an MD simulation over 250 ps without the removal of water to limit further dehydration and computed the diffusion profile in x-, y-, and z-direction with bins of 5 Å. Additionally, the initial perfect structures were re-simulated for dehydration, but with 5 and 10% less CaCl<sub>2</sub> to create voids. Furthermore, a perfect slab with the vacuum in the z-direction is re-simulated with an artificially removed region that represents a small crack. The z-direction was chosen because of the layered CaCl<sub>2</sub> structure in this direction, which significantly reduces the dehydration [131]. These new structures with artificially created imperfections are represented in the images of Figure 4.4e and f, the 5% void structure and the crack in z-direction, respectively.

From Figure 4.4a, it can be observed that all created imperfections increase the dehydration compared to the perfect crystals. The 5 and 10% voids show similar rates in all directions, indicating that these voids reduce the effect of the anisotropic morphology of the crystal on the water mobility within the crystal. When strongly disordered structures are formed by dehydration of H<sub>2</sub>O, the rates become similar between these different initial structures. The induced crack in z-direction, similar to the voids, resulted in increased dehydration but at a slightly lower rate. However, one must note that the crack was only present over half of the structure, where the voids were created over the entire system. From Figure 4.5a the top view of the initial structure 5% removed CaCl<sub>2</sub>



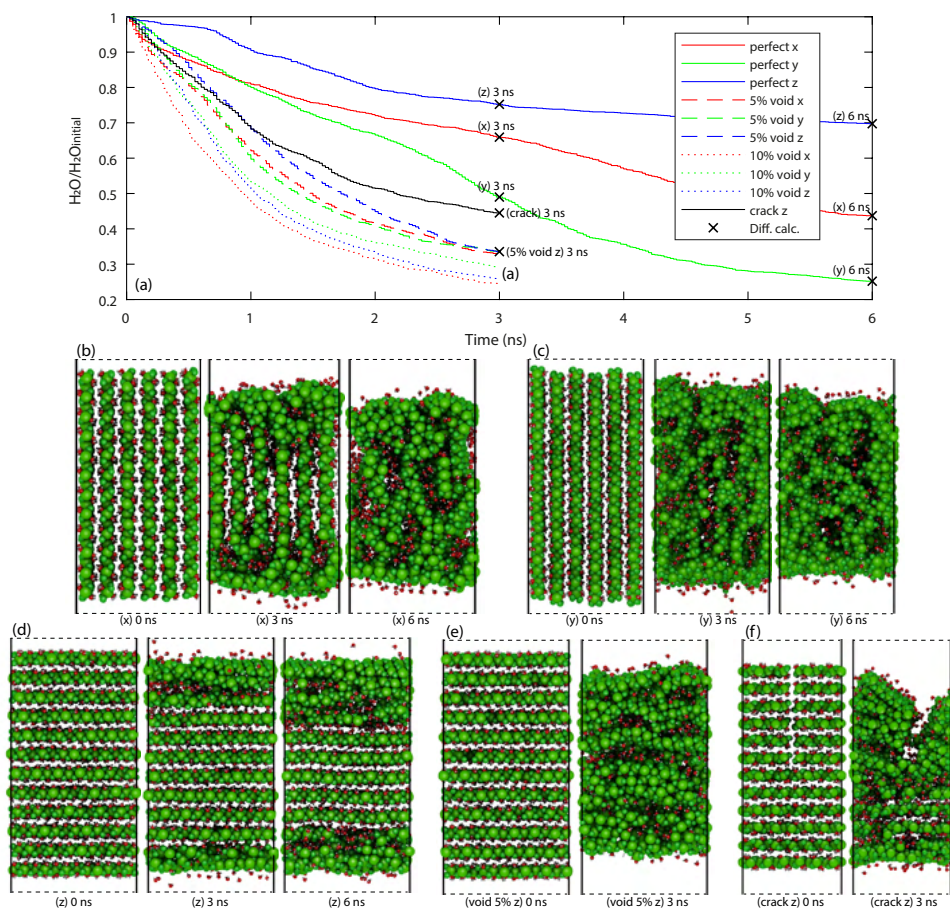


Figure 4.4: Dehydration of  $\text{CaCl}_2 \cdot 2\text{H}_2\text{O}$  crystal slabs in different directions, with the perfect initial structures from Chapter 3. The crosses (x) represent the moments considered as initial structures for further simulation and diffusion calculations, these structures are represented in the images (created with iRASP [215]).

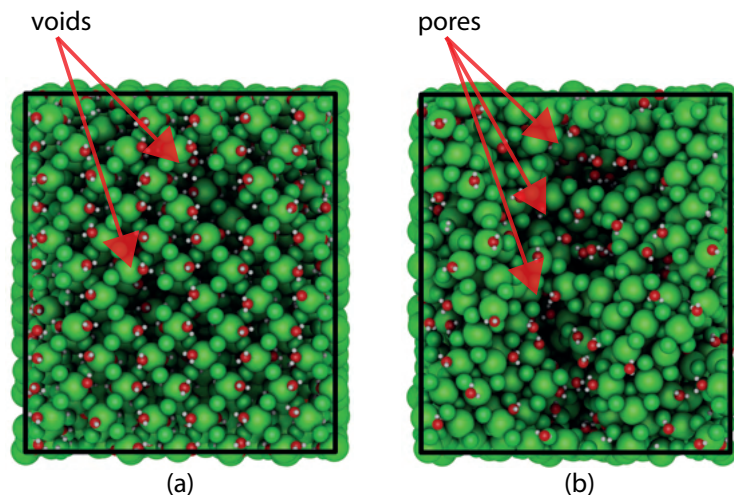


Figure 4.5: Top view of 5% void system with vacuum in  $z$ -direction, (a) 0 ns, (b) 3 ns.

molecules is given, in Figure 4.5b, the originated pores after 3 ns are clearly visible. These pores allow pathways for the water the diffuse out of the crystal.

#### 4.4.2. DIFFUSION IN $\text{CaCl}_2 \cdot 2\text{H}_2\text{O}$

To obtain self-diffusion coefficients for water in (dehydrated)  $\text{CaCl}_2 \cdot 2\text{H}_2\text{O}$  in the parallel plane of the slab (parallel to the surface and parallel to the bin), equation (4.7) was used. In the direction perpendicular to the slab (perpendicular to the bin, and in the direction of the vacuum), the survival probability given by equation (4.18) was used. The local diffusion coefficients were computed every Ångstrom with a 5 Å bin at every location (for example, at the location  $x = 10$  Ångstrom the diffusion was computed with the particles from  $x = 7.5$  to  $x = 12.5$ , at the next location  $x = 11$  Ångstrom the particles from  $x = 8.5$  to  $x = 13.5$  were used, etc.). All systems were simulated over 250 ps, and every 25 fs the coordinates were stored. The tracked  $\text{H}_2\text{O}$  molecules can either be pinned to a calcium atom or dissociated from the calcium atom by which they are free to diffuse. These two different states of a  $\text{H}_2\text{O}$  molecule result in completely different self-diffusion coefficients. In this sense, each set of  $\text{H}_2\text{O}$  trajectories was divided into 5 groups based on their displacement. Accordingly, the diffusion was determined for each set independently, and the overall diffusion coefficient was taken from the average of these groups.

It was already observed in Chapter 3 that at 300 K no significant dehydration occurs from the simulated slabs within the simulated MD time scale. This is below the hydration and dehydration temperature (336 and 344 K, respectively) of  $\text{CaCl}_2 \cdot 2\text{H}_2\text{O}$  [174]. Similarly, we simulated a  $\text{CaCl}_2 \cdot 2\text{H}_2\text{O}$  slab with a vacuum in  $z$ -direction at 300 K but no diffusion coefficient could be obtained. With a diffusion coefficient of  $10^{-10} \text{ m}^2/\text{s}$ , it would take in the order of 300 ps for a molecule to diffuse 2.5 Å (half of the bin-width), using  $D = l^2/2t$ . Since the simulations are performed over 250 ps, it can be concluded that when no diffusion coefficient can be obtained, the value is at least lower than  $10^{-10}$

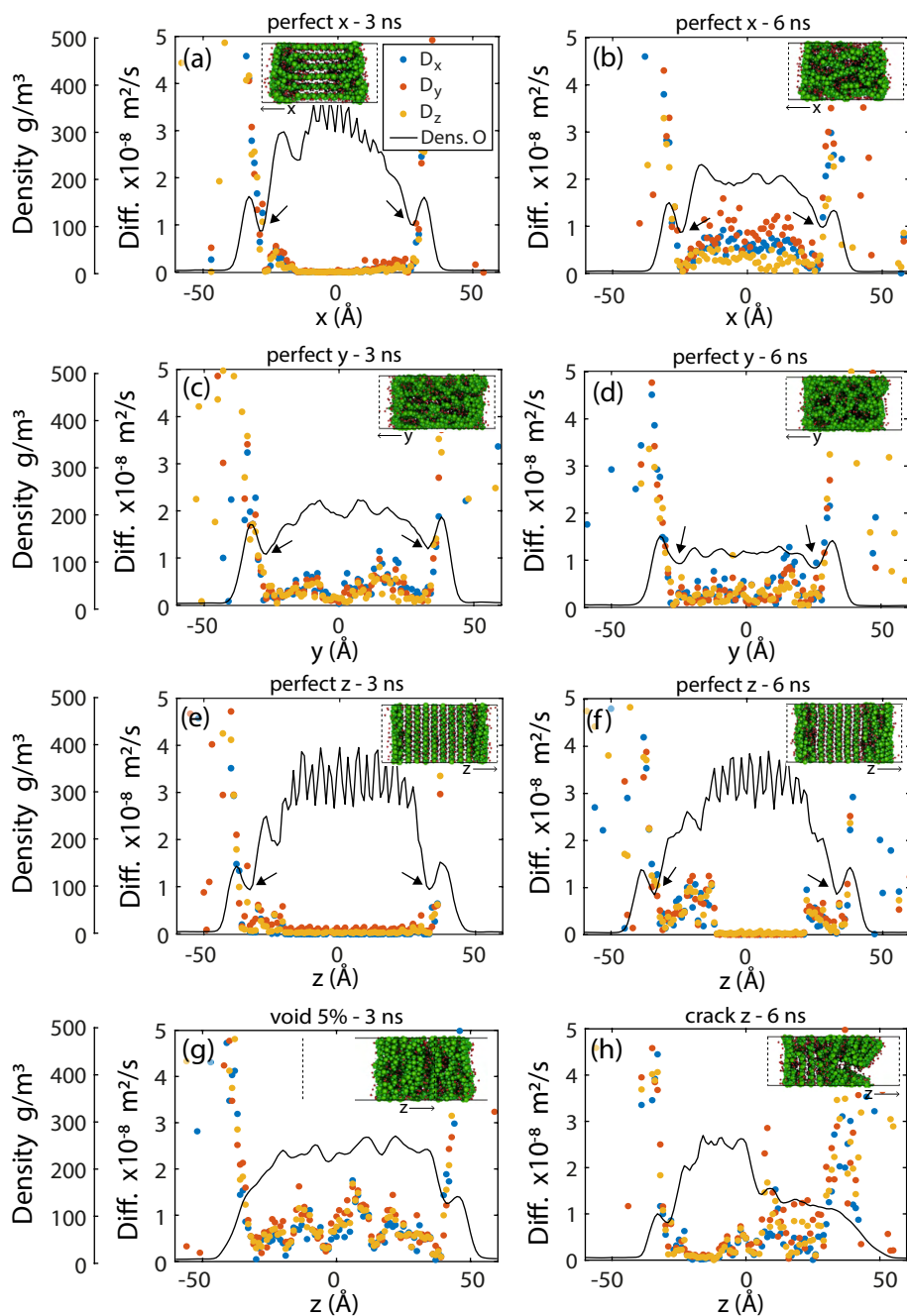


Figure 4.6: Diffusion coefficients for different dehydrated perfect (a-f) slabs, with 5% voids (g) or a crack in z-direction (h), as shown in Figure 4.4. The blue dots represents the diffusion in x-direction, the red dots represents the diffusion in y-direction, the yellow dots represents the diffusion in z-direction, in a 5  $\text{\AA}$  bin. The solid black line is the oxygen density, which is used to compute the PME.

m<sup>2</sup>/s. The very low/no H<sub>2</sub>O mobility in CaCl<sub>2</sub>·2H<sub>2</sub>O at 300 K corresponds with values found for the MgCl<sub>2</sub> · nH<sub>2</sub>O ( $n = 1, 2, 4, 6$ ) TCM, for which Pathak et al. [100] found diffusion coefficients in the order of  $10^{-11} - 10^{-10}$  m<sup>2</sup>/s. Additionally, Huinink et al. [53, 216] even found pinned (not diffusing) H<sub>2</sub>O in MgCl<sub>2</sub> · nH<sub>2</sub>O ( $n = 4, 6$ ) crystals.

The frames of Figure 4.4, indicated with a × after 3 and 6 ns of dehydration at 500 K, are used as input for new MD simulations for the diffusion calculations. The resulting diffusion profiles over the perfect slabs are given in Figure 4.7a-f. The imperfect (5% voids and artificially applied crack in z-direction) are simulated after 3 ns of dehydration at 500 K. The resulting diffusion profiles over the imperfect slabs are given in Figure 4.7g and h. For all systems, the center of mass was kept at the origin during the simulation to correct for evaporating H<sub>2</sub>O molecules, which otherwise cause a slow drift of the slab. In the Figures, the dots represent the computed diffusion coefficient with a 2.5 Å radius ( $\frac{1}{2} \times$  bin width) around that location. The solid black line represents the oxygen density profile which is used to obtain the PMF and approximated to be linear over the bins for the analytical solution of the Smoluchowski diffusion equation. Once more, from Figure 4.7, very low diffusion coefficients ( $< 10^{-10}$  m<sup>2</sup>/s) can be observed for the parts of the slabs which are still in a crystalline structure. These crystalline areas are clearly visible by the density profiles in Figure 4.7a, e, and f (perfect crystal with vacuum in x-direction at 3 ns; perfect crystal with vacuum in z-direction at 3 ns; and perfect crystal with vacuum in z-direction at 6 ns, respectively). The corresponding crystal structures can be found in Figure 4.4b and d. The other systems are found in a disordered state at the moments of the diffusion calculation. These disordered structures contain an inner region with some larger pores filled with H<sub>2</sub>O, and disordered CaCl<sub>2</sub> layers at the outer regions of the slab with some smaller pores (as shown in Figure 4.4). For the inner region, the diffusion coefficients are in the range from  $10^{-9}$  to  $10^{-8}$  m<sup>2</sup>/s. In the outer regions, a lower oxygen density can be observed as indicated with the black arrows in Figure 4.7, correlated to the dens CaCl<sub>2</sub> layers. In these outer regions, the diffusion also decreases slightly compared to the inner regions. At the surface, on top of the slab, a large increase in diffusion can be observed, corresponding to the free water molecules diffusing over the surface of the slab.

The diffusion profiles of the imperfect slabs, in z-direction at 500 K, are given in Figure 4.7g and h. From Figure 4.4, it was already observed that the system with 5% voids dehydrated much faster than the other structures. This is confirmed by the diffusion profile, in which diffusion coefficients around  $10^{-8}$  m<sup>2</sup>/s can be observed. Additionally, the CaCl<sub>2</sub> layers in z-direction can be observed from the local dips in the diffusion profile. However, due to the voids, the slab keeps dehydrating fast over the entire slab. For the system with the artificially crack, the crack was only over half of the slab (the region for  $z > 0$  in Figure 4.7h). In the part without the crack ( $z < 0$ ) the diffusion is low due to the strong crystalline structure. In the region with the crack, a high diffusion, above  $10^{-8}$  m<sup>2</sup>/s, can be found. A strongly increasing diffusive behavior towards the salt hydrate surface [100], or crystal voids [135] was also found by Pathak et al. for MgCl<sub>2</sub> · nH<sub>2</sub>O systems. For all studied systems, there was not a preferred direction for diffusion despite the strong anisotropic structure. It is plausible that there is an anisotropic effect for the crystalline structure, however, due to the low diffusion, the distinction cannot be made in this work. The regions with high diffusion are the disordered regions, which does re-

sult in isotropic diffusion behavior.

## 4.5. CONCLUSIONS

This work was motivated to better understand the effects of imperfections like cracks and pores in salt hydrates on the diffusion of water through the material. It has been experimentally observed that such a crack significantly changes the (de)hydration rates of the salt [177]. Insights in the diffusion are therefore crucial for an optimized design regarding thermochemical storage applications with salt TCMs. To accurately obtain the diffusion coefficients of water in confined or inhomogeneous regions, like pores and cracks in salt hydrates, a method was constructed based on the Smoluchowski diffusion equation [207]. This equation is used for small bins around the area of interest and can be analytically solved with the assumption of a linear density profile over these bins [205].

The results show that the diffusion at 300 K in the crystalline structure of  $\text{CaCl}_2 \cdot 2\text{H}_2\text{O}$  is very low  $< 10^{-10} \text{ m}^2/\text{s}$ , which is comparable with values found for  $\text{MgCl}_2 \cdot n\text{H}_2\text{O}$  ( $n = 1, 2, 4, 6$ ) [53, 100, 216]. At these temperatures, the dehydration is also found to be low [131], compared to a temperature of 500 K. To investigate the effects of cracks and pores on the diffusion, both perfect and imperfect  $\text{CaCl}_2 \cdot 2\text{H}_2\text{O}$  slabs were dehydrated. From the dehydration, in x- and y-direction, water was easily able to evaporate and pores filled with water were found for these (partly) dehydrated structures. In z-direction,  $\text{CaCl}_2$  layers impede dehydration. The impeding effect of  $\text{CaCl}_2$  layers is strongly reduced when pores or voids are present. At different moments of the dehydration, the structures were re-simulated in an MD–NVT ensemble to create atomic trajectories for the diffusion calculation. The diffusion is computed for these systems, at every Ångstrom with 5 Å bins, by fitting the analytical solution of the survival probability of the Smoluchowski equation to the survival probability obtained by MD.

The parts of the slab that remained crystalline were found to have a low diffusion ( $< 10^{-10} \text{ m}^2/\text{s}$ ). In imperfect regions, like amorphous areas, cracks, and voids, the diffusion is significantly higher (at least one order of magnitude). The deformed regions by dehydration of the  $\text{CaCl}_2 \cdot 2\text{H}_2\text{O}$  slab were found to have a diffusion coefficient in the order of  $10^{-9}$  to  $10^{-8} \text{ m}^2/\text{s}$ . An isotropic diffusion behavior was found for these deformed regions, and the dried anhydrous top  $\text{CaCl}_2$  layers reduced the diffusion near the surface. Both the artificially created voids and crack in the crystal structures caused quick deformation of the crystalline slab into a deformed slab and significantly increased the dehydration and diffusion.

The results indicate that in bulk TCM, the diffusion of water through the materials is likely dictated by the imperfections in the polycrystalline bulk material. These imperfections would positively affect the salt's kinetics and (de)hydration rates, thereby improving the power output of a potential thermochemical heat storage system.

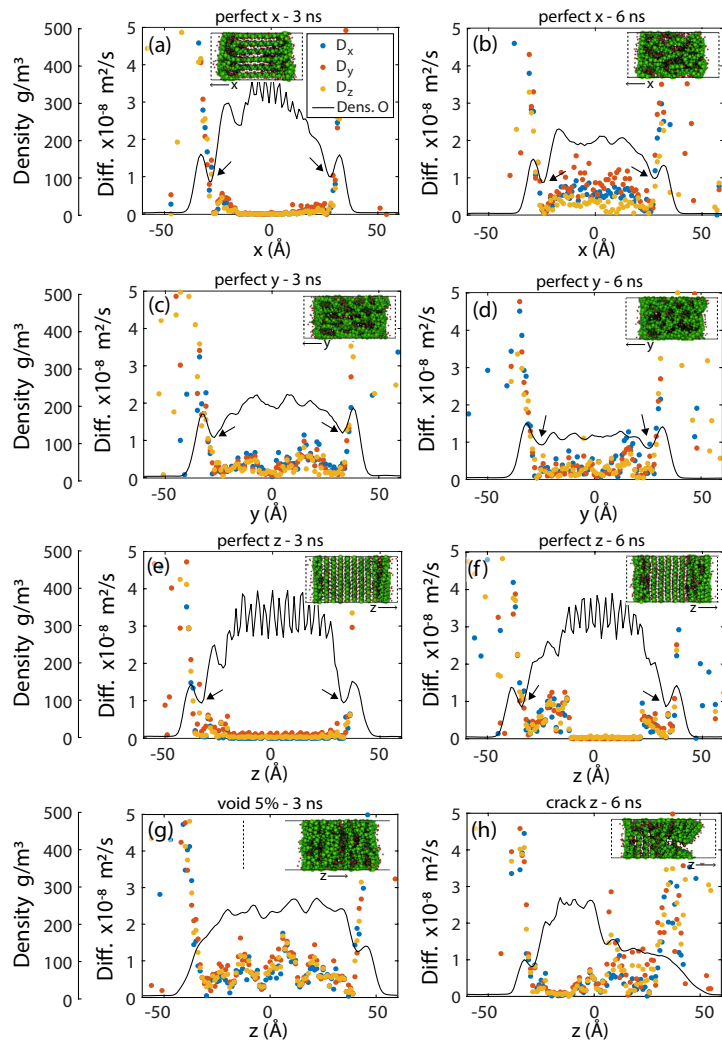


Figure 4.7: Diffusion coefficients for different dehydrated perfect (a-f) slabs, with 5% voids (g) or a crack in z-direction (h), as shown in Figure 4.4. The blue dots represents the diffusion in x-direction, the red dots represents the diffusion in y-direction, the yellow dots represents the diffusion in z-direction, in a 5 Å bin. The solid black line is the oxygen density, which is used to compute the PME.



# 5

## REAXFF FOR VAPOR–LIQUID EQUILIBRIUM

*The whole is simpler than its parts.*

attributed to Josiah Willard Gibbs

**ABSTRACT:** Absorption and reactive properties of fluids in porous media are key to the design and improvement of numerous energy related applications. Molecular simulations of these systems require accurate force fields that capture the involved chemical reactions and have the ability to describe the vapor–liquid equilibrium (VLE). Two new reactive force fields (ReaxFF) for CO<sub>2</sub> and H<sub>2</sub>O are developed, which are capable of not only modeling bond breaking and formation in reactive environments but also predicting their VLEs at saturation conditions. These new force fields include extra terms (ReaxFF–lg) to improve the long-range interactions between the molecules. For validation, we have developed a new Gibbs ensemble Monte Carlo (GEMC–ReaxFF) approach to predict the VLE. Computed VLE data show good agreement with National Institute of Standards and Technology reference data as well as existing nonreactive force fields. This validation proves the applicability of the GEMC–ReaxFF method to test new reactive force fields, and simultaneously it proves the applicability to extend newly developed ReaxFF force fields to other more complex reactive systems.

---

This chapter is published as peer reviewed article: Heijmans, K., Tranca, I.C., Smeulders, D.M.J., Vlucht, T.J.H. and Gaasstra-Nedea, S.V., Gibbs Ensemble Monte Carlo for Reactive Force Fields to Determine the Vapor–Liquid Equilibrium of CO<sub>2</sub> and H<sub>2</sub>O. *Journal of Chemical Theory and Computation*, 17(1), 322–329 (2021)

## 5.1. INTRODUCTION

In past decades, porous media such as metal–organic frameworks (MOFs), zeolitic imidazolate frameworks (ZIFs), and zeolites were intensively studied in combination with  $\text{H}_2\text{O}$  and  $\text{CO}_2$  [217–221]. These studies have aimed to tackle challenges in many energy related applications such as water-splitting [217], sorption heat storage [18],  $\text{CO}_2$  capture and sequestration [218, 219, 222], photoreduction [220, 221], separation of natural gas mixtures [223], and syngas production [224]. Within these fields, molecular simulations are frequently used to predict thermodynamic and kinetic properties [100, 135, 219, 222, 223, 225]. Molecular simulation is a useful tool for areas which are difficult or cumbersome to study using experimental approaches, and simultaneously offers fundamental insights on the underlying physics of the simulated system on micro/nanoscale [63, 226, 227].

The essential step for the successful use of molecular simulations is the development of a reliable force field, which is responsible for capturing relevant molecular interactions. Accurate force fields are required to reproduce the dynamic and static properties of a system. Furthermore, an important requirement for molecular studies of fluids in porous media is the correct description of the vapor–liquid equilibrium (VLE) by the force field [99, 228]. Numerous classical force fields have been developed, e.g. TIP4P/2005 [229] for  $\text{H}_2\text{O}$  and TraPPE [230] for  $\text{CO}_2$ . By using such a force field, important properties such as the adsorption and diffusion of fluids in porous media [95, 100, 225], and thermal behavior [69, 100] of materials can be predicted.

Classical force fields contain empirically based interatomic potentials to compute the energy between atoms based on their positions. The classical approximation is well-suited for noncovalent interactions between atoms, such as Coulombic, van der Waals, and angle-strain interactions. In practice, fitting the nonreactive classical force field parameters to the experimental VLE is often the first and most important step [99, 228]. It is important to note that chemical reactions often cannot be described with these classical force fields. This is a serious limitation, as many of the previously mentioned applications include at some point chemical reactions of  $\text{H}_2\text{O}$  and/or  $\text{CO}_2$ .

Simulations that take into account the electronic structures of atoms, such as Density Functional Theory (DFT), can be used to describe chemical reactions. The downside of DFT approaches is the computational cost, and therefore these simulations are limited to small systems and short time scales.

Reactive force fields (ReaxFF), developed by van Duin et al. [81, 82] aim to bridge the gap between DFT and classical force fields. The interatomic ReaxFF potentials are empirically based, such as the classical force fields, thereby gaining computational advantages compared to DFT. Besides the conventional classical interaction potentials, connection-dependent/bond-order potentials [119] are included. The connection dependent potentials allow ReaxFF to capture chemical reactions and open the way to model the dynamics of more complex multiphase processes, [119] without the need for expensive DFT calculations. Despite the importance of reactive force fields, to the best of our knowledge, there is no available ReaxFF force field which is able to accurately capture simultaneously the liquid, vapor, and transition phases of  $\text{H}_2\text{O}$  and  $\text{CO}_2$ . In this work, we parametrized two new ReaxFF force fields, one for  $\text{H}_2\text{O}$  and one for  $\text{CO}_2$ , and used these to predict the VLEs of these specific systems.



For the parametrization of ReaxFF, most often DFT data is used as a reference. Both methods focus at first instance on short-range interactions in order to capture the (short-range) chemical reactions. This causes a less accurate description of the long-range interactions in the simulated system. It is well-known that long-range dispersion interactions are crucial for an accurate description of VLEs [63]. In basic DFT, extra corrections are available, such as the DFT-D method of Grimme et al. [150] and the low-gradient (lg) method of Liu et al. [231], to include these long-range dispersion interactions. The dispersion correction in DFT studies resulted in significantly improved descriptions of liquids at saturation conditions, and predicted more accurate liquid properties [232, 233]. Similar to the lg method, Liu et al. developed an analogous extension for standard ReaxFF, named ReaxFF-lg [234]. This is a more sophisticated approach than basic ReaxFF due to the inclusion of the long-range London dispersion interactions, and it prevents modifications of the existing short-range (reactive) interactions. Here, we used this ReaxFF-lg methodology for the new force fields in order to correct for these long-range interactions. This enables the accurate reproduction of the phase diagrams for both H<sub>2</sub>O and CO<sub>2</sub>, and at the same time preserve the reactive properties.

The Gibbs ensemble Monte Carlo (GEMC) method is a comprehensive method to predict the VLE [63, 226, 227] and has been used for many nonreactive systems [223, 230, 235, 236]. Accordingly, a new GEMC-ReaxFF method was developed to be used to study VLEs in combination with reactive systems. Our GEMC-ReaxFF approach allowed us to validate the new ReaxFF-lg H<sub>2</sub>O and CO<sub>2</sub> force fields. The results were compared with experimental National Institute of Standards and Technology (NIST) reference data [237, 238], confirming the ability of the GEMC-ReaxFF method to predict equilibria in reactive systems.

## 5.2. METHODOLOGY

Two new ReaxFF force fields were developed, for H<sub>2</sub>O and CO<sub>2</sub>, which allows the study of these fluids in reactive systems. To validate the new force fields, their VLEs were studied using a new method which was designed to combine the reactive force field molecular dynamics approach with Gibbs ensemble Monte Carlo [63, 226, 227] (ReaxFF-GEMC). In the following sections, the ReaxFF, ReaxFF training, and GEMC methods are explained.

### 5.2.1. REAXFF

The mathematical formulation that describes the forces between particles is called a force field. Force fields describe different kinds of interactions between atoms, which together add up to the potential energy of the system. When only classical forces are described, the force field is considered as a classical or nonreactive force field. Typically, the classical formulation of the van der Waals interactions is described by a Lennard-Jones potential, and an electrostatic force is described by Coulomb terms [229, 230], which are respectively the first and second terms on the right-hand side of the following equation for the total interaction potential between atoms  $i$  and  $j$ :

$$U(r_{ij}) = 4\epsilon_{ij} \left[ \left( \frac{\sigma_{ij}}{r_{ij}} \right)^{12} - \left( \frac{\sigma_{ij}}{r_{ij}} \right)^6 \right] + \frac{q_i q_j}{4\pi\epsilon r_{ij}} \quad (5.1)$$

where  $r_{ij}$  is the interatomic distance;  $\epsilon_{ij}$ ,  $\sigma_{ij}$ ,  $q_i$ , and  $q_j$  are parametrized values of the Lennard-Jones energy parameter, Lennard-Jones size parameter, and partial charges for atoms  $i$  and  $j$ , respectively.  $\epsilon$  is the electric constant. In classical force fields, bonds within molecules are typically considered as rigid [229, 230] or described with harmonic terms. This is a practical approach that simplifies the force field and speeds up simulations, and when applied to a nonreactive region it does not result in major accuracy losses. However, when one is interested in a region where chemical reactions can occur, these classical force fields fail because the intramolecular bonds cannot be broken. The reactive force field method (ReaxFF) [81, 82] aims to solve this problem by including bond breaking and formation terms. ReaxFF has proven its success for a wide range of reactive dynamics [119], which were studied without requiring expensive DFT dynamics.

Similar to classical force fields, the ReaxFF potential is a summation of different energy terms:

$$E_{\text{system}} = E_{\text{vdW}} + E_{\text{Coul}} + E_{\text{bond}} + E_{\text{val}} + E_{\text{pen}} + E_{\text{under}} + E_{\text{over}} + E_{\text{tors}} + E_{\text{conj}} + E_{\text{others}}. \quad (5.2)$$

5

The nonbonded terms  $E_{\text{vdW}}$  and  $E_{\text{Coul}}$  are respectively the van der Waals, and Coulomb contributions, which are considered between all atoms. The van der Waals interaction are described with a distance-corrected Morse-potential, and the Coulomb interactions with a shielded Coulomb potential. The atomic charges are described with the Electron Equilibration Method [127, 239]. The  $E_{\text{bond}}$  term accounts for the bond energy of the  $\sigma$ ,  $\pi$ , and  $\pi\pi$ -bonds, and is directly related to interatomic distances. When atoms are bonded, the intramolecular terms  $E_{\text{under}}$ ,  $E_{\text{over}}$ ,  $E_{\text{val}}$ ,  $E_{\text{tors}}$ ,  $E_{\text{pen}}$ , and  $E_{\text{conj}}$  can be used to correct for under- and over-coordination, valence and torsion angle terms, "penalty" energies, and conjugated systems, respectively. The  $E_{\text{others}}$  term can be added to include other interactions such as H-bonds. A more detailed explanation of these different terms can be found in the original paper of van Duin et al. [81] It is important to note that the interatomic potentials are described in such a way that they are independent of the environment of the atom, which is required to allow chemical reactions (e.g., there is no difference between hydrogen atoms in  $\text{H}_2$ ,  $\text{H}_2\text{O}$ , or a  $\text{MgH}_2$  crystal).

To accurately capture the VLEs, long-range interactions play a key role [63, 232, 233]. This is reflected in the practical assumption of using nonreactive classical force fields in most GEMC simulations. In the ReaxFF potential, long-range van der Waals interactions ( $E_{\text{vdW}}$ ) are captured using a Morse potential, including a short-range repulsive part for the Pauli repulsion and a long-range attractive part for the van der Waals attractions. Historically, the main focus of ReaxFF is the short-range intramolecular dynamics, therefore, the Morse potential parameters are rather focused on these short-range interactions than the long-range ones. Most training of ReaxFF is based on Density Functional Theory (DFT), which suffers from similar phenomena. To adequately capture the long-range London dispersion interactions, standard DFT does not rely on first-principle methods, but uses empirical methods, such as the DFT-D method of Grimme et al. [150] and the low-gradient (lg) method of Liu et al. [231]. To solve this issue for ReaxFF, an extended method (ReaxFF-lg) was developed by Liu et al., [234] to improve the description of long-range interactions of ReaxFF. This method adds an extra term to the ReaxFF potential which is analogous to the low-gradient part for DFT. By adding

this extra term for the long-range interactions, an extensive refitting of the original vdW parameters in the Morse potential is avoided. Thereby, the original short-range reactive interactions remain intact, and a transferability similar to that for the original force field can be expected regarding chemical reactions. The additional lg term of the long-range interactions scales with  $1/r_{ij}^6$ :

$$E_{lg} = - \sum_{i,j,i < j}^N \frac{C_{lg,ij}}{r_{ij}^6 + dR_{eij}^6} \quad (5.3)$$

where  $C_{lg,ij}$  is the dispersion energy correction between atoms  $i$  and  $j$ .  $R_{e,ij}$  is the equilibrium vdW radius between the atoms, and  $d$  is a scaling factor. The vdW radii are taken from previous a study [234] based on the Universal force field (UFF) [240].

### REAXFF PARAMETRIZATION

To develop new reactive force fields for CO<sub>2</sub> and H<sub>2</sub>O, two existing force fields were used as the starting point. The ReaxFF developed by Chenoweth et al. [82] for the simulation of hydrocarbon oxidation was chosen as the starting point for the new ReaxFF-lg for CO<sub>2</sub>. The ReaxFF developed by Pathak et al. [100] for the simulation of salt hydrates was chosen as the starting point for the new H<sub>2</sub>O ReaxFF-lg, which fundamentally showed an accurate description of water at different temperatures[241]. These original force fields have already proved their ability to correctly describe chemical reactions [82, 100]. However, as a consequence of their focus on hydrocarbon oxidation and chemical bonding in salt hydrates, these force fields lack the ability to accurately predict the VLE. An example of the different contributing long-range energies, for the different nonreactive and reactive force fields, will be shown and discussed in Figure 5.2 of the Results section.

To (re-)parametrize some of the force field parameters, such as the newly added lg parameters, the Metropolis Monte Carlo (MMC) force field optimizer was used, which has proved itself for multiple force fields [40, 83, 100]. The MMC optimizer, developed by Iype et al. [83], is a high-dimensional and efficient training method, based on the simulated annealing Metropolis algorithm [128, 242–244], and aimed to minimize the cumulative error between a data set and the predicted results by ReaxFF:

$$\text{Error}_{\text{new}} = \sum_{i=1}^n \left[ \frac{X_{\text{ref},i} - X_{\text{ReaxFF},i}}{\sigma_i} \right]^2. \quad (5.4)$$

with  $X_{\text{ref},i}$  as the reference data (e.g., charges, energies, distances, heat of formation),  $X_{\text{ReaxFF},i}$  as corresponding estimated values by ReaxFF, and a weighting factor  $\sigma_i$  for each data point  $i$ . The MMC optimizer searches the global minimum of the cumulative squared error, by modifying each iteration a random fraction of some selected parameters in a random direction. After each modification,  $\text{Error}_{\text{new}}$  is calculated with the modified parameters, and the new force field is accepted according:

$$P = \min \left[ 1, \exp^{-\beta(\text{Error}_{\text{new}} - \text{Error}_{\text{old}})} \right]^2. \quad (5.5)$$

$\beta$  is the reciprocal of the thermodynamic temperature  $\beta = 1/(k_B T)$ ,  $k_B$  is the Boltzmann constant, and  $T$  is the artificial temperature. If the modifications are accepted,  $\text{Error}_{\text{new}}$  becomes  $\text{Error}_{\text{old}}$ .

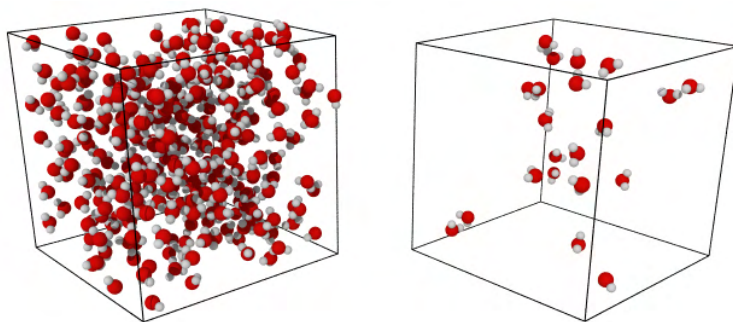


Figure 5.1: Example of liquid and gas boxes of a GEMC simulations. Besides thermalization, the two boxes can exchange molecules and volume.

## 5

As training data sets, for both force fields, multiple reference configurations were used. For intramolecular interactions, the ADF software package [187] was used to generate reference data, and single gas molecules were fully relaxed to establish bond lengths, bond angles, and charges. The reference molecule for the prediction of charges was equilibrated at every iteration of the MMC optimizer. To improve the long-range interactions, e.g. the newly added ReaxFF-lg parameters, reference configurations were generated by the TraPPE [230] ( $\text{CO}_2$ ) and TIP4P/2005 [229] ( $\text{H}_2\text{O}$ ) classical force fields, due to their accurate description of VLEs [230, 236]. This set of reference configurations consisted of multiple sets of controlled trajectories of dimers, MD trajectories of near dimers, and MD trajectories at different densities spanning the entire saturation density. A representation of the training dataset is given in Appendix E. The MMC optimizer ran multiple times, up to 20000 iterations, with a slowly decreasing simulated annealing temperature, and including some final iterations to minimize the best generated set of parameters. The target acceptance rate was set to 10%, with a maximum acceptance rate of 70%.

### 5.2.2. GIBBS ENSEMBLE MONTE CARLO

The Gibbs ensemble Monte Carlo (GEMC) algorithm is a method for the direct simulation of gas–liquid phase coexistence, and was first introduced by Panagiotopoulos et al. [226, 227]. GEMC simultaneously models the gas and liquid phases in two different simulation boxes, as shown in Figure 5.1. Both boxes start with a given number of molecules, a given volume, and thus a given density. During the simulation, molecules and volume are exchanged between the two boxes. One box will equilibrate to the gas phase and the other to the liquid phase. As a result, the phase coexistence of a fluid is modeled, at a given temperature and pressure, without an interfering interface between the phases. The Gibbs ensemble provides accurate coexistence densities for relatively small systems, provided that one is not too close to the critical point [63].

The basic GEMC algorithm includes three types of trial moves, from which every cycle one will be randomly selected. The combination of these three trial moves allows the sampling of the entire phase space. Besides trial moves for thermalization, trial moves to exchange molecules and volume between the boxes are carried out. After each trial move the new energy of the total system is calculated, and on the basis of the acceptance

rules (eqs 5.6, 5.7) the trial move is accepted or rejected. The probability for accepting a molecule exchange (e.g., remove from box 1 and insert in box 2) is given by [63]:

$$\text{acc}(o \rightarrow n) = \min \left[ 1, \frac{n_1(V - V_1)}{(N - n_1 + 1)V_1} \exp(-\beta[U_n - U_o]) \right] \quad (5.6)$$

where  $N$ ,  $n_1$ ,  $V$ , and  $V_1$  are the total number of molecules, number of molecules in box 1, total volume, and the volume of box 1 respectively.  $U_n$  and  $U_o$  are the new and old potential energies of the simulation boxes.  $\beta$  is the reciprocal of the thermodynamic temperature  $\beta = 1/k_B T$ , where  $k_B$  is the Boltzmann constant and  $T$  is the absolute temperature.

The probability for accepting volume exchange between the two boxes is given by [63]:

$$\text{acc}(o \rightarrow n) = \min \left[ 1, \left( \frac{V_{n,1}}{V_{o,1}} \right)^{n_1+1} \times \left( \frac{V - V_{n,1}}{V - V_{o,1}} \right)^{N-n_1+1} \exp(-\beta[U_n - U_o]) \right] \quad (5.7)$$

During the GEMC simulation, the total number of molecules  $N$  and the total volume  $V$  remain constant.

For thermalization trial moves, one can perform Monte Carlo trial moves and translate/rotate each molecule separately. Based on the energy change ( $U_n - U_o$ ) the thermalization is accepted or rejected. For convenience, we chose to perform a thermalization of all molecules in a single trial move by using a Molecular Dynamics (MD) algorithm. The MD is performed in the NVT ensemble with a Nosé–Hoover thermostat and a Velocity Verlet integration scheme, using the SCM software package [187]. Each MD trajectory was performed for 625 fs, with a time step of 0.25 fs, which was sufficient to sample the system. The equilibrated NVT trajectory allowed us to accept every thermalization step and sample the entire phase space of the system.

The critical point of the VLE can be calculated using fitting with the law of rectilinear diameters [63]:

$$\frac{\rho_l + \rho_g}{2} = \rho_c + A \left( 1 - \frac{T}{T_c} \right), \quad (5.8)$$

where  $\rho_l$ ,  $\rho_g$ , and  $\rho_c$ , are the liquid, gas, and critical density.  $T$  and  $T_c$  are the temperature and critical temperature. The density difference of the phases can be fitted to a scaling law:

$$\rho_l - \rho_g = B \left( 1 - \frac{T}{T_c} \right)^\gamma, \quad (5.9)$$

with  $\gamma$  as the critical exponent, which is  $\gamma = 0.32$  for 3D systems. The parameters  $A$  and  $B$  are obtained from the fit.

## 5.3. RESULTS

### 5.3.1. REAXFF-LG<sub>CO2</sub> & REAXFF-LG<sub>H2O</sub> VALIDATION

The MMC force field optimizer [83] was used to parametrize the new ReaxFF force fields. The scaling factor for the long-range interactions was set to  $d = 1$ , according to Liu et al. [234]. Hence, regarding the long-range interactions, only the  $C_{lg,ij}$  need to be fitted.

Table 5.1: ReaxFF-lg parameters of the new ReaxFF-lg CO<sub>2</sub> and H<sub>2</sub>O force fields.

Force field	Atom	$R_e$ (Å)	interaction	$C_{lg}$ (kcal/mol·Å <sup>6</sup> )
H <sub>2</sub> O	O	1.75	O-O	142.9733
CO <sub>2</sub>	C	1.9255	C-C	249.5817
	O	1.75	O-O	14.9286
			O-C	127.1788

Table 5.2: The predicted ReaxFF molecular parameters for the original and new force fields for CO<sub>2</sub> and H<sub>2</sub>O.

CO <sub>2</sub>				
		orig. ReaxFF [82]	ReaxFF-lg <sub>CO2</sub>	TraPPE [230]
bond distance (Å)	C-O	1.18	1.19	1.16
bond angle (deg)	O-C-O	180	180	180
Charge ( <i>e</i> )	C	+0.459	+0.693	+0.70
	O	-0.244	-0.346	-0.35

H <sub>2</sub> O				
		orig. ReaxFF [100]	ReaxFF-lg <sub>H2O</sub>	TIP4P/2005 [229]
bond distance (Å)	O-H	0.948	0.974	0.9572
bond angle (deg)	H-O-H	102.4	102.6	104.5
charge ( <i>e</i> )	O	-0.619	-0.648	-
	H	+ 0.310	+0.324	+0.5664
	M	-	-	-1.1328

The resulting parameters are listed in Table 5.1, and full details on the new force fields are provided in Appendix E. Detailed results from the parametrizations, and comparisons between the different potentials, can also be found in Appendix E.

The resulting intramolecular geometric parameters and partial charges of the new ReaxFF-lg are shown in Table 5.2, for CO<sub>2</sub> and H<sub>2</sub>O. The bond distances and angles from ReaxFF-lg follow from a geometry optimization, and are compared with the descriptions from the classical force fields [229, 230]. For these classical force fields, the bond angles and distances are fixed. The negative charge of the TIP4P/2005 water molecule is located at the fourth interaction site, called M, which is coplanar to the O-H-O atoms, at a distance of 0.1546 Å from the oxygen atom. Within the ReaxFF format the atomic charges follow from the numerical charge calculations with the Electron Equilibration Method [127, 239]. As shown in the Table 5.2, the bond lengths and bond angles are in close agreement with the reference values.

Different contributing intermolecular energies are shown in Figure 5.2 for the separation of two parallel CO<sub>2</sub> molecules. The Figure shows close agreement among the nonreactive TraPPE force field [230], competent in the prediction of the VLE, the original ReaxFF force field [82], competent in the prediction of chemical reactions for hydrocarbon oxidation, and the new ReaxFF-lg force field as a competent combination of the two. The differences between the red dashed lines are caused by the reparametrization of the ReaxFF parameters corresponding to the charge calculation. The differences be-

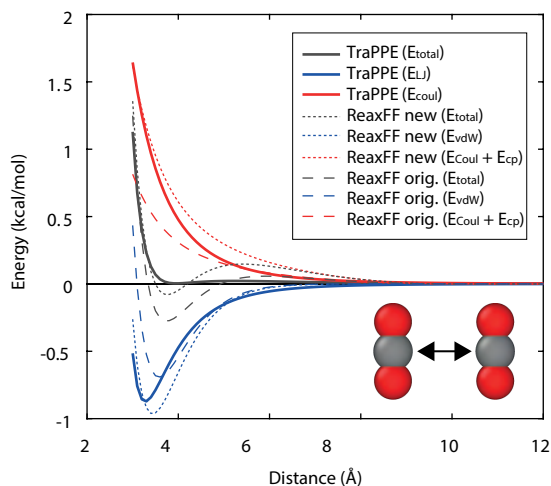


Figure 5.2: Comparison of different energy contributions regarding the dissociation of two parallel  $\text{CO}_2$  molecules. The gray lines represent the total energy. The blue line represents the Lennard-Jones energy contribution for the TraPPE force field and the van der Waals energy for the ReaxFF force fields. The red line represents the Coulomb energy contribution for the TraPPE force field and the summation of the Coulomb and polarization energy in the ReaxFF force fields. The orange line represents the DFT-D reference.

5

tween the blue dashed lines are caused by the added ReaxFF lg parameters. Both the van der Waals energy and Coulomb plus charge polarization energy increase in absolute value for the new ReaxFF-lg force field compared to the original ReaxFF force field. It is clear that our new ReaxFF force field more closely matches the nonreactive TraPPE force field, compared to the original ReaxFF, especially at smaller distances. Furthermore, the summation of all the different contributing energies, represented by the gray lines, is more balanced around 0 and shows a less deep well for the new ReaxFF-lg force field compared to the original. As a reference for the reactive component, the dimer interaction for two  $\text{CO}_2$  molecules, obtained by DFT-D, is added. For this reference the revPBE [245] exchange-correlation function is used, which is an improved version of the PBE functional regarding molecules. For the dispersion interactions, Grimme's latest dispersion correction D4 [246] was used. The DFT-D dimer reference acknowledges the well depth for the ReaxFF force fields. Note that figure 5.2 is a simplification of the system as only one of the infinite possibilities of  $\text{CO}_2$  dimer interactions is considered. In Appendix E other dimer interactions, also used in the parametrization, can be found. Furthermore, for the DFT reference many different exchange-correlation functions and dispersion corrections can be used [247, 248] which could result in different curves.

The new ReaxFF-lg  $\text{CO}_2$  and  $\text{H}_2\text{O}$  force fields are tested, using MD, at coexistence conditions starting from a random initial configuration, and are equilibrated at temperatures just below their critical temperatures (at 260, and 280 K for  $\text{CO}_2$ , and at 580, and 600 K for  $\text{H}_2\text{O}$ ). The resulting average density distributions (over 25 ps) are shown in figure 5.3. From these figures, it is clear that the boxes equilibrate in partly liquid and partly gas phases. The overall plateaus of the density profiles (solid lines) are in the same range



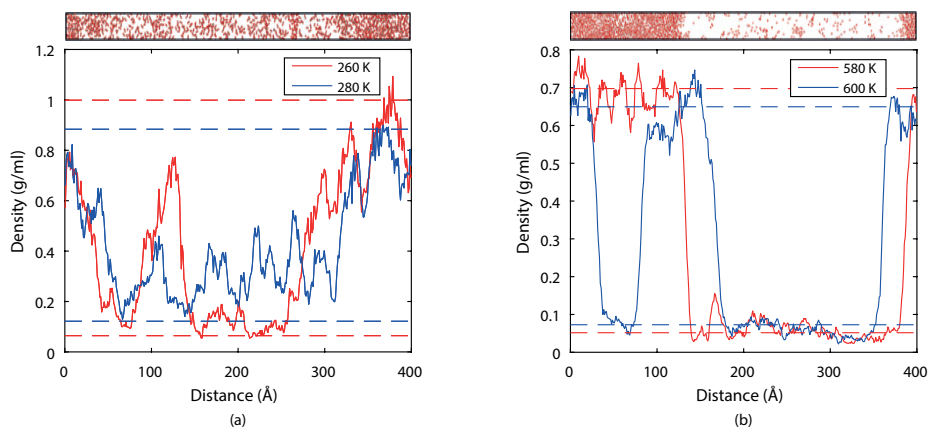


Figure 5.3: Average density distributions of the simulation boxes of (a) CO<sub>2</sub> and (b) H<sub>2</sub>O after MD simulation. The red solid and dashed lines are the simulation results and the experimental coexistence densities [237, 238] for the lower temperatures, respectively. The blue solid and dashed lines are the simulation results and the experimental coexistence densities for the higher temperatures, respectively. The top boxes are representations of the final configurations at 280 and 580 K for CO<sub>2</sub> and H<sub>2</sub>O, respectively.

5

as experimental coexisting densities (dashed lines). The of formation the gas and liquid phases, separated by an interface, is typically slow due to diffusion of the molecules. Eventually, the system will converge to a two-phase system.

### 5.3.2. GEMC–REAXFF VALIDATION

To test the GEMC–ReaxFF approach, two simulations for H<sub>2</sub>O were performed at 580 and 600 K with the new ReaxFF-Ig force field. The resulting densities of the simulation boxes are shown in figure 5.4 and compared with the experimental results [238]. It is clearly shown that, during the initialization of the system, one box equilibrates to liquid density, and the other box equilibrates to gas density. Both densities are in good agreement with experimental values [238].

### 5.3.3. VLE WITH GEMC–REAXFF

Because of moving droplets and interface effects, it is cumbersome to obtain accurate predictions of coexistence densities of the gas and liquid phases from figures 5.3. With the use of a GEMC algorithm this is avoided, as each simulation box represents only liquid phase or only gas phase, and no interface is present between the phases. By use of the newly developed GEMC–ReaxFF method and force fields, we are able to determine the equilibrium phase diagram of H<sub>2</sub>O and CO<sub>2</sub>. After both the force fields and GEMC–ReaxFF code were validated (sections 5.3.1 and 5.3.2), their VLE was generated.

Each temperature was simulated with five different starting configurations. After equilibration, ensemble averages were taken for each simulation over 200000 Monte Carlo cycles, resulting in a total of 1000000 cycles per temperature. All long-range interactions are computed with a taper function in combination with a 10 Å cutoff radius. For the CO<sub>2</sub> simulations, a total of 300 molecules were used; for the H<sub>2</sub>O simulations, a



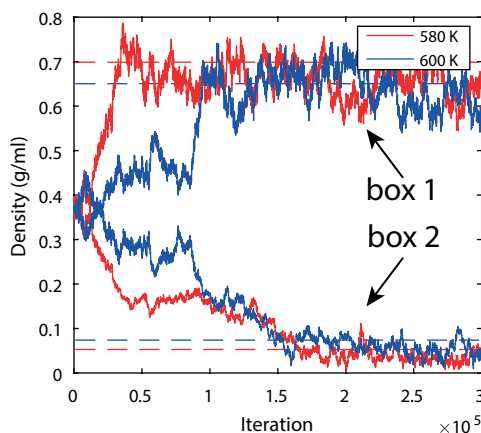


Figure 5.4: GEMC simulation of H<sub>2</sub>O at 580 and 600 K. The solid lines represent the densities of the two boxes simulated by the GEMC-ReaxFF, with red at 580 K and blue at 600 K. The dashed lines represent experimental coexistence data [238].

total of 320 molecules where used.

The CO<sub>2</sub> results are compared with the TraPPE [230] classical force fields. For these simulations the RASPA software package was used [129, 249], with 1000000 cycles, 156 molecules, a cutoff distance of 10 Å including analytic tail corrections, and the Lorentz–Berthelot mixing rules. The H<sub>2</sub>O results are compared with the TIP4P/2005 [229] classical force field, using 100000 cycles, 360 molecules, and a cutoff distance of 12 Å including analytic tail corrections. The corresponding VLEs for the different force fields are shown in figure 5.5.

As a reference, GEMC–ReaxFF calculations with the original ReaxFF force fields are included at a single temperature and a limited number of cycles. These results show the need for the (re)parametrization regarding the VLE. The original ReaxFF [82], aimed at hydrocarbon oxidations, converges the two boxes to similar densities at 280 K. Thereby, it underestimates the critical point, where its prediction can be even lower than 280 K. The original H<sub>2</sub>O ReaxFF [100] shows a similar behavior, underpredicts the critical temperature, and shows only a slight difference between the densities in the two simulation boxes at 600 K.

Except for the original ReaxFF force fields, the critical temperatures and densities for CO<sub>2</sub> and H<sub>2</sub>O are computed using eqs 5.8 and 5.9 and listed in Table 5.3. The critical temperatures of CO<sub>2</sub> are 300, 305, and 304 K for the new ReaxFF, the classical TraPPE force field [230], and experiments [237] respectively. The critical temperatures of H<sub>2</sub>O are 639, 645, and 647 K for the new ReaxFF, the classical TIP4P/2005 force field [229], and experiments [238] respectively. The critical densities of CO<sub>2</sub> are 0.50, 0.47, and 0.47 g/mL for the new ReaxFF, the classical TraPPE force field [230], and experiments [237] respectively. The critical densities of H<sub>2</sub>O are 0.30, 0.31, and 0.32 g/mL for the new ReaxFF, the classical TIP4P/2005 force field [229], and experiments [238], respectively. The ReaxFF force fields show excellent results, only with a few percentages deviation from the experi-

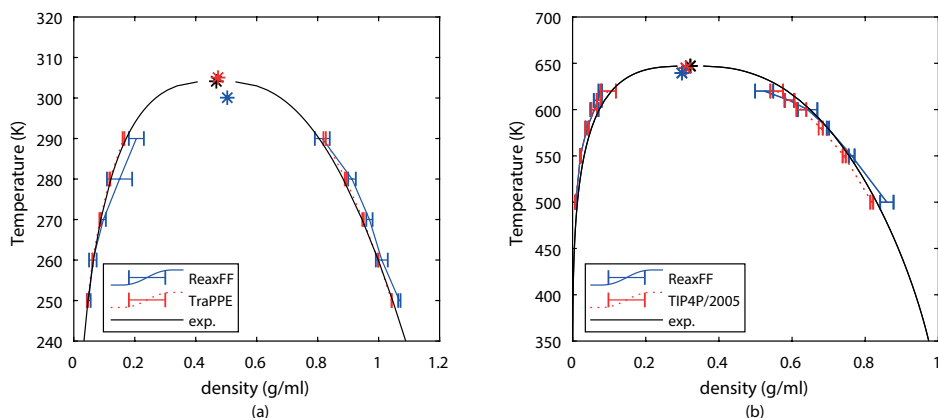


Figure 5.5: VLEs for (a)  $\text{CO}_2$  and (b)  $\text{H}_2\text{O}$ . The black lines represent the NIST reference data. The red lines represent the (a) TraPPE force field, and (b) TIP4P/2005 force field. The blue lines represent the predicted values by the new ReaxFF- $\text{lg}$  force fields. The orange results represent the predicted by the original (a)[100] (b)[82] ReaxFF. The asterisks are the computed critical points using eqs 5.8 and 5.9.

Table 5.3: Critical points of  $\text{CO}_2$  and  $\text{H}_2\text{O}$ .

$\text{CO}_2$			
	ReaxFF- $\text{lg}_{\text{CO}_2}$	TraPPE [230]	exp. [237]
$T_c$ (K)	300	305	304
$\rho_c$ (g/mL)	0.50	0.47	0.47

$\text{H}_2\text{O}$			
	ReaxFF- $\text{lg}_{\text{H}_2\text{O}}$	TIP4P/2005 [229]	exp. [238]
$T_c$ (K)	639	645	647
$\rho_c$ (g/mL)	0.30	0.31	0.32

ments. Moreover, the possibility is offered to include reactions in molecular simulations.

## 5.4. CONCLUSIONS

Two new reactive force fields were developed to capture the vapor-liquid equilibriums for  $\text{CO}_2$  and  $\text{H}_2\text{O}$ . Long-range dispersion interactions are key to accurately capturing the VLE with ReaxFF force fields. Therefore, an extended version of ReaxFF methodology, namely ReaxFF- $\text{lg}$ , was used for the newly developed force fields. The parameters were optimized by using accurate DFT and classical force field data and the MMC optimizer. MD simulations, at saturation conditions, showed the applicability of the newly developed force fields. Additionally, the new ReaxFF force fields were validated using the newly developed GEMC-ReaxFF method, and the VLEs for both liquids were computed. The GEMC-ReaxFF method shows an excellent agreement between the experimental

and the new ReaxFF VLEs. It is shown that ReaxFF-lg is capable of capturing both gas and liquid phases. The classical force fields from the literature slightly outperform the reactive force fields, but these classical force fields lack the applicability of capturing bond breaking and bond formation compared to the new ReaxFF force fields. The newly developed reactive force fields allow future studies on the effects of long-range interactions and chemical reactive events on fluid properties such as diffusion, surface tension, and viscosity. Additionally, the successful combination of GEMC and ReaxFF force fields allows the study of more complex systems such as binary systems for separation processes or loading of porous media with Grand-Canonical Monte Carlo simulations. These topics and implementations are not straightforward [99, 250, 251], and thereby outside the scope of this work. We feel that these are promising future research directions.



# 6

## REAXFF FOR HYDRATION CHARACTERISTICS OF SALTS

*Instead of choosing configurations randomly, then weighting them with  $\exp(-E/kT)$ , we choose configurations with a probability  $\exp(-E/kT)$  and weight them evenly.*

Metropolis et al. [128]

**ABSTRACT:** *The equilibrium temperature and pressure conditions are not always easy to predict for the salt hydrates. However, these conditions are crucial for the design of thermochemical heat storage systems. A biased Grand-Canonical Monte Carlo (GCMC) tool is developed, enabling the study of equilibrium conditions at the molecular level. The GCMC algorithm is combined with reactive force field molecular dynamics (ReaxFF), which allows bond formation within the simulation. The Weeks-Chandler-Andersen (WCA) potential is used to scan multiple trial positions for the GCMC algorithm at a small cost. The most promising trial positions can be selected for recomputation with the more expensive ReaxFF. The developed WCA-ReaxFF-GCMC tool was used to study the hydration of  $\text{MgCl}_2 \cdot n\text{H}_2\text{O}$ . The simulation results show a good agreement with experimental and thermodynamic equilibria for multiple hydration levels. The hydration shows that water, present at the surface of crystalline salt, deforms the surface layers and promotes further hydration of these deformed layers. Additionally, the WCA-ReaxFF-GCMC algorithm can be used to study other, non-TCM-related, reactive sorption processes.*

---

This chapter is accepted as peer reviewed article: Heijmans, K., Tranca, I.C., Chang, M.-W., Vlucht, T.J.H. Gaastra-Nedea, S.V. and Smeulders, D.M.J, Reactive Grand-Canonical Monte Carlo Simulations for Modeling Hydration of  $\text{MgCl}_2$  *ACS Omega* (2021)

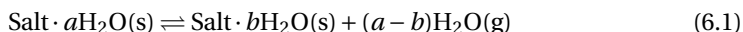
## 6.1. INTRODUCTION

Energy storage systems are a vital link in the sustainable energy infrastructure. Thermochemical energy storage can fulfill this essential link regarding thermal applications and is therefore widely studied [7, 18, 19, 21, 23]. Thermochemical energy storage is compelling because it can realize a relatively high thermal energy storage density and no thermal losses occur during storage [18]. The concept relies on a reversible endo-/exothermic chemical reaction between a sorbate ( $A$ ) and a sorbent ( $B$ ):



When there is a surplus of (thermal) energy, heat is used to separate material  $AB$  -via an endothermic reaction- into components  $A$  and  $B$ . These components are stored separately, and no energy dissipates during storage. In times of a lack in (thermal) energy, components  $A$  and  $B$  are combined and react -via an exothermic reaction- back to  $AB$ , releasing heat. The operation of the thermochemical energy storage is dictated by the given equilibrium conditions of the reaction as described by thermodynamics [28, 29].

Ideal thermochemical materials (TCMs) for such storage require high reaction energies between sorbate and sorbent, stability over many storage cycles, and a reaction equilibrium around desired operating temperatures and partial pressures of the sorbate. Salt hydrates are promising TCMs [11, 20, 169] for applications in the built environment because of the high sorption energy of water vapor and dehydration conditions, which are reachable by built environment climate systems. Their endo-/exothermic reversible chemical reaction of (de)hydration is described by:



Most common salts in their pure form suffer from drawbacks regarding their application as TCM [11, 20, 169]. For example, undesired irreversible side reactions which degrade the storage capacity [33, 40]; slow kinetics and low thermal conductivities [100], which decrease thermal in- and output power; a metastable zone around the equilibrium conditions [28, 29]; or the occurrence of undesired melting or deliquescence of the salts, which forms blocking agglomerates in the storage system. Deliquescence is the phenomenon of a water-soluble substance that absorbs so much water vapor from the atmosphere that the substance will dissolve in its own absorbed water. These drawbacks lower the stability and cyclability of the TCM and, thereby, the storage system.

Recently, much research focuses on enhancing pure salts to overcome the previously mentioned drawbacks - for example, a mixture of multiple salts [31], double salts [58, 130], encapsulation [43], composites [45], impregnation of salts in porous materials [47], or doping of pure salts [53, 54, 130]. For most common salts, the equilibrium conditions can be estimated from thermodynamic tables [252, 253]. However, due to the increased complexity of interacting elements that influence the equilibrium conditions, or missing thermodynamic tables for new enhanced salts, the reaction equilibrium description becomes increasingly complex compared to pure salts. As a result, the equilibrium can not always be described by simple thermodynamic rules without assumptions or educated guesses for unknown model parameters.

Molecular modeling could act as a solution; it can predict many material properties for these new complex TCMs. In this regard, quantum mechanical (QM) methods, such

as Density Functional Theory (DFT) as shown in Chapter 2, were used before to investigate chemical bonding between a new combination of sorbate and sorbent regarding heat storage systems, or to predict equilibrium conditions for gas-phase systems [60]. However, due to the high computational cost of QM simulations, it is limited to a relatively small number of atoms over a short time period. On a larger scale, force field-based Molecular Dynamics (MD) is a powerful method, which is computationally much cheaper and therefore applicable to much larger systems over a much longer time. However, when standard classical force fields are used, the ability to model bond breaking and formation like in DFT is lost. Thereby, the study of TCMs including reactions is not possible. This gap between quantum mechanical methods and MD, in terms of modeling bond formation and the required computational cost, is bridged by reactive force fields (ReaxFF) [81, 82, 124]. ReaxFF is able to model bond breaking and formation, but only at a slightly higher computational cost than nonreactive MD with classical force fields. As a result, ReaxFF has been used before to study dynamic properties such as hydrolysis, diffusion, and dehydration of TCMs [40, 100, 131]. Despite the lower computational cost, ReaxFF is still not used to study hydration, deliquescence, or equilibrium conditions of TCMs. These phenomena are related to rare events and/or high energy barriers, and the MD timescale is too short to overcome these barriers.

Molecular Monte Carlo methods (MC) are closely related to MD. However, where MD uses time integration methods to sample the phase space, MC is a stochastic approach to relate statistical properties to a mechanical property [63]. Because MC does not depend on the dynamical method of time integration, these high energy barriers and rare events can be circumvented by smart MC algorithms.

Herein, we introduce an advanced Grand-Canonical Monte Carlo (GCMC) model which is able to predict the chemical equilibrium at a given temperature and pressure between a sorbate and sorbent [254]. Moreover, it can reveal changes in the reaction equilibrium of salts upon chemical or physical enhancement. With the GCMC algorithm, molecules within a simulated system are exchanged with an infinite large reservoir at a constant chemical potential. These exchanges are accepted according to acceptance rules that enclose the phase space of the system. Consequently, for a large number of molecule exchanges, the system's chemical potential will equilibrate with the reservoir's chemical potential. In this way, a relation is established between the reservoir with an imposed pressure and temperature, and the number of molecules in the system. This makes GCMC practically preferable to study sorption over time-dependent molecular dynamics (MD) simulations that are hindered by a limited computationally available time regarding processes with high energy barriers like diffusion in confined regions.

MC in combination with reactive systems has been applied before, e.g. Reaction Ensemble Monte Carlo [255]. However, for such system the reaction product should be known. This is not the case for ReaxFF MD, where the reaction will follow from the dynamics, given the required chemical environment. The combination between GCMC and ReaxFF has been introduced by Senftle et al. [256–258]. It has been used in catalytic studies of oxidation [256, 258, 259], hydrogenation [256], and carbonation [256]. Islam et al. [260] used the same method for battery applications and studied lithium insertion in  $\alpha$ -sulfur. Jung et al. [261] developed a ReaxFF Grand-Canonical MD (GCMD) combination, which performed GCMC trial moves at predefined intervals in ReaxFF-

MD. These authors showed its applicability to gas-phase water formation from oxygen and hydrogen molecules on platinum catalysts. All the previous studies either focus on the gas-phase above mentioned surfaces [258, 261], or on bulk systems interactions with monatomic sorbents [256, 257, 259, 260]. When considering the gas phase, insertions are still practically feasible due to a large amount of available voids. However, in dense bulk materials, GCMC insertion of molecules becomes cumbersome due to the high possibility of overlapping atoms when random insertions are performed. Insertions that result in overlapping atoms will be rejected due to the corresponding high energy and these low acceptance probabilities make the system hard to reach equilibrium. To avoid overlaps between atoms, advanced GCMC algorithms are successfully developed [250, 254, 262–264] for dense systems, where a bias is used to prevent overlaps. In the existing ReaxFF–GCMC combination, molecular insertions have been increased using a forward bias that performs energy minimization after each insertion. Accordingly, this bias has to be counterbalanced to avoid unrealistic overloading. Senftle et al. [256] compensated the bias by reducing the accessible volume.

To study the hydration of  $\text{MgCl}_2 \cdot n\text{H}_2\text{O}$ , a nonmonatomic gas -  $\text{H}_2\text{O}$  - molecules need to be inserted. To counterbalance the energy minimization for an inserted  $\text{H}_2\text{O}$  molecule, via an assumed reduced volume, would be increasingly ambiguous for a molecule compared to atomic insertion. In this work, a novel ReaxFF–GCMC combination is developed with an alternative biasing scheme to increase its insertion efficiency. To avoid excessive energy calculations with ReaxFF for unrealistic overlapping insertions, first,  $k$  trial insertions are performed with a computationally cheap short-range Weeks-Chandler-Andersen (WCA) [265] interaction potential. From these cheaply calculated insertion trials, realistic insertions without hardcore overlaps can be selected for a recalculation with ReaxFF. Thus, this bias favors insertions that are more likely to be accepted, and as a result equilibrium can be reached for dense systems. Because the number of trial positions ( $k$ ) and their corresponding energies are exactly known, this bias is exactly known and can be counterbalanced in the acceptance rules of the GCMC algorithm.

The article is organized as follows. In Section 6.2, the basic GCMC algorithm is explained. Furthermore, the biased WCA–ReaxFF–GCMC algorithms are explained, which improve the insertion of molecules, together with the WCA and ReaxFF potentials. In Section 6.3, the GCMC algorithms are validated and accordingly used to study and discuss the hydration of  $\text{MgCl}_2 \cdot n\text{H}_2\text{O}$ . In Section 6.4, conclusions are drawn concerning the algorithm and its future potential use to study equilibrium conditions.

## 6.2. METHODOLOGY

### 6.2.1. GCMC

To study molecular properties, one could use statistical thermodynamic rules combined with an ensemble of atomic positions. The ensemble must contain all relevant states of a system and thereby resemble its entire phase space. Molecular Dynamics (MD) can obtain such an ensemble, in which successive molecular states are sampled by trajectories over time via integration of Newton's laws. Alternatively, one could sample relevant states using Monte Carlo methods, in which the states are generated according to the imposed probability distribution. Contrary to MD, states in MC are not sampled over



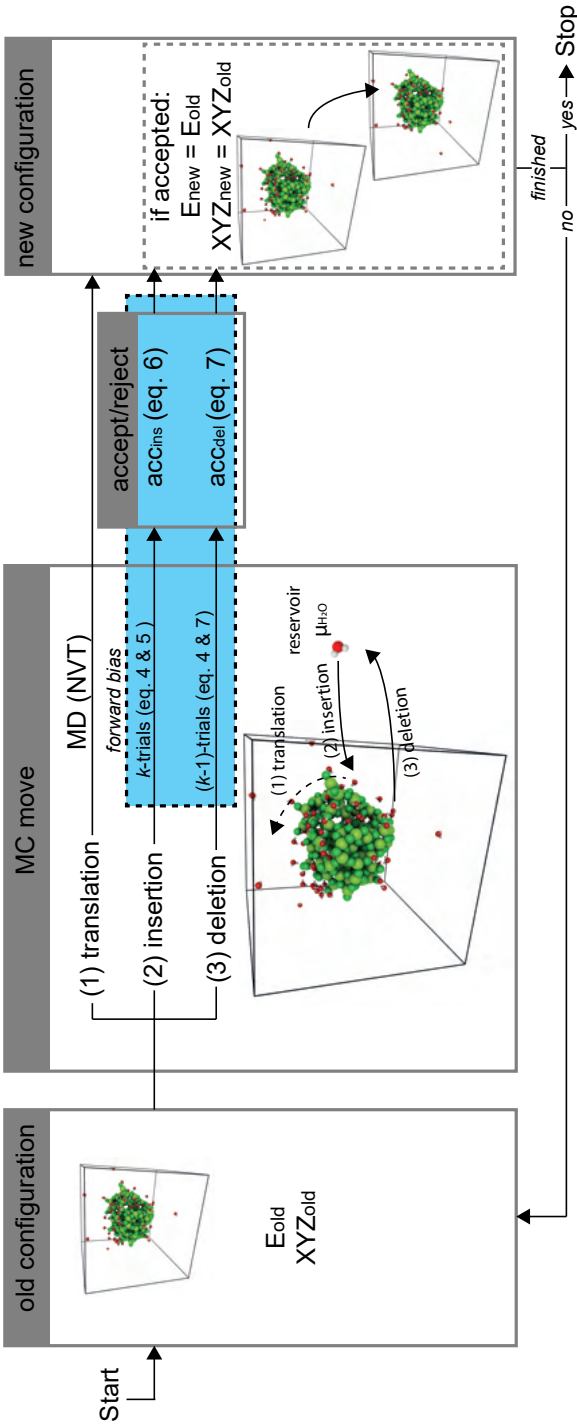


Figure 6.1: Visualization of the GCMC algorithm, including the newly developed biased algorithm given in blue. The conventional basic GCMC moves are (1) translations, (2) insertions, and (3) deletions.

time. This is the strength of MC, where one is not limited by time and/or slow diffusion to pass high energy barriers. For practical efficiency, new states in the MC ensemble are generated from the previous states -generating a Markov Chain- by performing trial moves which are accepted or rejected based on the probability of finding the system in a certain state and the probability of attempting the trial move [63, 129].

The Grand-Canonical Monte Carlo (GCMC) algorithm is the most commonly used method to predict sorption phase equilibria with numerical modeling. The algorithm relies on three basic trial moves that are successively and randomly selected: translation of molecules, insertion of molecules, and deletion of molecules. The first one, translation (thermalization) of molecules, can be a rotation, translation, sampling the inner degrees of a molecule, or a combination of these. To improve efficient sampling of translational moves for complex systems, multiple advanced MC algorithms are proposed, for example the AVBMC method [266]. In this work, due to practical ReaxFF implementations we choose to perform a short MD simulation in the canonical ensemble. With this approach, reaction will follow from the dynamics when the system is in the required chemical environment. The second one, the insertion trial move, is the insertion of a molecule within the system at a random location and random orientation. The inserted molecule is an 'ideal' gas molecule taken from an infinite large reservoir [63, 129, 262]. The trial move is accepted with probability:

$$\text{acc}_{\text{ins}} = \min \left[ 1, \frac{\beta f V}{(N+1)} \exp(-\beta(\Delta E - E_{\text{ig}})) \right] \quad (6.2)$$

in which  $\beta$  is the reciprocal of the thermodynamic temperature  $\left(\frac{1}{k_{\text{B}}T}\right)$  with  $k_{\text{B}}$  as Boltzmann constant, and  $T$  the absolute temperature;  $f$  is the gas-phase fugacity computed from the pressure by the Peng-Robinson equation of state [267]. The critical temperature of 647.3 K, a critical pressure of 221.2 bar, and an acentric factor of 0.344 were used for water [268]. However, at the given conditions encountered in this work fugacity and pressure are nearly identical as the pressure is low.  $V$  is the volume of the simulation box,  $E_{\text{ig}}$  is the intramolecular energy of the isolated molecule, and  $\Delta E$  is the change in energy of the system. The change in energy of the system is given by  $\Delta E = E_{\text{new}} - E_{\text{old}}$  where  $E_{\text{new}}$  is the energy of the new state of the system and  $E_{\text{old}}$  is the energy of the old state of the system. The third trial move of the GCMC algorithm is the deletion of a randomly selected molecule from the system. This trial move is accepted according to:

$$\text{acc}_{\text{del}} = \min \left[ 1, \frac{N}{\beta f V} \exp(-\beta(\Delta E + E_{\text{ig}})) \right] \quad (6.3)$$

in which  $\Delta E = E_{\text{new}} - E_{\text{old}}$ , and with  $E_{\text{ig}}$  as the intra-molecular energy of the molecule in the conformation as in the system. Visualization of the GCMC algorithm is presented in Figure 6.1, in which the blue area is the newly developed biased algorithm as explained in the following Sections.

### 6.2.2. BIASED REAXFF-GCMC

In the GCMC algorithm, new trial configurations are created based on old states and the corresponding acceptance rules (eqs. 6.2 and 6.3). These rules are created based on the

detailed balance condition [63] and it is key that the probability of creating the trial move from the old configuration to the new configuration is equal to the reverse way. Consequently, the insertion of a new molecule should be done at a random location and with a random orientation. This works well for inserting and deleting relatively small molecules in systems that contain many voids (e.g., MOFs [269, 270], and zeolites [271]). However, this will be difficult for dense systems with very little suitable locations to achieve successful insertions. When the used interaction potential to compute the new energy is a expensive calculation, this could lead to very long computational times before equilibrium is reached. Hence it makes sense to bias the position of inserted molecules towards more feasible positions.

### WCA-REAXFF-GCMC

We developed an advanced ReaxFF-GCMC method to avoid many unnecessary calculations with the ReaxFF formalism. In the case of an insertion trial move, our advanced ReaxFF-GCMC method first generates  $k$  trial positions that are evaluated with a computationally cheap WCA interaction potential ( $E_{\text{WCA}}$ ). The details of WCA interaction potential are explained in Section 6.2.3. Accordingly, from these  $k$  trials, one trial position is selected proportional to its normalized Rosenbluth factor [63, 262, 272]:

$$P_i = \frac{\exp[-\beta E_{\text{bias},i}]}{W_n}, \quad (6.4)$$

in which  $P_i$  is the probability of selecting trial  $i$ .  $E_{\text{bias},i}$  is the energy given by the computationally cheap WCA interaction potential ( $E_{\text{bias},i} = E_{\text{WCA},i}$ ) for trial position  $i$  in the new configuration, which is normalized with the total Rosenbluth weight:

$$W_n = \sum_{j=1}^k \exp[-\beta E_{\text{bias},j}]. \quad (6.5)$$

The energy of the selected trial position ( $k_i$ ) is recalculated with the more expensive ReaxFF formalism. Due to the applied forward bias in selecting promising trials, the acceptance probability changes to:

$$\text{acc}_{\text{ins}} = \min \left[ 1, \frac{\beta f V}{(N+1)} \exp(-\beta(\Delta E_{\text{RxFF}} - E_{\text{ig}} - E_{\text{bias},i})) \times \frac{W_n}{k} \right]. \quad (6.6)$$

where  $E_{\text{RxFF}}$  is the energy difference between the new and old configurations by ReaxFF. For the deletion of a molecule from the system, the Rosenbluth weight of the old configuration has to be computed, which is done by performing  $k-1$  random insertion trial positions, and the  $k^{\text{th}}$  position is the old configuration itself:

$$W_o = \exp(-\beta E_{\text{bias},i}) + \sum_{j=1}^{k-1} \exp[-\beta E_{\text{bias},j}], \quad (6.7)$$

in which  $E_{\text{bias},i}$  is the energy of the  $k^{\text{th}}$  position, the selected molecule for deletion, computed by the cheap WCA interaction potential. The modified acceptance rule is given by:

$$\text{acc}_{\text{del}} = \min \left[ 1, \frac{N}{\beta f V} \exp[-\beta(\Delta E + E_{\text{ig}} + E_{\text{bias},i})] \times \frac{k}{W_o} \right]. \quad (6.8)$$

In Appendix F.1 it is shown that Eqs. 6.6 and 6.8 obey the detailed balance condition.

### WCA–REAXFF–GCMC, WITH CENTER PREFERENCE

To study the hydration of  $\text{MgCl}_2$ , an anhydrous  $\text{MgCl}_2$  spherical cluster is placed in the center of a larger simulation box. This allows hydration on all the different surfaces of the anhydrous cluster. Since the cluster is placed in an empty simulation box, the possibility of sampling the empty space around the cluster is large compared to the dense region in and around the  $\text{MgCl}_2$  cluster. To increase selection of promising trial positions near the  $\text{MgCl}_2$  cluster, an extra biasing potential is applied in the form of a Gaussian energy distribution with its center at the center of the cluster, as illustrated in Figure 6.2. This

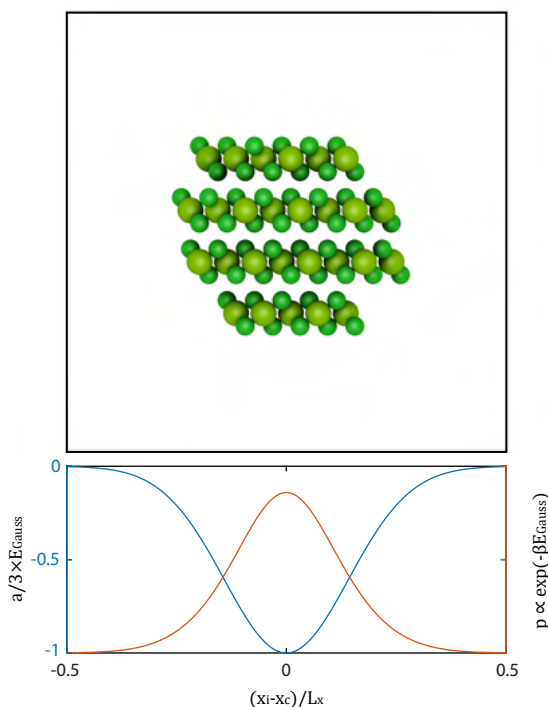


Figure 6.2: Example of preference selection by a Gaussian energy distribution. The x-axis is the relative  $x$  coordinate within  $L_x$  box size, the energy from the Gaussian distribution is in blue on the left y-axis, and in red on the right y-axis the proportional selection probability from the Gaussian bias energy.

added Gaussian energy distribution is described by:

$$E_{\text{Gauss}} = -a \times \exp \left[ -\frac{(x_i - x_c)^2}{4c^2} - \frac{(y_i - y_c)^2}{4c^2} - \frac{(z_i - z_c)^2}{4c^2} \right], \quad (6.9)$$

in which  $a$  is the height of the Gaussian distribution (in [kcal/mol], the same energy units as  $E_{\text{ReaxFF}}$  and  $E_{\text{WCA}}$ ),  $c$  is the width of the distribution,  $x_i$ ,  $y_i$ , and  $z_i$ , are the coordinates of the trial position, and  $x_c$ ,  $y_c$ , and  $z_c$ , are the center of the cluster. The energy term

$E_{\text{Gauss}}$  is added to the energy of the WCA interaction potential ( $E_{\text{bias}} = E_{\text{WCA}} + E_{\text{Gauss}}$ ). This modification results in the fact that if a successful trial is found in the center of the cluster, the probability of selecting this one for insertion is higher than a successful trial position further away from the center of the simulation box.

### 6.2.3. FORCE FIELDS

As explained in the previous section,  $k$  trial insertions are performed for each GCMC trial move with a relatively cheap WCA potential followed by the more expensive ReaxFF calculation.

#### REAXFF

ReaxFF MD [81, 82, 124] enables simulations including reactions. The ReaxFF interaction potential is a summation of different energy contributions:

$$E_{\text{RxFF}} = E_{\text{bond}} + E_{\text{vdW}} + E_{\text{Coul}} + E_{\text{val}} + E_{\text{pen}} + E_{\text{under}} + E_{\text{over}} + E_{\text{tors}} + E_{\text{conj}} + E_{\text{others}}. \quad (6.10)$$

The terms  $E_{\text{vdW}}$  and  $E_{\text{Coul}}$  are the noncovalent bonded van der Waals and Coulomb terms, respectively. The  $E_{\text{bond}}$  term accounts for the covalently bonded atoms. The terms  $E_{\text{val}}$ ,  $E_{\text{tors}}$ ,  $E_{\text{pen}}$ ,  $E_{\text{under}}$ ,  $E_{\text{over}}$ , and  $E_{\text{conj}}$  describe the valence and torsion contributions, 'penalty' energies, under- and over-coordination, and conjugated systems, respectively.  $E_{\text{others}}$  can include other terms for specific systems, such as H-bonds or extra dispersion interactions. The bond order (BO) between atoms is described by a summation of empirical relations for the  $\text{BO}_{ij}^{\sigma}$ ,  $\text{BO}_{ij}^{\pi}$ , and  $\text{BO}_{ij}^{\pi\pi}$  bond, which depend on the distance  $r_{ij}$  between the atoms  $i$  and  $j$  [81].

$$\begin{aligned} \text{BO}_{ij} &= \text{BO}_{ij}^{\sigma} + \text{BO}_{ij}^{\pi} + \text{BO}_{ij}^{\pi\pi} \\ &= \exp \left[ p_{\text{bo1}} \left( \frac{r_{ij}}{r_0^{\sigma}} \right)^{P_{\text{bo2}}} \right] + \exp \left[ p_{\text{bo3}} \left( \frac{r_{ij}}{r_0^{\pi}} \right)^{P_{\text{bo4}}} \right] \\ &\quad + \exp \left[ p_{\text{bo5}} \left( \frac{r_{ij}}{r_0^{\pi\pi}} \right)^{P_{\text{bo6}}} \right], \end{aligned} \quad (6.11)$$

in which  $r_0^{\sigma}$ ,  $r_0^{\pi}$ , and  $r_0^{\pi\pi}$  are the bond radii for the  $\sigma$ ,  $\pi$ , and  $\pi\pi$  bond, respectively. The  $p_{\text{bo}}$  values are fitted parameters to experimental or first-principle results. Each  $\text{BO}_{ij}$  term has a maximum value of 1, and when all bond-orders contribute BO could add up to 3. The empirical bond order approach of ReaxFF enables us to model bond breaking and formation without expensive quantum mechanical calculation.

To study the hydration of  $\text{MgCl}_2$  hydrates, we used the ReaxFF force field developed by Pathak et al. [40, 100] in combination with the long-range corrected  $\text{H}_2\text{O}$  ReaxFF force field, as shown in Chapter 5. This force field was not explicitly trained to recreate the phase diagram of the salt, however, a transferable force field for TCM application should be able to recreate it. Furthermore, the  $\text{MgCl}_2$  force field has proved itself useful for multiple hydration levels  $\text{MgCl}_2 \cdot n\text{H}_2\text{O}$  ( $n = 0, 1, 2, 4$ , and 6), and the  $\text{H}_2\text{O}$  force field is able to accurately capture both condensed and vapor phase at saturation conditions, shown in Chapter 5.

Table 6.1: WCA parameters

Element	$\epsilon$ [kcal/mol]	$\sigma$ [Å]
O	0.1	2.3
Mg	0.1	0.8
Cl	0.1	3

## WCA POTENTIAL

Prior to the ReaxFF insertion,  $k$  computationally inexpensive WCA potential trial insertions are computed. This Weeks-Chandler-Andersen [265] (WCA) interaction potential is relatively cheap because it only considers short-range repulsive interactions. In this way, hard overlaps between atoms are avoided. The WCA interaction potential is described by:

$$E_{\text{WCA},ij} = \begin{cases} 4\epsilon \left[ \left( \frac{\sigma}{r_{ij}} \right)^{12} - \left( \frac{\sigma}{r_{ij}} \right)^6 \right] + \epsilon, & r \leq 2^{1/6}\sigma \\ 0, & r > 2^{1/6}\sigma, \end{cases} \quad (6.12)$$

with  $\epsilon$  and  $\sigma$  as characteristic energy and distance parameters, respectively.

In this work, we used the WCA parameters as given in Table 6.1, combined with the Lorentz-Berthelot (LB) mixing rules between different elements. Careful determination of the WCA  $\sigma$  and  $\epsilon$  parameters is key to use the WCA bias effectively. If these parameters are too large, promising small voids in the dense  $\text{MgCl}_2$  structure will never be selected. However, when they are too small, many unrealistic insertions with overlapping atoms can still be selected, and the algorithm becomes ineffective again. The parameter  $\sigma$  corresponds to the atomic/molecule size. For the  $\text{H}_2\text{O}$  molecule, only the oxygen atom was considered in the WCA potential, with a diameter ( $\sigma$ ) corresponding to the Radial Distribution Function (RDF) O–O distance for liquid water obtained by the ReaxFF force field. Thereby, the oxygen in the WCA calculation resembles the diameter of a  $\text{H}_2\text{O}$  molecule in liquid, and excessive WCA interactions calculation with twice as much H-atoms are avoided. The magnesium and chlorine parameters were chosen such that the O–Mg and O–Cl repulsive part closely matches the repulsive distance of the ReaxFF force field. In Appendix E.2, the resulting O–O interaction potential is compared with the ReaxFF RDF, and the O–Mg, and O–Cl interaction potentials are compared with the ReaxFF interaction energy.

## 6.3. RESULTS & DISCUSSION

In sections 6.3.1 and 6.3.2, the biased GCMC algorithms are tested and validated. In Sections 6.3.3 and 6.3.4, the WCA–ReaxFF–GCMC algorithm is used to study  $\text{MgCl}_2 \cdot n\text{H}_2\text{O}$  hydration. Images to visualize  $\text{MgCl}_2 \cdot n\text{H}_2\text{O}$  hydration are created with iRASP [215].

### 6.3.1. WCA–GCMC VALIDATION

To test and validate the WCA–ReaxFF combination with the GCMC algorithm, the hydration of a  $\text{MgCl}_2$  crystal with an artificial cavity was studied for different numbers of  $k$  trial positions. In Figure 6.3, the resulting loading of  $\text{H}_2\text{O}$  is shown. These systems

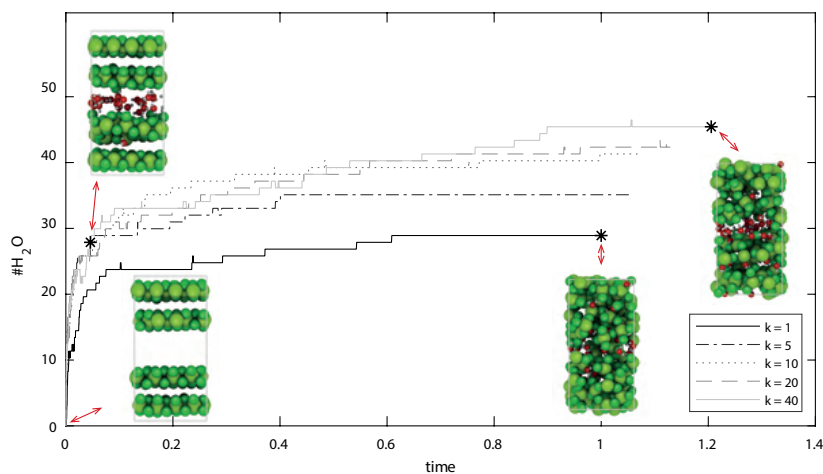


Figure 6.3: Loading of  $\text{MgCl}_2$  cavities, with  $k$  trial positions, normalized to the total required simulation time for  $k = 1$ . The insets are the structures at the indicated times.

were simulated at a given temperature of 300 K and a vapor pressure of 12 mbar. The simulation with  $k = 1$  is considered as a reference system, where it represents the conventional (unbiased) GCMC algorithm with  $k = 1$ . The computational times required for the other simulations were normalized to this  $k = 1$  reference. This reference system took 5.6 hours for 30,000 MC moves, initially including 288 Mg/Cl atoms, with single-core MC moves (insertion/deletion) energy calculations and 8-core ReaxFF-MD (translation) calculations, on a Haswell (Intel® Xeon® Processor E5-2690 v3) node. From Figure 6.3, the gain by the WCA bias is clear. The  $k = 1$  reference is loading much slower than the other structures and does not load more than 28  $\text{H}_2\text{O}$  water molecules over the entire simulation, where the other systems ( $k = 5$ ,  $k = 10$ ,  $k = 20$ , and  $k = 40$ ) already reach a similar loading at ca. 5–7% of the computational time. Furthermore, with multiple  $k$  trial positions, the final loading is much higher. The  $k = 40$  test even reaches a loading of 44 water molecules, at only 121% of the time of the  $k = 1$  simulation. It is doubtful if the reference  $k = 1$  case would ever reach such a loading within acceptable computational time, where it was not successful for the last ~40% of the time to insert another water molecule. In Appendix E.3 we show for a simple system, rarefied system where hardcore overlap is hardly present for insertion, that the number of  $k$ -trial positions does not change the final equilibrium. The insets of Figure 6.3 represent the systems at the indicated times. After approximately 5% of the time, the first successful insertion of a  $\text{H}_2\text{O}$  molecule outside the initial cavity occurred. Before this point, hydration only happened in the cavity. This indicates that the initial bulk  $\text{MgCl}_2$  layers are too densely packed to accept a  $\text{H}_2\text{O}$  molecule, and the created  $\text{H}_2\text{O}$  water layer in the cavity is needed to deform the densely packed layers and create a disordered region of salt and water. This phenomenon is more extensively discussed in Section 6.3.4.

### 6.3.2. GAUSSIAN PREFERENCE VALIDATION

To increase the loading of  $\text{H}_2\text{O}$  molecules near the  $\text{MgCl}_2 \cdot n\text{H}_2\text{O}$  spherical clusters, a Gaussian selection preference is used. This preference gives a higher selection probability for inserted  $\text{H}_2\text{O}$  molecules near the center of the box compared the outer vacuum region. In our systems, this center region is important because we use  $\text{MgCl}_2 \cdot n\text{H}_2\text{O}$  spherical cluster that are positioned at the center of the simulation box. This algorithm was first validated with an empty box at 400 K at 1 atmosphere. These results are shown in Appendix E.3. It shows that more insertion trial moves were selected near the center. Furthermore, the Gaussian preference selection bias for the center of the box, does not change the total loading of the box, where it correctly predicts a  $\text{H}_2\text{O}$  vapor density close to the NIST reference [238] value.

In Figure 6.4, the Gaussian preference is tested for a  $\text{MgCl}_2$  spherical cluster in the center of the simulation box. It is shown that when the Gaussian distribution is used to increase loading in the center of the box, near the  $\text{MgCl}_2$  spherical cluster, a marginal gain is achieved when the amount of water molecules is still low and as a consequence, the  $\text{MgCl}_2$  spherical cluster relatively small. However, if the amplitude of the Gaussian distribution  $a$  is set to high, it has a contrary effect. This is also the case when the Gaussian preference method is used without the WCA–GCMC algorithm since the possibility of atomic overlap is much higher in the center of the box. Due to the small gain with relatively small clusters, which could already provide relevant information regarding the hydration of  $\text{MgCl}_2$ , the remaining calculations are performed including this Gaussian bias.

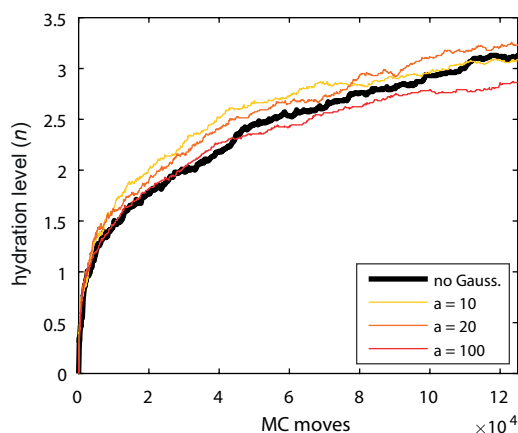


Figure 6.4: Gaussian preference test for a  $\text{MgCl}_2$  spherical cluster at 300 K with  $a$  (kcal/mol) as the height of the Gaussian distribution.

### 6.3.3. HYDRATION OF MAGNESIUM CHLORIDE HEXAHYDRATE CLUSTERS

The motivation of this work was to develop a tool that can provides insight into the hydration mechanism of complex (new) materials for thermochemical heat storage applications and predict equilibrium conditions at a given pressure and temperature. There-



fore, the deliquescence equilibrium and behavior are studied by means of a spherical  $\text{MgCl}_2 \cdot 6\text{H}_2\text{O}$  cluster of approximately 50 Å. In terms of hygroscopic salts as TCMs, this deliquescence could seriously affect the performance of the storage system. The experimental deliquescence equilibrium [173] line for  $\text{MgCl}_2$  is given by the black solid line in Figure 6.6. Under conditions below this deliquescence line solid  $\text{MgCl}_2 \cdot n\text{H}_2\text{O}$  crystals occurs, with  $n = 6$  as the highest hydrated close to the deliquescence equilibrium. Under conditions above this deliquescence line  $\text{MgCl}_2$  in an aqueous solution occurs.

In the GCMC simulation, the  $\text{MgCl}_2 \cdot 6\text{H}_2\text{O}$  spherical cluster is placed at the center of a vacuum box and hydrated at vapor pressures of 6, 12, and 50 mbar, which pressures around design conditions for thermochemical heat storage systems with domestic applications [11]. In Figure 6.5 (de)hydration trends from the WCA-ReaxFF-GCMC algorithm are shown for the 12 mbar systems. Upward triangles ▲ represent increasing trends (hydration), and downward triangles ▼ represent decreasing trends (dehydration). Black • are given for stable trends (nondehydrating, nonhydrating). The results for the 6 and 50 mbar vapor pressures are given in Appendix F4. These obtained trend symbols are plotted in Figure 6.6, and show a close match with the experimental deliquescence equilibrium [173], where the  $\text{MgCl}_2 \cdot 6\text{H}_2\text{O}$  spherical cluster hydrates above the experimental equilibrium line and dehydrates under conditions below this line. The WCA-ReaxFF-GCMC results, given in Figure 6.6, predict a slightly higher equilibrium temperature ( $\sim 10$  K) at lower vapor pressure. However, one must note that for the GCMC systems, steps of 10 K are used and it would be ambiguous to determine hydration or dehydration with smaller temperature steps (Figure 6.5). Furthermore, a higher equilibrium temperature is expected for micro-particles, since they have a higher solubility than the bulk material [273]. This is described by the Ostwald-Freundlich equation and caused by the relatively large factor of the surface energy for micro-particles compared to the bulk material. As a result, a shift of the equilibrium curve to higher temperatures/lower vapor pressure will be present.

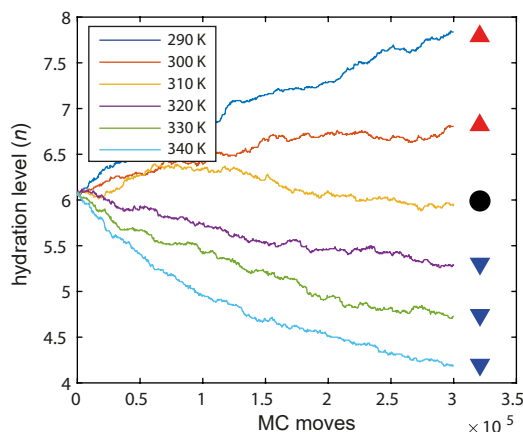


Figure 6.5: WCA-ReaxFF-GCMC results for a  $\text{MgCl}_2 \cdot 6\text{H}_2\text{O}$  spherical cluster at  $p = 12$  mbar, with  $k = 20$  trial positions, and  $a = 5$  kcal/mol, where  $n$  on the y-axis represents the hydration level ( $\text{MgCl}_2 \cdot n\text{H}_2\text{O}$ ), and the number of MC moves is given on the x-axis.

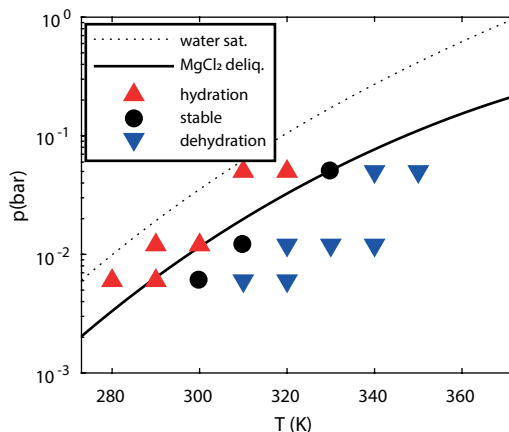


Figure 6.6:  $\text{MgCl}_2 \cdot 6\text{H}_2\text{O}$  deliquescence equilibrium, black solid line from experimental reference [173], and symbols GCMC prediction ( $\blacktriangle$  = hydration,  $\bullet$  = stable, and  $\blacktriangledown$  = dehydration) as shown in Figure 6.5 and in the SM.

#### 6.3.4. HYDRATION OF MAGNESIUM CHLORIDE CLUSTERS

Thermochemical heat storage systems for domestic heating are typically studied at a vapor pressure of 12 mbar, over a temperature range from 300 to 500 K [11]. In this sense, the  $\text{MgCl}_2 \cdot n\text{H}_2\text{O}$  clusters are studied at these conditions. Since the GCMC algorithm is computationally demanding, multiple starting structures are used at different relevant hydration levels ( $n = 0, 2$ , and  $6$ ), making the prediction of equilibrated hydration levels easier to estimate. These results are given in Figure 6.7. The corresponding estimated equilibrium hydration levels are compared with theoretical values, predicted by thermodynamics, in Figure 6.8. The computed equilibrium curves from thermodynamics, in which the left-hand side of chemical reaction eq 6.1 is in equilibrium with the right-hand side, are described by the thermodynamic relation [29]:

$$p_{\text{eq}} = p^0 \exp\left(\frac{-\Delta S^0}{R}\right) \exp\left(\frac{-\Delta H^0}{RT}\right) \quad (6.13)$$

in which  $\Delta H^0$  and  $\Delta S^0$  are the reaction enthalpy and entropy, respectively, per mole of water at standard conditions for the different components on the left-hand side and right-hand side of equilibrium 6.1.  $R$  is the universal gas constant,  $p^0$  is standard pressure, and  $p_{\text{eq}}$  the resulting vapor equilibrium pressure at a given temperature  $T$ . The exponential term in this equation makes the direct prediction of the equilibrium from entropy and enthalpy calculations (e.g., with DFT) hard, since small energy deviations can result in large equilibrium deviations. In Figure 6.8, the equilibrium curves are given for  $\text{MgCl}_2 \cdot n\text{H}_2\text{O}$  ( $n = 0, 1, 2, 4$ , and  $6$ ), in which  $\Delta H^0$  and  $\Delta S^0$  are taken from the NBS tables [168].

From Section 6.3.3, it was already shown that at 300 K and 12 mbar  $\text{MgCl}_2$  would go to a higher hydration than the hexahydrate ( $n = 6$ ). In Figure 6.7, this is observed for all simulated systems at different initial hydration settings ( $n = 6, 2$ , and  $0$ ). However, after

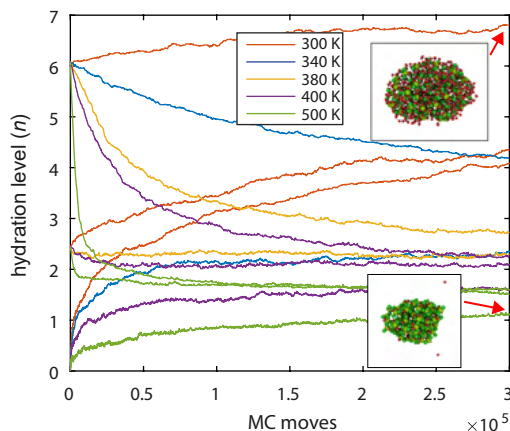


Figure 6.7: Hydration of  $\text{MgCl}_2 \cdot n\text{H}_2\text{O}$  clusters at different temperature (different colored lines) and different initial hydration levels ( $n = 0, 2$ , and  $6$ ) and a vapor pressure of 12 mbar. The insets visualize the highest hydrated cluster at 300 K with the initial  $\text{MgCl}_2 \cdot 6\text{H}_2\text{O}$  cluster; and the lowest hydrated structure at 500 K with the initial  $\text{MgCl}_2$  clusters.

300,000 MC moves, the systems which started at a hydration level  $n$  of 0 and 2, are still far from equilibrium. At 340 K, an estimated hydration level between 2 and 4 appears, from the thermodynamic values the tetrahydrate ( $n = 4$ ) crystalline structure is expected. At 380 and 400 K, the GCMC simulations equilibrate approximately around a hydration level of 2, where the thermodynamic dihydrate ( $n = 2$ ) can be found between 369 and 390 K, from eq 6.13, at the given vapor pressure. At 500 K, the GCMC algorithm predicts a hydration level of 1, where the thermodynamic rules indicates anhydrous  $\text{MgCl}_2$  ( $n = 0$ ). The deviations between the results from the GCMC algorithm and the calculated equilibrium lines from thermodynamic values (eq 6.13), can be explained by the use of disordered micro-particle (23-50 Å) in the simulations, versus the used crystalline bulk thermodynamic values ( $H^0, S^0$ ). This also indicates that it would required a much higher temperature to obtain a completely dry micro-particle, compared to the bulk material.

From Section 6.3.1, it was shown that the water layer on top of the salt crystal breaks the crystal itself and forms a disordered structure. This effect reappears in the hydration of the  $\text{MgCl}_2$  clusters, where the added water creates a disordered  $\text{MgCl}_2 \cdot n\text{H}_2\text{O}$  cluster that allows further hydration within the created voids of the disordered structure. This is according to the hypothesized theory of a two-step hydration process by Sögütöglü et al. [28, 29] in which the complete hydration process of a salt is described by two distinctive steps; step (1) water adsorption from the atmosphere to a wetting layer on the surface of the salt, and accordingly dissolution of ions; step (2) nucleation into the crystal of the final hydrate. This second step, the nucleation of a crystal, is a rare event which occurs on time scales far beyond MD time scales [274]. Hence, this second step is not reached by or observed in the GCMC hydration modeling. Due to the absence of nucleation in crystalline structures, smooth transitions are expected from the GCMC simulations, compared to the distinctive zones from thermodynamic calculations. To visualize

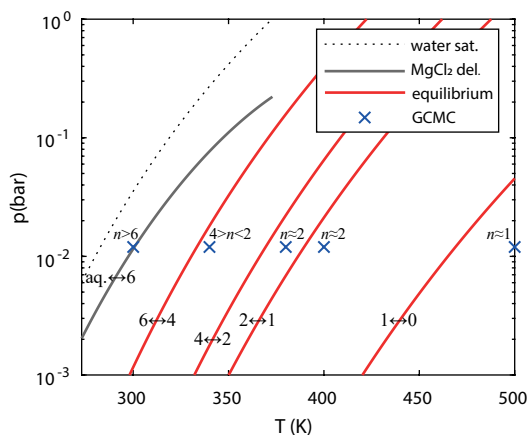


Figure 6.8: Phase diagram of  $\text{MgCl}_2 \cdot n\text{H}_2\text{O}$   $n=0, 1, 2, 4$ , and  $6$ , red lines are computed equilibrium lines by equation 6.1 and NBS thermodynamic values [168], gray line is the experimental  $\text{MgCl}_2 \cdot 6\text{H}_2\text{O}$  equilibrium line [173]. Blue crosses represent GCMC simulations conditions ( $T, p$ ) of Figure 6.7 and are given with the estimated water loading from the simulations. The black solid circles, are the estimated  $\text{MgCl}_2 \cdot 6\text{H}_2\text{O}$  deliquescence equilibrium from Figure 6.6. The dotted line is the water saturation equilibrium line.

## 6

the hydration, two movies of the  $\text{MgCl}_2$  cluster, at 300 K and 12 mbar vapor pressure are added to the supplementary material of the published paper of this Chapter. One movie shows the hydration of the particle from the first MC cycle until 250,000 cycles. The second movie shows a section at the center of the same particle in  $yz$ -plane, from the first MC cycle until 90,000 cycles. The initial wetting on the surface from the particle, the disordered development of the initial crystalline starting structures, and loading within the particle, can be observed from these movies.

## 6.4. CONCLUSIONS

The motivation of this work was to develop a molecular modeling tool that can be used to study the hydration of salt hydrates for thermochemical storage applications. In this sense, an efficient ReaxFF–GCMC model has been designed and implemented with a force field for  $\text{MgCl}_2 \cdot n\text{H}_2\text{O}$  [100]. To increase accepted water loading in dense salt hydrate structures, the ReaxFF–GCMC was combined with two forward bias methodologies, namely scanning of  $k$  insertion trials with the computationally cheap WCA potential, and a Gaussian preference selection of trials near the salt hydrates cluster. The WCA forward bias significantly increased the speed of the ReaxFF–GCMC algorithm, where it reached a much higher loading in a substantially shorter time. The Gaussian preference selection near the salt hydrate cluster showed a minor improvement, for relatively small clusters.

The biased WCA–ReaxFF–GCMC algorithm was used to study the hydration of micro-particles. The predicted results are in good agreement with the experimental deliquescence line of  $\text{MgCl}_2 \cdot 6\text{H}_2\text{O}$ , for a vapor pressure range from 6 to 50 mbar. Furthermore, different hydration levels were found over the temperature range from 300 to 500 K,

from the deliquescence phase to the monohydrate ( $n = 1$ ), respectively. The trend of the different predicted hydration levels is in agreement with thermodynamically computed values. However, with a slight deviation which can be attributed to the use of micro-particles compared to the thermodynamic values based on bulk crystalline hydrates. The studied hydrated structures are found to be in a disordered state, where nucleation to a given hydrated crystalline structure is beyond the timescale of MD [274].

From the hydration process, observed from the WCA-ReaxFF-GCMC simulations, it was shown that  $\text{H}_2\text{O}$  molecules first load on the surface of the salt. The presence of water at the surface creates a disordered  $\text{MgCl}_2$  region, consequently,  $\text{H}_2\text{O}$  molecules are also loaded within the salt itself. This fluidized nucleation process is according to the two-step hydration process formulated by Sögütöglu et al. [28, 29].

The given results from the biased ReaxFF-GCMC algorithm validate the potential of the method for future studies. For example, to use it for complex TCM (e.g., encapsulated, impregnated, double, doped, or mixed salts) for which thermodynamic values are not available in the literature. Additionally, not only the hydration of TCMs can be studied but also other sorption processes (e.g., oxidation, hydration, and carbonation) that involve larger sorbate gas molecules and dense sorbent material.



# 7

## REAXFF DEVELOPMENT AND APPLICATION FOR COMBINED SALT HYDRATES

*There's Plenty of Room at the Bottom.*

Richard Feynman

**ABSTRACT:** Building on the previous chapters, a new ReaxFF was developed to study doped  $\text{MgCl}_2 \cdot n\text{H}_2\text{O}$  and  $\text{CaCl}_2 \cdot n\text{H}_2\text{O}$  structures. Both salts are promising TCMs; however, combined structures of both salts could outperform the pure salts in terms of TCM characteristics. The newly developed ReaxFF was parameterized with the MMC optimizer and included relevant DFT reference data. Comparable to the DFT results, a lower stability was found for the doped structure than the pure salt. Similar to imperfections like cracks and pores, doping the salt hydrate increases the dehydration of the salt, thereby improving its applicability as TCM. Ca-doped  $\text{MgCl}_2 \cdot 2\text{H}_2\text{O}$  did not result in the desired hydrolysis reduction. The added calcium does reduce the H-Cl interaction. However, the lower stability by doping results in increased kinetics and thereby outweighed the lower H-Cl interaction. To exploit this delicate balance and find the optimal doping content, more elaborated doping studies utilizing the new ReaxFF are required.

## 7.1. INTRODUCTION

In the search towards a potential thermochemical heat storage material (TCM), both the chloride-based  $\text{MgCl}_2 \cdot n\text{H}_2\text{O}$  and  $\text{CaCl}_2 \cdot n\text{H}_2\text{O}$  are promising materials. Unfortunately, as discussed in the preceding Chapters, both salts suffer from inherent material characteristics that significantly hinder their actual use as TCM. For example, the low water transport through the salt crystals, as shown in Chapter 4, which reduces the power output and causes agglomerates that clog the thermochemical storage system. Other major drawbacks are the irreversible hydrolysis side reaction for the lower hydrates of  $\text{MgCl}_2 \cdot n\text{H}_2\text{O}$  upon dehydration at elevated temperatures ( $> 130^\circ\text{C}$ ) [33, 34] and the melting of the higher hydrates of  $\text{CaCl}_2 \cdot n\text{H}_2\text{O}$  at room conditions [25, 26]. A possible solution that increases the hydrolysis resistance is discussed in Chapter 2, where DFT chemical bond analysis showed that combining the two salts in terms of a double or compound salt could increase the hydrolysis resistance compared to the pristine  $\text{MgCl}_2 \cdot n\text{H}_2\text{O}$  salt. Chemical bond analysis revealed that chlorine bonds stronger to calcium than magnesium, and the  $\text{H}_2\text{O}$  molecule is less polar in a calcium environment. On the other side, it also showed that all explored salt structures that include both magnesium and calcium are less stable than the pure salts. In Chapter 4, it was shown that imperfections in the salt crystal, like cracks and pores, significantly increase the water mobility through the crystal. Thereby, it increases the hydration and dehydration rate. In Chapter 6, the hydration of salt  $\text{MgCl}_2 \cdot n\text{H}_2\text{O}$  is studied, and it is revealed that a water layer on top of the salt surface is needed to break the surface and initiate further hydration of the surface region.

The characterized phenomena in the previous chapters indicate that a doped salt hydrate might improve its TCM-related properties. It might increase the hydrolysis resistance of  $\text{MgCl}_2 \cdot n\text{H}_2\text{O}$ , reduce the surface stability, and increase the water diffusion through the salt. However, it simultaneously results in less stable structures, and the required amount of calcium for a significant hydrolysis reduction is unknown. To study these phenomena in-depth, we show the development and application of an  $\text{Mg}_{(1-x)}\text{Ca}_x\text{Cl}_4 \cdot n\text{H}_2\text{O}$  ReaxFF in this chapter.

The new  $\text{Mg}_{(1-x)}\text{Ca}_x\text{Cl}_4 \cdot n\text{H}_2\text{O}$  ReaxFF is a combination of the  $\text{MgCl}_2 \cdot n\text{H}_2\text{O}$  ( $n = 0, 1, 2, 4, 6$ ) force field developed in our group by Pathak et al. [40, 100], the  $\text{CaCl}_2 \cdot n\text{H}_2\text{O}$  ( $n = 0, 2$ ) force field as discussed in Chapter 3, and the  $\text{H}_2\text{O}$  force field that describes water at saturation conditions as discussed in Chapter 5. It is parameterized with the Metropolis Monte Carlo ReaxFF optimizer, developed by Iype et al. [83], which is extensively discussed in section 3.2.3. In section 7.2 of this chapter, the parameterization results are shown with respect to the used training data. After optimizing of the Mg–Ca interaction, we applied it to study doped  $\text{MgCl}_2 \cdot n\text{H}_2\text{O}$  and  $\text{CaCl}_2 \cdot n\text{H}_2\text{O}$  crystals in terms of stability, dehydration mechanisms, and HCl formation at elevated temperatures. All structures images in this chapter are created with OVITO [275].

## 7.2. REAXFF DEVELOPMENT

As explained in section 1.2.2, MD is a computational modeling method that describes atoms as point masses, lets them interact via interatomic potentials, and predicts their trajectories. From the particle trajectories, the dynamical behavior of the considered



atoms, many materialistic properties can be obtained via statistical thermodynamic rules [63]. We used the reactive force field formalism developed by van Duin et al. [81, 82, 124] to enable the modeling of chemical reactions that occur in the cycling of a TCM. This formalism is developed to bridge the gap between expensive quantum mechanical (QM) calculations (section 1.2.1) and classical non-reactive MD. QM is too expensive to use on large molecular systems over a time period, that is required to characterize the TCM, due to the expensive electronic calculations. Classical non-reactive MD can easily solve such large systems over a more extended time period due to its empirical description. However, it can not capture bond breaking and formation during the simulation. Like non-reactive MD, ReaxFF is also an empirical-based method. However, additionally it contains empirical bond-order terms that capture bond breaking and formation. This is key for the simulation of  $\text{MgCl}_2 \cdot n\text{H}_2\text{O}$ ,  $\text{CaCl}_2 \cdot n\text{H}_2\text{O}$ , and  $\text{Mg}_{(1-x)}\text{Ca}_x\text{Cl}_4 \cdot n\text{H}_2\text{O}$ . For example, MD simulations regarding the formation of HCl need to include covalent bond breaking and formation, thus requires ReaxFF. The different kinds of chemical atomic interactions are extensively analyzed and discussed in Chapter 2.

The ReaxFF potential is a summation of energy terms as given below:

$$E_{\text{system}} = E_{\text{bond}} + E_{\text{angle}} + E_{\text{torsion}} + E_{\text{H-bond}} + E_{\text{lp}} + E_{\text{over}} \\ + E_{\text{under}} + E_{\text{conj}} + E_{\text{vdW}} + E_{\text{Coul}} + E_{\text{others}}. \quad (7.1)$$

The  $E_{\text{vdW}}$  and  $E_{\text{Coul}}$  are the non-bonded van der Waals and Coulomb interactions between the atoms, respectively.  $E_{\text{others}}$  can be any additional interaction term assigned for some specific systems (e.g., H-bonds). The other terms are related to the bonded interactions. The energy terms are extensively discussed in Chapter 3. In order to model reactive molecular systems with Molecular Dynamics or Monte Carlo methods, accurate reactive force fields are essential. These force fields contain the parameters for the empirical interaction terms of (7.1). Combined, a ReaxFF contains easily  $\gg 100$  parameters, from which many need to be trained/parameterized.

### 7.2.1. MMC REAXFF PARAMETERIZATION

The parameterization of the newly – combined  $\text{Mg}_{(1-x)}\text{Ca}_x\text{Cl}_4 \cdot n\text{H}_2\text{O}$  – ReaxFF is done with the Metropolis Monte Carlo (MMC) optimizer, developed by Iype et al. [83]. This optimizer is based on the Metropolis Monte Carlo algorithm combined with simulated annealing. It enables multiple parameters optimization and allows escaping of local minima and exploration of an optimized global parameter configuration of the ReaxFF. In the search towards the optimal ReaxFF, the algorithm aims to minimize the cumulative squared error (Error) of the energy difference between ReaxFF and a reference data set:

$$\text{Error} = \sum_{i=1}^n \left[ \frac{X_{i,\text{ref}} - X_{i,\text{ReaxFF}}}{\sigma_i} \right]^2, \quad (7.2)$$

in which  $X_{i,\text{ref}}$  is the  $i$ th data point of the reference set,  $X_{i,\text{ReaxFF}}$  is the corresponding ReaxFF result, and  $\sigma_i$  is the weight given to that data point. An extensive explanation of the MMC optimizer can be found in Chapters 3 and 5. For the optimization of the  $\text{Mg}_{(1-x)}\text{Ca}_x\text{Cl}_4 \cdot n\text{H}_2\text{O}$  ReaxFF we used DFT data as references. The Amsterdam Density Functional (ADF) [187] was used, with the Perdew-Wang (GGA-PW92) exchange-correlation function [186], for the gas molecules reference data. For periodic molecular

reference structures, the Vienna Ab initio Simulation Package (VASP) [146], with the PBE [147] exchange-correlation functions were used with the PAW [148, 149] scheme. These were combined with the DFT-D3 [150, 151] corrections for long-range dispersion interactions. The structures were considered converged if all forces on the atoms are smaller than  $0.026 \text{ eV}/\text{\AA}$ . Both the ADF and VASP modeling packages have been used before to generate reference data, as discussed in Chapter 3 and by Pathak et al. [40, 59, 60, 100].

## MMC TRAINING RESULTS

The data set for the MMC optimization can contain all kinds of different data. However, relevant data must be included regarding the systems one wants to represent with the ReaxFF. Reference data for the pure  $\text{MgCl}_2 \cdot n\text{H}_2\text{O}$ ,  $\text{CaCl}_2 \cdot n\text{H}_2\text{O}$ , and  $\text{H}_2\text{O}$  saturation conditions were already successfully included by the independent force fields. Leaving the new Ca–Mg interaction open for necessary optimization. To obtain a valuable and transferable ReaxFF, the Ca–Mg reference data should include all possible forms that could occur in the (de)hydration of  $\text{Mg}_{(1-x)}\text{Ca}_x\text{Cl}_4 \cdot n\text{H}_2\text{O}$ . In this sense, we added gas molecule interactions of  $\text{MgCl}_2 \cdot n\text{H}_2\text{O}$  and  $\text{CaCl}_2 \cdot n\text{H}_2\text{O}$  gas molecules. We added equation of state bulk (periodic) structures, compressed and expanded  $\text{Mg}_{(1-x)}\text{Ca}_x\text{Cl}_4 \cdot n\text{H}_2\text{O}$ , comparable to the manually doped structures as introduced in Chapter 2. Furthermore, formation energy reference data was added for the most stable combined  $\text{Mg}_{(1-x)}\text{Ca}_x\text{Cl}_4$  structures found by USPEX [71–73] in Chapter 2. To ensure stable structures and simultaneously add non-zero temperature bulk structures, MD-generated frames were added to the reference set, which method is discussed in Chapter 3. Additionally, experimentally known tachyhydrite crystal structures [141, 166] were added.

Figure 7.1 shows the dissociation energy curves of different hydrated  $\text{MgCl}_2 \cdot n\text{H}_2\text{O}$  and  $\text{CaCl}_2 \cdot n\text{H}_2\text{O}$  gas molecules. From the DFT reference, it is shown that when  $\text{H}_2\text{O}$  is present, at the same distance ( $r$ ), multiple (meta) stable orientations can be found with different corresponding energies (see Figure 7.1 in the 3–4 Å range). These different orientations of the gas molecules cause the wrinkled energy profiles of the dissociation curves. Despite the complex wrinkled behavior, ReaxFF does accurately capture this dissociation.

Figure 7.2 shows a subset of the optimization results regarding the equation of state of  $\text{MgCl}_2 \cdot n\text{H}_2\text{O}$  structures. In Appendix G, other doping percentages and the tetrahydrate doped structures can be found. The figures show that the optimized ReaxFF can accurately capture the compression and stretching of doped crystal structures. From the optimization, it is found that the equation of states for the tachyhydrite structures is hard to accurately replicate. However, these tachyhydrite crystals are also found to be metastable structures themselves (as discussed in Chapter 2), which makes them hard to describe by a transferable force field.

Figure 7.3 shows the results of the formation energies by DFT and ReaxFF. The formation energy is the excess potential energy when the crystals' potential energy is subtracted by its constituent elements in their reference states – which equals the bonding energy between the constituent elements:

$$E_{\text{formation}} = E_{\text{crystal}} - N_{\text{CaCl}_2} \times E_{\text{CaCl}_2} - N_{\text{MgCl}_2} \times E_{\text{MgCl}_2}. \quad (7.3)$$

In which  $E_{\text{crystal}}$  is the energy of the crystal,  $N$  is the number of constituent elements in the crystal, and  $E_{\text{CaCl}_2}$  and  $E_{\text{MgCl}_2}$  are the corresponding gas molecule energies for  $\text{CaCl}_2$

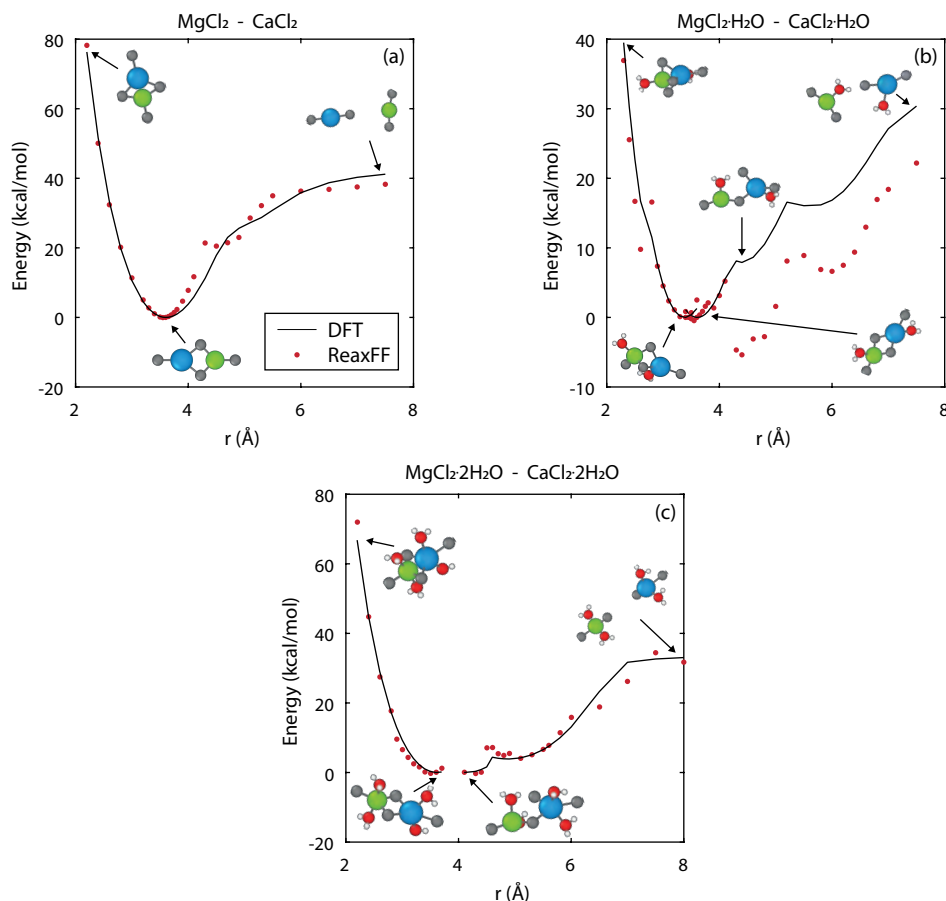


Figure 7.1: Dissociation energy of (a)  $\text{MgCl}_2 - \text{CaCl}_2$  gas molecules, (b)  $\text{MgCl}_2 \cdot \text{H}_2\text{O} - \text{CaCl}_2 \cdot \text{H}_2\text{O}$  gas molecules, and (c)  $\text{MgCl}_2 \cdot 2\text{H}_2\text{O} - \text{CaCl}_2 \cdot 2\text{H}_2\text{O}$  gas molecules. The insets represent the most stable structure add the indicated Ca–Mg distance, with blue as Ca, green as Mg, red as O, gray as Cl, and white as H. The solid black line represents the DFT reference value, and the red dots represent the ReaxFF energies.

and  $\text{MgCl}_2$ , respectively. The intermediate structures (33, 50, and 65%) were the most stable found structures for the anhydrous salt combinations by USPEX, as discussed in Chapter 2, 0% Ca content is the relaxed geometry of the known pure  $\text{MgCl}_2$  structure [139], and 100% Ca content is the relaxed geometry of the known pure  $\text{CaCl}_2$  structure [139]. The formation energy of the pure  $\text{MgCl}_2$  is under-predicted, and for  $\text{CaCl}_2$  slightly over-predicted. However, the resulting formation energies for the compound crystals match well with the given DFT reference.

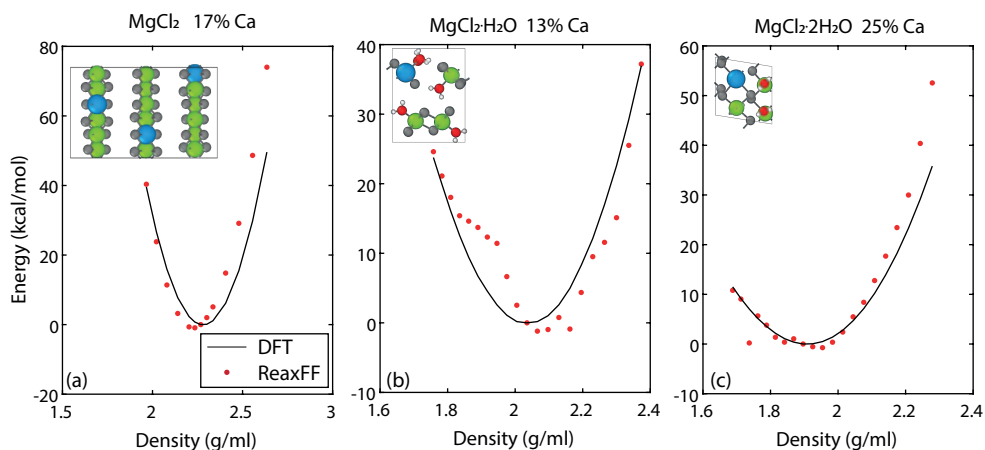


Figure 7.2: Compressed and stretched doped  $\text{MgCl}_2 \cdot n\text{H}_2\text{O}$  structures. (a)  $\text{MgCl}_2$  with 17% calcium, (b)  $\text{MgCl}_2 \cdot \text{H}_2\text{O}$  with 13% calcium, and (c)  $\text{MgCl}_2 \cdot 2\text{H}_2\text{O}$  with 25% calcium.

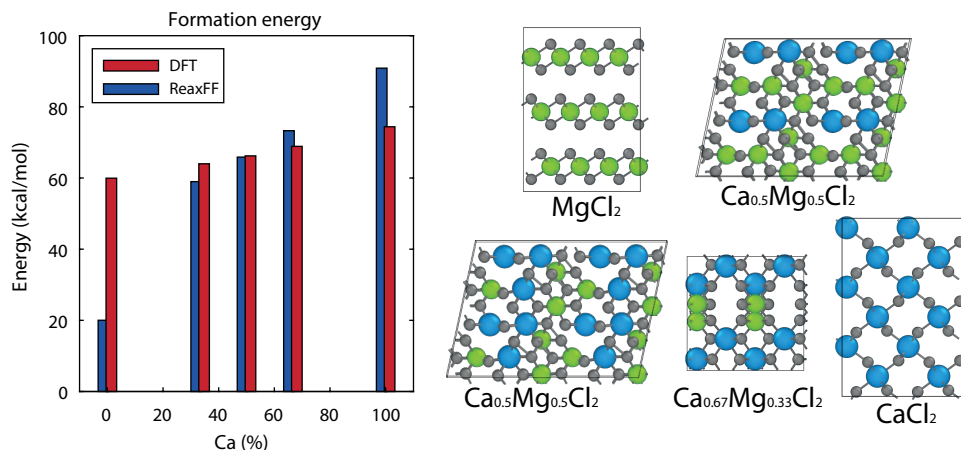


Figure 7.3: Formation energy of explored USPEX structures as given at the right-hand side. The x-axis gives the percentage of calcium of the total Ca/Mg atoms in the structure. The red bars represent the computed formation energies by DFT. The blue bars represent the ReaxFF calculated formation energies.

### 7.3. CHARACTERIZATION OF DOPED SALT HYDRATES

The newly developed ReaxFF for doped  $\text{CaCl}_2 \cdot 2\text{H}_2\text{O}$  and  $\text{MgCl}_2 \cdot 2\text{H}_2\text{O}$  is used to study the compound salt in terms of stability, dehydration mechanism, and hydrolysis.

#### 7.3.1. STABILITY DOPED STRUCTURES

To test the stability of the doped structures,  $\text{CaCl}_2 \cdot 2\text{H}_2\text{O}$  and  $\text{MgCl}_2 \cdot 2\text{H}_2\text{O}$  structures with 0, 10%, and 20% doping were slowly heated at constant atmospheric pressure. The pure crystals are the experimentally given structures for  $\text{CaCl}_2 \cdot 2\text{H}_2\text{O}$  [141] and  $\text{MgCl}_2 \cdot 2\text{H}_2\text{O}$

[140]. Figure 7.4a is a scatter plot of the potential energy for doped  $\text{CaCl}_2 \cdot 2\text{H}_2\text{O}$  structures as function of the temperature. The linear profiles at low temperatures indicate that the crystals remain in a crystalline structure. The non-linear behavior around 600–800 K, indicates the deformation transition of the structures. This temperature onset point for deformation is observed at lower temperatures when the amount of doping is increased, indicating the lower stability of the doped systems. Similar, Figure 7.4b is a scatter plot of the potential energy for doped  $\text{MgCl}_2 \cdot 2\text{H}_2\text{O}$  structures as function of the temperature. The deformation transition of the structures occurs around 600–700 K, and again at a slightly lower temperature for the doped  $\text{MgCl}_2 \cdot 2\text{H}_2\text{O}$  structures.

### 7.3.2. DEHYDRATION

In Chapter 3, it was shown that the morphology of the  $\text{CaCl}_2 \cdot 2\text{H}_2\text{O}$  slabs has a major influence on the dehydration mechanism and rate. It was shown that the dehydration in x-, and y-direction is much faster compared to the z-direction in which the layered  $\text{CaCl}_2$  structures impede  $\text{H}_2\text{O}$  molecules from evaporation. In Chapter 4, it was shown that not only the initial layered  $\text{CaCl}_2$  morphology has a major influence on the dehydration but also imperfections like cracks and voids. The appearance of cracks in (dehydrated) slabs creates pathways for the  $\text{H}_2\text{O}$  molecules to evaporate. Similar behavior was found for slabs with voids (5 and 10% deleted  $\text{CaCl}_2$  elements). In this sense, we studied the effect of imperfections by doping on the dehydration mechanisms. Similar to Chapter 3, pure  $\text{MgCl}_2 \cdot 2\text{H}_2\text{O}$  and  $\text{CaCl}_2 \cdot 2\text{H}_2\text{O}$  slabs were created, and accordingly with 10% doping. The simulated systems were first initialized within a periodic box over 150 ps, at atmospheric pressure, and at 500 K. The equilibrated systems were placed in a vacuum box, and every 25 ps, the evaporated  $\text{H}_2\text{O}$  molecules were deleted. The results of the  $\text{CaCl}_2 \cdot 2\text{H}_2\text{O}$  slabs are given in Figure 7.5. The solid lines represent the pure slabs and correspond with the systems of Chapter 3, the dashed lines represent the 10% Mg-doped  $\text{CaCl}_2 \cdot 2\text{H}_2\text{O}$  slabs. The figure shows that a  $\text{CaCl}_2 \cdot 2\text{H}_2\text{O}$  slab doped with 10% Mg initially dehydrates faster than the undoped structures, which can be attributed to the fast deformation in amorphous structures. The undoped structures in x- and y-directions become disordered after 3 ns and converge to the doped structures' dehydration rates. The snapshots show that the inner region of the undoped slab in z-direction remains crystalline, resulting in low water mobility. For the doped slab, the crystalline structure breaks easier, which results in increased dehydration.

In Figure 7.6, the dehydration of pure and doped  $\text{MgCl}_2 \cdot 2\text{H}_2\text{O}$  slabs are shown. This figure shows that the dehydration of the pure (undoped) slabs at 500 K is much slower than  $\text{CaCl}_2 \cdot 2\text{H}_2\text{O}$ , and initially, mainly the  $\text{H}_2\text{O}$  surface molecules dehydrate. This trend corresponds to experimental references, where  $\text{MgCl}_2 \cdot 2\text{H}_2\text{O}$  has a higher dehydration onset temperature than  $\text{CaCl}_2 \cdot 2\text{H}_2\text{O}$ , 400 K and 344 K, respectively [276]. Similar to the  $\text{CaCl}_2 \cdot 2\text{H}_2\text{O}$  structures, doping increases the dehydration rate significantly of  $\text{MgCl}_2 \cdot 2\text{H}_2\text{O}$ .

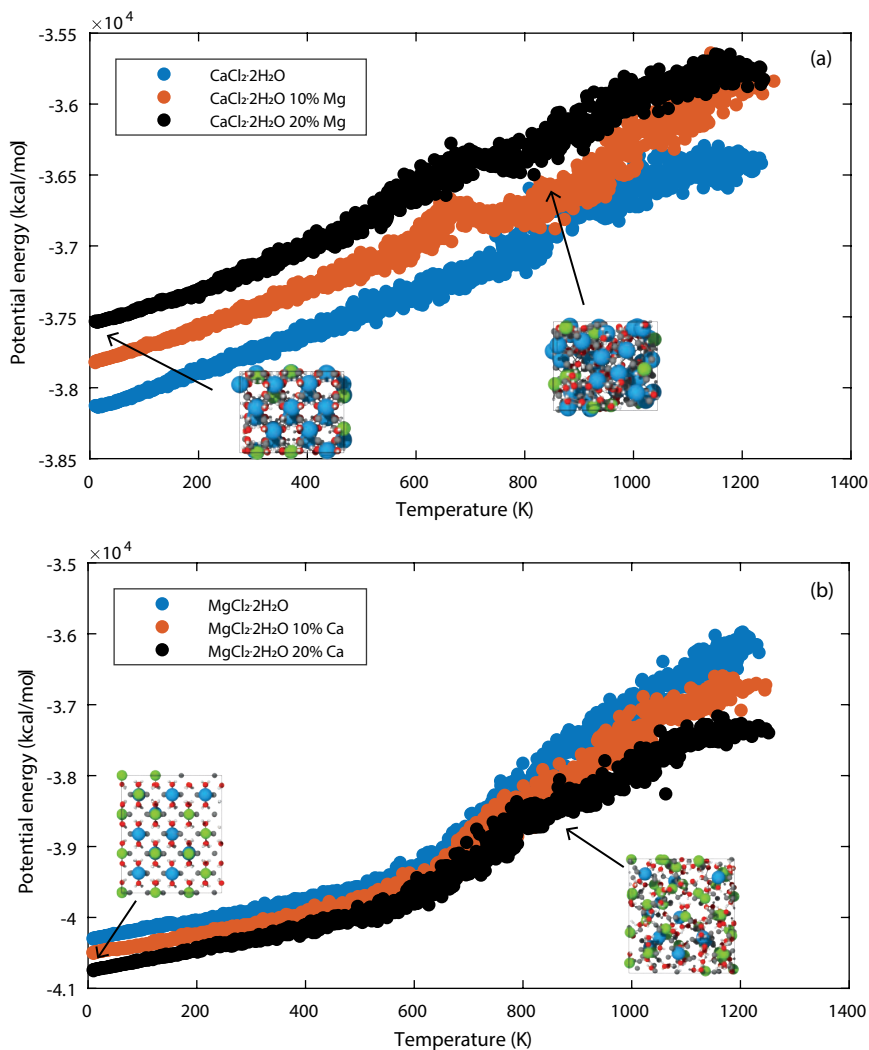


Figure 7.4: Potential energy of (a)  $\text{CaCl}_2 \cdot 2\text{H}_2\text{O}$ , and (b)  $\text{MgCl}_2 \cdot 2\text{H}_2\text{O}$ , structures versus the temperature of the system at 1 atm, with 0%, 10%, and 20% doping. The insets are representations of (a)  $\text{Ca}_{0.8}\text{Mg}_{0.2}\text{Cl}_2 \cdot 2\text{H}_2\text{O}$ , and (b)  $\text{Mg}_{0.8}\text{Ca}_{0.2}\text{Cl}_2 \cdot 2\text{H}_2\text{O}$  crystalline and disintegrated structures, at low and high temperatures, respectively

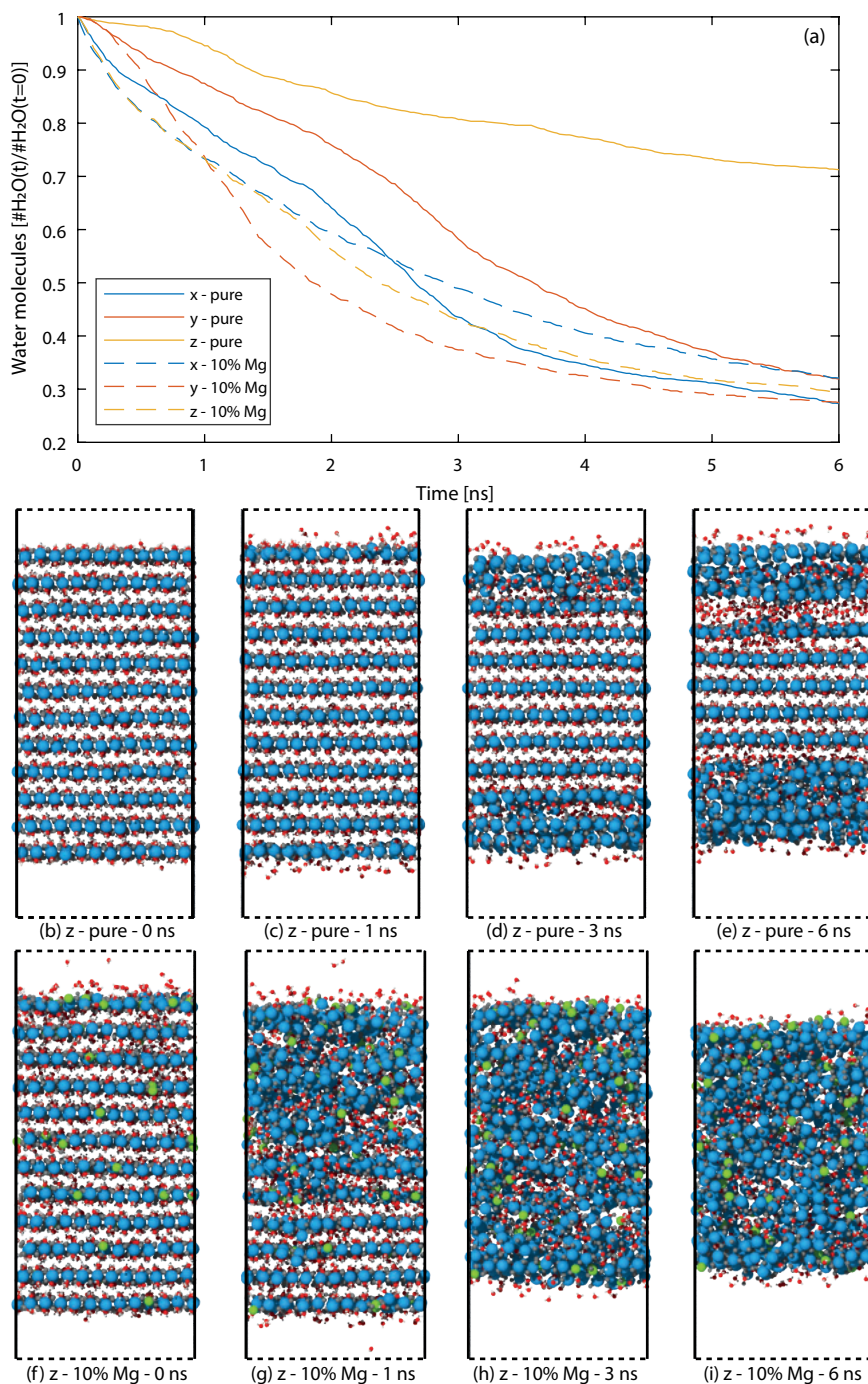


Figure 7.5: (a) dehydration of (doped)  $\text{CaCl}_2 \cdot 2\text{H}_2\text{O}$  at 500 K, with a vacuum in x-, y-, and z-direction, with solid lines for pure structures and dashed lines 10% Mg-doped structures. (b-i) corresponding snapshots of dehydrated frames, with blue as Ca, green as Mg, red as O, gray as Cl, and white as H.



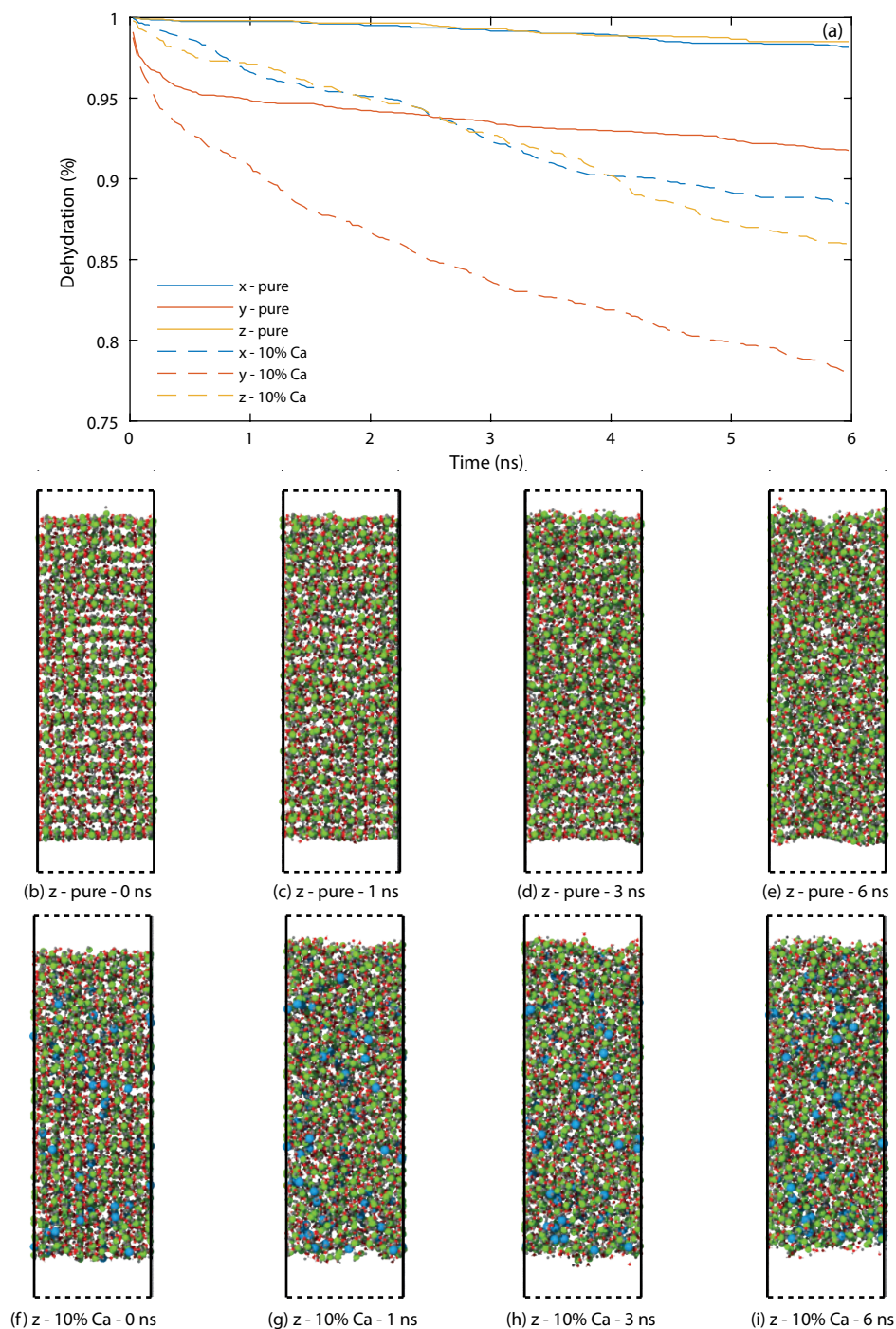


Figure 7.6: (a) dehydration of (doped)  $\text{MgCl}_2 \cdot 2\text{H}_2\text{O}$  at 500 K, with a vacuum in x-, y-, and z-direction, with solid lines for pure structures and dashed lines 10% Ca doped structures. (b-i) corresponding snapshots of dehydrated frames, with blue as Ca, green as Mg, red as O, gray as Cl, and white as H.



### 7.3.3. HYDROLYSIS RESISTANCE

From the DFT investigation in Chapter 2 of doped  $\text{MgCl}_2 \cdot 2\text{H}_2\text{O}$  and  $\text{CaCl}_2 \cdot 2\text{H}_2\text{O}$ , it was concluded that the H–Cl interaction decreases in a calcium environment compared to a magnesium environment. This is caused by the stronger Ca–Cl interaction and a less polar water molecule when bound to calcium. However, this chemical bonding analysis was performed on DFT optimized crystals, thus at 0 K. DFT–MD simulations would be too computationally expansive to perform. The DFT analysis also revealed that the doped structures are less stable than the pure structures, which was confirmed by the ReaxFF results in the previous section (Section 7.3.1).

Pathak et al. [40] already showed the applicability of ReaxFF–MD to study HCl formation of pure  $\text{MgCl}_2 \cdot \text{H}_2\text{O}$ . The newly developed ReaxFF enables the investigation of HCl formation of doped  $\text{MgCl}_2 \cdot 2\text{H}_2\text{O}$  and  $\text{CaCl}_2 \cdot 2\text{H}_2\text{O}$  structures. In Figure 7.7, the results are given for pure, 10%, and 20% doped slabs in a 1000 Å vacuum. The dihydrate structures are chosen because there are known structures for both salts. Similar to the results of Pathak et al., regarding the  $\text{MgCl}_2 \cdot \text{H}_2\text{O}$  (monohydrate), HCl formation is observed for pure  $\text{MgCl}_2 \cdot 2\text{H}_2\text{O}$  (dihydrate). Most Cl atoms that form HCl originate from the region close to the surface of the slab. Since the evaporated molecules from the slab are not removed from the vacuum box, which results in a vapor pressure around the salt hydrates, an equilibrium is reached in the first nano-second. From this point, both the dehydration and hydrolysis equilibrate. For  $\text{CaCl}_2 \cdot 2\text{H}_2\text{O}$ , hardly any HCl is observed, as expected from Chapter 2. Contrary to the expectation of the chemical bonding analysis of the static DFT calculations in Chapter 2, HCl formation is observed for the doped structures. This HCl formation can be attributed to the higher kinetics and crystal disintegration, related to the lower stability of the doped structures. In Section 7.3.2, it was already shown that this effect also increases the dehydration kinetics of the doped salts. The lower stability can also be found by figures 7.7c, 7.7e, and 7.7f (0%, 10%, and 20% doped  $\text{MgCl}_2 \cdot 2\text{H}_2\text{O}$ , respectively) where the pure structure has a crystalline central region, the 10% doped structure disintegrates in an amorphous cluster, and the 20% doped structure completely disintegrates in separated clusters. From this analysis, it can be concluded that the higher kinetics outweighs the fact of a lower HCl interaction in doped  $\text{MgCl}_2 \cdot 2\text{H}_2\text{O}$ . After  $\sim 0.5$  ns, Figure 7.7a shows a decrease of HCl caused by HCl solvation in (dehydrated-)water droplets within the simulation box, as shown by the inset. This effect is not present for pure  $\text{MgCl}_2 \cdot 2\text{H}_2\text{O}$  since less water is dehydrated, and as a result, no (dehydrated-)water droplet is present in the simulation box. As mentioned before, at some point, the 20% doped  $\text{MgCl}_2 \cdot 2\text{H}_2\text{O}$  structure disintegrates and separates in smaller clusters, increasing the HCl formation.

## 7.4. DISCUSSION

Based on the knowledge gained in the previous chapters, a new ReaxFF is successfully developed that can model  $\text{Mg}_{(1-x)}\text{Ca}_x\text{Cl}_4 \cdot n\text{H}_2\text{O}$ . This was done with the MMC optimizer [83] and included, among other data, compound and doped structures found in Chapter 2. The ReaxFF study confirmed the lower found stability of doped  $\text{MgCl}_2 \cdot 2\text{H}_2\text{O}$  and  $\text{CaCl}_2 \cdot 2\text{H}_2\text{O}$  compared to their pure forms. The created imperfections by doping the salts increase the dehydration of the salt hydrates significantly. This enhanced (de)hydration would benefit the TCM, as it enables higher water mobility and thus lower possibilities

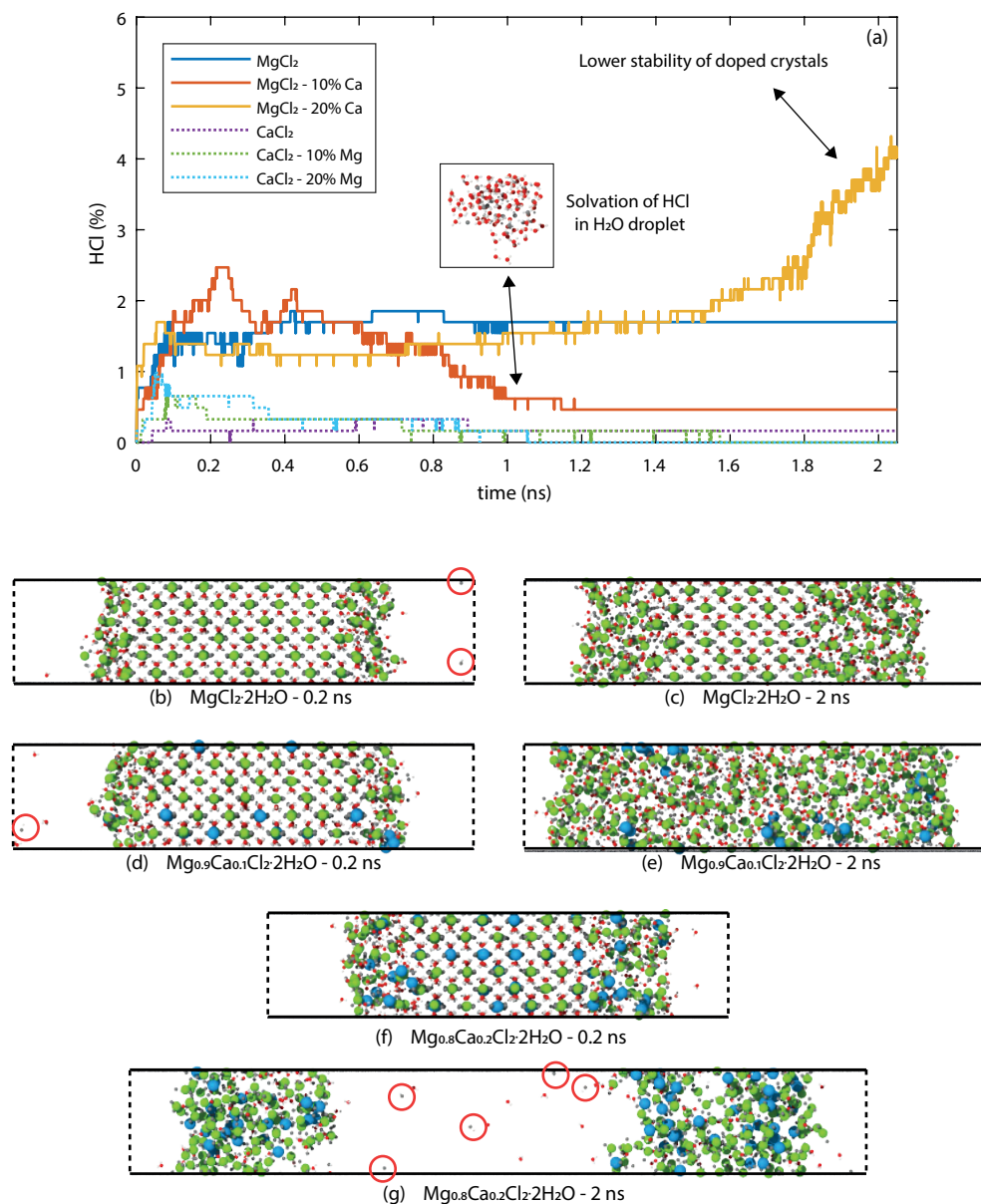


Figure 7.7: (a) HCl formation of (doped)  $\text{MgCl}_2 \cdot 2\text{H}_2\text{O}$  and  $\text{CaCl}_2 \cdot 2\text{H}_2\text{O}$  slabs in vacuum at 500 K. On the y-axis, the percentage of HCl molecules with respect to all Cl atoms are given. The inset represent a water droplet formed by dehydrated water for the doped  $\text{MgCl}_2 \cdot 2\text{H}_2\text{O}$  system. (b)-(c) snapshots of pure  $\text{MgCl}_2 \cdot 2\text{H}_2\text{O}$ . (d)-(e) snapshots of  $\text{MgCl}_2 \cdot 2\text{H}_2\text{O}$  with 10% Ca. (f)-(g) snapshots of  $\text{MgCl}_2 \cdot 2\text{H}_2\text{O}$  with 20% Ca. The red circles highlight HCl molecules.

of over-hydrated areas and agglomerations.

Contrary to what was found by chemical bonding analysis of Ca-doped  $\text{MgCl}_2 \cdot 2\text{H}_2\text{O}$ , the HCl formation is not reduced by doping. For equilibrated optimized structures (as in DFT), the H–Cl interaction decreases for doped  $\text{MgCl}_2 \cdot 2\text{H}_2\text{O}$ . However, doping also decreases the stability of the crystal. This lower stability increases the kinetics of the slabs, thereby not only increasing the water mobility but also the HCl formation. In this sense, it is recommended to investigate further the delicate balance between a decreased H–Cl interaction and increased kinetics of the less stable Ca-doped  $\text{MgCl}_2 \cdot n\text{H}_2\text{O}$ , regarding undesired hydrolysis of the TCM. To explore and find an optimized balance between these two phenomena, more systems should be considered – a larger range of doping, as well as different hydrates (e.g.  $n = 0, 1$ ), and a more extensive range of temperatures. Additionally, an experimental hydrolysis study, as proposed by the master thesis of Katyal within our research group [277], is essential to validate the hydrolysis findings. Furthermore, to exclude the HCl solvation effect within the ReaxFF-MD simulation, removing the evaporated HCl and  $\text{H}_2\text{O}$  molecules is recommended, as was done in the dehydration study.



# 8

## CONCLUSION & OUTLOOK

*Never trust Atoms!  
They make up everything.*

## 8.1. CONCLUSION

Thermochemical heat storage applications have the potential to serve as a vital link in the future renewable-based energy society regarding the storage of energy. This vital link bridges the mismatch between heat supply and heat demand via compact and efficient storage. Literature studies show that a selection of salt hydrates, including  $\text{MgCl}_2 \cdot n\text{H}_2\text{O}$  and  $\text{CaCl}_2 \cdot n\text{H}_2\text{O}$ , are promising thermochemical heat storage materials (TCMs) for the built environment. These are promising due to the equilibrium conditions of the reversible hydration reaction, which are in the operating region that can be reached with domestic applications. In theory, these salt hydrates can reach a high storage density up to  $1\text{--}3 \text{ GJ/m}^3$ . However, some practical challenges, related to the material characteristics, limit the application of these salt as truly valuable materials. Both salts suffer from a low thermal conductivity and slow water diffusion. The low thermal conductivity lowers the power output of the system and causes local hot spots. The low water diffusion also lowers the power output, and additionally, it can cause local over-hydration of the salt. If the water vapor pressure is too high, both salt experience deliquescence. At temperatures slightly above room conditions, the higher hydrates melt. Both the deliquescence and melting phenomena can cause agglomerates and clog the system. Another primary concern for the lower hydrates of  $\text{MgCl}_2$ , is the irreversible side reaction that forms  $\text{HCl}$ . These challenges result in numerous (ongoing) research towards modifying salt hydrates in favor of the thermochemical heat storage application. In this work, we studied vital TCM properties of  $\text{MgCl}_2 \cdot n\text{H}_2\text{O}$  and  $\text{CaCl}_2 \cdot n\text{H}_2\text{O}$  on a molecular and atomic level. Furthermore, we explored the feasibility of combining both salts in terms of doping and analyzed if these doped salts have superior material properties with respect to the pure forms. Some new reactive force fields and ReaxFF-MD modeling methods were developed to enable a fundamental analysis of these salts.

## 8

**Chemical analysis of doped salts hydrates** In Chapter 2, we explored the combination of  $\text{MgCl}_2 \cdot n\text{H}_2\text{O}$  and  $\text{CaCl}_2 \cdot n\text{H}_2\text{O}$  to form a double or doped salt on an electronic – DFT – level. This exploration was done by manually doping known pure  $\text{MgCl}_2 \cdot n\text{H}_2\text{O}$  ( $n = 0, 2, 4, 6$ ) with calcium, and vice versa. Additionally, the evolutionary algorithm US-PEX was used [71–73] to explore new possible  $\text{MgCl}_2$  and  $\text{CaCl}_2$  combinations. Using the convex Hull, we found that even the most stable configurations of the newly generated combined structures are less stable than the salts in their pure form. However, the energy difference between the convex Hull and the most stable structures is small. Thereby, decomposition of the doped salts into two separated pure salts will likely not occur. The hexahydrate structures are more affected than the lower hydrates, however, a crystal change above 25% calcium in the  $\text{MgCl}_2 \cdot 6\text{H}_2\text{O}$  salt crystal resulted in a stabilization of the hydrate structure compared to lower doped structures. Calcium atoms are larger than magnesium atoms, which results in an increased volume with an increase of calcium content. However, the volume increase is relatively larger than expected from interpolating the pure salts' crystal densities. The added calcium atoms create extra space and voids within the crystals. These effects decrease the volumetric energy density of the TCM. However, related research, revealed that the addition of calcium increases water mobility, especially near the surface of the salt.

Elaborative chemical bonding analysis with the DDEC6 and Bader Topological analy-

sis was applied to the most stable discovered hydrated structures. They validate a weaker Mg–Cl interaction compared to the Ca–Cl interaction. In combination with a more polar H<sub>2</sub>O molecule in a magnesium chloride environment, this weaker interaction gives rise to the HCl formation. This explains the experimentally found HCl formation at elevated temperatures for hydrated MgCl<sub>2</sub>, not for hydrated CaCl<sub>2</sub>.

**ReaxFF development** Additional to the first-principle DFT investigations of Chapter 2, MD studies are performed to characterize MgCl<sub>2</sub> · *n*H<sub>2</sub>O, CaCl<sub>2</sub> · *n*H<sub>2</sub>O, and their combination Mg<sub>(1−*x*)</sub>Ca<sub>*x*</sub>Cl<sub>4</sub> · *n*H<sub>2</sub>O as TCM application.

In Chapter 3, we showed and discussed the development of the CaCl<sub>2</sub> · *n*H<sub>2</sub>O (*n* = 0, 2) ReaxFF. To improve the force field, a new optimization protocol was used in combination with the Metropolis Monte Carlo (MMC) optimization algorithm of Iype et al. [83]. With intermediate generated force fields, MD-frames were generated; these frames were accordingly recomputed with DFT and added to the MMC training dataset. This protocol significantly increased the stability of CaCl<sub>2</sub> · *n*H<sub>2</sub>O structures, and the desired stability was validated with RDFs. Next to the newly developed CaCl<sub>2</sub> · *n*H<sub>2</sub>O force field, a MgCl<sub>2</sub> · *n*H<sub>2</sub>O (*n* = 0, 1, 2, 4, 6) force field was already developed within our group [100].

To accurately model the hydration and dehydration of the salts, the developed ReaxFF must describe water at saturation conditions. Thus, they must be able to describe the vapor–liquid equilibrium (VLE). In this sense, a H<sub>2</sub>O–lg ReaxFF was developed (and analogue a CO<sub>2</sub>–lg ReaxFF), as discussed in Chapter 5. To enable an accurate and complete description of the VLE, the addition of the lg–dispersion [234] parameters was required. These parameters allow optimization of the dispersion interaction within the ReaxFF without large interference of other pre-parameterized interactions. The lg parameters for H<sub>2</sub>O were trained with the MMC algorithm against the non-reactive TIP4P/2005 [229] long-range reference data and short-range DFT reference data. The ability of the newly H<sub>2</sub>O ReaxFF–lg to describe the VLE was validated with a newly developed ReaxFF Gibbs ensemble Monte Carlo (ReaxFF–GEMC) algorithm. The ReaxFF–GEMC algorithm showed an excellent agreement between the H<sub>2</sub>O–lg ReaxFF and experimental results of the VLE.

To study the characteristics of the combined salt (Mg<sub>(1−*x*)</sub>Ca<sub>*x*</sub>Cl<sub>4</sub> · *n*H<sub>2</sub>O), a new ReaxFF was developed. This force field combines the CaCl<sub>2</sub> · *n*H<sub>2</sub>O (*n* = 0, 2) force field as given in Chapter 3, with the MgCl<sub>2</sub> · *n*H<sub>2</sub>O (*n* = 0, 1, 2, 4, 6) force field of Pathak et al. [100], and the H<sub>2</sub>O ReaxFF–lg as given in Chapter 5. This newly combined reactive force field makes a fundamental analysis of heat and mass fluxes through the proposed combined salt possible. Additionally, it can provide information on non-zero temperature stabilities of the salt.

Next to the development of the new ReaxFFs, an advanced diffusion model was proposed and validated in Chapter 4. Accurate knowledge of local diffusion values is important since (cycled) TCM contain all kinds of local crystal imperfections like cracks and pores, which significantly influence the overall water mobility within the material. Where the conventional MD diffusion models – Einstein's' and Green–Kubo method – do not hold in a small inhomogeneous subregion, this method does. It is based on an analytical solution of the Smoluchowski diffusion equation for inhomogeneous matter and assumes a linear density profile over the considered subregion. The method was validated against the conventional diffusion calculation methods.

Regarding the molecular study on (de)hydration of TCMs, they mostly focused on dehydration until recently. This unilateral focus is related to the fact that MD studies of hydration are increasingly more cumbersome than dehydration studies. Dehydration driving forces can be increased by increasing the temperature. However, studying hydration is more cumbersome because it depends on rare events, nucleation rates, large (surface) hydration barriers, and slow water diffusion through the crystal. In this sense, we show the development of a WCA-ReaxFF-GCMC model in Chapter 6. This grand-canonical Monte Carlo (GCMC) model enables the loading of  $\text{H}_2\text{O}$  molecules within the TCM structure, without the MD-related required long-timescale hydration trajectories of the molecules. To avoid excessive ReaxFF calculations, numerous computationally cheap insertion trials preceded each ReaxFF-GCMC insertion trial. These cheap trials were performed with the short-range Weeks–Chandler–Andersen (WCA) potential. Accordingly, the most probable ones of the cheap trials have the highest probability of being recomputed with the more expensive ReaxFF potential. This combination increased the loading progress by more than an order of magnitude and significantly increased the final loading. The WCA-ReaxFF-GCMC model captured multiple equilibrium loadings of  $\text{MgCl}_2 \cdot n\text{H}_2\text{O}$  at a varying range from 6 to 50 mbar with a slight deviation from experimental equilibrium curves due to the use of a micro-particle in the model.

**Chloride-based TCM characteristics** With the newly developed  $\text{CaCl}_2 \cdot n\text{H}_2\text{O}$  force field, it was shown that the thermal conductivity of this salt is in the order 0.5–1.1 W/mK, comparable with reference values. These low values limit the power output of the storage system. However, it also showed that the thermal conductivity changes for different directions, related to the anisotropic morphology of the crystal. This anisotropic morphology also influences the dehydration of the salt, and it was observed that the dehydration in the z-direction – xy-plane – is significantly slower than the other two directions due to the layered  $\text{CaCl}_2$  morphology. Similar, dense dehydrated  $\text{CaCl}_2$  surface regions impede dehydration in all directions but especially in the z-direction due to the morphology. Contrary, arose pores increase the dehydration of  $\text{H}_2\text{O}$ . The developed advanced diffusion model confirmed the water mobility hypothesis of the dehydrated structures. It showed (at 500 K) hardly any diffusion in crystalline regions of the  $\text{CaCl}_2 \cdot 2\text{H}_2\text{O}$  ( $< 10^{-10} \text{ m}^2/\text{s}$ ) and a significant higher diffusion in and around cracks and pores of the salt ( $10^{-9}$  to  $10^{-8} \text{ m}^2/\text{s}$ ). These cracks and pores are formed upon cycling of the TCMs [177], which makes it highly probable that imperfections of the crystal largely dictate the water fluxes in TCM. Both the dehydration and diffusion studies showed hardly any  $\text{H}_2\text{O}$  movement at 300 K (within the accessible MD simulation time), which agrees with an experimental hydration and dehydration temperature of 336 and 344 K, respectively [174].

The WCA-ReaxFF-GCMC model enabled the hydration study of salts. The deliquescence equilibrium and the trend of multiple hydration levels of  $\text{MgCl}_2 \cdot n\text{H}_2\text{O}$  were successfully resembled by the model. From the studied hydration process, a fluidized nucleation process was observed [28, 29]. It shows that water first loads at the surface of the salt. Accordingly, this water layer breaks the salts' surface crystalline structure, thereby creating a disordered  $\text{MgCl}_2 + \text{H}_2\text{O}$  region. Consequently, the water can penetrate deeper into the deformed salt. This hydration process means that a deformed crystal salt structure would take up water faster than a "perfect" crystalline salt.



In agreement with the convex hull computed with DFT in Chapter 2, the newly developed  $\text{Mg}_{(1-x)}\text{Ca}_x\text{Cl}_4 \cdot n\text{H}_2\text{O}$  ReaxFF showed that doped crystals are stable in the crystalline morphology corresponding to the host salt. However, the doped structures are less stable than the pure salts, and therefore disintegrate at a lower temperature. As mentioned before, the water mobility in perfect crystalline bulk structures is extremely low, but by adding dopant, the water mobility increases significantly, which benefits the thermochemical storage application. From chemical bonding analysis, it was shown that the H–Cl interaction in a Ca-doped environment decreases compared to pure  $\text{MgCl}_2 \cdot 2\text{H}_2\text{O}$ . However, the increased instability of the doped salts outweighs this effect, and no decrease is found in terms of HCl formation for the studied (10% and 20%) Ca-doped  $\text{MgCl}_2 \cdot 2\text{H}_2\text{O}$  systems by ReaxFF simulations.

## 8.2. OUTLOOK

This work showed the value of using molecular models (DFT, MD, and MC) to characterize (new) TCMs, and applied them to chloride-based salt hydrates. These models can be used to compute or – in the case of new material – predict fundamental TCM properties, which are cumbersome to obtain from experiments. Next to the benefit of studying experimentally complex observable phenomena, these computational models can be used (pre-)analyze a wide variety of materials before expensive experimental methods are needed.

A first recommendation would be to further exploit the new  $\text{Mg}_{(1-x)}\text{Ca}_x\text{Cl}_4 \cdot n\text{H}_2\text{O}$  reactive force field, e.g., to study a more extensive range of doping percentages and compute important TCM properties like hydrolysis. Additionally, an experimental study of  $\text{Mg}_{(1-x)}\text{Ca}_x\text{Cl}_4 \cdot n\text{H}_2\text{O}$  salt could validate the findings and explore properties on a macroscopic scale. For example, the thesis of Katyal [277], showed the synthesis of the combined  $\text{Mg}_{(1-x)}\text{Ca}_x\text{Cl}_4 \cdot n\text{H}_2\text{O}$  salt and proposed a method to study the HCl release of these salts.

The developed computational methods in this work can be used to characterize future/unexplored new materials. The WCA–ReaxFF–GCMC can investigate equilibrium properties of new combinations of materials, such as stabilized salts by porous media, additives, or encapsulation. An important point not to forget is the final energy storage density for these new (combinations of) materials. This storage density is the key advantage of thermochemical energy storage systems over conventional storage methods and can be reduced quickly by combining low-/non-reactive materials. At this moment, numerous salts are considered and studied as possible TCM. However, many (~3000) of earth-abundant and inexpensive salts are still open to being characterized as TCM. In this sense, within our university [278], an open-access thermal energy storage platform is proposed and under development. This platform will focus on identifying or developing more efficient computational methods to study a more extensive set of materials and, using these new modeling approaches, to find new materials to store heat at the desired temperatures and pressures. The open database of the models and materials will allow for a fast development of new thermochemical storage systems collaboratively.

The computational ReaxFF models can aid not only in the discovery of new salt hydrates for TCMs but by all means in numerous other research fields. A bottleneck for such a wide implementation is the required development of (reactive) force fields. This

ReaxFF development is challenging and demanding due to the high dimensionality and many-body character of the potential energy surface of interatomic potentials. Subsequently, significant human effort is required to parameterize the force fields and determine the optimal balance of fitting against different target properties. To minimize this bottleneck of intensive force field development, a very recent and active research field is the use of ML-based optimization methods of (reactive) force fields [279]. Next to that, Neural Networks are recently developed not with the aim to train the force field but replace it [280]. They capture the potential energy surface of atomic interaction within the Neural Network. These latest Neural Networks can be complemented with (on-the-fly) active learning [281, 282]. As a result, the accuracy keeps increasing, and the models can be used outside the scope of the (original) training set. A more developed and mature field of this latest development of models that train or replace the conventional force fields, in combination with the developed MD methods, can ease the molecular study of new/unidentified materials.

# A

## APPENDIX – DEVELOPED REACTIVE FORCE FIELDS

Developed/modified ReaxFF force fields in this work:

- $\text{CaCl}_2 \cdot n\text{H}_2\text{O}$  ( $n = 0, 2$ ) (Appendix A.1.), discussed in Chapter 3
- $\text{H}_2\text{O}$ -lg (Appendix A.2.), discussed in Chapter 5
- $\text{CO}_2$ -lg (Appendix A.3.), discussed in Chapter 5
- $\text{Mg}_{(1-x)}\text{Ca}_x\text{Cl}_4 \cdot n\text{H}_2\text{O}$  ( $n = 0, 1, 2, 4, 6$ ) (Appendix A.4.), discussed in Chapter 7

These force fields are optimized using the Metropolis Monte Carlo (MMC) based algorithm which results are given in the following sections, and can be read by ReaxFF algorithms. Each listed parameter is either set to known physical values, non-active, or MMC optimized. For full detail of every parameter, we refer to the original work of van Duin et al. [81, 82]. The first line of the ReaxFF contains the description of the force field. This first line can also include the tag that enables the lg-dispersion interactions. Accordingly, it contains 7 sections which all include parameters corresponding to different kind of interactions. The first section contains 39 general parameters, which are usually the same for all force fields. The second section contains a list of generally transferable atomic parameters of all included atoms. The follow third–seventh sections contain bond, off-diagonal, valance, torsion, and hydrogen interactions, respectively.

## A.1. CALCIUM CHLORIDE HYDRATES

Reactive MD-force field: Ca/Cl/H/O

```

39      ! Number of general parameters
50.0000 !p_boc1 Eq(4c): Overcoordination parameter
9.5469 !p_boc2 Eq(4d): Overcoordination parameter
26.5405 !p_coa2 Eq(15): Valency angle conjugation
1.7224 !p_trip4 Eq(20): Triple bond stabilisation
6.8702 !p_trip3 Eq(20): Triple bond stabilisation
60.4850 !k_c2 Eq(19): C2-correction
1.0588 !p_ovun6 Eq(12): Undercoordination
4.6000 !p_trip2 Eq(20): Triple bond stabilisation
12.1176 !p_ovun7 Eq(12): Undercoordination
13.3056 !p_ovun8 Eq(12): Undercoordination
-70.5044 !p_trip1 Eq(20): Triple bond stabilization
0.0000 !Lower Taper-radius (must be 0)
10.0000 !R_cut Eq(21): Upper Taper-radius
2.8793 !p_fe1 Eq(6a): Fe dimer correction
33.8667 !p_val6 Eq(13c): Valency undercoordination
6.0891 !p_lp1 Eq(8): Lone pair param
1.0563 !p_val9 Eq(13f): Valency angle exponent
2.0384 !p_val10 Eq(13g): Valency angle parameter
6.1431 !p_fe2 Eq(6a): Fe dimer correction
6.9290 !p_pen2 Eq(14a): Double bond/angle param
0.3989 !p_pen3 Eq(14a): Double bond/angle param
3.9954 !p_pen4 Eq(14a): Double bond/angle param
-2.4837 !p_fe3 Eq(6a): Fe dimer correction
5.7796 !p_tor2 Eq(16b): Torsion/BO parameter
10.0000 !p_tor3 Eq(16c): Torsion overcoordination
1.9487 !p_tor4 Eq(16c): Torsion overcoordination
-1.2327 !p_elho Eq(26a): electron-hole interaction
2.1645 !p_cot2 Eq(17b): Conjugation if tors13=0
1.5591 !p_vdW1 Eq(23b): vdWaaals shielding
0.1000 !Cutoff for bond order (*100)
2.1365 !p_coa4 Eq(15): Valency angle conjugation
0.6991 !p_ovun4 Eq(11b): Over/Undercoordination
50.0000 !p_ovun3 Eq(11b): Over/Undercoordination
1.8512 !p_val8 Eq(13d): Valency/lone pair param
0.5000 !X_soft Eq(25): ACKS2 softness for X_ij
20.0000 !d Eq(23d): Scale factor in lg-dispersion
5.0000 !p_val Eq(27): Gauss exponent for electrons
0.0000 !l Eq(13e): disable undecoord in val angle
2.6962 !p_coa3 Eq(15): Valency angle conjugation
5      ! Nr of atoms; cov.r; valency;a.m;Rvdw;Evdw;gammaEEM;cov.r2;#
      alfa;gammavdW;valency;Eunder;Eover;chiEEM;etaEEM;n.u.
      cov r3;Elp;Heat inc.;bol131;bol132;bol133;softcut;n.u.
      ov/un;vall;n.u.;val3,vval4
C      1.3817 4.0000 12.0000 1.8903 0.1838 0.9000 1.1341 4.0000
      9.7559 2.1346 4.0000 34.9350 79.5548 5.9666 7.0000 0.0000
      1.2114 0.0000 202.5551 8.9539 34.9289 13.5366 0.8563 0.0000
      -2.8983 2.5000 1.0564 4.0000 2.9663 0.0000 0.0000 0.0000
H      0.8930 1.0000 1.0080 1.3550 0.0930 0.8203 -0.1000 1.0000
      8.2230 33.2894 1.0000 0.0000 121.1250 3.7248 9.6093 1.0000
      -0.1000 0.0000 61.6606 3.0408 2.4197 0.0003 1.0698 0.0000
      -19.4571 4.2733 1.0338 1.0000 2.8793 0.0000 0.0000 0.0000
O      1.2450 2.0000 15.9990 2.3890 0.1000 1.0898 1.0548 6.0000
      9.7300 13.8449 4.0000 37.5000 116.0768 8.5000 8.3122 2.0000
      0.9049 0.4056 59.0626 3.5027 0.7640 0.0021 0.9745 0.0000
      -3.5500 2.9000 1.0493 4.0000 2.9225 0.0000 0.0000 0.0000
Cl      1.7140 1.0000 35.4500 3.0207 0.0568 0.3640 -1.0000 7.0000
      10.5008 10.1330 1.0000 0.0000 0.0000 10.0000 6.0403 2.0000
      -1.0000 3.5750 143.1770 6.2290 35.2290 40.1540 20.8560 30.0000
      -10.2080 2.9867 1.0338 6.2998 2.5791 0.0000 0.0000 0.0000
Ca      1.9927 2.0000 40.0870 2.7005 0.1848 0.7939 1.0000 2.0000

```

```

10.6123 27.5993 3.0000 38.0000 0.0000 -1.9372 6.5275 0.0000
-1.3000 0.0000 220.0000 49.9248 0.3370 0.0000 0.0000 0.0000
-2.0000 4.0000 1.0564 6.2998 2.9663 0.0000 0.0000 0.0000
13 ! Nr of bonds; Ediss1;LPpen;n.u.;pbel;pbo5;13corr;pbo6
    pbe2;pbo3;pbo4;n.u.;pbo1;pbo2;ovcorr
1 1 158.2004 99.1897 78.0000 -0.7738 -0.4550 1.0000 37.6117 0.4147
    0.4590 -0.1000 9.1628 1.0000 -0.0777 6.7268 1.0000 0.0000
1 2 169.4760 0.0000 0.0000 -0.6083 0.0000 1.0000 6.0000 0.7652
    5.2290 1.0000 0.0000 1.0000 -0.0500 6.9136 0.0000 0.0000
2 2 153.3934 0.0000 0.0000 -0.4600 0.0000 1.0000 6.0000 0.7300
    6.2500 1.0000 0.0000 1.0000 -0.0790 6.0552 0.0000 0.0000
1 3 158.6946 107.4583 23.3136 -0.4240 -0.1743 1.0000 10.8209 1.0000
    0.5322 -0.3113 7.0000 1.0000 -0.1447 5.2450 0.0000 0.0000
3 3 142.2858 145.0000 50.8293 0.2506 -0.1000 1.0000 29.7503 0.6051
    0.3451 -0.1055 9.0000 1.0000 -0.1225 5.5000 1.0000 0.0000
2 3 160.0000 0.0000 0.0000 -0.5725 0.0000 1.0000 6.0000 0.5626
    1.1150 1.0000 0.0000 1.0000 -0.0920 4.2790 0.0000 0.0000
2 4 150.6697 0.0000 0.0000 -0.6499 -0.2000 0.0000 16.0000 0.8645
    3.8414 -0.2000 15.0000 1.0000 -0.2000 6.8063 0.0000 0.0000
3 4 0.0000 0.0000 0.0000 0.5000 0.0000 0.0000 16.0000 0.5000
    1.0001 -0.2000 15.0000 1.0000 -0.1000 15.0000 0.0000 0.0000
4 4 7.1986 0.0000 0.0000 0.4564 -0.2000 0.0000 16.0000 0.5104
    -0.4028 -0.2000 15.0000 1.0000 -0.1070 15.0000 0.0000 0.0000
2 5 11.1950 0.0000 0.0000 -0.0203 -0.1418 1.0000 13.1260 0.0230
    7.2684 -0.1310 0.0000 1.0000 -0.2692 6.4254 0.0000 24.4461
3 5 62.4691 0.0000 43.3991 0.4608 -0.3000 1.0000 36.0000 0.1013
    -0.0555 -0.2500 12.0000 1.0000 -0.0906 7.3386 1.0000 24.4461
5 5 10.5739 0.0000 0.0000 -0.2046 -0.2000 0.0000 16.0000 0.3791
    -0.0653 -0.2000 10.0000 1.0000 -0.0766 4.0237 0.0000 0.0000
5 4 70.7290 0.0000 0.0000 -0.3145 -0.2000 0.0000 16.0000 0.1492
    34.8673 -0.2000 15.0000 0.9915 -0.0289 4.8584 0.0000 0.0000
8 ! Nr of off-diagonal terms; Ediss;Ro;gamma;rsigma;rpi;rp2
1 2 0.1239 1.4004 9.8467 1.1210 -1.0000 -1.0000
2 3 0.0283 1.2885 10.9190 0.9215 -1.0000 -1.0000
1 3 0.1156 1.8520 9.8317 1.2854 1.1352 1.0706
2 4 0.1695 1.6156 9.7834 1.4740 -1.0000 -1.0000
3 4 0.1491 2.3500 10.1159 -1.0000 -1.0000 -1.0000
2 5 0.0100 1.6000 13.2979 -1.0000 -1.0000 -1.0000
3 5 0.1106 1.5902 13.2197 1.9305 -1.0000 -1.0000
5 4 0.3234 2.1332 10.2014 1.4542 -1.0000 -1.0000
34 ! Nr of angles;at1;at2;at3;Thetao,o;ka;kb;pv1;pv2
1 1 1 59.0573 30.7029 0.7606 0.0000 0.7180 6.2933 1.1244
1 1 2 65.7758 14.5234 6.2481 0.0000 0.5665 0.0000 1.6255
2 1 2 70.2607 25.2202 3.7312 0.0000 0.0050 0.0000 2.7500
1 2 2 0.0000 0.0000 6.0000 0.0000 0.0000 0.0000 1.0400
1 2 1 0.0000 3.4110 7.7350 0.0000 0.0000 0.0000 1.0400
2 2 2 0.0000 27.9213 5.8635 0.0000 0.0000 0.0000 1.0400
1 1 3 49.6811 7.1713 4.3889 0.0000 0.7171 10.2661 1.0463
1 3 3 77.7473 40.1718 2.9802 -25.3063 1.6170 -46.1315 2.2503
2 1 3 65.0000 13.8815 5.0583 0.0000 0.4985 0.0000 1.4900
1 3 1 73.5312 44.7275 0.7354 0.0000 3.0000 0.0000 1.0684
1 3 3 79.4761 36.3701 1.8943 0.0000 0.7351 67.6777 3.0000
3 3 3 80.7324 30.4554 0.9953 0.0000 1.6310 50.0000 1.0783
1 3 2 70.1880 20.9562 0.3864 0.0000 0.0050 0.0000 1.6924
2 3 3 75.6935 50.0000 2.0000 0.0000 1.0000 0.0000 1.1680
2 3 2 85.8000 9.8453 2.2720 0.0000 2.8635 0.0000 1.5800
1 2 3 0.0000 25.0000 3.0000 0.0000 1.0000 0.0000 1.0400
3 2 3 0.0000 15.0000 2.8900 0.0000 0.0000 0.0000 2.8774
2 2 3 0.0000 8.5744 3.0000 0.0000 0.0000 0.0000 1.0421
3 2 4 0.0000 0.5102 0.0100 0.0000 0.0000 0.0000 1.3399
4 2 4 0.0000 5.0000 1.0000 0.0000 1.0000 0.0000 1.2500
3 5 3 9.4193 6.5874 0.1170 0.0000 0.5754 0.0000 1.9245
5 3 5 5.3223 15.1865 2.1599 0.0000 1.9819 0.0000 2.0308
2 3 5 50.5960 3.4274 11.0889 0.0000 0.0500 0.0000 1.0571
3 3 5 73.1181 25.3522 1.0106 0.0000 1.0000 0.0000 1.1208

```

5	4	5	18.1000	-27.0162	5.9208	-2.5668	1.0000	0.0000	1.0307
4	5	4	128.9965	-18.4910	18.7610	0.0859	1.0000	0.0000	1.0614
3	5	4	49.9564	-3.3582	6.4075	0.0000	1.0000	0.0000	2.6422
2	5	2	0.0000	51.5084	0.2095	0.0000	2.1642	0.0000	2.3541
2	2	5	0.0000	39.4044	2.8341	0.0000	1.1378	0.0000	1.0860
5	2	5	0.0000	0.7476	0.5163	0.0000	0.8491	0.0000	4.6650
2	5	5	0.0000	9.0927	0.3829	0.0000	3.5143	0.0000	1.1566
2	5	3	0.0000	36.0055	0.3339	0.0000	0.9089	0.0000	1.9411
5	4	4	4.2053	10.4848	0.4567	0.0000	1.0094	0.0000	1.3668
5	4	2	133.5715	10.4411	1.4862	0.0000	0.0000	0.0000	1.0142
29	! Nr of torsions;at1;at2;at3;at4;;V1;V2;V3;V2(BO);vconj;n.u;n								
1	1	1	1	-0.2500	34.7453	0.0288	-6.3507	-1.6000	0.0000
1	1	1	2	-0.2500	29.2131	0.2945	-4.9581	-2.1802	0.0000
2	1	1	2	-0.2500	31.2081	0.4539	-4.8923	-2.2677	0.0000
1	1	1	3	-0.3495	22.2142	-0.2959	-2.5000	-1.9066	0.0000
2	1	1	3	0.0646	24.3195	0.6259	-3.9603	-1.0000	0.0000
3	1	1	3	-0.5456	5.5756	0.8433	-5.1924	-1.0180	0.0000
1	1	3	1	1.7555	27.9267	0.0072	-2.6533	-1.0000	0.0000
1	1	3	2	-1.4358	36.7830	-1.0000	-8.1821	-1.0000	0.0000
2	1	3	1	-1.3959	34.5053	0.7200	-2.5714	-2.1641	0.0000
2	1	3	2	-2.5000	70.0597	1.0000	-3.5539	-2.9929	0.0000
1	1	3	3	0.6852	11.2819	-0.4784	-2.5000	-2.1085	0.0000
2	1	3	3	0.1933	80.0000	1.0000	-4.0590	-3.0000	0.0000
3	1	3	1	-1.9889	76.4820	-0.1796	-3.8301	-3.0000	0.0000
3	1	3	2	0.2160	72.7707	-0.7087	-4.2100	-3.0000	0.0000
3	1	3	3	-2.5000	71.0772	0.2542	-3.1631	-3.0000	0.0000
1	3	3	1	2.5000	-0.6002	1.0000	-3.4297	-2.8858	0.0000
1	3	3	2	-2.5000	-3.3822	0.7004	-5.4467	-2.9586	0.0000
2	3	3	2	2.5000	-4.0000	0.9000	-2.5000	-1.0000	0.0000
1	3	3	3	1.2329	-4.0000	1.0000	-2.5000	-1.7479	0.0000
2	3	3	3	0.8302	-4.0000	-0.7763	-2.5000	-1.0000	0.0000
3	3	3	3	-2.5000	-4.0000	1.0000	-2.5000	-1.0000	0.0000
0	1	2	0	0.0000	0.0000	0.0000	0.0000	0.0000	0.0000
0	2	2	0	0.0000	0.0000	0.0000	0.0000	0.0000	0.0000
0	2	3	0	0.0000	0.1000	0.0200	-2.5415	0.0000	0.0000
0	1	1	0	0.0000	50.0000	0.3000	-4.0000	-2.0000	0.0000
0	3	3	0	0.5511	25.4150	1.1330	-5.1903	-1.0000	0.0000
1	1	3	3	-2.0000	73.0530	1.5000	-9.0000	-2.0000	0.0000
1	3	3	1	0.0002	80.0000	-1.5000	-2.5000	-2.0000	0.0000
3	1	3	3	-1.8835	20.0000	1.5000	-9.0000	-2.0000	0.0000
3	! Nr of hydrogen bonds;at1;at2;at3;Rhb;Dehb;vhb1								
3	2	3	2.1200	-3.5800	1.4500	19.5000			
3	2	4	1.8833	-3.6250	1.4500	19.5000			
4	2	3	1.8487	-0.0100	1.4500	19.5000			

## A.2. WATER LIQUID-VAPOR EQUILIBRIUM

```
[ lgDispersion=1 ] Reactive MD-force field for VLE of H2O
39      ! Number of general parameters
50.0000 !p_boc1 Eq(4c): Overcoordination parameter
9.5469 !p_boc2 Eq(4d): Overcoordination parameter
26.5405 !p_coa2 Eq(15): Valency angle conjugation
1.7224 !p_trip4 Eq(20): Triple bond stabilisation
6.8702 !p_trip3 Eq(20): Triple bond stabilisation
60.4850 !k_c2 Eq(19): C2-correction
1.0588 !p_ovun6 Eq(12): Undercoordination
4.6000 !p_trip2 Eq(20): Triple bond stabilisation
12.1176 !p_ovun7 Eq(12): Undercoordination
13.3056 !p_ovun8 Eq(12): Undercoordination
-70.5044 !p_trip1 Eq(20): Triple bond stabilization
0.0000 !Lower Taper-radius (must be 0)
10.0000 !R_cut Eq(21): Upper Taper-radius
2.8793 !p_fel Eq(6a): Fe dimer correction
33.8667 !p_val6 Eq(13c): Valency undercoordination
6.0891 !p_lp1 Eq(8): Lone pair param
1.0563 !p_val9 Eq(13f): Valency angle exponent
2.0384 !p_val10 Eq(13g): Valency angle parameter
6.1431 !p_fe2 Eq(6a): Fe dimer correction
6.9290 !p_pen2 Eq(14a): Double bond/angle param
0.3989 !p_pen3 Eq(14a): Double bond/angle param
3.9954 !p_pen4 Eq(14a): Double bond/angle param
-2.4837 !p_fe3 Eq(6a): Fe dimer correction
5.7796 !p_tor2 Eq(16b): Torsion/BO parameter
10.0000 !p_tor3 Eq(16c): Torsion overcoordination
1.9487 !p_tor4 Eq(16c): Torsion overcoordination
-1.2327 !p_elho Eq(26a): electron-hole interaction
2.1645 !p_cot2 Eq(17b): Conjugation if torsl3=0
1.5591 !p_vdW1 Eq(23b): vdWaaals shielding
0.1000 !Cutoff for bond order (*100)
2.1365 !p_coa4 Eq(15): Valency angle conjugation
0.6991 !p_ovun4 Eq(11b): Over/Undercoordination
50.0000 !p_ovun3 Eq(11b): Over/Undercoordination
1.8512 !p_val8 Eq(13d): Valency/lone pair param
0.5000 !X_soft Eq(25): ACKS2 softness for X_ij
1.0000 !d Eq(23d): Scale factor in lg-dispersion
5.0000 !p_val Eq(27): Gauss exponent for electrons
0.0000 !l Eq(13e): disable undecoord in val angle
2.6962 !p_coa3 Eq(15): Valency angle conjugation
2      ! Nr of atoms; cov.r; valency;a.m;Rvdw;Evdw;gammaEEM;cov.r2;#
      alfa;gammavdW;valency;Eunder;Eover;chiEEM;etaEEM;n.u.
      cov_r3;Elp;Heat inc.;bo131;bo132;bo133;softcut;n.u.
      ov/un;vall;n.u.;val3,vval4
H      0.8930 1.0000 1.0080 1.3550 0.0930 0.8203 -0.1000 1.0000
      8.2230 33.2894 1.0000 0.0000 121.1250 4.3065 8.3445 1.0000
      -0.1000 0.0000 61.6606 3.0408 2.4197 0.0003 1.0698 0.0000
      -19.4571 4.2733 1.0338 1.0000 2.8793 0.0000 0.0000 0.0000
      0.0000 0.0000
O      1.2450 2.0000 15.9990 2.3890 0.1000 1.0898 1.0548 6.0000
      9.7300 13.8449 4.0000 37.5000 116.0768 7.8651 7.8466 2.0000
      0.9049 0.4056 59.0626 3.5027 0.7640 0.0021 0.9745 0.0000
      -3.5500 2.9000 1.0493 4.0000 2.9225 0.0000 0.0000 0.0000
      142.9733 1.7500
3      ! Nr of bonds; Edisl;LPpen;n.u.;pbe1;pbo5;13corr;pbo6;
      pbe2;pbo3;pbo4;n.u.;pbo1;pbo2;ovcorr
1 1 153.3934 0.0000 0.0000 -0.4600 0.0000 1.0000 6.0000 0.7300
      6.2500 1.0000 0.0000 1.0000 -0.0790 6.0552 0.0000 0.0000
2 2 142.2858 145.0000 50.8293 0.2506 -0.1000 1.0000 29.7503 0.6051
      0.3451 -0.1055 9.0000 1.0000 -0.1225 5.5000 1.0000 0.0000
```

```

1 2 160.0000 0.0000 0.0000 -0.5725 0.0000 1.0000 6.0000 0.5626
    1.1150 1.0000 0.0000 1.0000 -0.0920 4.2790 0.0000 0.0000
1 ! Nr of off-diagonal terms; Ediss;Ro;gamma;rsigma;rpi;rpi2
1 2 0.0283 1.2885 10.9190 0.9215 -1.0000 -1.0000 0.0000
6 ! Nr of angles;at1;at2;at3;Thetao,o;ka;kb;pv1;pv2
1 1 1 0.0000 27.9213 5.8635 0.0000 0.0000 0.0000 1.0400
2 2 2 80.7324 30.4554 0.9953 0.0000 1.6310 50.0000 1.0783
1 2 2 75.6935 50.0000 2.0000 0.0000 1.0000 0.0000 1.1680
1 2 1 85.8000 9.8453 2.2720 0.0000 2.8635 0.0000 1.5800
2 1 2 0.0000 15.0000 2.8900 0.0000 0.0000 0.0000 2.8774
1 1 2 0.0000 8.5744 3.0000 0.0000 0.0000 0.0000 1.0421
6 ! Nr of torsions;at1;at2;at3;at4;V1;V2;V3;V2(BO);vconj;n.u;n
1 2 2 1 2.5000 -4.0000 0.9000 -2.5000 -1.0000 0.0000 0.0000
1 2 2 2 0.8302 -4.0000 -0.7763 -2.5000 -1.0000 0.0000 0.0000
2 2 2 2 -2.5000 -4.0000 1.0000 -2.5000 -1.0000 0.0000 0.0000
0 1 1 0 0.0000 0.0000 0.0000 0.0000 0.0000 0.0000 0.0000
0 1 2 0 0.0000 0.1000 0.0200 -2.5415 0.0000 0.0000 0.0000
0 2 2 0 0.5511 25.4150 1.1330 -5.1903 -1.0000 0.0000 0.0000
1 ! Nr of hydrogen bonds;at1;at2;at3;Rhb;Dehb;vhb1
2 1 2 2.1200 -3.5800 1.4500 19.5000

```



### A.3. CARBON DIOXIDE LIQUID-VAPOR EQUILIBRIUM

```
[ lgDispersion=1 ] Reactive MD-force field for VLE of CO2
39      ! Number of general parameters
50.0000 !p_boc1 Eq(4c): Overcoordination parameter
9.5469  !p_boc2 Eq(4d): Overcoordination parameter
26.5405 !p_coa2 Eq(15): Valency angle conjugation
1.5105  !p_trip4 Eq(20): Triple bond stabilisation
6.6630  !p_trip3 Eq(20): Triple bond stabilisation
0.0000  !k_c2 Eq(19): C2-correction
1.0588  !p_ovun6 Eq(12): Undercoordination
4.6000  !p_trip2 Eq(20): Triple bond stabilisation
12.1176 !p_ovun7 Eq(12): Undercoordination
13.3056 !p_ovun8 Eq(12): Undercoordination
-70.1292 !p_trip1 Eq(20): Triple bond stabilization
0.0000  !Lower Taper-radius (must be 0)
10.0000 !R_cut Eq(21): Upper Taper-radius
0.0000  !p_fel Eq(6a): Fe dimer correction
33.8667 !p_val6 Eq(13c): Valency undercoordination
6.0891  !p_lp1 Eq(8): Lone pair param
1.0563  !p_val9 Eq(13f): Valency angle exponent
2.0384  !p_val10 Eq(13g): Valency angle parameter
6.1431  !p_fe2 Eq(6a): Fe dimer correction
6.9290  !p_pen2 Eq(14a): Double bond/angle param
0.3989  !p_pen3 Eq(14a): Double bond/angle param
3.9954  !p_pen4 Eq(14a): Double bond/angle param
0.0000  !p_fe3 Eq(6a): Fe dimer correction
5.7796  !p_tor2 Eq(16b): Torsion/BO parameter
10.0000 !p_tor3 Eq(16c): Torsion overcoordination
1.9487  !p_tor4 Eq(16c): Torsion overcoordination
0.0000  !p_elho Eq(26a): electron-hole interaction
2.1645  !p_cot2 Eq(17b): Conjugation if torsl3=0
1.5591  !p_vdW1 Eq(23b): vdWals shielding
0.1000  !Cutoff for bond order (*100)
2.1365  !p_coa4 Eq(15): Valency angle conjugation
0.6991  !p_ovun4 Eq(11b): Over/Undercoordination
50.0000 !p_ovun3 Eq(11b): Over/Undercoordination
1.8512  !p_val8 Eq(13d): Valency/lone pair param
0.0000  !X_soft Eq(25): ACKS2 softness for X_ij
0.0000  !d Eq(23d): Scale factor in lg-dispersion
0.0000  !p_val Eq(27): Gauss exponent for electrons
0.0000  !l Eq(13e): disable undecoord in val angle
2.6962  !p_coa3 Eq(15): Valency angle conjugation
3      ! Nr of atoms; cov.r; valency;a.m;Rvdw;Evdw;gammaEEM;cov.r2;#
      alfa;gammavdW;valency;Eunder;Eover;chiEEM;etaEEM;n.u.
      cov_r3;Elp;Heat inc.;bo131;bo132;bo133;softcut;n.u.
      ov/un;vall;n.u.;val3,vval4
C      1.3825  4.0000  12.0000  1.9133  0.1853  0.9000  1.1359  4.0000
      9.7602  2.1346  4.0000  33.2433  79.5548  0.9350  8.7378  0.0000
      1.2104  0.0000  199.0303  8.6991  34.7289  13.3894  0.8563  0.0000
      -2.8983  2.5000  1.0564  4.0000  2.9663  0.0000  0.0000  0.0000
      249.5817  1.9255
H      0.7853  1.0000  1.0080  1.5904  0.0419  1.0206  -0.1000  1.0000
      9.3557  5.0518  1.0000  0.0000  121.1250  5.3200  7.4366  1.0000
      -0.1000  0.0000  62.4879  1.9771  3.3517  0.7571  1.0698  0.0000
      -15.7683  2.1488  1.0338  1.0000  2.8793  0.0000  0.0000  0.0000
      0.0000  1.4430
O      1.2477  2.0000  15.9990  1.9236  0.0904  1.0503  1.0863  6.0000
      10.2127  7.7719  4.0000  36.9573  116.0768  6.5498  8.2012  2.0000
      0.9088  1.0003  60.8726  20.4140  3.3754  0.2702  0.9745  0.0000
      -3.6141  2.7025  1.0493  4.0000  2.9225  0.0000  0.0000  0.0000
      14.9286  1.7500
6      ! Nr of bonds; Edis1;LPpen;n.u.;pbe1;pbo5;13corr;pbo6
```

A

```

pbe2;pbo3;pbo4;n.u.;pbo1;pbo2;ovcorr
1 1 156.5953 100.0397 80.0000 -0.8157 -0.4591 1.0000 37.7369 0.4235
   0.4527 -0.1000 9.2605 1.0000 -0.0750 6.8316 1.0000 0.0000
1 2 170.2316 0.0000 0.0000 -0.5931 0.0000 1.0000 6.0000 0.7140
   5.2267 1.0000 0.0000 1.0000 -0.0500 6.8315 0.0000 0.0000
2 2 156.0973 0.0000 0.0000 -0.1377 0.0000 1.0000 6.0000 0.8240
   2.9907 1.0000 0.0000 1.0000 -0.0593 4.8358 0.0000 0.0000
1 3 160.4802 105.1693 23.3059 -0.3873 -0.4867 1.0000 36.5037 1.0000
   0.5341 -0.6251 2.7677 1.0000 -0.1463 5.2913 0.0000 0.0000
3 3 60.1463 176.6202 51.1430 -0.2802 -0.1244 1.0000 29.6439 0.9114
   0.2441 -0.1239 7.6487 1.0000 -0.1302 6.2919 1.0000 0.0000
2 3 180.4373 0.0000 0.0000 -0.8074 0.0000 1.0000 6.0000 0.5514
   1.2490 1.0000 0.0000 1.0000 -0.0657 5.0451 0.0000 0.0000
3 ! Nr of off-diagonal terms; Ediss;Ro;gamma;rsigma;rpi;rp12
1 2 0.1219 1.4000 9.8442 1.1203 -1.0000 -1.0000 0.0000
2 3 0.0344 1.6800 10.3247 0.9013 -1.0000 -1.0000 0.0000
1 3 0.1131 1.8523 9.8442 1.2775 1.1342 1.0621 127.1788
18 ! Nr of angles;at1;at2;at3;Thetao,o;ka;kb;pv1;pv2
1 1 1 67.2326 22.0695 1.6286 0.0000 1.7959 15.4141 1.8089
1 1 2 65.2527 14.3185 6.2977 0.0000 0.5645 0.0000 1.1530
2 1 2 70.0840 25.3540 3.4508 0.0000 0.0050 0.0000 3.0000
1 2 2 0.0000 0.0000 6.0000 0.0000 0.0000 0.0000 1.0400
2 2 1 0.0000 3.4110 7.7350 0.0000 0.0000 0.0000 1.0400
2 2 2 0.0000 27.9213 5.8635 0.0000 0.0000 0.0000 1.0400
1 1 3 49.5561 7.3771 4.9568 0.0000 0.7533 15.9906 1.0010
3 1 3 77.1171 39.8746 2.5403 -24.3902 1.7740 -42.9758 2.1240
2 1 3 65.0000 14.2057 4.8649 0.0000 0.3504 0.0000 1.7185
1 3 1 74.3994 44.7500 0.7982 0.0000 3.0000 0.0000 1.0528
1 3 3 77.9854 36.6201 2.0201 0.0000 0.7434 67.0264 3.0000
3 3 3 80.7324 30.4554 0.9953 0.0000 1.6310 50.0000 1.0783
1 3 2 71.5018 21.7062 0.4735 0.0000 0.5186 0.0000 1.1793
2 3 3 84.9468 23.3540 1.5057 0.0000 2.6374 0.0000 1.3023
2 3 2 77.0645 10.4737 1.2895 0.0000 0.9924 0.0000 1.1043
1 2 3 0.0000 25.0000 3.0000 0.0000 1.0000 0.0000 1.0400
3 2 3 0.0000 0.0148 6.0000 0.0000 0.0000 0.0000 1.0400
2 2 3 0.0000 9.7025 6.0000 0.0000 0.0000 0.0000 1.0400
26 ! Nr of torsions;at1;at2;at3;at4;V1;V2;V3;V2(BO);vconj;n.u;n
1 1 1 1 -0.2500 11.5822 0.1879 -4.7057 -2.2047 0.0000 0.0000
1 1 1 2 -0.2500 31.2596 0.1709 -4.6391 -1.9002 0.0000 0.0000
2 1 1 2 -0.1770 30.0252 0.4340 -5.0019 -2.0697 0.0000 0.0000
1 1 1 3 -0.7098 22.2951 0.0060 -2.5000 -2.1688 0.0000 0.0000
2 1 1 3 -0.3568 22.6472 0.6045 -4.0088 -1.0000 0.0000 0.0000
3 1 1 3 -0.0528 6.8150 0.7498 -5.0913 -1.0000 0.0000 0.0000
1 1 3 1 2.0007 25.5641 -0.0608 -2.6456 -1.1766 0.0000 0.0000
1 1 3 2 -1.1953 42.1545 -1.0000 -8.0821 -1.0000 0.0000 0.0000
2 1 3 1 -0.9284 34.3952 0.7285 -2.5440 -2.4641 0.0000 0.0000
2 1 3 2 -2.5000 79.6980 1.0000 -3.5697 -2.7501 0.0000 0.0000
1 1 3 3 -0.0179 5.0603 -0.1894 -2.5000 -2.0399 0.0000 0.0000
2 1 3 3 -0.5583 80.0000 1.0000 -4.4000 -3.0000 0.0000 0.0000
3 1 3 1 -2.5000 76.0427 -0.0141 -3.7586 -2.9000 0.0000 0.0000
3 1 3 2 0.0345 78.9586 -0.6810 -4.1777 -3.0000 0.0000 0.0000
3 1 3 3 -2.5000 66.3525 0.3986 -3.0293 -3.0000 0.0000 0.0000
1 3 3 1 2.5000 -0.5332 1.0000 -3.5096 -2.9000 0.0000 0.0000
1 3 3 2 -2.5000 3.3219 0.7180 -5.2021 -2.9330 0.0000 0.0000
2 3 3 2 2.2500 -6.2288 1.0000 -2.6189 -1.0000 0.0000 0.0000
1 3 3 3 0.0531 -17.3983 1.0000 -2.5000 -2.1584 0.0000 0.0000
2 3 3 3 0.4723 -12.4144 -1.0000 -2.5000 -1.0000 0.0000 0.0000
3 3 3 3 -2.5000 -25.0000 1.0000 -2.5000 -1.0000 0.0000 0.0000
0 1 2 0 0.0000 0.0000 0.0000 0.0000 0.0000 0.0000 0.0000
0 2 2 0 0.0000 0.0000 0.0000 0.0000 0.0000 0.0000 0.0000
0 2 3 0 0.0000 0.1000 0.0200 -2.5415 0.0000 0.0000 0.0000
0 1 1 0 0.0000 50.0000 0.3000 -4.0000 -2.0000 0.0000 0.0000
0 3 3 0 0.5511 25.4150 1.1330 -5.1903 -1.0000 0.0000 0.0000
1 ! Nr of hydrogen bonds;at1;at2;at3;Rhb;Dehb;vhb1
3 2 3 1.9682 -4.4628 1.7976 3.0000

```

## A.4. MIXED MAGNESIUM–CALCIUM CHLORIDE HYDRATES

```
[ lgDispersion=1 ]Reactive MD-force field salt hydrates (CaMgCl - H2O)
39      ! Number of general parameters
50.0000 !p_boc1 Eq(4c): Overcoordination parameter
9.5469  !p_boc2 Eq(4d): Overcoordination parameter
26.5405 !p_coa2 Eq(15): Valency angle conjugation
1.7224  !p_trip4 Eq(20): Triple bond stabilisation
6.8702  !p_trip3 Eq(20): Triple bond stabilisation
60.4850 !k_c2 Eq(19): C2-correction
1.0588  !p_ovun6 Eq(12): Undercoordination
4.6000  !p_trip2 Eq(20): Triple bond stabilisation
12.1176 !p_ovun7 Eq(12): Undercoordination
13.3056 !p_ovun8 Eq(12): Undercoordination
-70.5044 !p_trip1 Eq(20): Triple bond stabilization
0.0000  !Lower Taper-radius (must be 0)
10.0000 !R_cut Eq(21): Upper Taper-radius
2.8793  !p_fel Eq(6a): Fe dimer correction
33.8667 !p_val6 Eq(13c): Valency undercoordination
6.0891  !p_lp1 Eq(8): Lone pair param
1.0563  !p_val9 Eq(13f): Valency angle exponent
2.0384  !p_val10 Eq(13g): Valency angle parameter
6.1431  !p_fe2 Eq(6a): Fe dimer correction
6.9290  !p_pen2 Eq(14a): Double bond/angle param
0.3989  !p_pen3 Eq(14a): Double bond/angle param
3.9954  !p_pen4 Eq(14a): Double bond/angle param
-2.4837 !p_fe3 Eq(6a): Fe dimer correction
5.7796  !p_tor2 Eq(16b): Torsion/BO parameter
10.0000 !p_tor3 Eq(16c): Torsion overcoordination
1.9487  !p_tor4 Eq(16c): Torsion overcoordination
-1.2327 !p_elho Eq(26a): electron-hole interaction
2.1645  !p_cot2 Eq(17b): Conjugation if torsl3=0
1.5591  !p_vdW1 Eq(23b): vdWals shielding
0.1000  !Cutoff for bond order (*100)
2.1365  !p_coa4 Eq(15): Valency angle conjugation
0.6991  !p_ovun4 Eq(11b): Over/Undercoordination
50.0000 !p_ovun3 Eq(11b): Over/Undercoordination
1.8512  !p_val8 Eq(13d): Valency/lone pair param
0.5000  !X_soft Eq(25): ACKS2 softness for X_ij
1.0000  !d Eq(23d): Scale factor in lg-dispersion
5.0000  !p_val Eq(27): Gauss exponent for electrons
0.0000  !l Eq(13e): disable undecoord in val angle
2.6962  !p_coa3 Eq(15): Valency angle conjugation
6      ! Nr of atoms; cov.r; valency;a.m;Rvdw;Evdw;gammaEEM;cov.r2;#
      alfa;gammavdW;valency;Eunder;Eover;chiEEM;etaEEM;n.u.
      cov_r3;Elp;Heat inc.;bol131;bol132;bol133;softcut;n.u.
      ov/un;vall;n.u.;val3,vval4
C      1.3817  4.0000  12.0000  1.8903  0.1838  0.9000  1.1341  4.0000
      9.7559  2.1346  4.0000  34.9350  79.5548  5.9666  7.0000  0.0000
      1.2114  0.0000  202.5551  8.9539  34.9289  13.5366  0.8563  0.0000
      -2.8983  2.5000  1.0564  4.0000  2.9663  0.0000  0.0000  0.0000
      0.0000  0.0000
H      0.8930  1.0000  1.0080  1.3550  0.0930  0.8203  -0.1000  1.0000
      8.2230  33.2894  1.0000  0.0000  121.1250  4.3065  8.3445  1.0000
      -0.1000  0.0000  61.6606  3.0408  2.4197  0.0003  1.0698  0.0000
      -19.4571  4.2733  1.0338  1.0000  2.8793  0.0000  0.0000  0.0000
      0.0000  0.0000
O      1.2450  2.0000  15.9990  2.3890  0.1000  1.0898  1.0548  6.0000
      9.7300  13.8449  4.0000  37.5000  116.0768  7.8651  7.8466  2.0000
      0.9049  0.4056  59.0626  3.5027  0.7640  0.0021  0.9745  0.0000
      -3.5500  2.9000  1.0493  4.0000  2.9225  0.0000  0.0000  0.0000
      142.9733  1.7500
Mg     1.8315  2.0000  24.3050  2.2494  0.1830  0.4805  1.0000  2.0000
```

A

		10.8448	27.1205	3.0000	38.0000	0.0000	0.1595	6.1918	0.0000
		-1.3000	0.0000	34.5160	49.9248	0.3370	0.0000	0.0000	0.0000
		-1.0823	2.3663	1.0564	6.0000	2.9663	0.0000	0.0000	0.0000
		0.0000	0.0000						
C1		1.7140	1.0000	35.4500	3.0207	0.0568	0.3640	-1.0000	7.0000
		10.5008	10.1330	1.0000	0.0000	0.0000	10.0000	6.0403	2.0000
		-1.0000	3.5750	143.1770	6.2290	35.2290	40.1540	20.8560	30.0000
		-10.2080	2.9867	1.0338	6.2998	2.5791	0.0000	0.0000	0.0000
		0.0000	0.0000						
Ca		1.9927	2.0000	40.0870	2.7005	0.1848	0.7939	1.0000	2.0000
		10.6123	27.5993	3.0000	38.0000	0.0000	-1.9372	6.5275	0.0000
		-1.3000	0.0000	220.0000	49.9248	0.3370	0.0000	0.0000	0.0000
		-2.0000	4.0000	1.0564	6.2998	2.9663	0.0000	0.0000	0.0000
		0.0000	0.0000						
18	! Nr of bonds; Edisl;LPpen;n.u.;pbel;pbo5;13corr;pbo6 pbe2;pbo3;pbo4;n.u.;pbo1;pbo2;ovcorr								
	1	1	158.2004	99.1897	78.0000	-0.7738	-0.4550	1.0000	37.6117
			0.4590	-0.1000	9.1628	1.0000	-0.0777	6.7268	1.0000
	1	2	169.4760	0.0000	0.0000	-0.6083	0.0000	1.0000	6.0000
			5.2290	1.0000	0.0000	1.0000	-0.0500	6.9136	0.0000
	2	2	153.3934	0.0000	0.0000	-0.4600	0.0000	1.0000	6.0000
			6.2500	1.0000	0.0000	1.0000	-0.0790	6.0552	0.0000
	1	3	158.6946	107.4583	23.3136	-0.4240	-0.1743	1.0000	10.8209
			0.5322	-0.3113	7.0000	1.0000	-0.1447	5.2450	0.0000
	3	3	142.2858	145.0000	50.8293	0.2506	-0.1000	1.0000	29.7503
			0.3451	-0.1055	9.0000	1.0000	-0.1225	5.5000	1.0000
	2	3	160.0000	0.0000	0.0000	-0.5725	0.0000	1.0000	6.0000
			1.1150	1.0000	0.0000	1.0000	-0.0920	4.2790	0.0000
	2	4	0.0000	0.0000	0.0000	0.5000	-0.2000	0.0000	16.0000
			1.0001	-0.2000	15.0000	1.0000	-0.1000	15.0000	0.0000
	3	4	132.5742	0.0000	0.0000	-0.6075	-0.3000	1.0000	36.0000
			1.4013	-0.2500	12.0000	1.0000	-0.0955	5.0000	1.0000
	4	4	0.0000	0.0000	0.0000	0.5000	-0.2000	0.0000	16.0000
			1.0001	-0.2000	15.0000	1.0000	-0.1000	15.0000	0.0000
	2	5	150.6697	0.0000	0.0000	-0.6499	-0.2000	0.0000	16.0000
			3.8414	-0.2000	15.0000	1.0000	-0.2000	6.8063	0.0000
	3	5	0.0000	0.0000	0.0000	0.5000	-0.2000	0.0000	16.0000
			1.0001	-0.2000	15.0000	1.0000	-0.1000	15.0000	0.0000
	4	5	101.4236	0.0000	0.0000	-0.1106	-0.2000	0.0000	16.0000
			4.6006	-0.2000	15.0000	1.0000	-0.1115	5.0026	0.0000
	5	5	7.1986	0.0000	0.0000	0.4564	-0.2000	0.0000	16.0000
			-0.4028	-0.2000	15.0000	1.0000	-0.1070	15.0000	0.0000
	2	6	11.1950	0.0000	0.0000	-0.0203	-0.1418	1.0000	13.1260
			7.2684	-0.1310	0.0000	1.0000	-0.2692	6.4254	0.0000
	3	6	62.4691	0.0000	43.3991	0.4608	-0.3000	1.0000	36.0000
			-0.0555	-0.2500	12.0000	1.0000	-0.0906	7.3386	1.0000
	6	6	10.5739	0.0000	0.0000	-0.2046	-0.2000	0.0000	16.0000
			-0.0653	-0.2000	10.0000	1.0000	-0.0766	4.0237	0.0000
	6	5	70.7290	0.0000	0.0000	-0.3145	-0.2000	0.0000	16.0000
			34.8673	-0.2000	15.0000	0.9915	-0.0289	4.8584	0.0000
	4	6	13.7218	0.0000	0.0000	0.1145	-0.2000	0.0000	16.0000
			22.9795	-0.2000	12.5000	1.0000	-0.0202	4.5161	0.0000
12	! Nr of off-diagonal terms; Ediss;Ro;gamma;rsigma;rpi;rpi2								
	1	2	0.1239	1.4004	9.8467	1.1210	-1.0000	-1.0000	0.0000
	2	3	0.0283	1.2885	10.9190	0.9215	-1.0000	-1.0000	0.0000
	1	3	0.1156	1.8520	9.8317	1.2854	1.1352	1.0706	0.0000
	2	4	0.0200	1.4000	9.0000	0.0001	-1.0000	-1.0000	0.0000
	3	4	0.3480	1.5557	11.4921	1.4819	-1.0000	-1.0000	0.0000
	2	5	0.1695	1.6156	9.7834	1.4740	-1.0000	-1.0000	0.0000
	3	5	0.1491	2.3500	10.1159	-1.0000	-1.0000	-1.0000	0.0000
	4	5	0.2097	1.5865	13.9807	1.4737	-1.0000	-1.0000	0.0000
	2	6	0.0100	1.6000	13.2979	-1.0000	-1.0000	-1.0000	0.0000
	3	6	0.1106	1.5902	13.2197	1.9305	-1.0000	-1.0000	0.0000
	6	5	0.3234	2.1332	10.2014	1.4542	-1.0000	-1.0000	0.0000
	4	6	0.1711	1.8677	13.6543	1.9354	-1.0000	-1.0000	0.0000

```

50      ! Nr of angles;at1;at2;at3;Thetao,o;ka;kb;pv1;pv2
1 1 1 59.0573 30.7029 0.7606 0.0000 0.7180 6.2933 1.1244
1 1 2 65.7758 14.5234 6.2481 0.0000 0.5665 0.0000 1.6255
2 1 2 70.2607 25.2202 3.7312 0.0000 0.0050 0.0000 2.7500
1 2 2 0.0000 0.0000 6.0000 0.0000 0.0000 0.0000 1.0400
1 2 1 0.0000 3.4110 7.7350 0.0000 0.0000 0.0000 1.0400
2 2 2 0.0000 27.9213 5.8635 0.0000 0.0000 0.0000 1.0400
1 1 3 49.6811 7.1713 4.3889 0.0000 0.7171 10.2661 1.0463
3 1 3 77.7473 40.1718 2.9802 -25.3063 1.6170 -46.1315 2.2503
2 1 3 65.0000 13.8815 5.0583 0.0000 0.4985 0.0000 1.4900
1 3 1 73.5312 44.7275 0.7354 0.0000 3.0000 0.0000 1.0684
1 3 3 79.4761 36.3701 1.8943 0.0000 0.7351 67.6777 3.0000
3 3 3 80.7324 30.4554 0.9953 0.0000 1.6310 50.0000 1.0783
1 3 2 70.1880 20.9562 0.3864 0.0000 0.0050 0.0000 1.6924
2 3 3 75.6935 50.0000 2.0000 0.0000 1.0000 0.0000 1.1680
2 3 2 85.8000 9.8453 2.2720 0.0000 2.8635 0.0000 1.5800
1 2 3 0.0000 25.0000 3.0000 0.0000 1.0000 0.0000 1.0400
1 2 4 0.0000 0.0019 6.0000 0.0000 0.0000 0.0000 1.0400
3 2 3 0.0000 15.0000 2.8900 0.0000 0.0000 0.0000 2.8774
2 2 3 0.0000 8.5744 3.0000 0.0000 0.0000 0.0000 1.0421
2 4 2 0.0000 49.8261 0.2093 0.0000 2.0870 0.0000 2.2895
2 2 4 0.0000 40.0366 3.1505 0.0000 1.1296 0.0000 1.1110
4 2 4 0.0000 0.5047 0.8000 0.0000 0.8933 0.0000 4.6650
2 4 4 0.0000 8.7037 0.0827 0.0000 3.5597 0.0000 1.1198
3 4 3 24.6431 4.8250 7.8421 0.0000 0.3049 0.0000 1.0643
4 3 4 61.4607 23.5645 8.1273 0.0000 3.9792 0.0000 1.8938
2 3 4 61.1006 2.4162 3.6237 0.0000 2.7588 0.0000 1.1276
2 3 3 0.0000 35.0000 0.3447 0.0000 1.0000 0.0000 1.9494
3 4 3 70.0000 20.0000 1.0000 0.0000 1.0000 0.0000 1.2500
3 2 5 0.0000 0.5102 0.0100 0.0000 0.0000 0.0000 1.3399
5 2 5 0.0000 5.0000 1.0000 0.0000 1.0000 0.0000 1.2500
4 5 4 7.3884 7.5202 0.3350 0.0000 1.0000 0.0000 1.0000
5 4 5 0.0813 8.5009 1.6291 0.0000 1.0000 0.0000 1.3706
3 4 5 0.4054 5.9491 7.8439 0.0000 1.0000 0.0000 2.0657
3 6 3 9.4193 6.5874 0.1170 0.0000 0.5754 0.0000 1.9245
6 3 6 5.3223 15.1865 2.1599 0.0000 1.9819 0.0000 2.0308
2 3 6 50.5960 3.4274 11.0889 0.0000 0.0500 0.0000 1.0571
3 3 6 73.1181 25.3522 1.0106 0.0000 1.0000 0.0000 1.1208
6 5 6 18.1000 -27.0162 5.9208 -2.5668 1.0000 0.0000 1.0307
5 6 5 128.9965 -18.4910 18.7610 0.0859 1.0000 0.0000 1.0614
3 6 5 49.9564 -3.3582 6.4075 0.0000 1.0000 0.0000 2.6422
4 5 6 125.2917 -9.7400 14.7858 0.0000 1.0000 0.0000 2.4350
2 6 2 0.0000 51.5084 0.2095 0.0000 2.1642 0.0000 2.3541
2 2 6 0.0000 39.4044 2.8341 0.0000 1.1378 0.0000 1.0860
6 2 6 0.0000 0.7476 0.5163 0.0000 0.8491 0.0000 4.6650
2 6 6 0.0000 9.0927 0.3829 0.0000 3.5143 0.0000 1.1566
2 6 3 0.0000 36.0055 0.3339 0.0000 0.9089 0.0000 1.9411
6 5 5 4.2053 10.4848 0.4567 0.0000 1.0094 0.0000 1.3668
6 5 2 133.5715 10.4411 1.4862 0.0000 0.0000 0.0000 1.0142
6 3 4 63.6111 18.3063 10.0294 0.0000 2.9806 0.0000 1.1857
6 5 4 76.4277 -3.3823 23.7434 0.0000 1.0000 0.0000 1.0611
29      ! Nr of torsions;at1;at2;at3;at4;V1;V2;V3;V2(BO);vconj;n.u;n
1 1 1 1 -0.2500 34.7453 0.0288 -6.3507 -1.6000 0.0000 0.0000
1 1 1 2 -0.2500 29.2131 0.2945 -4.9581 -2.1802 0.0000 0.0000
2 1 1 2 -0.2500 31.2081 0.4539 -4.8923 -2.2677 0.0000 0.0000
1 1 1 3 -0.3495 22.2142 -0.2959 -2.5000 -1.9066 0.0000 0.0000
2 1 1 3 0.0646 24.3195 0.6259 -3.9603 -1.0000 0.0000 0.0000
3 1 1 3 -0.5456 5.5756 0.8433 -5.1924 -1.0180 0.0000 0.0000
1 1 3 1 1.7555 27.9267 0.0072 -2.6533 -1.0000 0.0000 0.0000
1 1 3 2 -1.4358 36.7830 -1.0000 -8.1821 -1.0000 0.0000 0.0000
2 1 3 1 -1.3959 34.5053 0.7200 -2.5714 -2.1641 0.0000 0.0000
2 1 3 2 -2.5000 70.0597 1.0000 -3.5539 -2.9929 0.0000 0.0000
1 1 3 3 0.6852 11.2819 -0.4784 -2.5000 -2.1085 0.0000 0.0000
2 1 3 3 0.1933 80.0000 1.0000 -4.0590 -3.0000 0.0000 0.0000
3 1 3 1 -1.9889 76.4820 -0.1796 -3.8301 -3.0000 0.0000 0.0000

```

```

3 1 3 2 0.2160 72.7707 -0.7087 -4.2100 -3.0000 0.0000 0.0000
3 1 3 3 -2.5000 71.0772 0.2542 -3.1631 -3.0000 0.0000 0.0000
1 3 3 1 2.5000 -0.6002 1.0000 -3.4297 -2.8858 0.0000 0.0000
1 3 3 2 -2.5000 -3.3822 0.7004 -5.4467 -2.9586 0.0000 0.0000
2 3 3 2 2.5000 -4.0000 0.9000 -2.5000 -1.0000 0.0000 0.0000
1 3 3 3 1.2329 -4.0000 1.0000 -2.5000 -1.7479 0.0000 0.0000
2 3 3 3 0.8302 -4.0000 -0.7763 -2.5000 -1.0000 0.0000 0.0000
3 3 3 3 -2.5000 -4.0000 1.0000 -2.5000 -1.0000 0.0000 0.0000
0 1 2 0 0.0000 0.0000 0.0000 0.0000 0.0000 0.0000 0.0000
0 2 2 0 0.0000 0.0000 0.0000 0.0000 0.0000 0.0000 0.0000
0 2 3 0 0.0000 0.1000 0.0200 -2.5415 0.0000 0.0000 0.0000
0 1 1 0 0.0000 50.0000 0.3000 -4.0000 -2.0000 0.0000 0.0000
0 3 3 0 0.5511 25.4150 1.1330 -5.1903 -1.0000 0.0000 0.0000
1 1 3 3 -2.0000 73.0530 1.5000 -9.0000 -2.0000 0.0000 0.0000
1 3 3 1 0.0002 80.0000 -1.5000 -2.5000 -2.0000 0.0000 0.0000
3 1 3 3 -1.8835 20.0000 1.5000 -9.0000 -2.0000 0.0000 0.0000
3
! Nr of hydrogen bonds;at1;at2;at3;Rhb;Dehb;vhb1
3 2 3 2.1200 -3.5800 1.4500 19.5000
3 2 5 1.8833 -3.6250 1.4500 19.5000
5 2 3 1.8487 -0.0100 1.4500 19.5000

```

# B

## APPENDIX – CHEMICAL ANALYSIS OF DOPED SALTS HYDRATES

### B.1. CRYSTAL STRUCTURE CHANGE

Crystal structure change of  $\text{MgCl}_2 \cdot 6\text{H}_2\text{O}$  upon doping with calcium

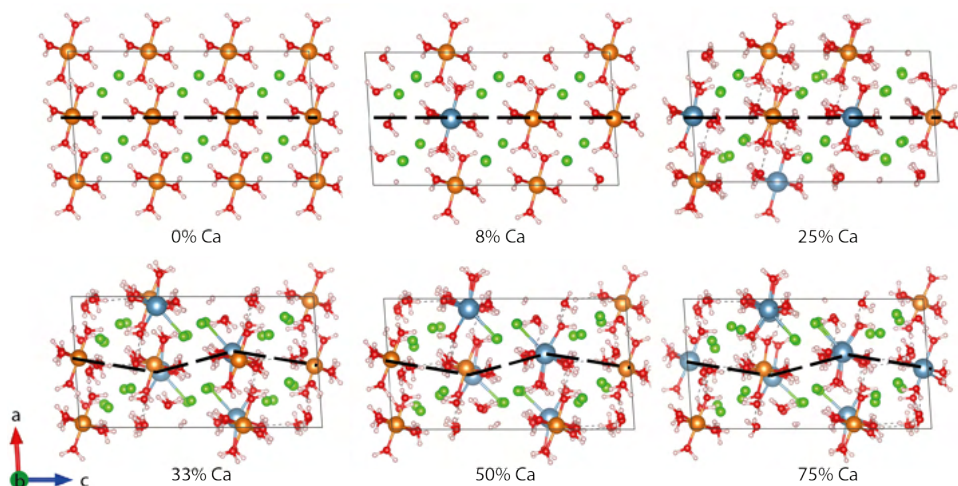


Figure B.1: Energy minimized structures of manually doped  $\text{MgCl}_2 \cdot 6\text{H}_2\text{O}$ , by swapping magnesium ions with calcium ions. The dashed line highlights the crystal change for calcium contents above 25%.







# APPENDIX – REAXFF CALCIUM CHLORIDE HYDRATES

## C.1. DEHYDRATION

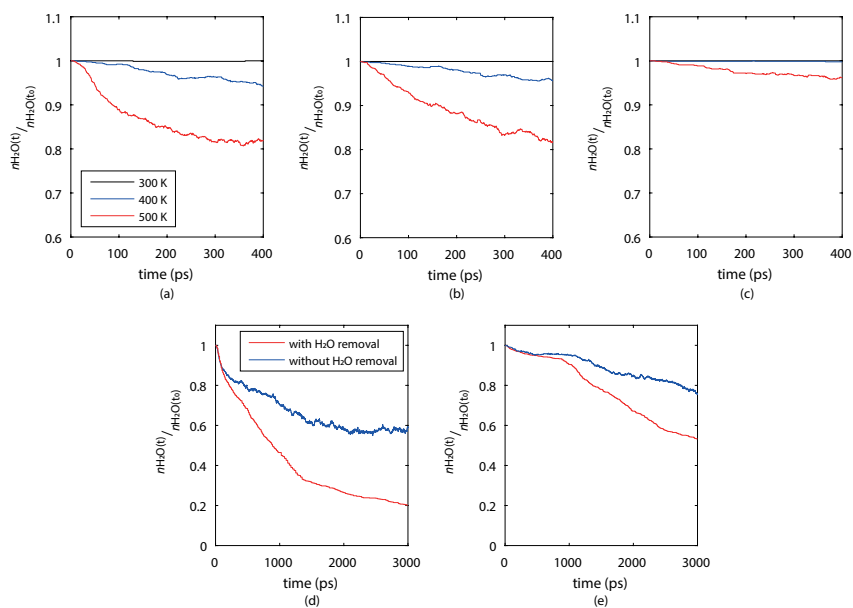


Figure C.1: Dehydration of  $\text{CaCl}_2\cdot\text{H}_2\text{O}$ . (a) Dehydration without water removal with vacuum in x-direction. (b) Dehydration without water removal with vacuum in y-direction. (c) Dehydration without water removal with vacuum in z-direction. (d) Dehydration with- and without water removal with vacuum in x-direction. (e) Dehydration with- and without water removal with vacuum in z-direction.

## C.2. STRUCTURES FOR SURFACE ENERGY CALCULATION

(Surface) direction	Bulk			Surface		
	[100]	[010]	[001]	[100]	[010]	[001]
Reference	6.24	6.43	4.2	-	-	-
DFT	6.19	6.37	4.16	6.22	6.35	4.28
ReaxFF	6.37	6.17	4.30	6.14	6.11	4.31

Table C.1:  $\text{CaCl}_2$ ; Ca–Ca distance (Å) between first surface Ca atom and Ca atom in second surface layer, in the normal direction.

(Surface) direction	Bulk			Surface		
	[100]	[010]	[001]	[100]	[010]	[001]
Reference	5.89	7.47	6.04*	-	-	-
DFT	5.86	7.43	6.00*	5.80	7.44	6.00*
ReaxFF	6.22	7.35	6.70*	6.14	7.37	6.70*

Table C.2:  $\text{CaCl}_2 \cdot 2\text{H}_2\text{O}$ ; Ca–Ca distance (Å) between first surface Ca atom and Ca atom in second surface layer, in the normal direction. \* In [001] direction the second Ca atom (in the direction normal to the surface) is located in the 3rd layer. Furthermore, regarding ReaxFF, there is an additional shift between these layers (see,  $\text{CaCl}_2 \cdot 2\text{H}_2\text{O}$  [010] ReaxFF surface image). Therefore, the normal distance to the center of the surface layer and the second layer is considered for this direction.

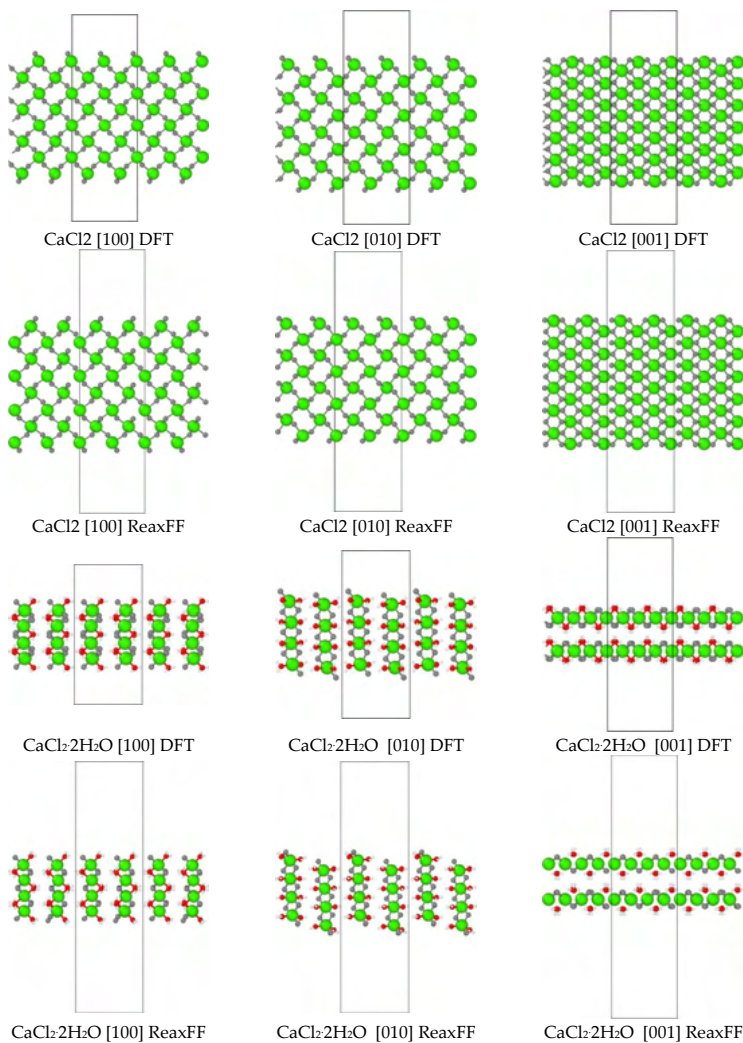


Figure C.2: Corresponding relaxed crystal surfaces for Table C.1 and C.2



# *D*

## APPENDIX – DERIVATION SMOLUCHOWSKI SURVIVAL PROBABILITY

### D.1. HOMOGENEOUS SURVIVAL PROBABILITY

Suppose we have a bounded domain  $[0, L]$  through which particles freely diffuse. What would be the probability of these particles staying within this domain over time, assuming you start tracking the particles at  $0.5L$ ? We call this the survival probability. We start with the diffusion equation, which describes the motion of freely diffusing particles. In order to solve this diffusion equation and obtain a survival probability of particles in the domain, we follow the general solution of the heat equation by separation of variables [283].

$$\frac{\partial p(x, t)}{\partial t} = D \frac{\partial^2 p(x, t)}{\partial x^2}. \quad (\text{D.1})$$

We start tracking a particle whenever it passes  $0.5L$ . When a trajectory is started,  $t = 0$  for every trajectory. This gives our initial condition, which is a Dirac delta function at  $x = 0.5L$  as every trajectory starts at  $x = 0.5L$ , as given in equation (4.11). We stop tracking a particle whenever it passes either boundary, thus the probability of finding a particle at the boundary equals 0. This gives our Dirichlet boundary condition as given by equation (4.11). The separable solution – which separates the function into a product of a function of time  $T(t)$  and a function of position  $X(x)$  – of the diffusion equation (D.1) is given by:

$$p(x, t) = X(x)T(t). \quad (\text{D.2})$$

Plugging this in the diffusion equation and rewriting gives:

$$\frac{1}{DT} T' = \frac{1}{X} X'' = -\lambda, \quad (\text{D.3})$$

where  $\lambda$  is some constant, and gives to the following eigenvalue problems:

$$X'' + \lambda X = 0, \quad (\text{D.4})$$

$$T' + \lambda DT = 0. \quad (\text{D.5})$$

The solution of the eigenvalue problem (D.4) is given by using the boundary conditions of equation (4.10):

$$\begin{cases} X'' + \lambda X = 0, \\ X(0) = X(L) = 0. \end{cases} \quad (\text{D.6})$$

The general solution of this eigenvalue problem is:

$$X(x) = A \cos(\sqrt{\lambda}x) + B \sin(\sqrt{\lambda}x), \quad (\text{D.7})$$

With  $A$  and  $B$  some constant.

$$X(0) = 0 \rightarrow A = 0, \quad (\text{D.8})$$

$$X(L) = 0 \rightarrow B \sin(\sqrt{\lambda}L) = 0. \quad (\text{D.9})$$

$B$  can not be 0 as this would be a trivial solution, thus

$$\sin(\sqrt{\lambda}L) = 0 \rightarrow \sqrt{\lambda}L = n\pi \rightarrow \lambda = \left(\frac{n\pi}{L}\right)^2, \quad (\text{D.10})$$

giving

$$X_n(x) = B_n \sin\left(\frac{n\pi}{L}x\right), \quad n = 1, 2, \dots \quad (\text{D.11})$$

Next, the general solution of eigenvalue problem (D.5) is given by:

$$T = Ae^{-D\lambda t} \quad (\text{D.12})$$

With  $A$  some constant. Substituting  $\lambda$  gives:

$$T_n = A_n e^{-D\left(\frac{n\pi}{L}\right)^2 t}, \quad n = 1, 2, \dots \quad (\text{D.13})$$

Which gives the solution to our separation of variables function:

$$p_n(x, t) = X_n(x) T_n(t), \quad n = 1, 2, \dots \quad (\text{D.14})$$

All solution to  $p_n$  satisfy the boundary conditions, therefore the sum of solutions is also a solution:

$$p(x, t) = \sum_{n=1}^{\infty} A_n \sin\left(\frac{n\pi}{L}x\right) e^{-D\left(\frac{n\pi}{L}\right)^2 t}. \quad (\text{D.15})$$

Where constant  $B_n$  is now part of constant  $A_n$ . To obtain the constant  $A_n$  we need to consider the initial condition:

$$p(x, 0) = \sum_{n=1}^{\infty} A_n \sin\left(\frac{n\pi}{L}x\right) = \phi(x), \quad (\text{D.16})$$

where  $\phi(x)$  is the initial Dirac delta condition (4.11). Using the orthogonality property of eigenfunctions, it is shown that:

$$A_n = \frac{\langle X_n(x), \phi(x) \rangle}{\langle X_n(x), X_n(x) \rangle}, \quad \langle f(x), g(x) \rangle = \int_{\Omega} f(x)g(x)dx. \quad (D.17)$$

This gives:

$$A_n = \frac{\int_0^L \sin\left(\frac{n\pi}{L}x\right) \delta(x - \frac{1}{2}L) dx}{\int_0^L \sin^2\left(\frac{n\pi}{L}x\right) dx} = \frac{2}{L} \int_0^L \sin\left(\frac{n\pi}{L}x\right) \delta(x - \frac{1}{2}L) dx = \frac{2}{L} \sin\left(\frac{n\pi}{2}\right), \quad (D.18)$$

and the density probability function:

$$p(x, t) = \frac{2}{L} \sum_{n=1}^{\infty} \sin\left(\frac{n\pi}{2}\right) \sin\left(\frac{n\pi}{L}x\right) e^{-D\left(\frac{n\pi}{L}\right)^2 t} \quad (D.19)$$

## D.2. INHOMOGENEOUS SURVIVAL PROBABILITY

Here we have a similar problem as the one in D.1. However, with an extra 'force' created by the inhomogeneity, that depends on the position  $x$ , and acts on the particles. We call this force the Potential of Mean Force (PMF). Franco et al. [205] showed that a linear PMF can be assumed when the change of PMF in the domain is only marginal. As discussed before, this simplifies the Smoluchowski equation (4.5) to a advection--diffusion equation:

$$\frac{\partial p(x, t)}{\partial t} = D \frac{\partial^2 p(x, t)}{\partial x^2} + v \frac{\partial p(x, t)}{\partial x}, \quad (D.20)$$

in which we will substituted  $-D\omega$  for  $v$  for convenient solving. In order to solve this equation, we will first aim to rewrite this equation to the basic diffusion equation. We do the following transformation with the aim to write the diffusion equation in respect to the variable  $u$ :

$$p(x, t) = A(x, t)u(x, t). \quad (D.21)$$

Substitution of the transformation in the simplified Smoluchowski equation (D.20) becomes

$$A_t u + A u_t = D(A_{xx}u + 2A_x u_x + A u_{xx}) + v(A_x u + A u_x), \quad (D.22)$$

in which the subscript notation is used to indicate partial differentiation. We rewrite to

$$u_t = D u_{xx} + \left( \frac{2DA_x + vA}{A} \right) u_x + \left( \frac{DA_{xx} - A_t + vA_x}{A} \right) u. \quad (D.23)$$

In order to get this as the basic diffusion equation, we want the terms in front of  $u_x$  and  $u$  to be zero:

$$2DA_x + vA = 0, \quad (D.24)$$

$$DA_{xx} - A_t + vA_x = 0. \quad (D.25)$$

Equation (D.24), is an ODE which is solved as

$$A(x, t) = C(t)e^{\left(\frac{-v}{2D}x\right)}. \quad (D.26)$$

Substituting this solution into equation (D.25) we get:

$$\frac{dC(t)}{dt} + \frac{v^2}{4D} C(t) = 0, \quad (\text{D.27})$$

which is another ODE, solved as:

$$C(t) = C_1 e^{\left(-\frac{v^2}{4D} t\right)}. \quad (\text{D.28})$$

Combining (D.26) and (D.28):

$$A(x, t) = C_1 e^{\left(-\frac{v^2}{4D} t - \frac{v}{2D} x\right)}. \quad (\text{D.29})$$

Now using this in equation (D.23), we obtain the diffusion equation in terms of  $u$

$$u_t = D u_{xx}. \quad (\text{D.30})$$

With the transformation, the new Dirichlet boundary conditions become:

$$p(0, t) = A(0, t) u(0, t) = 0 \rightarrow u(0, t) = 0, \quad (\text{D.31})$$

$$p(L, t) = A(L, t) u(L, t) = 0 \rightarrow u(L, t) = 0, \quad (\text{D.32})$$

and the new initial Dirac delta condition becomes:

$$A(x, 0) u(x, 0) = \delta\left(x - \frac{1}{2}L\right) \rightarrow u(x, 0) = \frac{\delta\left(x - \frac{1}{2}L\right)}{A(x, 0)} = \frac{\delta\left(x - \frac{1}{2}L\right)}{C_1 e^{\left(-\frac{v}{2D} x\right)}}. \quad (\text{D.33})$$

Analogous to the homogeneous case, we can solve the diffusion equation in terms of  $u$ . However, with a slightly different initial condition. Resulting in:

$$u(x, t) = \frac{2}{C_1 L} e^{\left(\frac{vL}{4D}\right)} \sum_{n=1}^{\infty} \sin\left(\frac{n\pi}{2}\right) \sin\left(\frac{n\pi}{L} x\right) e^{-D\left(\frac{n\pi}{L}\right)^2 t}. \quad (\text{D.34})$$

Back transformation to  $p(x, t)$  with equation (D.29) and (D.34), and re-substitution of  $-D\omega = v$ , gives the final distribution function for the inhomogeneous case:

$$p(x, t) = \frac{2}{L} e^{\left(-\frac{wL}{4} + \frac{w}{2} x\right)} \sum_{n=1}^{\infty} \sin\left(\frac{n\pi}{2}\right) \sin\left(\frac{n\pi}{L} x\right) e^{-\left(\left(\frac{n\pi}{L}\right)^2 + \frac{w^2}{4}\right)Dt}. \quad (\text{D.35})$$



*E*


**APPENDIX – H<sub>2</sub>O & CO<sub>2</sub> REAXFF  
OPTIMIZATION**

## E.1. CO<sub>2</sub> – REAXFF MMC OPTIMIZATION


### E.1.1. GEOMETRY OPTIMIZATION OF SINGLE MOLECULE

Geometry optimized CO<sub>2</sub> molecules with revPBE D4 [245, 246], original ReaxFF force field [82], the new parameterized ReaxFF-lg force field, and the non-reactive TraPPE force field [230].


#### CO<sub>2</sub> molecule – DFT: revPBE D4

	Bond distance (Å)	O-C	1.18
	Bond angle (deg)	O-C-O	180


#### CO<sub>2</sub> molecule – original ReaxFF

	Bond distance (Å)	O-C	1.25
	Bond angle (deg)	O-C-O	180
	Charge ( <i>e</i> )	C	+ 0.459
		O	- 0.224

#### CO<sub>2</sub> molecule – new ReaxFF-lg

	Bond distance (Å)	O-C	1.19
	Bond angle (deg)	O-C-O	180
	Charge ( <i>e</i> )	C	+ 0.70
		O	- 0.35

#### CO<sub>2</sub> molecule – TraPPE [230]

	Bond distance (Å)	O-C	1.16
	Bond angle (deg)	O-C-O	180
	Charge ( <i>e</i> )	C	+ 0.70
		O	- 0.35

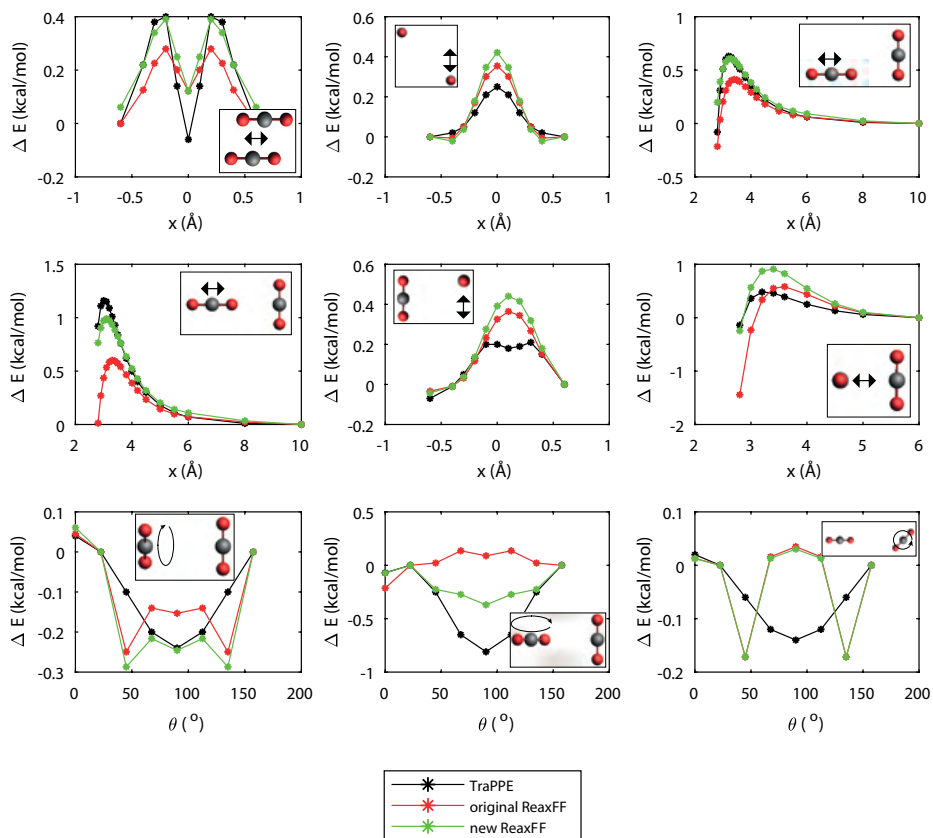


Figure E.1: Different dimer interactions used in the parameterization of the ReaxFF force field.  $\Delta E$  is the energy difference with a reference dimer in the set. Black is represents the reference TraPPE force field [230], red is the original ReaxFF force field, green is the new ReaxFF–lg force field.

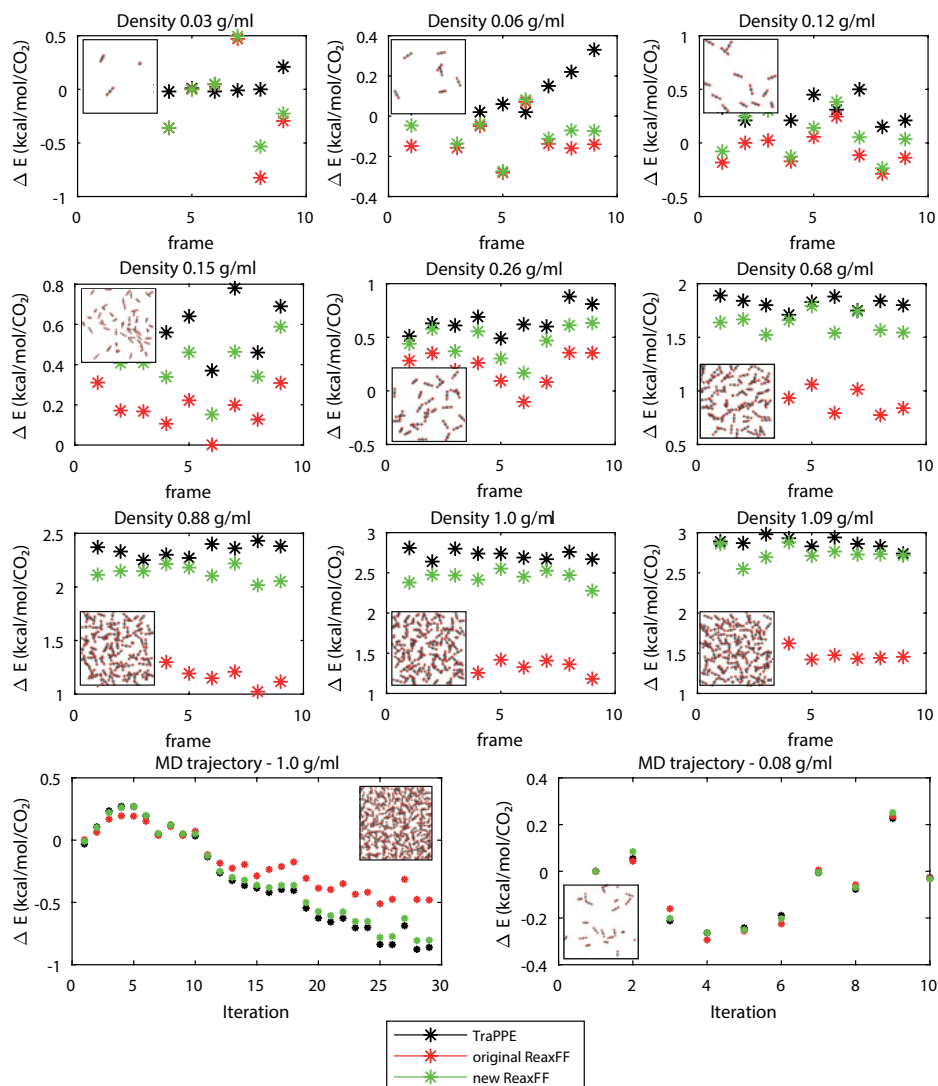
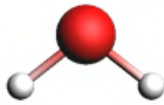


Figure E.2: Different MD trajectories at different densities used in the parameterization of the ReaxFF force field.  $\Delta E$  is the energy difference with a reference frame within the set. Black is represents the reference TraPPE force field [230], red is the original ReaxFF force field, green is the new ReaxFF-Ig force field

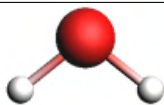
## E.2. H<sub>2</sub>O

Geometry optimized H<sub>2</sub>O molecules with revPBE D4 [245, 246], original ReaxFF force field [100], the new parameterized ReaxFF–lg force field, and the non-reactive TIP4P/2005 force field [229].

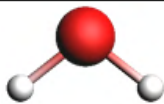
### H<sub>2</sub>O molecule – DFT: revPBE D4

	Bond distance (Å)	O-H	0.975
	Bond angle (deg)	O-H-O	102.9

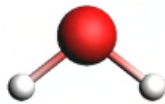
### H<sub>2</sub>O molecule – original ReaxFF

	Bond distance (Å)	O-H	0.948
	Bond angle (deg)	O-H-O	102.4
	Charge ( <i>e</i> )	H	+ 0.310
		O	- 0.619

### H<sub>2</sub>O molecule – new ReaxFF–lg

	Bond distance (Å)	O-H	0.974
	Bond angle (deg)	O-H-O	102.6
	Charge ( <i>e</i> )	H	+ 0.324
		O	- 0.648

### H<sub>2</sub>O molecule – TIP4P/2005

	Bond distance (Å)	O-H	1.16
	Bond angle (deg)	O-H-O	180
	Charge ( <i>e</i> )	H	+ 0.5664
		O	–
		M	- 1.1328

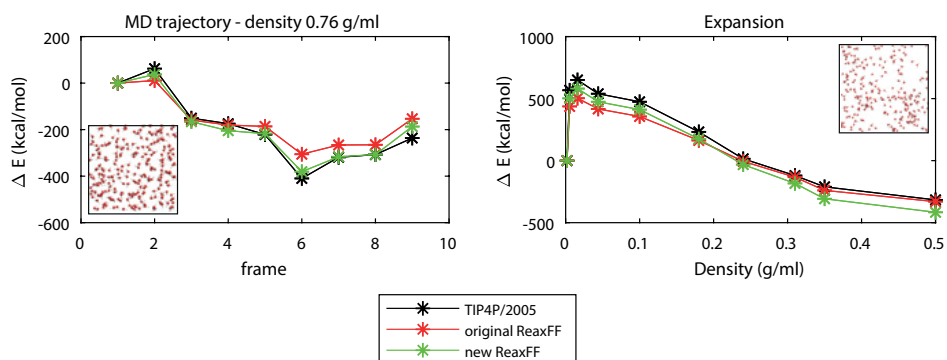


Figure E.3: Different MD trajectories at different densities used in the parameterization of the ReaxFF force field.  $\Delta E$  is the energy difference with a reference frame within the set. Black is represents the reference TIP4P/2005 force field [229], red is the original ReaxFF force field, green is the new ReaxFF-Ig force field.

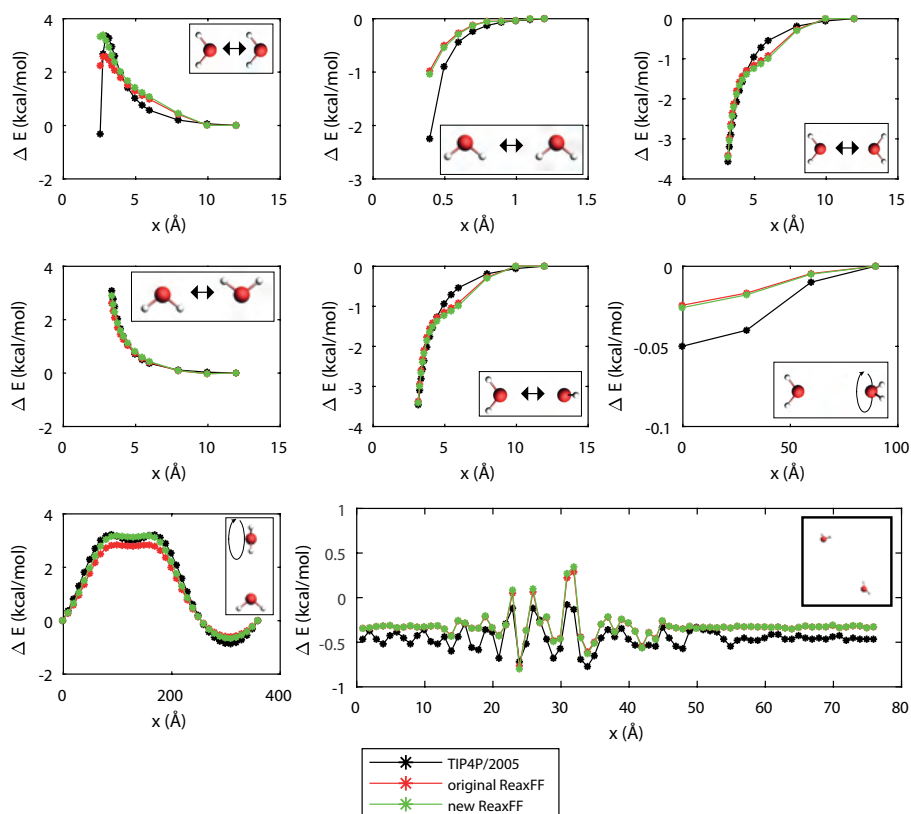


Figure E.4: Different dimer interactions used in the parameterization of the ReaxFF force field.  $\Delta E$  is the energy difference with a reference dimer in the set. Black is represents the reference TIP4P/2005 force field [229], red is the original ReaxFF force field, green is the new ReaxFF–lg force field.





# F

## APPENDIX – GCMC

### F.1. ACCEPTANCE RULES FOR GCMC

For the derivation of the acceptance rules for GCMC insertion and deletion trials, we follow the book of Frenkel & Smit [63]. In Monte Carlo trial moves it is convenient to obey detailed balance in the Markov Chain, which means that the flow of configurations going from the old configuration ( $o$ ) to the new ( $n$ ), equals the flow in the reverse direction ( $\mathcal{K}(o \rightarrow n) = \mathcal{K}(n \rightarrow o)$ ). For insertion and deletion of a molecule this gives:

$$\mathcal{K}(N \rightarrow N+1) = \mathcal{K}(N+1 \rightarrow N), \quad (\text{E1})$$

where  $\mathcal{K}(N \rightarrow N+1)$  is the flow of going from  $N$  molecules to  $N+1$ , and visa versa for  $\mathcal{K}(N+1 \rightarrow N)$ . The flow is given by the product of the probability of being in the old configuration  $\mathcal{N}(o)$ , the probability of generating a trial move from the old to the new configuration  $\alpha(o \rightarrow n)$ , and the acceptance probability of the trial move  $\text{acc}(o \rightarrow n)$ . For insertion this gives:

$$\mathcal{K}(N \rightarrow N+1) = \mathcal{N}(N) \times \alpha(N \rightarrow N+1) \times \text{acc}(N \rightarrow N+1), \quad (\text{E2})$$

and for deletion:

$$\mathcal{K}(N+1 \rightarrow N) = \mathcal{N}(N+1) \times \alpha(N+1 \rightarrow N) \times \text{acc}(N+1 \rightarrow N). \quad (\text{E3})$$

The probability of finding state  $\mathbf{s}^N$  with  $N$  particles is proportional to the partition function, for the Grand – Canonical ensemble this gives:

$$\mathcal{N}(\mathbf{s}^N) \propto \frac{\exp[\beta\mu N] V^N}{\Lambda^{3N} N!} \exp[-\beta E(\mathbf{s}^N)]. \quad (\text{E4})$$

With  $E(\mathbf{s}^N)$  as the potential energy of the state, and  $\Lambda$  as the Broglie wave length of a gas particle. The chemical potential  $\mu$  of a gas particle is related to the reference chemical potential of an ideal gas particle via  $\beta\mu = \beta\mu_{\text{ig}}^0 + \ln(\beta f)$ . With  $f$  as the fugacity and

$$\mu_{\text{ig}}^0 \equiv \ln \frac{\Lambda^3}{\beta}. \quad (\text{E5})$$

The probability of accepting an insertion trial move can be given by combining equation E2 and E3:

$$\frac{\text{acc}(N \rightarrow N+1)}{\text{acc}(N+1 \rightarrow N)} = \frac{\mathcal{N}(N+1)}{\mathcal{N}(N)} \times \frac{\alpha(N+1 \rightarrow N)}{\alpha(N \rightarrow N+1)}. \quad (\text{F6})$$

With the constraint for non-biased selection  $\alpha(N \rightarrow N+1) = \alpha(N+1 \rightarrow N)$  and substituting equation F4 and E5, the acceptance rule for insertion is given by:

$$\text{acc}_{N \rightarrow N+1} = \min \left[ 1, \frac{\beta f V}{N+1} \exp[-\beta(E(\mathbf{s}^{N+1}) - E(\mathbf{s}^N))] \right]. \quad (\text{F7})$$

Similarly, the acceptance rule for deletion is:

$$\text{acc}_{N+1 \rightarrow N} = \min \left[ 1, \frac{N}{\beta f V} \exp[-\beta(E(\mathbf{s}^N) - E(\mathbf{s}^{N+1}))] \right]. \quad (\text{F8})$$

In energy biased GCMC, the probability of selecting an insertion trial move is given by equation 6.4:

$$\alpha(o \rightarrow n) = \alpha(N \rightarrow N+1) = \frac{\exp[-\beta E_{\text{bias},n}]}{W_n}, \quad (\text{F9})$$

and for the reverse trial move:

$$\alpha(n \rightarrow o) = \alpha(N+1 \rightarrow N) = \frac{\exp[-\beta E_{\text{bias},o}]}{W_o}, \quad (\text{F10})$$

with  $W_n$  and  $W_o$  given by eqs 6.5 and 6.7, and  $E_{\text{bias}}$  as the energy from the forward bias. For the reverse way, the molecule is inserted in an ideal gas reservoir, thus equation F10 equals:

$$\alpha(n \rightarrow o) = \alpha(N+1 \rightarrow N) = \frac{1}{k}. \quad (\text{F11})$$

Substituting equation F9, and F11, the acceptance rule for biased insertion is given by:

$$\text{acc}_{N \rightarrow N+1} = \min \left[ 1, \frac{\beta f V}{(N+1)} \exp[-\beta(E(\mathbf{s}^{N+1}) - E(\mathbf{s}^N))] \times \frac{W_n}{k} \right]. \quad (\text{F12})$$

and similarly, the modified acceptance rule for deletion follows:

$$\text{acc}_{N+1 \rightarrow N} = \min \left[ 1, \frac{N}{\beta f V} \exp[-\beta(E(\mathbf{s}^N) - E(\mathbf{s}^{N+1}))] \times \frac{k}{W_o} \right]. \quad (\text{F13})$$

## F.2. WCA PARAMETERS

The WCA parameters  $\sigma$  and  $\epsilon$  are carefully chosen such that the repulsive part is slightly shorter ranged than for the ReaxFF force field. Figures F.1 give the comparison between the two interaction potentials. The ReaxFF reference is given in solid blue, the WCA potential in dashed blue. Furthermore, probability function  $P(r)$  is given in red, which represents the probability of selecting a trial at distance  $r$  out of a total of 10 trial positions. For the O–O interaction, the O–O RDF of liquid water is given as reference, since there is no uniform H<sub>2</sub>O ReaxFF interaction potential because of the different dimer interaction angles. Figure F.1c confirms the validity of the used ReaxFF force field regarding liquid water by means of a comparable RDF with experimental results [284].

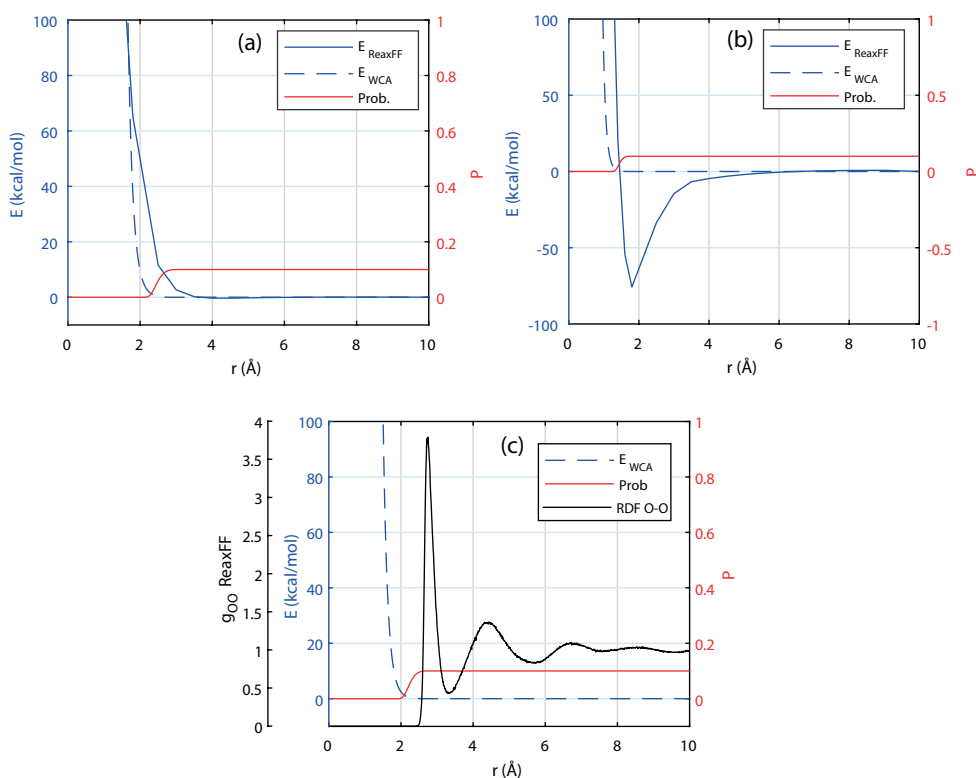
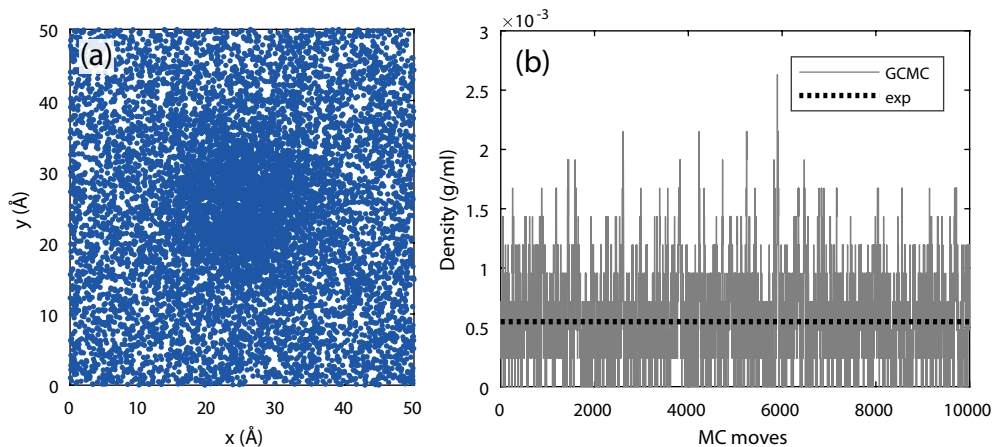


Figure F.1: (a) Cl–O interaction potentials. (b) Mg–O interaction potentials. (c) O–O interaction potentials. In dashed blue the WCA potential, in solid blue the ReaxFF reference, in red the selection probability out of 10 trials, and solid black as the ReaxFF O–O RDF for liquid water.

### F.3. GAUSSIAN PREFERENCE

Gaussian preference selection of insertions near the center. Figure E3a, shows the insertion locations in the box with use of the Gaussian preference selection for the center of the box. Figure E3b, shows the resulting water vapor density in gray, which is comparable with NIST reference values.



F

Figure E2: GCMC of an empty box at 400 K and 1 atmosphere, with  $\text{H}_2\text{O}$  insertion with Gaussian preference for center of the box. (a) blue dots are all selected insertion points from  $k = 10$  trials, the amplitude  $a$  (eq. 6.9) was set at  $a = 10$  kcal/mol. (b) the gray line is the density predicted by GCMC ( $\rho = 5.988 \times 10^{-4}$  g/ml), dotted line is the NIST reference [238] ( $\rho = 5.476 \times 10^{-4}$  g/ml).

## F.4. GCMC HYDRATION RESULTS

Hydration results for  $\text{MgCl}_2 \cdot 6\text{H}_2\text{O}$  with WCA-ReaxFF-GCMC.

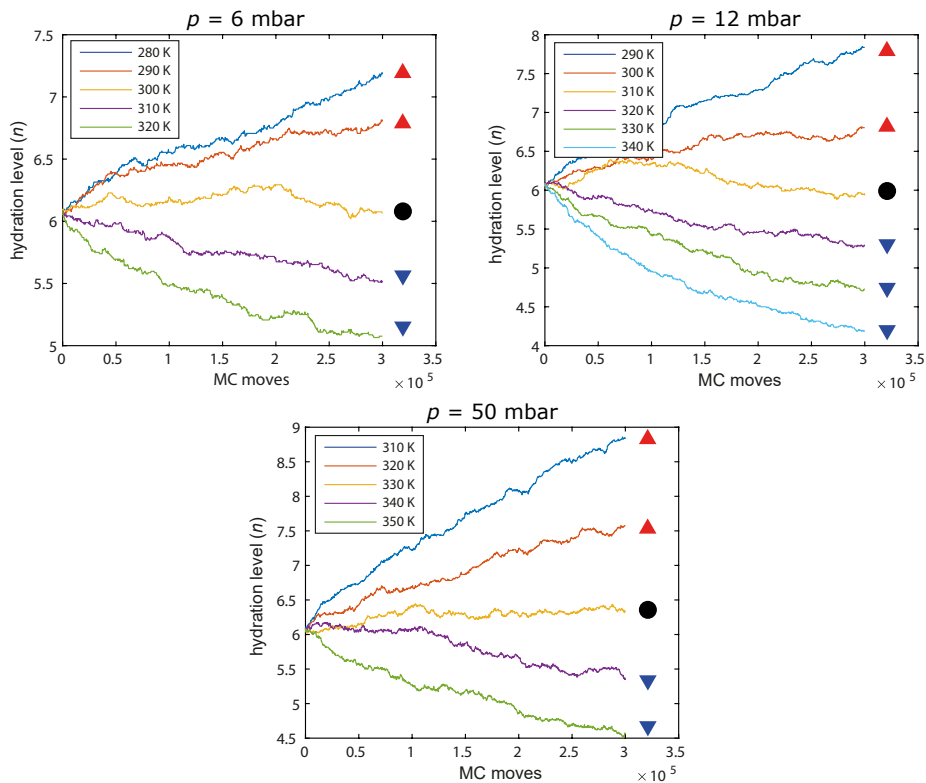


Figure F3: Loading of  $\text{MgCl}_2 \cdot 6\text{H}_2\text{O}$  with  $\text{H}_2\text{O}$  molecules.





**APPENDIX – MMC RESULTS  
CALCIUM–MAGNESIUM HYDRATES  
COMBINED FORCE FIELD**

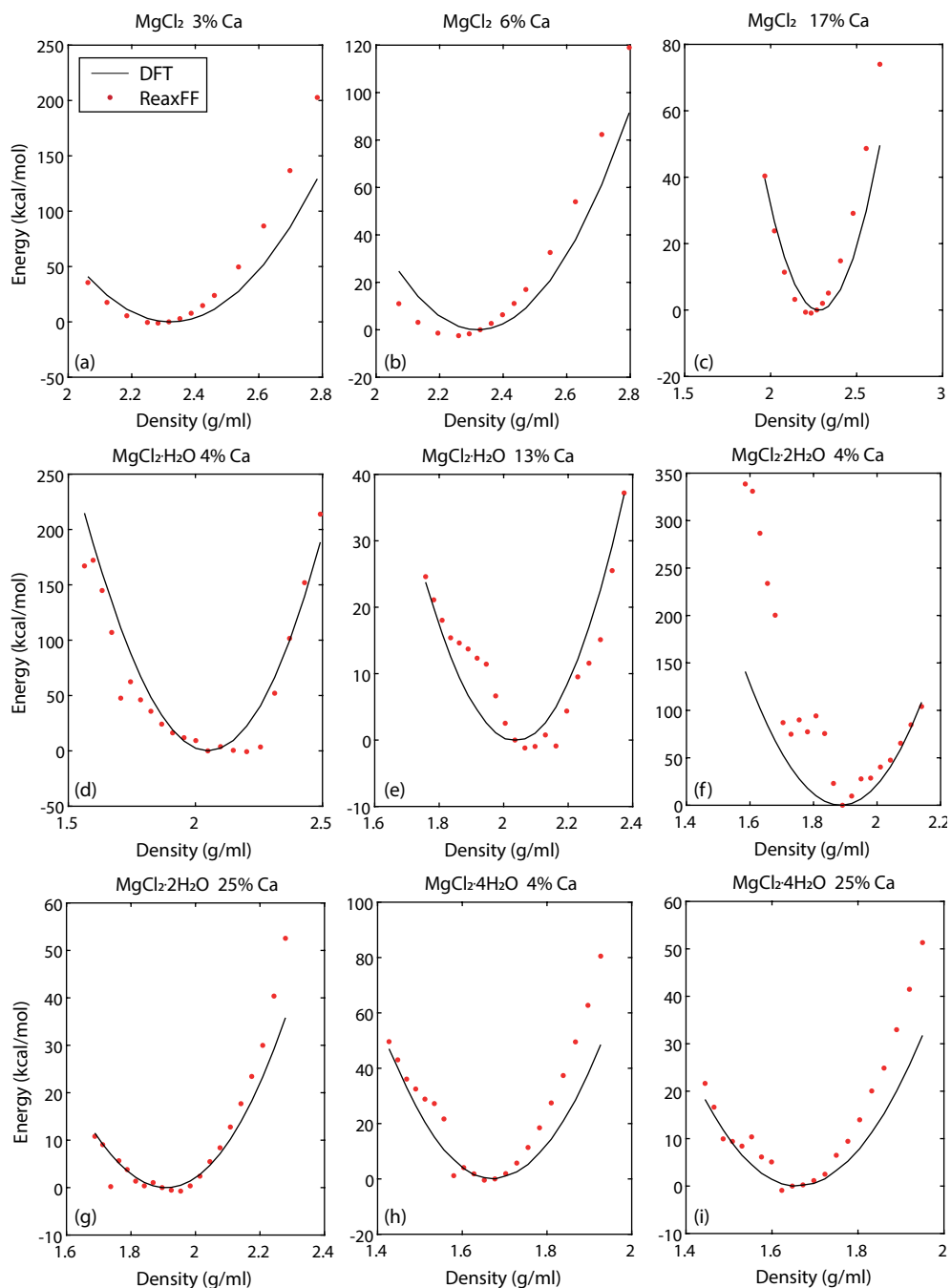


Figure G.1



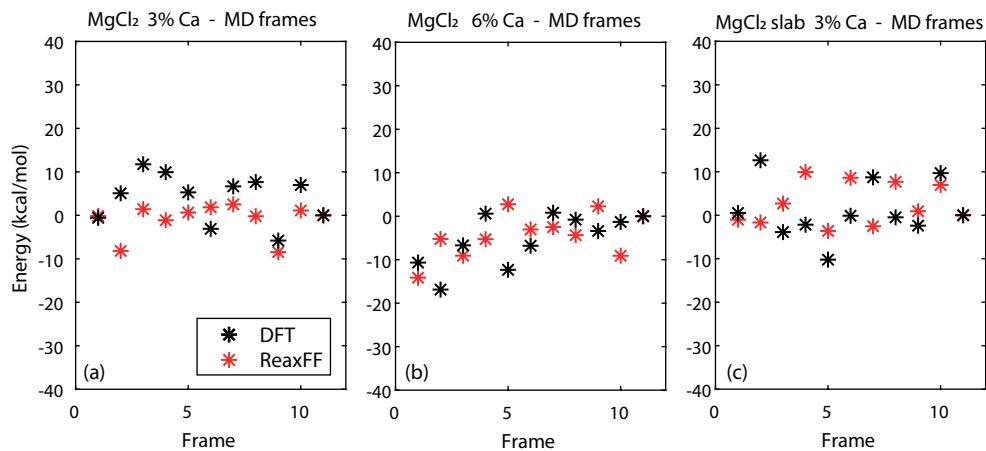


Figure G.2

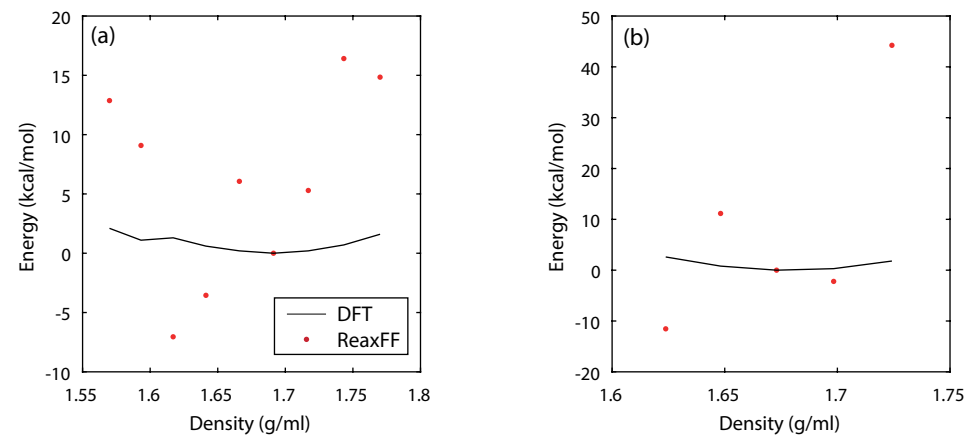


Figure G.3



# REFERENCES

- [1] European Commission, “European Green Deal,” 2020. (accessed: March 13, 2021).
- [2] United Nations, “The Paris Agreement,” 2015. (accessed: March 13, 2021).
- [3] Fraunhofer and et al., “Mapping and Analysis of the Current and Future (2020-2030) heating/cooling fuel deployment (fossils/renewables),” 2016. (accessed: June 25, 2020).
- [4] D. Lefebvre and F. H. Tezel, “A review of energy storage technologies with a focus on adsorption thermal energy storage processes for heating applications,” *Renewable and Sustainable Energy Reviews*, vol. 67, pp. 116–125, 2017.
- [5] E. H. Lysen, “The trias energica: solar energy strategies for developing countries,” 1996.
- [6] L. B. Hyman, *Sustainable thermal storage systems: planning, design, and operations*. McGraw-Hill Education, 2011.
- [7] K. E. N’tsoukpoe, H. Liu, N. Le Pierrès, and L. Luo, “A review on long-term sorption solar energy storage,” *Renewable Sustainable Energy Rev.*, vol. 13, no. 9, pp. 2385–2396, 2009.
- [8] P. Tatsidjodoung, N. Le Pierrès, and L. Luo, “A review of potential materials for thermal energy storage in building applications,” *Renewable and Sustainable Energy Reviews*, vol. 18, pp. 327–349, 2013.
- [9] H. Mehling and L. F. Cabeza, *Heat and cold storage with PCM*, vol. 308. Springer, 2008.
- [10] J. Jänchen, D. Ackermann, H. Stach, and W. Brösicke, “Studies of the water adsorption on zeolites and modified mesoporous materials for seasonal storage of solar heat,” *Solar energy*, vol. 76, no. 1-3, pp. 339–344, 2004.
- [11] P. A. J. Donkers, L. C. Sögütoglu, H. P. Huinink, H. R. Fischer, and O. C. G. Adan, “A review of salt hydrates for seasonal heat storage in domestic applications,” *Appl. Energy*, vol. 199, pp. 45–68, 2017.
- [12] A. Sharma, V. V. Tyagi, C. Chen, and D. Buddhi, “Review on thermal energy storage with phase change materials and applications,” *Renewable and Sustainable energy reviews*, vol. 13, no. 2, pp. 318–345, 2009.

- [13] L. Cabeza, A. Castell, C. Barreneche, A. de Gracia, and A. Fernández, "Materials used as PCM in thermal energy storage in buildings: A review," *Renewable and Sustainable Energy Reviews*, vol. 15, no. 3, pp. 1675–1695, 2011.
- [14] B. Zalba, J. M. Marin, L. F. Cabeza, and H. Mehling, "Review on thermal energy storage with phase change: materials, heat transfer analysis and applications," *Applied thermal engineering*, vol. 23, no. 3, pp. 251–283, 2003.
- [15] I. Dincer and M. Rosen, *Thermal energy storage: systems and applications*. John Wiley & Sons, 2002.
- [16] P. Pinel, C. A. Cruickshank, I. Beausoleil-Morrison, and A. Wills, "A review of available methods for seasonal storage of solar thermal energy in residential applications," *Renewable and Sustainable Energy Reviews*, vol. 15, no. 7, pp. 3341–3359, 2011.
- [17] K. E. N'Tsoukpoe and F. Kuznik, "A reality check on long-term thermochemical heat storage for household applications," *Renewable and Sustainable Energy Reviews*, vol. 139, p. 110683, 2021.
- [18] L. Scapino, H. A. Zondag, J. Van Bael, J. Diriken, and C. C. M. Rindt, "Sorption heat storage for long-term low-temperature applications: A review on the advancements at material and prototype scale," *Applied Energy*, vol. 190, pp. 920–948, 2017.
- [19] Y. Zhang and R. Wang, "Sorption thermal energy storage: Concept, process, applications and perspectives," *Energy Storage Mater.*, 2020.
- [20] F. Trausel, A.-J. De Jong, and R. Cuypers, "A review on the properties of salt hydrates for thermochemical storage," *Energy Procedia*, vol. 48, pp. 447–452, 2014.
- [21] N. Yu, R. Wang, and L. Wang, "Sorption thermal storage for solar energy," *Prog. Energy Combust. Sci.*, vol. 39, no. 5, pp. 489–514, 2013.
- [22] R.-J. Clark, A. Mehrabadi, and M. Farid, "State of the art on salt hydrate thermochemical energy storage systems for use in building applications," *J. Energy Storage*, vol. 27, p. 101145, 2020.
- [23] P. Pardo, A. Deydier, Z. Anxionnaz-Minvielle, S. Rougé, M. Cabassud, and P. Cognet, "A review on high temperature thermochemical heat energy storage," *Renewable Sustainable Energy Rev.*, vol. 32, pp. 591–610, 2014.
- [24] V. Van Essen, J. Cot Gores, L. Bleijendaal, H. Zondag, R. Schuitema, M. Bakker, and W. Van Helden, "Characterization of salt hydrates for compact seasonal thermochemical storage," in *ASME 2009 3rd international conference on energy sustainability collocated with the heat transfer and InterPACK09 conferences, July 19-23, San Francisco, USA*, pp. 825–830, American Society of Mechanical Engineers Digital Collection, 2009.
- [25] W. M. Haynes, *CRC handbook of chemistry and physics*. CRC press, 2014.

- 
- [26] B. Carlsson, H. Stymne, and G. Wettermark, "An incongruent heat-of-fusion system  $\text{CaCl}_2 \cdot 6\text{H}_2\text{O}$  - made congruent through modification of the chemical composition of the system," *Sol. Energy*, vol. 23, no. 4, pp. 343–350, 1979.
  - [27] C. J. Ferchaud, H. A. Zondag, J. B. J. Veldhuis, and R. De Boer, "Study of the reversible water vapour sorption process of  $\text{MgSO}_4 \cdot 7\text{H}_2\text{O}$  and  $\text{MgCl}_2 \cdot 6\text{H}_2\text{O}$  under the conditions of seasonal solar heat storage," in *J. Phys.: Conf. Ser.*, vol. 395, p. 012069, IOP Publishing, 2012.
  - [28] L.-C. Sögütoglu, M. Steiger, J. Houben, D. Biemans, H. R. Fischer, P. Donkers, H. Huinink, and O. C. Adan, "Understanding the hydration process of salts: the impact of a nucleation barrier," *Crystal Growth & Design*, vol. 19, no. 4, pp. 2279–2288, 2019.
  - [29] L.-C. Sögütoglu, F. Birkelbach, A. Werner, H. Fischer, H. Huinink, and O. Adan, "Hydration of salts as a two-step process: Water adsorption and hydrate formation," *Thermochimica Acta*, vol. 695, p. 178819, 2021.
  - [30] C. Barreneche, A. I. Fernández, L. F. Cabeza, and R. Cuypers, "Thermophysical characterization and thermal cycling stability of two TCM:  $\text{CaCl}_2$  and zeolite," *Applied Energy*, vol. 137, pp. 726–730, 2015.
  - [31] H. U. Rammelberg, T. Osterland, B. Priehs, O. Opel, and W. K. Ruck, "Thermochemical heat storage materials—performance of mixed salt hydrates," *Sol. Energy*, vol. 136, pp. 571–589, 2016.
  - [32] A. U. Rehman, Z. Maosheng, and A. Hayat, "Hydration performance and cycling stability of three TCM:  $\text{MgSO}_4$ ,  $\text{ZnSO}_4$  and  $\text{FeSO}_4$ ," *International Journal of Energy Research*, vol. 44, no. 8, pp. 6981–6990, 2020.
  - [33] H. A. Zondag, V. M. Van Essen, L. P. J. Bleijendaal, B. W. J. Kikkert, and M. Bakker, "Application of  $\text{MgCl}_2 \cdot 6\text{H}_2\text{O}$  for thermochemical seasonal solar heat storage," in *5th International Renewable Energy Storage Conference (IRES 2010), Berlin, Germany, Nov 22-24, 2010*, 2010.
  - [34] G. J. Kipouros and D. R. Sadoway, "A thermochemical analysis of the production of anhydrous  $\text{MgCl}_2$ ," *Journal of Light Metals*, vol. 1, no. 2, pp. 111–117, 2001.
  - [35] B. Warnqvist, "Comments on thermochemical data and fusion temperature for pure sodium sulfide," *Thermochimica Acta*, vol. 37, no. 3, pp. 343–345, 1980.
  - [36] Á. G. Fernández and L. F. Cabeza, "Corrosion inhibitors for TES material at high temperature for CSP plants," in *Eurotherm Seminar# 112-Advances in Thermal Energy Storage. Universitat de Lleida, 15-17th May 2019. Edicions de la Universitat de Lleida. ISBN: 978-84-9144-155-7. pp. R-108-1-R-108-7*, Edicions de la Universitat de Lleida, 2019.
  - [37] A. Solé, L. Miró, C. Barreneche, I. Martorell, and L. F. Cabeza, "Corrosion test of salt hydrates and vessel metals for thermochemical energy storage," *Energy Procedia*, vol. 48, pp. 431–435, 2014.

- [38] A.-J. de Jong, R. Stevens, C. Rentrop, and C. Hoegaerts, "Coatings for heat storage reactors with hygroscopic salts," *Energy Procedia*, vol. 70, pp. 182–192, 2015.
- [39] A. Palacios, L. Cong, M. Navarro, Y. Ding, and C. Barreneche, "Thermal conductivity measurement techniques for characterizing thermal energy storage materials—a review," *Renewable and Sustainable Energy Reviews*, vol. 108, pp. 32–52, 2019.
- [40] A. D. Pathak, S. Nedeia, A. C. T. Van Duin, H. A. Zondag, C. C. M. Rindt, and D. M. J. Smeulders, "Reactive force field development for magnesium chloride hydrates and its application for seasonal heat storage," *Phys. Chem. Chem. Phys.*, vol. 18, no. 23, pp. 15838–15847, 2016.
- [41] H. U. Rammelberg, M. Myrau, T. Schmidt, and W. Ruck, "An optimization of salt hydrates for thermochemical heat storage," in *Touka Shobo (Hg.): Innovative Materials for Processes in Energy Systems*, (ed.) Saha B. B., Koyama M., Takata Y., Hamamoto Y., Miyazaki T., Masamichi K., Ito K. IMPRES, pp. 550–555, 2013.
- [42] M.-M. Druske, A. Fopah-Lele, K. Korhammer, H. U. Rammelberg, N. Wegscheider, W. Ruck, and T. Schmidt, "Developed materials for thermal energy storage: synthesis and characterization," *Energy procedia*, vol. 61, pp. 96–99, 2014.
- [43] B. G. van Ravensteijn, P. A. Donkers, R. C. Ruliaman, J. Eversdijk, H. R. Fischer, H. P. Huinink, and O. C. G. Adan, "Encapsulation of salt hydrates by polymer coatings for low-temperature heat storage applications," *ACS Applied Polymer Materials*, 2021.
- [44] A. Shkatulov, J. Ryu, Y. Kato, and Y. Aristov, "Composite material "Mg(OH)<sub>2</sub>/vermiculite": A promising new candidate for storage of middle temperature heat," *Energy*, vol. 44, no. 1, pp. 1028–1034, 2012.
- [45] A. I. Shkatulov, J. Houben, H. Fischer, and H. P. Huinink, "Stabilization of K<sub>2</sub>CO<sub>3</sub> in vermiculite for thermochemical energy storage," *Renewable Energy*, vol. 150, pp. 990–1000, 2020.
- [46] S. Salviati, F. Carosio, F. Cantamessa, L. Medina, L. A. Berglund, G. Saracco, and A. Fina, "Ice-templated nanocellulose porous structure enhances thermochemical storage kinetics in hydrated salt/graphite composites," *Renewable Energy*, vol. 160, pp. 698–706, 2020.
- [47] M. Gaeini, A. L. Rouws, J. W. O. Salari, H. A. Zondag, and C. C. M. Rindt, "Characterization of microencapsulated and impregnated porous host materials based on calcium chloride for thermochemical energy storage," *Applied energy*, vol. 212, pp. 1165–1177, 2018.
- [48] H. A. Ousaleh, S. Sair, S. Mansouri, Y. Abboud, A. Faik, and A. El Bouari, "New hybrid graphene/inorganic salt composites for thermochemical energy storage: Synthesis, cyclability investigation and heat exchanger metal corrosion protection performance," *Solar Energy Materials and Solar Cells*, vol. 215, p. 110601, 2020.

- 
- [49] G. Whiting, D. Grondin, S. Bennici, and A. Auroux, "Heats of water sorption studies on zeolite-MgSO<sub>4</sub> composites as potential thermochemical heat storage materials," *Solar energy materials and solar cells*, vol. 112, pp. 112–119, 2013.
- [50] K. Korhammer, M.-M. Druske, A. Fopah-Lele, H. U. Rammelberg, N. Wegscheider, O. Opel, T. Osterland, and W. Ruck, "Sorption and thermal characterization of composite materials based on chlorides for thermal energy storage," *Applied Energy*, vol. 162, pp. 1462–1472, 2016.
- [51] E. Courbon, P. D'Ans, A. Permyakova, O. Skrylnyk, N. Steunou, M. Degrez, and M. Frère, "Further improvement of the synthesis of silica gel and CaCl<sub>2</sub> composites: Enhancement of energy storage density and stability over cycles for solar heat storage coupled with space heating applications," *Solar Energy*, vol. 157, pp. 532–541, 2017.
- [52] L. Garzón-Tovar, J. Pérez-Carvajal, I. Imaz, and D. Maspoch, "Composite salt in porous metal-organic frameworks for adsorption heat transformation," *Advanced Functional Materials*, vol. 27, no. 21, p. 1606424, 2017.
- [53] H. P. Huinink, S. Sansotta, and D. Zahn, "Defect-driven water migration in MgCl<sub>2</sub> tetra- and hexahydrates," *Journal of Solid State Chemistry*, vol. 277, pp. 221–228, 2019.
- [54] C. Huang, M. Xu, and X. Huai, "Experimental investigation on thermodynamic and kinetic of calcium hydroxide dehydration with hexagonal boron nitride doping for thermochemical energy storage," *Chemical Engineering Science*, vol. 206, pp. 518–526, 2019.
- [55] D. Müller, C. Knoll, T. Ruh, W. Artner, J. M. Welch, H. Peterlik, E. Eitenberger, G. Friedbacher, M. Harasek, P. Blaha, *et al.*, "Calcium doping facilitates water dissociation in magnesium oxide," *Adv. Sustainable Syst.*, vol. 2, no. 1, p. 1700096, 2018.
- [56] A. Shkatulov, T. Krieger, V. Zaikovskii, Y. Chesalov, and Y. Aristov, "Doping magnesium hydroxide with sodium nitrate: A new approach to tune the dehydration reactivity of heat-storage materials," *ACS applied materials & interfaces*, vol. 6, no. 22, pp. 19966–19977, 2014.
- [57] A. Shkatulov and Y. Aristov, "Calcium hydroxide doped by KNO<sub>3</sub> as a promising candidate for thermochemical storage of solar heat," *RSC advances*, vol. 7, no. 68, pp. 42929–42939, 2017.
- [58] H. A. Ousaleh, S. Sair, A. Zaki, A. Faik, J. M. Igartua, and A. El Bouari, "Double hydrates salt as sustainable thermochemical energy storage materials: Evaluation of dehydration behavior and structural phase transition reversibility," *Solar Energy*, vol. 201, pp. 846–856, 2020.

- [59] A. D. Pathak, S. Nedea, H. Zondag, C. Rindt, and D. Smeulders, "A DFT-based comparative equilibrium study of thermal dehydration and hydrolysis of  $\text{CaCl}_2$  hydrates and  $\text{MgCl}_2$  hydrates for seasonal heat storage," *Phys. Chem. Chem. Phys.*, vol. 18, no. 15, pp. 10059–10069, 2016.
- [60] A. D. Pathak, I. Tranca, S. V. Nedea, H. A. Zondag, C. C. M. Rindt, and D. M. J. Smeulders, "First-principles study of chemical mixtures of  $\text{CaCl}_2$  and  $\text{MgCl}_2$  hydrates for optimized seasonal heat storage," *J. Phys. Chem. C*, vol. 121, no. 38, pp. 20576–20590, 2017.
- [61] N. Metropolis, "The beginning of the Monte Carlo method," *Los Alamos Science*, vol. 15, pp. 125–130, 1987.
- [62] T. Haigh, M. Priestley, and C. Rope, "Los Alamos bets on ENIAC: Nuclear Monte Carlo simulations, 1947-1948," *IEEE Annals of the History of Computing*, vol. 36, no. 3, pp. 42–63, 2014.
- [63] D. Frenkel and B. Smit, *Understanding molecular simulation 2nd edition*. Academic Press, London, UK, 2002.
- [64] P. A. Freiburger and M. R. Swaine, "ENIAC," *Encyclopedia Britannica*. (accessed: 16 June 2021).
- [65] A. Khan, H. Sim, S. S. Vazhkudai, A. R. Butt, and Y. Kim, "An analysis of system balance and architectural trends based on Top500 supercomputers," in *The International Conference on High Performance Computing in Asia-Pacific Region*, pp. 11–22, 2021.
- [66] A. Yakunchikov and V. Kosyanchuk, "Application of event-driven molecular dynamics approach to rarefied gas dynamics problems," *Computers & Fluids*, vol. 170, pp. 121–127, 2018.
- [67] B. Dias, F. Bariselli, A. Turchi, A. Frezzotti, P. Chatelain, and T. Magin, "Development of a melting model for meteors," in *AIP Conference Proceedings*, vol. 1786, p. 160004, AIP Publishing LLC, 2016.
- [68] Z. Duan, N. Møller, and J. H. Weare, "Molecular dynamics simulation of PVT properties of geological fluids and a general equation of state of nonpolar and weakly polar gases up to 2000 K and 20,000 bar," *Geochimica et Cosmochimica Acta*, vol. 56, no. 10, pp. 3839–3845, 1992.
- [69] K. Heijmans, A. D. Pathak, P. Solano-López, D. Giordano, S. Nedea, and D. Smeulders, "Thermal boundary characteristics of homo-/heterogeneous interfaces," *Nanomaterials*, vol. 9, no. 5, p. 663, 2019.
- [70] S. A. Hollingsworth and R. O. Dror, "Molecular dynamics simulation for all," *Neuron*, vol. 99, no. 6, pp. 1129–1143, 2018.



- 
- [71] A. R. Oganov and C. W. Glass, "Crystal structure prediction using ab initio evolutionary techniques: Principles and applications," *J. Chem. Phys.*, vol. 124, no. 24, p. 244704, 2006.
- [72] A. R. Oganov, Y. Ma, A. O. Lyakhov, M. Valle, and C. Gatti, "Evolutionary crystal structure prediction as a method for the discovery of minerals and materials," *Rev. Mineral. Geochem.*, vol. 71, no. 1, pp. 271–298, 2010.
- [73] A. O. Lyakhov, A. R. Oganov, H. T. Stokes, and Q. Zhu, "New developments in evolutionary structure prediction algorithm USPEX," *Comput. Phys. Commun.*, vol. 184, no. 4, pp. 1172–1182, 2013.
- [74] M. Korth, "Large-scale virtual high-throughput screening for the identification of new battery electrolyte solvents: evaluation of electronic structure theory methods," *Physical Chemistry Chemical Physics*, vol. 16, no. 17, pp. 7919–7926, 2014.
- [75] P. Hohenberg and W. Kohn, "Inhomogeneous electron gas," *Physical review*, vol. 136, no. 3B, p. B864, 1964.
- [76] W. Kohn and L. J. Sham, "Self-consistent equations including exchange and correlation effects," *Physical review*, vol. 140, no. 4A, p. A1133, 1965.
- [77] R. M. Martin, *Electronic structure: basic theory and practical methods*. Cambridge university press, 2020.
- [78] C. Fiolhais, F. Nogueira, and M. A. L. Marques, *A primer in density functional theory*, vol. 620. Springer Science & Business Media, 2003.
- [79] I. Tranca and K. Schroeder, "Density functional study of molecular adsorption on the Cu (011) surface: oxalic acid and 2, 5 pyrazine di-carboxylic acid," tech. rep., RWTH Aachen University, 2011.
- [80] N. Goga, L. Mayrhofer, I. Tranca, S. Nedeia, K. Heijmans, V. Ponnuchamy, and A. Vasilateanu, "A review of recent developments in molecular dynamics simulations of the photoelectrochemical water splitting process," *Catalysts*, vol. 11, no. 7, 2021.
- [81] A. C. Van Duin, S. Dasgupta, F. Lorant, and W. A. Goddard, "ReaxFF: a reactive force field for hydrocarbons," *The Journal of Physical Chemistry A*, vol. 105, no. 41, pp. 9396–9409, 2001.
- [82] K. Chenoweth, A. C. Van Duin, and W. A. Goddard, "ReaxFF reactive force field for molecular dynamics simulations of hydrocarbon oxidation," *The Journal of Physical Chemistry A*, vol. 112, no. 5, pp. 1040–1053, 2008.
- [83] E. Iype, M. Hütter, A. P. J. Jansen, S. V. Nedeia, and C. C. M. Rindt, "Parameterization of a reactive force field using a Monte Carlo algorithm," *Journal of Computational Chemistry*, vol. 34, no. 13, pp. 1143–1154, 2013.

- [84] M. Born and R. Oppenheimer, "Zur quantentheorie der molekeln," *Annalen der physik*, vol. 389, no. 20, pp. 457–484, 1927.
- [85] R. Haunschild, A. Barth, and B. French, "A comprehensive analysis of the history of DFT based on the bibliometric method RPYS," *Journal of Cheminformatics*, vol. 11, no. 1, pp. 1–15, 2019.
- [86] J. Gibbs, "Elementary principles in statistical mechanics (New York: Charles scribner's sons)," 1902.
- [87] R. C. Tolman, *The principles of statistical mechanics*. Courier Corporation, 1979.
- [88] F. Reif, *Fundamentals of statistical and thermal physics*. Waveland Press, 2009.
- [89] B. J. Alder and T. E. Wainwright, "Molecular dynamics by electronic computers," *Transport processes in statistical mechanics*, pp. 97–131, 1958.
- [90] D. Ceperley, "Berni Alder (1925-2020)," *Nature*, vol. 586, no. 7829, p. 356, 2020.
- [91] J. Gibson, A. N. Goland, M. Milgram, and G. Vineyard, "Dynamics of radiation damage," *Physical Review*, vol. 120, no. 4, p. 1229, 1960.
- [92] L. Verlet, "Computer" experiments" on classical fluids. I. thermodynamical properties of Lennard-Jones molecules," *Physical review*, vol. 159, no. 1, p. 98, 1967.
- [93] M. G. Martin and J. I. Siepmann, "Transferable potentials for phase equilibria. 1. united-atom description of n-alkanes," *The Journal of Physical Chemistry B*, vol. 102, no. 14, pp. 2569–2577, 1998.
- [94] M. G. Martin and J. I. Siepmann, "Novel configurational-bias Monte Carlo method for branched molecules. transferable potentials for phase equilibria. 2. united-atom description of branched alkanes," *The Journal of Physical Chemistry B*, vol. 103, no. 21, pp. 4508–4517, 1999.
- [95] D. Dubbeldam, S. Calero, T. J. H. Vlught, R. Krishna, T. L. M. Maesen, and B. Smit, "United atom force field for alkanes in nanoporous materials," *The Journal of Physical Chemistry B*, vol. 108, no. 33, pp. 12301–12313, 2004.
- [96] B. Liu, B. Smit, F. Rey, S. Valencia, and S. Calero, "A new united atom force field for adsorption of alkenes in zeolites," *The Journal of Physical Chemistry C*, vol. 112, no. 7, pp. 2492–2498, 2008.
- [97] S. Calero, D. Dubbeldam, R. Krishna, B. Smit, T. J. H. Vlught, J. F. M. Denayer, J. A. Martens, and T. L. M. Maesen, "Understanding the role of sodium during adsorption: A force field for alkanes in sodium-exchanged faujasites," *Journal of the American Chemical Society*, vol. 126, no. 36, pp. 11377–11386, 2004.
- [98] D. Dubbeldam, S. Calero, T. J. H. Vlught, R. Krishna, T. L. M. Maesen, E. Beerdsen, and B. Smit, "Force field parametrization through fitting on inflection points in isotherms," *Physical review letters*, vol. 93, no. 8, p. 088302, 2004.

- 
- [99] A. Garcia-Sanchez, C. O. Ania, J. B. Parra, D. Dubbeldam, T. J. H. Vlugt, R. Krishna, and S. Calero, "Transferable force field for carbon dioxide adsorption in zeolites," *The Journal of Physical Chemistry C*, vol. 113, no. 20, pp. 8814–8820, 2009.
- [100] A. D. Pathak, K. Heijmans, S. Nedeia, A. C. T. van Duin, H. Zondag, C. Rindt, and D. Smeulders, "Mass diffusivity and thermal conductivity estimation of chloride-based salt hydrates for thermo-chemical heat storage: A molecular dynamics study using the reactive force field.," *Int. J. Heat Mass Transfer*, vol. 149, p. 119090, 2020.
- [101] P. P. Ewald, "Die berechnung optischer und elektrostatischer gitterpotentiale," *Annalen der physik*, vol. 369, no. 3, pp. 253–287, 1921.
- [102] T. Liang, Y. K. Shin, Y.-T. Cheng, D. E. Yilmaz, K. G. Vishnu, O. Vernalis, C. Zou, S. R. Phillpot, S. B. Sinnott, and A. C. Van Duin, "Reactive potentials for advanced atomistic simulations," *Annual review of materials research*, vol. 43, pp. 109–129, 2013.
- [103] M. S. Daw and M. I. Baskes, "Embedded-atom method: Derivation and application to impurities, surfaces, and other defects in metals," *Physical Review B*, vol. 29, no. 12, p. 6443, 1984.
- [104] M. S. Daw and M. I. Baskes, "Semiempirical, quantum mechanical calculation of hydrogen embrittlement in metals," *Physical review letters*, vol. 50, no. 17, p. 1285, 1983.
- [105] M. W. Finnis and J. E. Sinclair, "A simple empirical n-body potential for transition metals," *Philosophical Magazine A*, vol. 50, no. 1, pp. 45–55, 1984.
- [106] M. I. Baskes, "Application of the embedded-atom method to covalent materials: a semiempirical potential for silicon," *Physical review letters*, vol. 59, no. 23, p. 2666, 1987.
- [107] F. H. Stillinger and T. A. Weber, "Computer simulation of local order in condensed phases of silicon," *Physical review B*, vol. 31, no. 8, p. 5262, 1985.
- [108] G. C. Abell, "Empirical chemical pseudopotential theory of molecular and metallic bonding," *Physical Review B*, vol. 31, no. 10, p. 6184, 1985.
- [109] J. Tersoff, "New empirical model for the structural properties of silicon," *Physical review letters*, vol. 56, no. 6, p. 632, 1986.
- [110] J. Tersoff, "Empirical interatomic potential for carbon, with applications to amorphous carbon," *Physical Review Letters*, vol. 61, no. 25, p. 2879, 1988.
- [111] D. W. Brenner, "Empirical potential for hydrocarbons for use in simulating the chemical vapor deposition of diamond films," *Physical review B*, vol. 42, no. 15, p. 9458, 1990.

- [112] D. W. Brenner, O. A. Shenderova, J. A. Harrison, S. J. Stuart, B. Ni, and S. B. Sinnott, "A second-generation reactive empirical bond order (rebo) potential energy expression for hydrocarbons," *Journal of Physics: Condensed Matter*, vol. 14, no. 4, p. 783, 2002.
- [113] T. Liang, B. Devine, S. R. Phillpot, and S. B. Sinnott, "Variable charge reactive potential for hydrocarbons to simulate organic-copper interactions," *The Journal of Physical Chemistry A*, vol. 116, no. 30, pp. 7976–7991, 2012.
- [114] B. Devine, T.-R. Shan, Y.-T. Cheng, A. J. H. McGaughey, M. Lee, S. R. Phillpot, S. B. Sinnott, *et al.*, "Atomistic simulations of copper oxidation and Cu/Cu<sub>2</sub>O interfaces using charge-optimized many-body potentials," *Physical Review B*, vol. 84, no. 12, p. 125308, 2011.
- [115] Y.-T. Cheng, T.-R. Shan, B. Devine, D. Lee, T. Liang, B. B. Hinojosa, S. R. Phillpot, A. Asthagiri, and S. B. Sinnott, "Atomistic simulations of the adsorption and migration barriers of Cu adatoms on ZnO surfaces using comb potentials," *Surface science*, vol. 606, no. 15-16, pp. 1280–1288, 2012.
- [116] T.-R. Shan, B. D. Devine, J. M. Hawkins, A. Asthagiri, S. R. Phillpot, S. B. Sinnott, *et al.*, "Second-generation charge-optimized many-body potential for si/sio 2 and amorphous silica," *Physical Review B*, vol. 82, no. 23, p. 235302, 2010.
- [117] Y. Li, T.-R. Shan, T. Liang, S. B. Sinnott, and S. R. Phillpot, "Classical interatomic potential for orthorhombic uranium," *Journal of Physics: Condensed Matter*, vol. 24, no. 23, p. 235403, 2012.
- [118] J. Yu, S. B. Sinnott, and S. R. Phillpot, "Charge optimized many-body potential for the Si/SiO<sub>2</sub> system," *Physical Review B*, vol. 75, no. 8, p. 085311, 2007.
- [119] T. P. Senftle, S. Hong, M. M. Islam, S. B. Kylasa, Y. Zheng, Y. K. Shin, C. Junkermeier, R. Engel-Herbert, M. J. Janik, H. M. Aktulga, T. Verstraelen, and A. C. Grama Ananth, van Duin, "The ReaxFF reactive force-field: development, applications and future directions," *npj Computational Materials*, vol. 2, no. 1, pp. 1–14, 2016.
- [120] M. Elstner, D. Porezag, G. Jungnickel, J. Elsner, M. Haugk, T. Frauenheim, S. Suhai, and G. Seifert, "Self-consistent-charge density-functional tight-binding method for simulations of complex materials properties," *Physical Review B*, vol. 58, no. 11, p. 7260, 1998.
- [121] T. Qi, C. W. Bauschlicher, J. W. Lawson, T. G. Desai, E. J. Reed, and A. Lenfant, "Addendum to "comparison of ReaxFF, DFTB, and DFT for phenolic pyrolysis. 1. molecular dynamics simulations" and "comparison of ReaxFF, DFTB, and DFT for phenolic pyrolysis. 2. elementary reaction paths", " *The Journal of Physical Chemistry A*, vol. 118, no. 28, pp. 5355–5357, 2014.

- 
- [122] H.-J. Qian, A. C. T. van Duin, K. Morokuma, and S. Irle, "Reactive molecular dynamics simulation of fullerene combustion synthesis: ReaxFF vs DFTB potentials," *Journal of chemical theory and computation*, vol. 7, no. 7, pp. 2040–2048, 2011.
- [123] R. Perriot, C. F. Negre, S. D. McGrane, and M. J. Cawkwell, "Density functional tight binding calculations for the simulation of shocked nitromethane with latte-lammmps," in *AIP Conference Proceedings*, vol. 1979, p. 050014, AIP Publishing LLC, 2018.
- [124] "ReaxFF 2020, SCM, theoretical chemistry0."
- [125] E. Iype, Z. S. A. Khalfay, R. G. Chaudhuri, and B. P. Kumar, "Epsomite dehydration: A molecular dynamics study," *Journal of Energy Storage*, vol. 20, pp. 337–343, 2018.
- [126] X.-Q. Zhang, E. Iype, S. V. Nedea, A. P. Jansen, B. M. Szyja, E. J. Hensen, and R. A. van Santen, "Site stability on cobalt nanoparticles: a molecular dynamics ReaxFF reactive force field study," *The Journal of Physical Chemistry C*, vol. 118, no. 13, pp. 6882–6886, 2014.
- [127] W. J. Mortier, S. K. Ghosh, and S. Shankar, "Electronegativity-equalization method for the calculation of atomic charges in molecules," *Journal of the American Chemical Society*, vol. 108, no. 15, pp. 4315–4320, 1986.
- [128] N. Metropolis, A. W. Rosenbluth, M. N. Rosenbluth, A. H. Teller, and E. Teller, "Equation of state calculations by fast computing machines," *The journal of chemical physics*, vol. 21, no. 6, pp. 1087–1092, 1953.
- [129] D. Dubbeldam, A. Torres-Knoop, and K. S. Walton, "On the inner workings of Monte Carlo codes," *Molecular Simulation*, vol. 39, no. 14-15, pp. 1253–1292, 2013.
- [130] K. Heijmans, I. C. Tranca, S. V. Gaastra-Nedea, and D. M. J. Smeulders, "Exploring the electronic structure of new doped salt hydrates,  $\text{Mg}_{1-x}\text{Ca}_x\text{Cl}_2 \cdot n\text{H}_2\text{O}$ , for thermochemical energy storage," *The Journal of Physical Chemistry C*, 2020.
- [131] K. Heijmans, S. Nab, B. Klein Holkenborg, A. D. Pathak, S. Gaastra-Nedea, and D. Smeulders, "Development of a reactive force field for  $\text{CaCl}_2 \cdot n\text{H}_2\text{O}$ , and the application to thermochemical energy storage," *Computational Materials Science*, vol. 197, p. 110595, 2021.
- [132] K. Heijmans, I. C. Tranca, D. M. J. Smeulders, T. J. H. Vlugt, and S. V. Gaastra-Nedea, "Gibbs ensemble Monte Carlo for reactive force fields to determine the vapor–liquid equilibrium of  $\text{CO}_2$  and  $\text{H}_2\text{O}$ ," *Journal of Chemical Theory and Computation*, 2020.
- [133] Y. Zhang, H. Dong, R. Wang, and P. Feng, "Air humidity assisted sorption thermal battery governed by reaction wave model," *Energy Storage Mater.*, vol. 27, pp. 9–16, 2020.

- [134] K. Heijmans, I. Tranca, S. Nedea, and D. Smeulders, "Ab-initio study of doped salt hydrates crystal stabilities for thermochemical heat storage," in *Advances in Thermal Energy Storage, Eurotherm Seminar #112, Lleida, Spain, 25-17 May 2019*, pp. 123–131, 2019.
- [135] A. D. Pathak, S. Nedea, H. Zondag, C. Rindt, and D. Smeulders, "Diffusive transport of water in magnesium chloride dihydrate under various external conditions for long term heat storage: A ReaxFF-md study," *Eur. J. Mech. B Fluids*, vol. 64, pp. 93–101, 2017.
- [136] X. L. Hu, J. Carrasco, J. Klimeš, and A. Michaelides, "Trends in water monomer adsorption and dissociation on flat insulating surfaces," *Phys. Chem. Chem. Phys.*, vol. 13, no. 27, pp. 12447–12453, 2011.
- [137] A. Abhat and T. Huy, "Heat and mass transfer considerations in a thermochemical energy storage system based on solid-gas reactions," *Solar Energy*, vol. 30, no. 2, pp. 93–98, 1983.
- [138] C. Oses, E. Gossett, D. Hicks, F. Rose, M. J. Mehl, E. Perim, I. Takeuchi, S. Sanvito, M. Scheffler, Y. Lederer, *et al.*, "AFLOW-CHULL: cloud-oriented platform for autonomous phase stability analysis," *J. Chem. Inf. Model.*, vol. 58, no. 12, pp. 2477–2490, 2018.
- [139] R. W. G. Wyckoff, "Crystal structures, second edition," pp. 239–444, 1963.
- [140] J. A. Kaduk, "Use of the inorganic crystal structure database as a problem solving tool," *Acta Crystallogr. B Struct. Sci.*, vol. 58, no. 3, pp. 370–379, 2002.
- [141] A. Leclaire and M. Borel, "Le dichlorure de calcium dihydraté," *Acta Crystallogr., Sect. B: Struct. Crystallogr. Cryst. Chem.*, vol. 33, no. 5, pp. 1608–1610, 1977.
- [142] H. Schmidt, E. Hennings, and W. Voigt, "Magnesium chloride tetrahydrate,  $\text{MgCl}_2 \cdot 4\text{H}_2\text{O}$ ," *Acta Crystallogr., Sect. C: Cryst. Struct. Commun.*, vol. 68, no. 1, pp. i4–i6, 2012.
- [143] A. Leclaire, M. Borel, and J. Monier, "La forme  $\gamma$  du dichlorure de calcium tétrahydraté," *Acta Crystallogr., Sect. B: Struct. Crystallogr. Cryst. Chem.*, vol. 36, no. 11, pp. 2757–2759, 1980.
- [144] P. A. Agron and W. R. Busing, "Magnesium dichloride hexahydrate,  $\text{MgCl}_2 \cdot 6\text{H}_2\text{O}$ , by neutron diffraction," *Acta Crystallogr., Sect. C: Cryst. Struct. Commun.*, vol. 41, no. 1, pp. 8–10, 1985.
- [145] A. Leclaire and M. M. Borel, "Le dichlorure et le dibromure de calcium hexahydrates," *Acta Crystallogr., Sect. B: Struct. Crystallogr. Cryst. Chem.*, vol. 33, no. 9, pp. 2938–2940, 1977.
- [146] G. Kresse and J. Furthmüller, "Efficient iterative schemes for ab initio total-energy calculations using a plane-wave basis set," *Phys. Rev. B*, vol. 54, no. 16, p. 11169, 1996.

- 
- [147] J. P. Perdew, K. Burke, and M. Ernzerhof, "Generalized gradient approximation made simple," *Phys. Rev. Lett.*, vol. 77, no. 18, p. 3865, 1996.
- [148] P. E. Blöchl, "Projector augmented-wave method," *Phys. Rev. B*, vol. 50, no. 24, p. 17953, 1994.
- [149] G. Kresse and D. Joubert, "From ultrasoft pseudopotentials to the projector augmented-wave method," *Phys. Rev. B*, vol. 59, no. 3, p. 1758, 1999.
- [150] S. Grimme, J. Antony, S. Ehrlich, and H. Krieg, "A consistent and accurate ab initio parametrization of density functional dispersion correction (DFT-D) for the 94 elements H-Pu," *The Journal of Chemical Physics*, vol. 132, no. 15, p. 154104, 2010.
- [151] S. Grimme, S. Ehrlich, and L. Goerigk, "Effect of the damping function in dispersion corrected density functional theory," *J. Comput. Chem.*, vol. 32, no. 7, pp. 1456–1465, 2011.
- [152] A. R. Oganov, A. O. Lyakhov, and M. Valle, "How evolutionary crystal structure prediction works - and why," *Acc. Chem. Res.*, vol. 44, no. 3, pp. 227–237, 2011.
- [153] P. V. Bushlanov, V. A. Blatov, and A. R. Oganov, "Topology-based crystal structure generator," *Comput. Phys. Commun.*, vol. 236, pp. 1–7, 2019.
- [154] A. O. Lyakhov, A. R. Oganov, and M. Valle, "Crystal structure prediction using evolutionary approach," *Mod. Methods Cryst. Struct. Predict.*, pp. 147–180, 2010.
- [155] T. A. Manz and N. G. Limas, "Introducing DDEC6 atomic population analysis: part 1. charge partitioning theory and methodology," *RSC Adv.*, vol. 6, no. 53, pp. 47771–47801, 2016.
- [156] N. G. Limas and T. A. Manz, "Introducing DDEC6 atomic population analysis: part 2. computed results for a wide range of periodic and nonperiodic materials," *RSC Adv.*, vol. 6, no. 51, pp. 45727–45747, 2016.
- [157] T. A. Manz, "Introducing DDEC6 atomic population analysis: part 3. comprehensive method to compute bond orders," *RSC Adv.*, vol. 7, no. 72, pp. 45552–45581, 2017.
- [158] T. Chen and T. A. Manz, "Bond orders of the diatomic molecules," *RSC Adv.*, vol. 9, no. 30, pp. 17072–17092, 2019.
- [159] R. Y. Rohling, I. C. Tranca, E. J. Hensen, and E. A. Pidko, "Correlations between density-based bond orders and orbital-based bond energies for chemical bonding analysis," *J. Phys. Chem. C*, vol. 123, no. 5, pp. 2843–2854, 2019.
- [160] I.-C. Man, I. Trancă, and S.-G. Soriga, "First principle studies of oxygen reduction reaction on n doped graphene: Impact of n concentration, position and co-adsorbate effect," *Appl. Surf. Sci.*, vol. 510, p. 145470, 2020.

- [161] R. Y. Rohling, I. C. Tranca, E. J. Hensen, and E. A. Pidko, "Electronic structure analysis of the diels–alder cycloaddition catalyzed by alkali-exchanged faujasites," *J. Phys. Chem. C*, vol. 122, no. 26, pp. 14733–14743, 2018.
- [162] R. F. W. Bader, "Atoms in molecules: A quantum theory," 1998.
- [163] D. Vega and D. Almeida, "AIM-UC: An application for QTAIM analysis," *J. Comput. Methods Sci. Eng.*, vol. 14, no. 1-3, pp. 131–136, 2014.
- [164] F. C. Matta and J. R. Boyd, "The quantum theory of atoms in molecules: From solid state to DNA and drug design," 2007.
- [165] D. Cremer and E. Kraka, "Chemical bonds without bonding electron density - does the difference electron-density analysis suffice for a description of the chemical bond?," *Angew. Chem., Int. Ed. Engl.*, vol. 23, no. 8, pp. 627–628, 1984.
- [166] J. R. Clark, H. T. Evans, and R. C. Erd, "Tachyhydrite, dimagnesium calcium chloride 12-hydrate," *Acta Crystallogr., Sect. B: Struct. Crystallogr. Cryst. Chem.*, vol. 36, no. 11, pp. 2736–2739, 1980.
- [167] A. Leclaire, M. M. Borel, and J. C. Monier, "Structure de la tachyhydrite," *Acta Crystallogr., Sect. B: Struct. Crystallogr. Cryst. Chem.*, vol. 36, pp. 2734–2735, 1980.
- [168] D. D. Wagman, W. H. Evans, V. B. Parker, R. H. Schumm, I. Halow, S. M. Bailey, K. L. Churney, and R. L. Nuttall, *The NBS tables of chemical thermodynamic properties. Selected values for inorganic and C1 and C2 organic substances in SI units*. 1982.
- [169] K. E. N'Tsoukpoe, T. Schmidt, H. U. Rammelberg, B. A. Watts, and W. K. Ruck, "A systematic multi-step screening of numerous salt hydrates for low temperature thermochemical energy storage," *Applied Energy*, vol. 124, pp. 1–16, 2014.
- [170] A. Gil, M. Medrano, I. Martorell, A. Lázaro, P. Dolado, B. Zalba, and L. F. Cabeza, "State of the art on high temperature thermal energy storage for power generation. part 1 - concepts, materials and modellization," *Renewable and sustainable energy reviews*, vol. 14, no. 1, pp. 31–55, 2010.
- [171] D. Zhu, H. Wu, and S. Wang, "Experimental study on composite silica gel supported CaCl<sub>2</sub> sorbent for low grade heat storage," *International Journal of Thermal Sciences*, vol. 45, no. 8, pp. 804–813, 2006.
- [172] H. U. Rammelberg, T. Schmidt, and W. Ruck, "Hydration and dehydration of salt hydrates and hydroxides for thermal energy storage-kinetics and energy release," *Energy Procedia*, vol. 30, pp. 362–369, 2012.
- [173] L. Greenspan, "Humidity fixed points of binary saturated aqueous solutions," *Journal of research of the national bureau of standards*, vol. 81, no. 1, pp. 89–96, 1977.
- [174] A. Lannung, "Dampfdruckmessungen des systems calciumchlorid–wasser," *Zeitschrift für anorganische und allgemeine Chemie*, vol. 228, no. 1, pp. 1–18, 1936.



- [175] T. Yamaguchi, S. Hayashi, and H. Ohtaki, "X-ray diffraction study of calcium (ii) chloride hydrate melts:  $\text{CaCl}_2 \cdot r\text{H}_2\text{O}$  ( $r = 4.0, 5.6, 6.0$ , and  $8.6$ ).," *Inorganic Chemistry*, vol. 28(12), pp. 2434–2439, 1989.
- [176] M. Molenda, J. Stengler, M. Linder, and A. Wörner, "Reversible hydration behavior of  $\text{CaCl}_2$  at high  $\text{H}_2\text{O}$  partial pressures for thermochemical energy storage," *Thermochimica acta*, vol. 560, pp. 76–81, 2013.
- [177] M. A. J. M. Beving, A. J. H. Frijns, C. C. M. Rindt, and D. M. J. Smeulders, "Effect of cycle-induced crack formation on the hydration behaviour of  $\text{K}_2\text{CO}_3$  particles: Experiments and modelling," *Thermochimica Acta*, vol. 692, p. 178752, 2020.
- [178] K. Posern and C. Kaps, "Calorimetric studies of thermochemical heat storage materials based on mixtures of  $\text{MgSO}_4$  and  $\text{MgCl}_2$ ," *Thermochimica Acta*, vol. 502, no. 1-2, pp. 73–76, 2010.
- [179] R. Cuypers, A. de Jong, J. Eversdijk, J. van't Spijker, H. Oversloot, B. Ingenhut, R. Cremers, and N. Papen-Botterhuis, "Microencapsulation of salts for enhanced thermochemical storage materials," in *40th Annual Meeting and Exposition of the Controlled Release Society, 21-24 July 2013, Honolulu, Hawaii, USA, 1-2, 2013*.
- [180] T. Kohler, T. Biedermann, and K. Müller, "Experimental study of  $\text{MgCl}_2 \cdot 6\text{H}_2\text{O}$  as thermochemical energy storage material," *Energy Technology*, vol. 6, no. 10, pp. 1935–1940, 2018.
- [181] Y. I. Aristov, M. Tokarev, G. Cacciola, and G. Restuccia, "Selective water sorbents for multiple applications, 1.  $\text{CaCl}_2$  confined in mesopores of silica gel: sorption properties," *Reaction Kinetics and Catalysis Letters*, vol. 59, no. 2, pp. 325–333, 1996.
- [182] J. Jänchen, D. Ackermann, E. Weiler, H. Stach, and W. Brösicke, "Calorimetric investigation on zeolites, alpo4's and  $\text{CaCl}_2$  impregnated attapulgit for thermochemical storage of heat," *Thermochimica Acta*, vol. 434, no. 1-2, pp. 37–41, 2005.
- [183] Y. Y. Tanashev, A. V. Krainov, and Y. I. Aristov, "Thermal conductivity of composite sorbents "salt in porous matrix" for heat storage and transformation," *Applied thermal engineering*, vol. 61, no. 2, pp. 401–407, 2013.
- [184] A. Svobodova-Sedlackova, C. Barreneche, G. Alonso, A. I. Fernandez, and P. Gamallo, "Effect of nanoparticles in molten salts—md simulations and experimental study," *Renewable Energy*, vol. 152, pp. 208–216, 2020.
- [185] A. Pathak, *In silico characterization of chloride-based salt hydrates for thermochemical heat storage: a multi-scale study*. PhD thesis, Technische Universiteit Eindhoven, 2017.
- [186] J. P. Perdew, J. A. Chevary, S. H. Vosko, K. A. Jackson, M. R. Pederson, D. J. Singh, and C. Fiolhais, "Atoms, molecules, solids, and surfaces: Applications of the generalized gradient approximation for exchange and correlation," *Physical Review B*, vol. 46, no. 11, p. 6671, 1992.

- [187] G. te Velde, F. M. Bickelhaupt, E. J. Baerends, C. Fonseca Guerra, S. J. A. van Gisbergen, J. G. Snijders, and T. Ziegler, "Chemistry with ADF," *J. Comput. Chem.*, vol. 22, no. 9, pp. 931–967, 2001.
- [188] C. F. Guerra, J. Snijders, G. T. te Velde, and E. J. Baerends, "Towards an order-n DFT method," *Theoretical Chemistry Accounts*, vol. 99, no. 6, pp. 391–403, 1998.
- [189] C. M. Widdifield and D. L. Bryce, "A multinuclear solid-state magnetic resonance and GIPAW DFT study of anhydrous calcium chloride and its hydrates," *Canadian Journal of Chemistry*, vol. 89, no. 7, pp. 754–763, 2011.
- [190] C. Ferchaud, "Experimental study of salt hydrates for thermochemical seasonal heat storage," *Technische Universiteit Eindhoven*, 2016.
- [191] R. Wyckoff, "Interscience publishers, new york, new york rocksalt structure," *Crystal structures*, vol. 1, pp. 85–237, 1963.
- [192] P. K. Schelling, S. R. Phillpot, and P. Keblinski, "Comparison of atomic-level simulation methods for computing thermal conductivity," *Physical Review B*, vol. 65, no. 14, p. 144306, 2002.
- [193] G. Chen, *Nanoscale energy transport and conversion: a parallel treatment of electrons, molecules, phonons, and photons*. Oxford university press, 2005.
- [194] P. Chantrenne and J.-L. Barrat, "Finite size effects in determination of thermal conductivities: comparing molecular dynamics results with simple models," *J. Heat Transfer*, vol. 126, no. 4, pp. 577–585, 2004.
- [195] H. Karamitaheri, N. Neophytou, M. K. Taheri, R. Faez, and H. Kosina, "Calculation of confined phonon spectrum in narrow silicon nanowires using the valence force field method," *Journal of electronic materials*, vol. 42, no. 7, pp. 2091–2097, 2013.
- [196] Z. Aksamija and I. Knezevic, "Anisotropy and boundary scattering in the lattice thermal conductivity of silicon nanomembranes," *Physical Review B*, vol. 82, no. 4, p. 045319, 2010.
- [197] A. McCurdy, H. Maris, and C. Elbaum, "Anisotropic heat conduction in cubic crystals in the boundary scattering regime," *Physical Review B*, vol. 2, no. 10, p. 4077, 1970.
- [198] K. Wang, J. Wu, R. Wang, and L. Wang, "Effective thermal conductivity of expanded graphite–CaCl<sub>2</sub> composite adsorbent for chemical adsorption chillers," *Energy conversion and management*, vol. 47, no. 13–14, pp. 1902–1912, 2006.
- [199] G. A. Lane, "Low temperature heat storage with phase change materials," *International Journal of Ambient Energy*, vol. 1, no. 3, pp. 155–168, 1980.
- [200] R. Rabani, G. Heidarinejad, J. Harting, and E. Shirani, "Interplay of wall force field and wall physical characteristics on interfacial phenomena of a nano-confined gas medium," *International Journal of Thermal Sciences*, vol. 153, p. 106394, 2020.

- 
- [201] R. J. Stevens, L. V. Zhigilei, and P. M. Norris, "Effects of temperature and disorder on thermal boundary conductance at solid–solid interfaces: Nonequilibrium molecular dynamics simulations," *International Journal of Heat and Mass Transfer*, vol. 50, no. 19-20, pp. 3977–3989, 2007.
- [202] M. Molenda, J. Stengler, M. Linder, and A. Wörner, "Reversible hydration behavior of  $\text{CaCl}_2$  at high  $\text{H}_2\text{O}$  partial pressures for thermochemical energy storage," *Thermochimica Acta*, vol. 560, pp. 76–81, 2013.
- [203] J. Y. Wu, Q. L. Liu, Y. Xiong, A. M. Zhu, and Y. Chen, "Molecular simulation of water/alcohol mixtures' adsorption and diffusion in zeolite 4A membranes," *The Journal of Physical Chemistry B*, vol. 113, no. 13, pp. 4267–4274, 2009.
- [204] D. Dubbeldam and R. Snurr, "Recent developments in the molecular modeling of diffusion in nanoporous materials," *Molecular Simulation*, vol. 33, no. 4-5, pp. 305–325, 2007.
- [205] L. F. M. Franco, M. Castier, and I. G. Economou, "Anisotropic parallel self-diffusion coefficients near the calcite surface: A molecular dynamics study," *The Journal of chemical physics*, vol. 145, no. 8, p. 084702, 2016.
- [206] P. Liu, E. Harder, and B. Berne, "On the calculation of diffusion coefficients in confined fluids and interfaces with an application to the liquid-vapor interface of water," *The Journal of Physical Chemistry B*, vol. 108, no. 21, pp. 6595–6602, 2004.
- [207] M. V. Smoluchowski, "Über brownische molekularbewegung unter einwirkung äußerer kräfte und deren zusammenhang mit der verallgemeinerten diffusionsgleichung," *Annalen der Physik*, vol. 353, no. 24, pp. 1103–1112, 1916.
- [208] G. Hummer, "Position-dependent diffusion coefficients and free energies from bayesian analysis of equilibrium and replica molecular dynamics simulations," *New Journal of Physics*, vol. 7, no. 1, p. 34, 2005.
- [209] L. F. Mercier Franco, M. Castier, and I. G. Economou, "Diffusion in homogeneous and in inhomogeneous media: a new unified approach," *Journal of chemical theory and computation*, vol. 12, no. 11, pp. 5247–5255, 2016.
- [210] W. C. Swope, H. C. Andersen, P. H. Berens, and K. R. Wilson, "A computer simulation method for the calculation of equilibrium constants for the formation of physical clusters of molecules: Application to small water clusters," *The Journal of chemical physics*, vol. 76, no. 1, pp. 637–649, 1982.
- [211] H. J. Berendsen, J. v. Postma, W. F. van Gunsteren, A. DiNola, and J. R. Haak, "Molecular dynamics with coupling to an external bath," *The Journal of chemical physics*, vol. 81, no. 8, pp. 3684–3690, 1984.
- [212] B. Guillot, "A reappraisal of what we have learnt during three decades of computer simulations on water," *Journal of Molecular Liquids*, vol. 101, no. 1, pp. 219–260, 2002. Molecular Liquids. Water at the New Millenium.

- [213] A. Luzar, S. Svetina, and B. Žekš, "The contribution of hydrogen bonds to the surface tension of water," *Chemical Physics Letters*, vol. 96, no. 4, pp. 485–490, 1983.
- [214] Q. Du, R. Superfine, E. Freysz, and Y. R. Shen, "Vibrational spectroscopy of water at the vapor/water interface," *Physical Review Letters*, vol. 70, no. 15, p. 2313, 1993.
- [215] D. Dubbeldam, S. Calero, and T. J. H. Vlugt, "iRASP: GPU-accelerated visualization software for materials scientists," *Molecular Simulation*, vol. 44, no. 8, pp. 653–676, 2018.
- [216] H. P. Huinink and D. Zahn, "Elucidating water dynamics in  $\text{MgCl}_2$  hydrates from molecular dynamics simulation," *Solid State Sciences*, vol. 69, pp. 64–70, 2017.
- [217] M. Zhang, Q. Dai, H. Zheng, M. Chen, and L. Dai, "Novel MOF-derived Co@N-C bifunctional catalysts for highly efficient Zn–air batteries and water splitting," *Advanced Materials*, vol. 30, no. 10, p. 1705431, 2018.
- [218] R. W. Flaig, T. M. Osborn Popp, A. M. Fracaroli, E. A. Kapustin, M. J. Kalmutzki, R. M. Altamimi, F. Fathieh, J. A. Reimer, and O. M. Yaghi, "The chemistry of  $\text{CO}_2$  capture in an amine-functionalized metal–organic framework under dry and humid conditions," *Journal of the American Chemical Society*, vol. 139, no. 35, pp. 12125–12128, 2017.
- [219] L.-C. Lin, A. H. Berger, R. L. Martin, J. Kim, J. A. Swisher, K. Jariwala, C. H. Rycroft, A. S. Bhowm, M. W. Deem, M. Haranczyk, and B. Smit, "In silico screening of carbon-capture materials," *Nature materials*, vol. 11, no. 7, pp. 633–641, 2012.
- [220] Y. Liu, Y. Yang, Q. Sun, Z. Wang, B. Huang, Y. Dai, X. Qin, and X. Zhang, "Chemical adsorption enhanced  $\text{CO}_2$  capture and photoreduction over a copper porphyrin based metal organic framework," *ACS applied materials & interfaces*, vol. 5, no. 15, pp. 7654–7658, 2013.
- [221] Y. Xie, Z. Fang, L. Li, H. Yang, and T.-F. Liu, "Creating chemisorption sites for enhanced  $\text{CO}_2$  photoreduction activity through alkylamine modification of MIL-101-Cr," *ACS applied materials & interfaces*, vol. 11, no. 30, pp. 27017–27023, 2019.
- [222] M. Ramdin, S. P. Balaji, J. M. Vicent-Luna, J. J. Gutierrez-Sevillano, S. Calero, T. W. de Loos, and T. J. H. Vlugt, "Solubility of the precombustion gases  $\text{CO}_2$ ,  $\text{CH}_4$ ,  $\text{CO}$ ,  $\text{H}_2$ ,  $\text{N}_2$ , and  $\text{H}_2\text{S}$  in the ionic liquid [bmim][Tf<sub>2</sub>N] from Monte Carlo simulations," *The Journal of Physical Chemistry C*, vol. 118, no. 41, pp. 23599–23604, 2014.
- [223] M. Ramdin, S. Jamali, T. Becker, and T. J. H. Vlugt, "Gibbs ensemble Monte Carlo simulations of multicomponent natural gas mixtures," *Molecular Simulation*, vol. 44, no. 5, pp. 377–383, 2018.
- [224] J. R. Rostrup-Nielsen, "Production of synthesis gas," *Catalysis today*, vol. 18, no. 4, pp. 305–324, 1993.

- 
- [225] A. Poursaeidesfahani, M. F. de Lange, F. Khodadadian, D. Dubbeldam, M. Rigutto, N. Nair, and T. J. H. Vlucht, "Product shape selectivity of MFI-type, MEL-type, and BEA-type zeolites in the catalytic hydroconversion of heptane," *Journal of Catalysis*, vol. 353, pp. 54–62, 2017.
- [226] A. Z. Panagiotopoulos, "Direct determination of phase coexistence properties of fluids by Monte Carlo simulation in a new ensemble," *Molecular Physics*, vol. 61, no. 4, pp. 813–826, 1987.
- [227] A. Z. Panagiotopoulos, N. Quirke, M. Stapleton, and D. J. Tildesley, "Phase equilibria by simulation in the Gibbs ensemble: alternative derivation, generalization and application to mixture and membrane equilibria," *Molecular Physics*, vol. 63, no. 4, pp. 527–545, 1988.
- [228] I. Matito-Martos, J. Álvarez-Ossorio, J. J. Gutiérrez-Sevillano, M. Doblaré, A. Martín-Calvo, and S. Calero, "Zeolites for the selective adsorption of sulfur hexafluoride," *Physical Chemistry Chemical Physics*, vol. 17, no. 27, pp. 18121–18130, 2015.
- [229] J. L. Abascal and C. Vega, "A general purpose model for the condensed phases of water: TIP4P/2005," *The Journal of Chemical Physics*, vol. 123, no. 23, p. 234505, 2005.
- [230] J. J. Potoff and J. I. Siepmann, "Vapor–liquid equilibria of mixtures containing alkanes, carbon dioxide, and nitrogen," *AIChE journal*, vol. 47, no. 7, pp. 1676–1682, 2001.
- [231] Y. Liu and W. A. Goddard III, "First-principles-based dispersion augmented density functional theory: From molecules to crystals," *The Journal of Physical Chemistry Letters*, vol. 1, no. 17, pp. 2550–2555, 2010.
- [232] M. J. McGrath, I.-F. W. Kuo, J. N. Ghogomu, C. J. Mundy, and J. I. Siepmann, "Vapor–liquid coexistence curves for methanol and methane using dispersion-corrected density functional theory," *The Journal of Physical Chemistry B*, vol. 115, no. 40, pp. 11688–11692, 2011.
- [233] M. D. Baer, C. J. Mundy, M. J. McGrath, I.-F. W. Kuo, J. I. Siepmann, and D. J. Tobias, "Re-examining the properties of the aqueous vapor–liquid interface using dispersion corrected density functional theory," *The Journal of Chemical Physics*, vol. 135, no. 12, p. 124712, 2011.
- [234] L. Liu, Y. Liu, S. V. Zybin, H. Sun, and W. A. Goddard III, "ReaxFF-Ig: Correction of the ReaxFF reactive force field for london dispersion, with applications to the equations of state for energetic materials," *The Journal of Physical Chemistry A*, vol. 115, no. 40, pp. 11016–11022, 2011.
- [235] M. Ramdin, T. M. Becker, S. H. Jamali, M. Wang, and T. J. H. Vlucht, "Computing equation of state parameters of gases from Monte Carlo simulations," *Fluid Phase Equilibria*, vol. 428, pp. 174–181, 2016.

- [236] C. Vega, J. Abascal, and I. Nezbeda, "Vapor-liquid equilibria from the triple point up to the critical point for the new generation of TIP4P-like models: TIP4P/ew, TIP4P/2005, and TIP4P/ice," *The Journal of Chemical Physics*, vol. 125, no. 3, p. 034503, 2006.
- [237] R. Span and W. Wagner, "A new equation of state for carbon dioxide covering the fluid region from the triple-point temperature to 1100 K at pressures up to 800 MPa," *Journal of physical and chemical reference data*, vol. 25, no. 6, pp. 1509–1596, 1996.
- [238] W. Wagner and A. Pruß, "The iapws formulation 1995 for the thermodynamic properties of ordinary water substance for general and scientific use," *Journal of Physical and Chemical Reference Data*, vol. 31, no. 2, pp. 387–535, 2002.
- [239] G. O. A. Janssens, B. G. Baekelandt, H. Toufar, W. J. Mortier, and R. A. Schoonheydt, "Comparison of cluster and infinite crystal calculations on zeolites with the electronegativity equalization method (EEM)," *The Journal of Physical Chemistry*, vol. 99, no. 10, pp. 3251–3258, 1995.
- [240] A. K. Rappé, C. J. Casewit, K. S. Colwell, W. A. Goddard III, and W. M. Skiff, "UFF, a full periodic table force field for molecular mechanics and molecular dynamics simulations," *Journal of the American chemical society*, vol. 114, no. 25, pp. 10024–10035, 1992.
- [241] E. Iype, "In silico characterisation of magnesium salt hydrates as energy storage materials," 2014.
- [242] S. Kirkpatrick, C. D. Gelatt, and M. P. Vecchi, "Optimization by simulated annealing," *Science*, vol. 220, no. 4598, pp. 671–680, 1983.
- [243] S. Pongsai, "Combination of the metropolis Monte Carlo and lattice statics method for geometry optimization of H-(Al)-ZSM-5," *Journal of computational chemistry*, vol. 31, no. 10, pp. 1979–1985, 2010.
- [244] A. Caflisch, P. Niederer, and M. Anliker, "Monte Carlo minimization with thermalization for global optimization of polypeptide conformations in cartesian coordinate space," *Proteins: Structure, Function, and Bioinformatics*, vol. 14, no. 1, pp. 102–109, 1992.
- [245] Y. Zhang and W. Yang, "Comment on "generalized gradient approximation made simple"," *Physical Review Letters*, vol. 80, no. 4, p. 890, 1998.
- [246] E. Caldeweyher, S. Ehlert, A. Hansen, H. Neugebauer, S. Spicher, C. Bannwarth, and S. Grimme, "A generally applicable atomic-charge dependent london dispersion correction," *The Journal of chemical physics*, vol. 150, no. 15, p. 154122, 2019.
- [247] S. Grimme, "Density functional theory with london dispersion corrections," *Wiley Interdisciplinary Reviews: Computational Molecular Science*, vol. 1, no. 2, pp. 211–228, 2011.

- 
- [248] M. K. Rana, H. S. Koh, J. Hwang, and D. J. Siegel, "Comparing van der waals density functionals for CO<sub>2</sub> adsorption in metal organic frameworks," *The Journal of Physical Chemistry C*, vol. 116, no. 32, pp. 16957–16968, 2012.
- [249] D. Dubbeldam, S. Calero, D. E. Ellis, and R. Q. Snurr, "Raspa: molecular simulation software for adsorption and diffusion in flexible nanoporous materials," *Molecular Simulation*, vol. 42, no. 2, pp. 81–101, 2016.
- [250] T. J. H. Vlugt, M. G. Martin, B. Smit, J. I. Siepmann, and R. Krishna, "Improving the efficiency of the configurational-bias Monte Carlo algorithm," *Molecular Physics*, vol. 94, no. 4, pp. 727–733, 1998.
- [251] G. A. Orozco, I. G. Economou, and A. Z. Panagiotopoulos, "Optimization of intermolecular potential parameters for the CO<sub>2</sub>/H<sub>2</sub>O mixture," *The Journal of Physical Chemistry B*, vol. 118, no. 39, pp. 11504–11511, 2014.
- [252] H. D. B. Jenkins and L. Glasser, "Difference rule a new thermodynamic principle: Prediction of standard thermodynamic data for inorganic solvates," *Journal of the American Chemical Society*, vol. 126, no. 48, pp. 15809–15817, 2004.
- [253] L. Glasser, "Thermodynamics of inorganic hydration and of humidity control, with an extensive database of salt hydrate pairs," *Journal of Chemical & Engineering Data*, vol. 59, no. 2, pp. 526–530, 2014.
- [254] W. Shi and E. J. Maginn, "Continuous fractional component Monte Carlo: an adaptive biasing method for open system atomistic simulations," *Journal of chemical theory and computation*, vol. 3, no. 4, pp. 1451–1463, 2007.
- [255] T. W. Rosch and E. J. Maginn, "Reaction ensemble monte carlo simulation of complex molecular systems," *J. Chem. Theory Comput.*, vol. 7, no. 2, pp. 269–279, 2011.
- [256] T. P. Senftle, M. J. Janik, and A. C. T. Van Duin, "A ReaxFF investigation of hydride formation in palladium nanoclusters via Monte Carlo and molecular dynamics simulations," *The Journal of Physical Chemistry C*, vol. 118, no. 9, pp. 4967–4981, 2014.
- [257] T. P. Senftle, R. J. Meyer, M. J. Janik, and A. C. T. van Duin, "Development of a ReaxFF potential for Pd/O and application to palladium oxide formation," *The Journal of chemical physics*, vol. 139, no. 4, p. 044109, 2013.
- [258] P. Valentini, T. E. Schwartzentruber, and I. Cozmuta, "ReaxFF grand canonical Monte Carlo simulation of adsorption and dissociation of oxygen on platinum (111)," *Surface science*, vol. 605, no. 23-24, pp. 1941–1950, 2011.
- [259] B. Kirchhoff, L. Braunwarth, C. Jung, H. Jónsson, D. Fantauzzi, and T. Jacob, "Simulations of the oxidation and degradation of platinum electrocatalysts," *Small*, vol. 16, no. 5, p. 1905159, 2020.

- [260] M. M. Islam, A. Ostadhossein, O. Borodin, A. T. Yeates, W. W. Tipton, R. G. Hennig, N. Kumar, and A. C. T. Van Duin, "ReaxFF molecular dynamics simulations on lithiated sulfur cathode materials," *Physical Chemistry Chemical Physics*, vol. 17, no. 5, pp. 3383–3393, 2015.
- [261] C. K. Jung, L. Braunwarth, and T. Jacob, "Grand canonical ReaxFF molecular dynamics simulations for catalytic reactions," *Journal of chemical theory and computation*, vol. 15, no. 11, pp. 5810–5816, 2019.
- [262] R. Q. Snurr, A. T. Bell, and D. N. Theodorou, "Prediction of adsorption of aromatic hydrocarbons in silicalite from grand canonical Monte Carlo simulations with biased insertions," *The Journal of Physical Chemistry*, vol. 97, no. 51, pp. 13742–13752, 1993.
- [263] T. J. H. Vlugt, R. Krishna, and B. Smit, "Molecular simulations of adsorption isotherms for linear and branched alkanes and their mixtures in silicalite," *The Journal of Physical Chemistry B*, vol. 103, no. 7, pp. 1102–1118, 1999.
- [264] A. Rahbari, R. Hens, M. Ramdin, O. A. Moulτος, D. Dubbeldam, and T. J. H. Vlugt, "Recent advances in the continuous fractional component Monte Carlo methodology," *Molecular Simulation*, vol. 47, pp. 804–823, 2021.
- [265] J. D. Weeks, D. Chandler, and H. C. Andersen, "Role of repulsive forces in determining the equilibrium structure of simple liquids," *The Journal of chemical physics*, vol. 54, no. 12, pp. 5237–5247, 1971.
- [266] B. Chen and J. I. Siepmann, "A novel monte carlo algorithm for simulating strongly associating fluids: Applications to water, hydrogen fluoride, and acetic acid," *The Journal of Physical Chemistry B*, vol. 104, no. 36, pp. 8725–8734, 2000.
- [267] D.-Y. Peng and D. B. Robinson, "A new two-constant equation of state," *Industrial & Engineering Chemistry Fundamentals*, vol. 15, no. 1, pp. 59–64, 1976.
- [268] R. C. Reid, J. M. Prausnitz, and T. K. Sherwood, *The properties of gases and liquids, Third Edition*. McGraw-Hill, New York, 1977.
- [269] A. Liu, X. Peng, Q. Jin, S. K. Jain, J. M. Vicent-Luna, S. Calero, and D. Zhao, "Adsorption and diffusion of benzene in Mg-MOF-74 with open metal sites," *ACS Applied Materials & Interfaces*, vol. 11, no. 4, pp. 4686–4700, 2019.
- [270] A. Luna-Triguero, J. M. Vicent-Luna, A. Poursaeidesfahani, T. J. H. Vlugt, R. Sánchez-de Armas, P. Gómez-Álvarez, and S. Calero, "Improving olefin purification using metal organic frameworks with open metal sites," *ACS Applied Materials & Interfaces*, vol. 10, no. 19, pp. 16911–16917, 2018.
- [271] J. Kuhn, J. M. Castillo-Sanchez, J. Gascon, S. Calero, D. Dubbeldam, T. J. H. Vlugt, F. Kapteijn, and J. Gross, "Adsorption and diffusion of water, methanol, and ethanol in all-silica DD3R: experiments and simulation," *The Journal of Physical Chemistry C*, vol. 113, no. 32, pp. 14290–14301, 2009.



- 
- [272] V. Lachet, A. Boutin, B. Tavitian, and A. H. Fuchs, "Grand canonical Monte Carlo simulations of adsorption of mixtures of xylene molecules in faujasite zeolites," *Faraday Discussions*, vol. 106, pp. 307–323, 1997.
- [273] J. Sun, F. Wang, Y. Sui, Z. She, W. Zhai, C. Wang, and Y. Deng, "Effect of particle size on solubility, dissolution rate, and oral bioavailability: evaluation using coenzyme q10 as naked nanocrystals," *International journal of nanomedicine*, vol. 7, p. 5733, 2012.
- [274] G. C. Sosso, J. Chen, S. J. Cox, M. Fitzner, P. Pedevilla, A. Zen, and A. Michaelides, "Crystal nucleation in liquids: Open questions and future challenges in molecular dynamics simulations," *Chemical reviews*, vol. 116, no. 12, pp. 7078–7116, 2016.
- [275] A. Stukowski, "Visualization and analysis of atomistic simulation data with OVITO-the Open Visualization Tool," *MODELLING AND SIMULATION IN MATERIALS SCIENCE AND ENGINEERING*, vol. 18, no. 1, 2010.
- [276] L. Glasser, "Thermodynamics of inorganic hydration and of humidity control, with an extensive database of salt hydrate pairs," *Journal of Chemical & Engineering Data*, vol. 59, no. 2, pp. 526–530, 2014.
- [277] S. Katyal, "Experimental assessment of mixed salt hydrates for thermochemical energy storage," 2020.
- [278] I. Tranca and A. Shkatulov, "private communication," 2021.
- [279] F. Guo, Y.-S. Wen, S.-Q. Feng, X.-D. Li, H.-S. Li, S.-X. Cui, Z.-R. Zhang, H.-Q. Hu, G.-Q. Zhang, and X.-L. Cheng, "Intelligent-reaxff: Evaluating the reactive force field parameters with machine learning," *Computational Materials Science*, vol. 172, p. 109393, 2020.
- [280] P. Yoo, M. Sakano, S. Desai, M. M. Islam, P. Liao, and A. Strachan, "Neural network reactive force field for c, h, n, and o systems," *npj Computational Materials*, vol. 7, no. 1, pp. 1–10, 2021.
- [281] L. Zhang, D.-Y. Lin, H. Wang, R. Car, and W. E, "Active learning of uniformly accurate interatomic potentials for materials simulation," *Phys. Rev. Materials*, vol. 3, p. 023804, Feb 2019.
- [282] R. Jinnouchi, K. Miwa, F. Karsai, G. Kresse, and R. Asahi, "On-the-fly active learning of interatomic potentials for large-scale atomistic simulations," *The Journal of Physical Chemistry Letters*, vol. 11, no. 17, pp. 6946–6955, 2020.
- [283] P. J. Olver, *Introduction to partial differential equations*. Springer, 2014.
- [284] G. N. I. Clark, C. D. Cappa, J. D. Smith, R. J. Saykally, and T. Head-Gordon, "The structure of ambient water," *Molecular Physics*, vol. 108, no. 11, pp. 1415–1433, 2010.



# ACKNOWLEDGEMENTS

This dissertation is the result of four years of research at the Eindhoven University of Technology. The process was sometimes tough but mostly a joyful, exciting, and learning full ride. During this period, actually already from my first year of study, the university was much more than a daily workplace; it shaped me into who I am today. As a Ph.D. candidate, some tasks had to be done on my own, but fortunately, most parts were shared with colleagues, friends (in- and outside the university), and family. Therefore, I want to show my gratitude to those who joined me on this ride and without whom this dissertation was not as it is now.

First of all, I would like to thank Silvia Gaastra–Nedea, who not only supervised me the past four years but already since I started my masters' graduation project. Silvia, you made me interested in the field of Molecular Dynamics, I learned a lot from you during our fruitful discussions, and you pointed me in the right direction when I was lost. I would like to thank my promoter prof. David Smeulders for his advice and for giving me the opportunity as a PhD candidate. I would also like to express my great appreciation to all committee members, prof. Vianney Koelman, prof. Sofia Calero, prof. Thijs Vlugt, prof. Luisa Cabeza, prof. Evert Jan Meijer, and prof. Jens Harting, for assessing my manuscript. On top of that, I would emphasize my thanks to prof. Thijs Vlugt for his needful advice on Monte Carlo simulations.

I would like to give special thanks to Ionut Tranca, who introduced me to the world of DFT and was a sparring partner during many rewarding technical discussions. You helped me a lot and definitely contributed to the outcome of this manuscript. I would like to thank Amar Pathak, who gave me a head-start on reactive force field simulations. I would also like to thank all supervised students who contributed in their own way to my research and dissertation. Especially Sophie and Bern, for their thorough and dedicated work.

Furthermore, I would like to thank my colleagues. Jan Hasker for assistance on IT-related tasks, without whom my computational research could not be done. Linda Essink for assistance on many overall necessary tasks. Of course also big thanks to my friends, office mates, and coffee break group, Max, Luca, Mauro, Ruud, Menting, Shahin, Shravan, Raluca, Manoj, Camila, Sebastian, Hakan, Özer, Jaap, Jan-Paul, Cong, Mohammadreza, Qiang, Ruben, Patty, and Svetlana. Next to the countless coffees, we had some nice parties, movie nights, drinks, dinners, Thursday fry-days, and many more activities outside office hours. I am glad that the university's closing due to the COVID measurements did not withhold us from reaching out. Ruud, we had some good evening runs. Shahin, thanks for the good moments outside our shared MD struggles. Luca and Mauro, you taught me how to express yourself without words, introduced me to your delicious cui-

sine, and taught me that food is much more than just fuel for your body. Of course, I will also not forget Max's never saturated stomach for cakes and his sense of humor.

Als laatste zou ik mijn familie en vrienden buiten de PhD willen bedanken. Mijn vrienden voor alle geweldige avonturen, mooie avonden onder het genot van een biertje en gedeelde sport momenten. Mijn schoonfamilie en niet alleen voor jullie oudste dochter / zus maar ook omdat jullie, ondanks dat het niet altijd te volgen was, toch geïnteresseerd bleven luisteren naar waar ik nu toch eigenlijk mee bezig was. Tante Greetje en ome Nico voor het lekkere eten en jullie interesse in mijn voortgang. Mijn zussen, voor het er altijd voor me te zijn, ik ben trots op jullie en natuurlijk ook op mijn neefjes en nichtje. Mijn ouders, pap, mam, bedankt. Zonder jullie motivatie, steun en vertrouwen was ik niet waar ik nu ben en ik kon ik niet zeggen dat de 'formule' nu wel af is. Natuurlijk wil ik ook mijn vrouw en liefde Sophie bedanken, voor haar steun tijdens alle ups en downs, op wie ik altijd kan terugvallen, wie me weer motiveert precies op het moment dat nodig is en wie me altijd een glimlach bezorgt.

*Every morning in Africa, a gazelle wakes up, it knows it must outrun the fastest lion or it will be killed. Every morning in Africa, a lion wakes up, it knows it must run faster than the slowest gazelle, or it will starve. It doesn't matter whether you're the lion or a gazelle. When the sun comes up, you'd better be running.*

Dan Montano

# CURRICULUM VITÆ

## Koen HEIJMANS

Koen Heijmans was born on the 7th of November 1990. He received his Bachelor of Science in Architecture, Building and Planning in 2013 at Eindhoven University of Technology, specializing in Climatic Design. After some extracurricular activities, he started in 2014 the master program Sustainable Energy Technology at the Mechanical Engineering department of Eindhoven University of Technology and received his Master of Science degree in 2017. After which he started as a Ph.D. candidate within the Energy Technology group of David Smeulders in the Mechanical Engineering department of the Eindhoven University of technology. Under the supervision of Silvia Gaastra-Nedea, he performed numerical molecular level research on thermochemical heat storage materials. The results of this research are presented in this dissertation. Next to the Ph.D. research, he was a teaching assistant for the *Heat and flow in microsystems* and assisted the development of two Coursera courses, namely *Microscale Modeling of Heat Storage Materials*, and *Thermal Energy Storage & Demand*.



# LIST OF PUBLICATIONS

## JOURNAL PUBLICATIONS

- **Heijmans, K.**, Pathak, A.D., Solano-López, P., Giordano, D., Nedeá, S. and Smeulders, D., Thermal boundary characteristics of homo-/heterogeneous interfaces. *Nanomaterials*, 9(5), p.663. (2019)
- **Heijmans, K.**, Tranca, I.C., Gaastra-Nedeá, S.V. and Smeulders, D.M.J., Exploring the Electronic Structure of New Doped Salt Hydrates,  $\text{Mg}_{1-x}\text{Ca}_x\text{Cl}_2 \cdot n\text{H}_2\text{O}$ , for Thermochemical Energy Storage. *The Journal of Physical Chemistry C*, 124(45), pp.24580-24591 (2020)
- Pathak, A.D., **Heijmans, K.**, Nedeá, S., van Duin, A.C., Zondag, H., Rindt, C. and Smeulders, D., Mass diffusivity and thermal conductivity estimation of chloride-based salt hydrates for thermo-chemical heat storage: A molecular dynamics study using the reactive force field. *International Journal of Heat and Mass Transfer*, 149, p.119090. (2020)
- **Heijmans, K.**, Tranca, I.C., Smeulders, D.M.J., Vlugt, T.J.H. and Gaastra-Nedeá, S.V., Gibbs Ensemble Monte Carlo for Reactive Force Fields to Determine the Vapor-Liquid Equilibrium of  $\text{CO}_2$  and  $\text{H}_2\text{O}$ . *Journal of Chemical Theory and Computation*, 17(1), 322–329 (2021)
- **Heijmans, K.**, Klein Holkenborg, B., Nab, S., Pathak, A.D., Gaastra-Nedeá, S.V. and Smeulders, D.M.J., Development of a Reactive Force Field for  $\text{CaCl}_2 \cdot n\text{H}_2\text{O}$ , and the Application to Thermochemical Energy Storage. *Computational Material Science*, 197, 110595 (2021)
- **Heijmans, K.**, Tranca, I.C., Chang, M.-W., Vlugt, T.J.H. Gaastra-Nedeá, S.V. and Smeulders, D.M.J., Reactive Grand-Canonical Monte Carlo Simulations for Modeling Hydration of  $\text{MgCl}_2$  *ACS Omega* (2021)
- **Heijmans, K.**, Klein Holkenborg, B., Gaastra-Nedeá, S., Smeulders, D. Advanced diffusion methods for  $\text{H}_2\text{O}$  in salt hydrates *submitted*
- Goga, N., Maryhofer, L., Tranca, I., Nedeá, S., **Heijmans, K.**, Ponnuchamy, V., Vasilateanu, A., A Review of Recent Developments in Molecular Dynamics Simulations of the Photoelectrochemical Water Splitting Process, *Catalysts*, 11(7), 807, (2021)

## CONFERENCE PROCEEDINGS

- **Heijmans, K.**, Gaastra-Nedeá, S., Thermal characteristics of reactive solid interfaces. *Proceedings of the 5th European Conference on Microfluidics –  $\mu\text{Flu}18$  3rd European Conference on Non-Equilibrium Gas Flows* 132, 28 feb 2018
- **Heijmans, K.**, Tranca, I., Gaastra - Nedeá, S., and Smeulders, D., Ab-initio study of doped salt hydrates crystal stabilities for thermochemical heat storage. *Eurotherm Seminar #112 Advances in Thermal Energy Storage* 123-132 E150, June 2019